Spintronic terahertz emitters based on ferro- and ferrimagnetic thin film systems

Dissertation

zur Erlangung des akademischen Grades
Dr. rer. nat.

eingereicht an der
Mathematisch-Naturwissenschaftlich-Technischen Fakultät
der Universität Augsburg

von
Mario Fix

Augsburg, April 2022

Erstgutachter: Prof. Dr. Manfred Albrecht

Zweitgutachter: Prof. Dr. Rudolf Bratschitsch

Datum der mündlichen Prüfung: 19.07.2022

Contents

CHAPTER 1

Introduction

Terahertz (THz) electromagnetic radiation is loosely defined by the frequency range of 0.1–30 THz. [1] It is located in the electromagnetic spectrum between the microwave and the mid-infrared bands and has, in historical context, also been referred to as far-infrared or sub-millimeter radiation (see figure 1.1). [2] Applications for this frequency band can be found, for example, in wireless communication technologies [3–5] and security imaging [6–8], for which typically continuous THz sources are applied. On the other hand, also a great variety of applications are enabled by pulsed broadband THz sources. [9] In many materials, molecular rotations and vibrations, as well as phonons in crystalline materials, can be excited by THz radiation. [10] Thus, the specific absorption spectra offer a fingerprint of certain materials [2] and, in particular, make THz time-domain spectroscopy (THz-TDS) a powerful characterization tool that can be applied for biomedical applications [10, 11], industrial process monitoring [12–14], and for fundamental studies of condensed matter [15]. Recently, also several studies on nonlinear THz responses of materials have been realized by using strong THz fields. [16–19] Such experiments can, for example, offer new insights into spin-lattice coupling [20, 21] or open a novel way for the manipulation of the magnetic order in a material [22, 23].

The first investigations in the THz frequency regime can be traced back to measurements of the solar spectrum by astronomers in the late 18$^{\text{th}}$ century with the bolometers newly invented

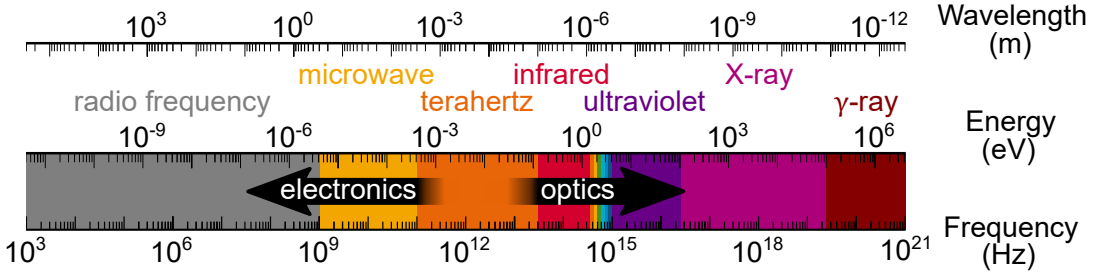

Figure 1.1: Comparison of the frequencies, energies, and wavelengths of the electromagnetic spectrum from radio frequencies to γ-rays.

back then. [24, 25] Despite the great variety of possible applications, until the end of the 19$^{\text{th}}$ century, THz spectroscopy has been mainly used by astronomers and Earth scientists for remote sensing of thermal emission lines of light molecules. [26] This is owed to the fact that, in contrast to the neighboring frequency bands, emitters and detectors for the THz band have been rather limited. The well-established emission and detection techniques based on electronic devices work efficiently only up to frequencies in the high gigahertz regime. On the other hand, optical techniques that are based on interband transitions can be used down to several tens of THz. Thus, for a long time, the intermediate band has been referred to as the so-called THz gap. [10] In the last decades, this gap has been gradually filled by a variety of different emitter types. As continuous-wave sources, quantum cascade lasers [27–29], as well as, for the lower THz regime, Schottky-diode-based multipliers [30, 31], photomixers [5, 32], and transistor-based integrated circuits [33, 34] have been established. Furthermore, since the development of the first photoconductive emitter driven by excitation with short optical pulses in 1975 [35], also a great variety of pulsed broadband THz emitter systems, optically driven by femtosecond laser pulses, has been developed. This progress in tabletop emitter systems, which especially has been driven by improvements in the ultrafast laser technologies, opened the way for THz-TDS [36] and also THz-TDS imaging [37]. An overview of the approximate spectral coverage and the peak electric fields emitted by different emitter types is shown in figure 1.2. THz emitting photoconductive antennas (PCAs) typically consist of metal contacts deposited with a gap of several micrometers on photoconductive substrates such as, for example, GaAs [38–43], InGaAs [44–46], or ZnSe [47]. Photoexcited charge carriers that are accelerated by an externally applied bias field lead to the emission of THz radiation. [48] A different class of pulsed THz emitters are nonlinear crystals such as inorganic ZnTe [49–53], GaP [54], and $LiNbO_3$ [55, 56], as well as organic compounds abbreviated by DAST [57, 58], DSTMS [57, 59–61], and OH1 [57, 60]. The laser-excited THz emission of these systems is based on optical rectification, a second-order nonlinear optical process, and was first demonstrated in $LiNbO_3$ in 1971. [62, 63] Another THz emission process is based on laser-excited plasma generation and has been first demonstrated in 1993. [64] With this emitter type, gapless bandwidths of more than 100 THz have been realized, which are limited only by the length of the excitation pulses. [65, 66] Nevertheless, all of the emitter types mentioned above suffer from different disadvantages [67, 68]: The polar semiconductors typically applied in PCAs have strong optical phonon resonances in the THz regime, leading to gaps in the emission spectra. Besides, PCAs have relatively high fabrication costs due to the necessary microlithography. One of the key drawbacks of emitters based on optical rectification in inorganic, nonlinear crystals is that the group velocity of the optical pump pulse needs to match the THz phase velocity in order to achieve a high THz output. Furthermore, also in these emitters, optical phonons cause a THz absorbing Reststrahlen band that leads to substantial gaps in the emission spectra. In nonlinear organic crystals, vibrational absorption bands lead to gaps in the frequency region from 0.1–10 THz. For THz generation based on

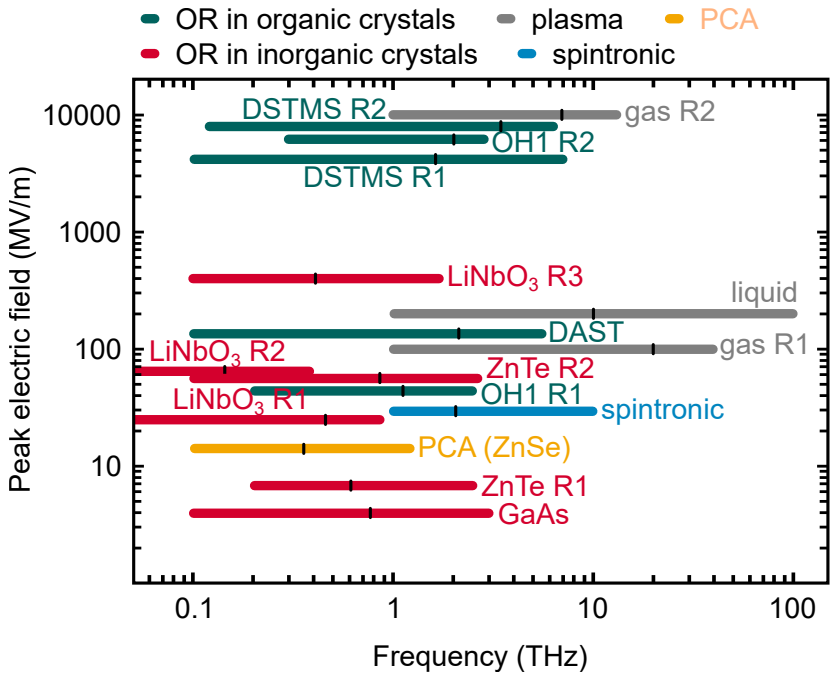

Figure 1.2: Comparison between different laser-driven pulsed THz emitters based on optical rectification (OR) in inorganic and organic crystals, laser-induced plasma generation in liquids and gases, spintronic processes, and a photoconductive antenna (PCA). The graph shows some of the highest reported values of the emitted peak electric fields as well as the approximate spectral coverage of several exemplary systems, representing the different emitter types. The spectral coverage refers to the width at 10% of the peak amplitude. The short, black vertical lines indicate the approximate frequencies of the spectral peaks. The values shown in this graph have been taken from the following references: GaAs [69], ZnTe R1 [70], R2 [71], PCA (ZnSe) [47], $LiNbO_3$ R1 [72], R2 [73], R3 [56], spintronic [74], OH1 R1 [75], R2 [60], gas R1 [76], R2 [77], DAST [78], liquid [79], DSTMS R1 [80], R2 [60]. The figure is adapted from [67].

laser-induced plasma generation, the major disadvantage is given by the high laser pump fluences that are necessary for the generation of the plasma.

A novel THz emitter concept that is based on a laser-induced spin current excitation in ferromagnetic/non-magnetic thin film systems and a spin-to-charge current conversion via the inverse spin Hall effect was proposed by Kampfrath *et al.* in 2013. [81] In the following years, these so-called spintronic THz emitter systems have been drastically improved in power and bandwidth. [82, 83] Even though spintronic emitters are still outperformed by different emitter types with regard to the amplitude of the emitted field [67], they offer several advantages. In contrast to most other emitter types, the spintronic emitters offer gapless broadband emission spectra ranging from the high gigahertz regime up to several tens of THz. [82] Furthermore, the emitter concept allows for control of the THz polarization by application of external magnetic fields. [84] Another advantage compared to other typical emitter systems is that the spintronic emitters can be cost-efficiently produced by standard thin film deposition techniques without involving lithography steps and that they can easily be scaled up in

THz emitters commonly used in THz-TDS		Key characteristics desired in a THz emitter			
		Electric field $> 100\,\mathrm{kV/cm}$	Bandwidth $> 10\,\mathrm{THz}$	Gapless spectrum over 0.1–10 THz	Excitation with nJ pulse energies
PCAs	**GaAs**	✔ [39]	✔ [40, 41]	✘	✔ [38, 40–43]
	InGaAs	✘	✘	✘	✔ [44–46]
Inorganic crystals	**ZnTe**	✘	✔ [49–51]	✘	✔ [49, 50, 52, 53]
	GaP	✘	✘	✘	✔ [54]
	$LiNbO_3$	✔ [55, 56]	✘	✘	✘
Organic crystals	**DAST**	✔ [57]	✔ [58]	✘	✔ [58]
	DSTMS	✔ [57, 59, 60]	✔ [59, 60]	✘	✔ [61]
	OH1	✔ [57, 60]	✔ [60]	✘	✘
	Air plasma	✔ [85]	✔ [65, 66]	✔ [65, 66]	✘
	Spintronic	✔ [74]	✔ [74, 82]	✔ [74, 82]	✔ [82]

Table 1.1: Comparison of some key characteristics that are desired for THz emitter systems used in THz-TDS of different commonly used emitter types. The table is adapted from [68].

size. [74] Thus, spintronic emitters offer a promising alternative for THz-TDS applications. Table 1.1 shows a comparison of some key characteristics that are desired for emitters in THz-TDS of the different emitter types presented above. A more detailed comparison between the different emitter types can be found in the review article by Fülöp *et al.* [67].

As spintronic THz emission is a relatively new concept, many recent works focus on the optimization of the emitter systems with regard to the amplitude of the emitted electromagnetic waves, as well as on the functionality of the emitter systems, such as, for example, the polarization control, but also on the investigation of the underlying microscopic processes that finally lead to the emitted THz radiation. [68] Embedded in this context, the present work shows studies of spintronic THz emitter systems that are based on different magnetic thin films combined with Pt and W layers. The experimental studies can be divided into two parts. The main goal of the first part was to investigate how the magnetic properties of different ferromagnetic (FM) and in particular also ferrimagnetic (FI) materials are reflected in the THz emission properties of a spintronic emitter system. Therefore, thin film bilayer systems consisting of FM Co_xFe_{1-x}, or FI Tb_xFe_{1-x} or Gd_xFe_{1-x} alloy thin films with varying composition ($0 \leq x \leq 1$), combined with Pt layers have been prepared. The

laser-excited spintronic THz emission has been investigated in dependence on the applied magnetic field, and the results have been explained with regard to a detailed characterization of the structural, magnetic, electrical, and optical properties of the samples. The second goal of this work was set on the development of more functional emitter systems that allow for the control of the THz emission amplitude between a high- and a low-amplitude state and also might open the way for higher THz emission amplitudes. Based on the results of the previously investigated bilayer emitter system employing compensated ferrimagnets, a new concept of a THz emitter that can be switched by a temperature change from a high- to a low-amplitude state has been developed. Additionally, the use of a magnetic spin-valve system as a spintronic emitter system that allows for the switching of the emission amplitude by small applied magnetic fields has been demonstrated.

The work is separated into the following parts. Chapter 2 gives an overview of the fundamentals of magnetism in solids with respect to the used material system. A review of laser-induced ultrafast magnetization dynamics with the focus set on the spintronic THz emission is presented in chapter 3. The experimental techniques used for the sample preparation and characterization are explained in chapters 4 and 5. In chapters 6–8, the results on the Pt/Co_xFe_{1-x}, Pt/Tb_xFe_{1-x} and Pt/Gd_xFe_{1-x} bilayer studies are shown. The thermally and magnetically switchable emitter systems are presented in chapters 9 and 10, respectively. Chapter 11 gives a short conclusion and an outlook on future works.

CHAPTER 2

Magnetism in thin film systems

This chapter gives a brief overview of some fundamentals of magnetism in solids (sections 2.1 and 2.2). Furthermore, an introduction to superparamagnetism (section 2.3), coupling mechanisms in magnetic multilayer thin film systems (section 2.4), as well as a survey of the magnetic properties of the FM Co_xFe_{1-x} alloys (section 2.5) and the FI rare earth-transition metal alloys (section 2.6) investigated in this work, will be given.

2.1 Fundamentals of magnetism in solids

The following introductory section is based on the books by Coey [86] and Blundell [87].

Besides the small magnetic moment of the atomic nucleus, there are three sources that can cause the magnetic moment of a free atom. (i) External magnetic fields $\boldsymbol{H}$ give rise to an induced diamagnetic moment, (ii) the electron spin $\boldsymbol{s}$, and (iii) the orbital momentum of the electron with respect to the atomic nucleus $\boldsymbol{l}$ of each electron can lead to a paramagnetic contribution to the magnetic moment. The total angular momentum $\boldsymbol{J}_{\mathrm{tot}}$ of light atoms, where the spin-orbit interaction is weak, with n electrons can be described by the so-called L-S (Russel-Saunders) coupling:

$$\boldsymbol{J}_{\mathrm{tot}} = \sum_{i=1}^{n} \boldsymbol{l}_i + \sum_{i=1}^{n} \boldsymbol{s}_i = \boldsymbol{L} + \boldsymbol{S} \ , \tag{2.1}$$

with the total orbital angular momentum $\boldsymbol{L}$ and the total spin angular momentum $\boldsymbol{S}$. For heavier elements with stronger spin-orbit coupling, the spin and the orbital momentum of each electron first couple to the angular momentum $\boldsymbol{j}$. The total angular momentum for the so-called j-j coupling is described by

$$\boldsymbol{J}_{\mathrm{tot}} = \sum_{i=1}^{n} (\boldsymbol{l}_i + \boldsymbol{s}_i) = \sum_{i=1}^{n} \boldsymbol{j}_i \ . \tag{2.2}$$

In solids, exchange interactions between the individual moments of the atoms can cause a long-range magnetic order. The exchange coupling between the localized many-electron atomic spins $\boldsymbol{S}_1$ and $\boldsymbol{S}_2$ can be described by the Heisenberg Hamiltonian [86, 88]:

$$\mathcal{H} = -2J\hat{\boldsymbol{S}}_1\hat{\boldsymbol{S}}_2 \ , \tag{2.3}$$

where the spins are represented by dimensionless spin operators $\hat{\boldsymbol{S}}$. The coupling between the spins is described by the exchange integral J that has the dimension of an energy. For a lattice, the Hamiltonian can be generalized by using the sum over all pairs of atoms on the lattice sites i and j [86]:

$$\mathcal{H} = -2\sum_{i>j} J_{ij}\hat{\boldsymbol{S}}_i\hat{\boldsymbol{S}}_j \ . \tag{2.4}$$

The exchange integral J_{ij} simplifies to a single exchange constant J if only nearest-neighbor interactions are considered. Figure 2.1 shows some of the most prominent examples of the alignments of magnetic moments.

For $J > 0$, a parallel alignment of the magnetic moments is energetically favored, and therefore the material is ferromagnetic below the so-called Curie temperature T_C. This leads to a spontaneous magnetization without the presence of an applied magnetic field. The strong magnetic stray fields lead to the formation of magnetic domains with different orientations of the magnetic moments that are separated from each other by domain walls. In order to minimize the Zeeman energy, the domains tend to align along an applied magnetic field $\boldsymbol{H}$.

For $J < 0$, an antiparallel alignment of the moments is energetically favored. This leads to antiferromagnetic (AFM) materials that are characterized by two magnetic sublattices with equal absolute moments that are aligned antiparallel. Therefore, the net magnetization is zero. The critical temperature up to which the antiferromagnetic order exists is called Néel temperature T_N.

FI materials also exhibit two magnetic sublattices with an antiparallel alignment. However, the magnetic moments of the sublattices do not cancel out each other entirely, and therefore, similar to ferromagnets, a non-zero spontaneous net magnetization arises for temperatures below the Curie temperature T_C. As the temperature dependence of the magnetic moments

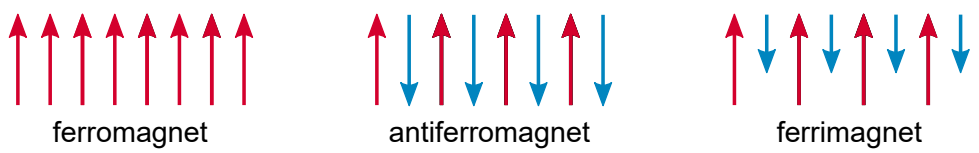

Figure 2.1: Schematic of three prominent alignments of magnetic moments in solids. The blue and red arrows symbolize the magnetic moments of the atoms of the different magnetic sublattices.

is in general different for the two magnetic sublattices, some ferrimagnets exhibit a magnetic compensation temperature T_{comp}, where the net magnetization is zero. Also for ferrimagnets, the magnetic stray fields lead to the formation of magnetic domains.

The Heisenberg model only describes the direct exchange coupling between the spins. Therefore, it fails for a correct description of a large variety of materials, especially for systems in which the total angular momentum is dominated by the orbital momentum rather than by the spin angular momentum. Thus, for many systems also coupling of the magnetic moments due to, for example, superexchange [89, 90], Dzyaloshinsky–Moriya interaction (DMI) [91, 92], Ruderman–Kittel–Kasuya–Yosida (RKKY) [93–95] interaction or double exchange [96] has to be considered. Furthermore, for the description of the magnetic coupling in metals, interactions of the delocalized electrons also have to be included. An overview of the different coupling mechanisms is, for example, given in [86] and [87].

2.2 Magnetic anisotropy

The FM or FI domains are usually naturally aligned along one or more directions that are energetically preferred. In thin film systems, the direction perpendicular to the film plane, which is referred to as out-of-plane (oop) within this work, and any of the directions that lie in the film plane, which are referred to as in-plane (ip), are often of particular interest. The energetically favored direction for the alignment of domains is called easy axis, whereas the unfavorable direction is referred to as hard axis. The energy that is needed to align the magnetic domains along the hard axis is represented by the effective magnetic anisotropy energy density K_{eff}. [97] It can be calculated from in-plane and out-of-plane magnetic hysteresis loops by using the area that is enclosed by the two loops:

$$K_{\mathrm{eff}} = \int_0^{H_{\mathrm{S,\,oop}}} M_{\mathrm{oop}}\mu_0 \mathrm{d}H_{\mathrm{oop}} - \int_0^{H_{\mathrm{S,\,ip}}} M_{\mathrm{ip}}\mu_0 \mathrm{d}H_{\mathrm{ip}} \ , \tag{2.5}$$

with the vacuum permeability μ_0, and the magnetization measured in out-of-plane direction M_{oop} and in-plane direction M_{ip} with respect to the applied magnetic fields H_{oop} and H_{ip}, respectively. The saturation magnetic fields are denoted with $H_{\mathrm{S,\,oop}}$ and $H_{\mathrm{S,\,ip}}$. For the determination of K_{eff}, the hysteresis of the loops has to be removed by averaging the branches of the loops. [97] Schematic hysteresis loops measured in the hard and easy axis direction with the area representing K_{eff} are displayed in figure 2.2. According to equation 2.5, systems with $K_{\mathrm{eff}} < 0$ have an in-plane magnetic easy axis whereas systems with $K_{\mathrm{eff}} > 0$ have an out-of-plane magnetic easy axis. A detailed discussion of the determination of K_{eff} values from superconducting quantum interference device-vibrating sample magnetometry $M(H)$ loops and the related uncertainties is given in subsection 5.4.3.

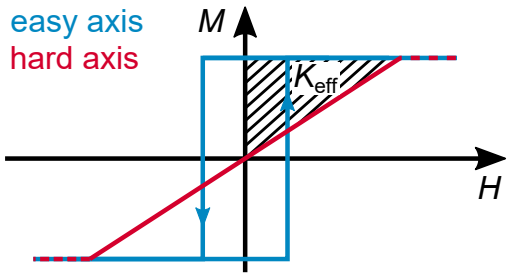

Figure 2.2: Schematic hard and easy axis $M(H)$ loops. The shaded area represents the effective magnetic anisotropy K_{eff}.

The main sources of the magnetic anisotropy are the magnetic dipolar interaction and the spin-orbit interaction. In the following, a brief introduction to the main contributions to the magnetic anisotropy focusing on thin FM films will be given. More detailed explanations can be found, for example, in the book by Fernando [98] or the review paper by Johnson *et al.* [97] on which this section is mainly based. A discussion of the magnetic anisotropy in amorphous FI rare earth-transition metal alloys is given in subsection 2.6.3.

2.2.1 Magnetic dipolar anisotropy (shape anisotropy)

One of the most important sources of magnetic anisotropy, especially in thin films, is given by long-range dipolar interactions. This contribution is closely related to the sample shape and, therefore, often referred to as shape anisotropy. In general, it can be described by the magnetostatic energy density [97, 98]

$$E_{\mathrm{d}} = -\frac{\mu_0}{2V}\int \boldsymbol{M}\cdot\boldsymbol{H}_{\mathrm{d}}\mathrm{d}V \ , \tag{2.6}$$

with the magnetization $\boldsymbol{M}$, the volume V, and the demagnetization field H_{d}. The demagnetization field is described by $\boldsymbol{H}_{\mathrm{d}} = -\mathcal{N}\boldsymbol{M}$, with the shape-dependent demagnetization tensor $\mathcal{N}$. An analytical solution of $\mathcal{N}$ can only be achieved for simple geometries. For thin films, the calculation can be simplified by setting all tensor elements, except the direction perpendicular to the film, to zero and $\mathcal{N}_{\mathrm{oop}} = 1$. Thus, the magnetostatic energy density is given by [97, 99]

$$E_{\mathrm{d}} = \frac{1}{2}\mu_0 M_{\mathrm{S}}^2 \cos^2\theta \ , \tag{2.7}$$

with the saturation magnetization M_{S} and the angle θ between the out-of-plane direction and the direction of the magnetization $\boldsymbol{M}$. Therefore, E_{d} is minimized for the saturation of the sample in the in-plane direction ($\theta = \pm 90°$). The difference between E_{d} for the magnetic saturation of the sample in the in-plane ($\theta = \pm 90°$) and out-of-plane ($\theta = 0°$) direction describes the shape anisotropy of thin FM films [99]

$$K_{\mathrm{shape}} = -\frac{1}{2}\mu_0 M_{\mathrm{S}}^2 \ . \tag{2.8}$$

Due to the dependence on M_S^2, the shape anisotropy typically leads to an in-plane magnetic easy axis for films with high M_S. Within the thin film limit, K_{shape} is independent of the layer thickness t. However, it should be mentioned here that for very thin films of a few monolayers, the film should not be treated as a magnetic continuum any more but rather as discrete magnetic dipoles on a regular lattice. Calculations by Draaisma and Jonge [99] demonstrated that depending on the symmetry of the interface, the dipolar anisotropy of the outer layers of thin films can be significantly lower compared to the inner layers. However, the contribution of the dipolar interface anisotropy is often small compared to interface anisotropies caused by spin-orbit interaction.

2.2.2 Magnetocrystalline anisotropy

In FM or FI crystals, another contribution to the magnetic anisotropy is caused by the crystal structure of the material, leading to a preferred magnetization alignment along certain crystallographic orientations. [100] The so-called magnetocrystalline anisotropy has its origin in the spin-orbit interaction that causes spheroidal charge distributions of the atoms that are dependent on the crystal structure and on the spin directions. Thus, for the different crystallographic orientations, the overlap of the electron distributions is different. Consequently, a rotation of the electron spins with an applied field leads to a change of the exchange energy as well as of the electrostatic interaction energy. An example of the different magnetization axes in an fcc crystal and schematic $M(H)$ loops measured along these axes are shown in figure 2.3.

2.2.3 Magnetoelastic anisotropy

External stress or strain that is applied to a magnetic material can lead to changes in the lattice parameters and, as a consequence, also to variations in the magnetocrystalline anisotropy.

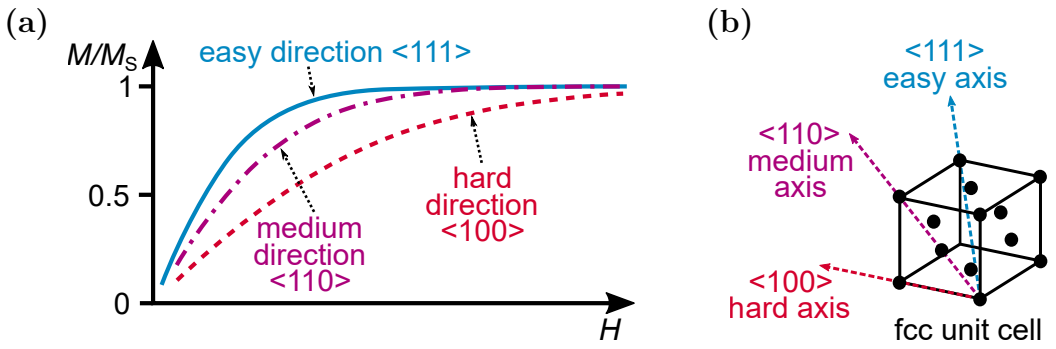

Figure 2.3: (a) displays schematic $M(H)$ loops for the possible magnetization axes in an fcc crystal shown in (b). In the example, the <111> direction is the easy magnetization axis, whereas the hard axis lies in the <100> direction. The figure is based on [98].

The inverse of this magnetoelastic anisotropy is the so-called magnetostriction, which describes the variation of the sample dimensions by an alternation of the magnetization direction. The energy density for an elastically isotropic medium with isotropic magnetostriction can be described by [97]

$$E_{\mathrm{me}} = -K_{\mathrm{me}} \cos^2 \theta \ , \tag{2.9}$$

with $K_{\mathrm{me}} = -3/2\lambda\sigma$. Here, σ describes the stress, λ is the magnetostriction constant, and θ is the angle between the magnetization direction and the applied stress. The stress can be applied externally but also be induced by the film growth. For thin film systems, the strain induced by the lattice mismatch at the interface between two layers of different materials is of particular interest. The resulting magnetoelastic anisotropy in that case consequently also shows a dependence on the layer thickness. Thus, the magnetoelastic anisotropy plays an important role in magnetic multilayers with thin layer thicknesses. In certain systems, the magnetoelastic anisotropy overcomes the shape anisotropy and, therefore, can cause a magnetic easy axis in the out-of-plane direction. [97, 101–103]

2.3 Superparamagnetism

The following explanations are mainly following the book by Blundell [87].

For FM (or FI) particles that are sufficiently small (typically with diameters between 10 nm and 150 nm, depending on the material [104]), a single domain state becomes energetically preferred. [105, 106] Such particles typically exhibit a magnetic easy axis along a certain direction due to magnetocrystalline anisotropy, shape anisotropy, or magnetoelastic anisotropy. Thus, the energy density of a particle contains the term $K \sin\theta$, with the anisotropy density with regard to the magnetic easy axis K and the angle between the magnetization direction and the magnetic easy axis θ. The energy is therefore minimized for $\theta = 0$ and $\theta = \pi$. The energy $\Delta E = KV$, with the volume of the particle V, is necessary to flip the domain between the two energetically preferred states (see figure 2.4a, solid line). For sufficiently small particles, for which $k_{\mathrm{B}}T \gg KV$, the magnetization can be easily flipped by thermal fluctuations. If a magnetic field is applied along the magnetic easy axis, one of the minima becomes energetically favored (see figure 2.4a, dashed line). Therefore, ΔE and consequently also the switching probability becomes different for the two switching directions along the magnetic easy axis.

An ensemble of such (uncoupled) particles behaves like a paramagnet and is therefore called a superparamagnet. In contrast to a normal paramagnet, the independent magnetic moments are not atomic but the magnetic moments of the FM particles. At high temperatures, the magnetic moments fluctuate on a short time scale (compared to the measurement time).

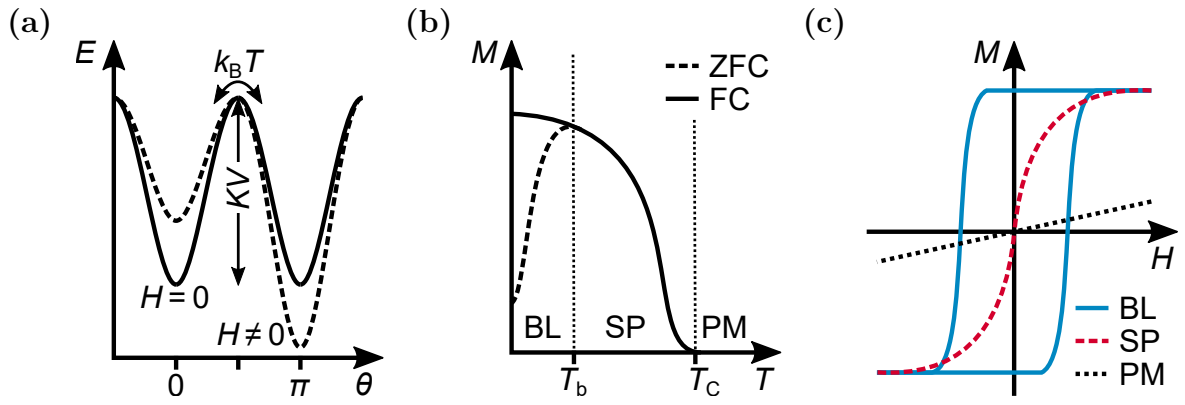

Figure 2.4: (a) shows the magnetic potential energy E of a small FM particle as a function of the angle θ between the magnetization direction and the magnetic easy axis in the absence of an applied magnetic field (solid line) and in the presence of an applied magnetic field H along the anisotropy axis (dashed line). (b) displays schematic zero-field cooled (ZFC) and (FC) $M(T)$ curves of a superparamagnetic sample. For temperatures T below the blocking temperature T_b, the sample is in a blocked (BL) state, for $T_\mathrm{b} < T < T_\mathrm{C}$, the sample is in a superparamagnetic (SP) state, and for $T > T_\mathrm{C}$, the sample is in a paramagnetic (PM) state. (c) shows a schematic comparison between the $M(H)$ loops of these different sample states. (a) is adapted from [108].

Therefore, a non-zero average magnetic moment in that state can only be observed if a magnetic field is applied that induces an energetically preferred magnetization direction. For temperatures below the so-called blocking temperature T_b, the probability for the switching of the magnetic moments by thermal fluctuations becomes small (with respect to the measurement time), and the particles appear to be locked in one of the energetic minima. In this so-called blocked state, the sample shows hysteretic behavior in the magnetization reversal.

The blocking temperature can be determined by performing zero-field cooled (ZFC) and field cooled (FC) $M(T)$ measurements in the following way: The sample is first cooled down without an applied magnetic field. Then, a small magnetic field is applied, and the magnetization is recorded while the temperature is increased (ZFC curve). Afterward, the sample is cooled down with the field still applied, and the magnetization is again measured for increasing temperatures (FC curve). The maximum of the ZFC curve is at the blocking temperature T_b. [107] The temperature at which the ZFC curve departs from the FC curve is called irreversibility temperature T_irr. [107] Figure 2.4b shows schematic ZFC and FC $M(T)$ measurements of a superparamagnetic sample. A comparison between schematic $M(H)$ loops of a superparamagnetic sample in its different magnetic states is displayed in figure 2.4c.

Superparamagnetic states can also be observed in sufficiently thin rough magnetic films with layer thicknesses $t \lesssim 3\,\mathrm{nm}$ for which the films become (partially) discontinuous. [109–112] Within this work, superparamagnetism could be observed in $\mathrm{Pt}(2.5\,\mathrm{nm})/\mathrm{Co}_x\mathrm{Fe}_{1-x}(1\,\mathrm{nm})$ (see section 6.3) as well as in a $\mathrm{Pt}(5\,\mathrm{nm})/\mathrm{Gd}_{0.3}\mathrm{Fe}_{0.7}(1\,\mathrm{nm})$ thin films (see section 9.2).

2.4 Coupling effects in magnetic multilayer systems

Several coupling phenomena can be observed between different magnetic layers in multilayer thin film systems. This section gives an overview of coupling effects leading to a ferromagnetic alignment (subsection 2.4.1) and interlayer exchange coupling (subsection 2.4.2) between magnetic layers that are separated by an interlayer as well as on the exchange bias effect (subsection 2.4.3).

2.4.1 Coupling mechanisms leading to ferromagnetic alignment

In bilayer systems consisting of FM (or FI) and non-magnetic metal (NM) layers (the term non-magnetic metal is used within this work for all metals that do not exhibit a spontaneous magnetic order, i.e., paramagnetic or diamagnetic materials), it has been demonstrated that close to the FM/NM interface, the NM film can become magnetized due to the so-called magnetic proximity effect. [115–118] In FM/NM/FM trilayers (or multilayer systems) with thin NM interlayers, the induced magnetic moments can lead to the ferromagnetic coupling between the FM layers (see figure 2.5a). [113, 119] The coupling strength $J_{\mathrm{pe}} \sim 1/\sinh(t_{\mathrm{NM}})$ between the FM layers is dependent on the NM layer thickness t_{NM}. [113]

Another direct coupling mechanism is given by discontinuities in the NM layer, so-called pinholes. The direct contact between the FM (or FI) layers given through the pinholes leads to a ferromagnetic coupling between the layers (see figure 2.5b). This mechanism is strongly dependent on the film preparation method and can appear in sputtered multilayers with thicknesses below 2 nm. [114]

Furthermore, correlated rough interfaces can also lead to the ferromagnetic so-called orange peel coupling, which is based on dipolar interactions between the magnetostatic charges that appear at the interfaces (see figure 2.5c). [114, 120] The coupling strength J_{op} is dependent on the saturation magnetization M_{S}, the height h_{t} and the period L of the terraces, and the NM layer thickness t_{NM} and can be described by $J_{\mathrm{op}} \sim (M_{\mathrm{S}}^2 h_{\mathrm{t}}^2/L)\exp(-t_{\mathrm{NM}}/L)$. [114, 121]

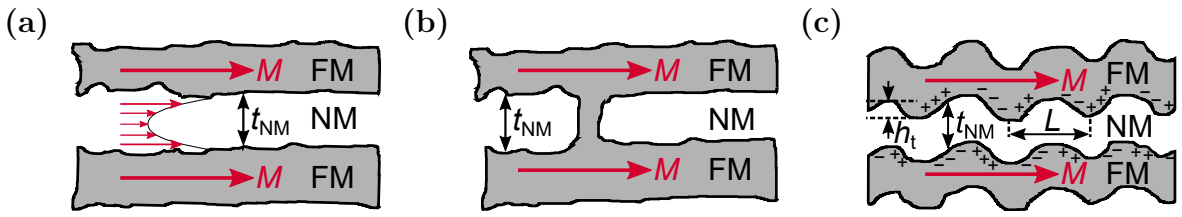

Figure 2.5: Schematics of different coupling mechanisms leading to a ferromagnetic coupling between two FM layers that are separated by a thin NM layer with the thickness t_{NM}. (a) shows the coupling by induced magnetic moments, (b) the coupling due to ferromagnetic pinholes, and (c) the so-called orange peel coupling. The red arrows mark the magnetization M. The height and the period of the terraces in (c) are denoted with h_{t} and L, respectively. (a) is based on [113], (b) and (c) are adapted from [114].

2.4.2 Interlayer exchange coupling

Besides the ferromagnetic coupling described above, also an indirect magnetic exchange coupling between FM (or FI) layers that are separated by thin NM layers can occur.

In 1986 Grünberg *et al.* [122, 123] demonstrated the antiparallel coupling of two thin Fe layers that are separated by a Cr spacer layer with a thickness of $0.4\,\mathrm{nm} \lesssim t_{\mathrm{Cr}} \lesssim 0.8\,\mathrm{nm}$. Parkin *et al.* [124] showed that the coupling of the FM layers in Co/Ru, Co/Cr, and Fe/Cr multilayer systems follows an oscillatory behavior with respect to the Ru and Cr spacer layer thicknesses. Several theoretical models have been proposed to describe this coupling behavior. [125, 126] One of the most prominent approaches is given by the extension of the RKKY spin coupling theory [93–95] to the interlayer exchange coupling [127, 128]. This leads to a coupling constant $J_{\mathrm{RKKY}}(t_{\mathrm{NM}}) \sim -\sin(t_{\mathrm{NM}})/t_{\mathrm{NM}}^2$ [125, 129] that is dependent on the interlayer thickness t_{NM}. Detailed discussions of different theoretical approaches are given, for example, in [125, 130].

2.4.3 Exchange bias effect

The following brief introduction of the exchange bias effect is mainly based on the review article by Nogués and Schuller [131].

The most common exchange bias (EB) systems are bilayers consisting of an AFM and a FM layer. When such a bilayer is field cooled from above to below the so-called blocking temperature T_{b} of the AFM layer (with the Curie temperature T_{C} of the FM layer being higher than T_{b}), an exchange anisotropy is induced in the FM layer. [132] The blocking temperature is related to the Néel temperature T_{N} of the AFM layer but can also be lower ($T_{\mathrm{b}} \leq T_{\mathrm{N}}$), especially for thin films. Since the first observation of the exchange bias effect by Meiklejohn and Bean in 1956 [133] the effect has been demonstrated in a great variety of thin film and nanoparticle systems. [134–136] Qualitatively, the exchange bias can be understood by assuming an exchange interaction at the AFM/FM interface. [132, 134] A schematic displaying the magnetic states of an AFM/FM bilayer for the setting of the exchange anisotropy is shown in figure 2.6a. At temperatures $T_{\mathrm{b}} < T < T_{\mathrm{C}}$, an external magnetic field H is applied, and the magnetic moments of the FM layer align according to this field, whereas the AFM layer stays in a disordered state. When the system is cooled down below T_{b} with the field still applied, in the AFM layer, the moments order antiferromagnetically and couple at the interface to the FM layer (in the image, a ferromagnetic coupling at the interface is assumed). As the AFM layer is in a compensated magnetization state and, therefore, independent of the external magnetic field, a unidirectional magnetic anisotropy is induced in the FM layer due to the exchange coupling at the AFM/FM interface. A schematic magnetization loop of the system after the field cooling procedure is shown in figure 2.6b. At high magnetic fields, the system is saturated (1). At (2), the external field is sufficiently high to overcome the

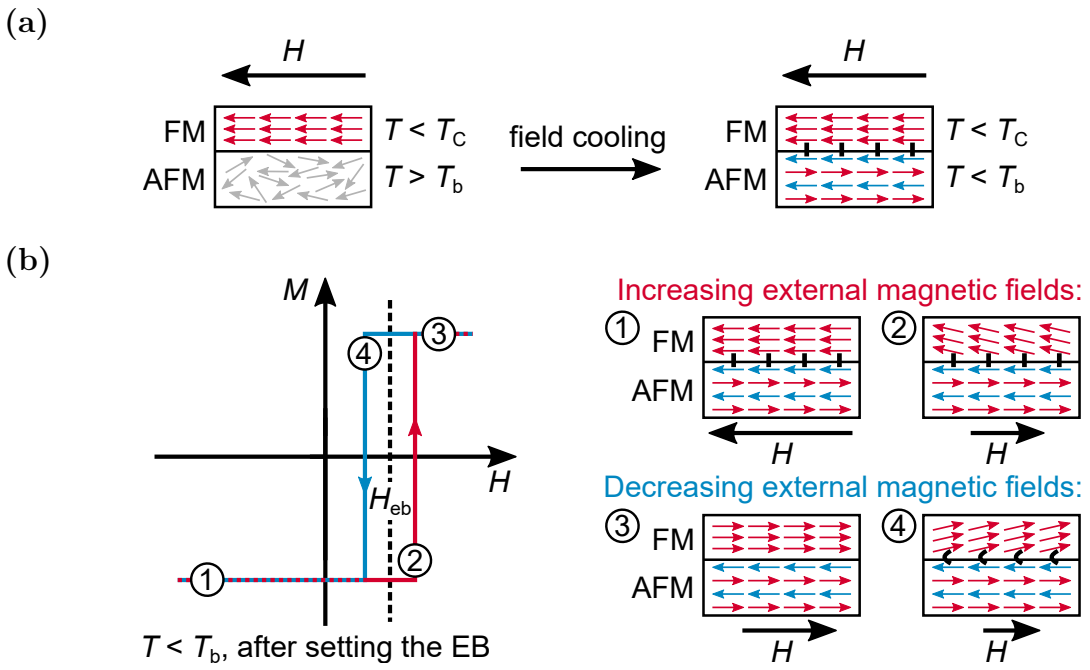

Figure 2.6: Phenomenological schematic of the exchange bias effect. (a) shows the setting of the exchange anisotropy. In (b), the schematic loop of an exchange-biased FM layer and the magnetic states of some characteristic points in the loop are displayed. A more detailed discussion of the image can be found in the main text. The figure is based on [131].

exchange coupling at the AFM/FM interface. The loop shift field H_{eb} is called exchange bias field. Coming from the saturated state in positive field direction (3), at a certain positive field (4), the exchange bias field overcomes the external magnetic field and causes the magnetic moments in the FM layer to reorientate.

Although the described simple model gives an intuitive picture of the exchange bias, different aspects, such as the influence of the interface roughness [137–139] and the spin configurations at the interface [137, 139–141] on the exchange bias effect are neglected. Furthermore, in this simple picture, an uncompensated spin configuration at the AFM surface would be necessary. However, the exchange bias effect has also been demonstrated in various systems with a compensated spin configuration at the AFM surface. [137–142] Especially on the microscopic level, the effect is still not fully understood. A detailed review of the role of the different parameters for the exchange bias effect (such as the spin configuration at the interface, interface disorder, roughness, crystallinity, AFM grain size, interface impurity layers, training effect, blocking temperature) can be found in [131]. Nevertheless, concerning this work, the simple phenomenological picture is sufficient.

The exchange bias effect has been shown in many different studies to be approximately inversely proportional to the thickness t_{FM} of the FM layer (down to thicknesses for which the film becomes discontinuous), $H_{\mathrm{eb}} \sim 1/t_{\mathrm{FM}}$. [142–148] The correlation between the exchange bias field and the thickness of the AFM layer is more complicated and dependent on the

microstructure of the AFM layer and the temperature. [142, 146, 147, 149] For small AFM layer thicknesses, T_b is usually below room temperature, and therefore the exchange bias only appears at low temperatures. Above a certain AFM film thickness on the order of 10 nm the exchange bias often is thickness independent. [142, 146, 147, 149–151] However, in some systems, also a maximum of the exchange bias at a certain thickness [142, 146, 150] or a decrease in the exchange bias for large AFM thicknesses [142, 146, 149, 150] has been observed, which might be due to microstructural changes in the AFM layer. Besides the loop shift, usually, also an increase in the coercivity of the FM layer can be observed for $T < T_b$ that becomes largest for small anisotropies of the AFM layer. [142, 144, 147, 151] Consequently this effect is large for temperatures close to T_b.

One application of the exchange bias effect are spin-valve AFM/FM_1/IN/FM_2 systems consisting of a "pinned" ferromagnetic layer FM_1 that is exchange-biased by an AFM layer and a second "free" ferromagnetic layer FM_2 which is magnetically decoupled from FM_1 by a metallic interlayer IN. [152–155] The most prominent usage of such layer stacks is given by the giant magneto-resistance (GMR) effect. [156, 157] Depending on the relative magnetization alignment of the two FM layers, the resistivity of the system will either be high (for an antiparallel alignment) or low (for a parallel alignment). Therefore, these systems can be used in sensor applications. In this work, the usage of spin-valve systems as magnetically switchable spintronic THz emitters is demonstrated (see chapter 10).

2.5 Magnetic properties of Co_xFe_{1-x} alloys

This section is mainly based on the review article by Scheunert *et al.* [158] and on the book by Coey [86].

Soft magnetic Co_xFe_{1-x} alloys are well known for their high saturation magnetization as well as their high Curie temperature and low magnetocrystalline anisotropy. As early as 1912, Weiss [159] reported that Co_xFe_{1-x} alloys with small Co content x possess a significantly higher saturation magnetic moment than pure Fe. Since then, many experimental and theoretical studies confirmed an unchallenged high saturation magnetization at room temperature, reaching values of $M_S \approx 1900\,\mathrm{kA/m}$ for Co contents of $0.2 \leq x \leq 0.4$. [160–163] This makes the material an interesting choice for applications like, for example, in high moment magnetic recording heads. [164–166]

The magnetic properties of the FM 3d transition metals (Fe, Ni, Co) are mainly based on the delocalized moments of the 3d valence electrons. In solids, the orbital moments of the electrons are mostly quenched by the crystal field. Thus, the magnetic moment is mainly given by the total electron spin $\boldsymbol{S} = \sum_{i=1}^{n} \boldsymbol{s}_i$. The interatomic coupling between the magnetic moments of the neighboring atoms can be described by a direct (Heisenberg) exchange of the

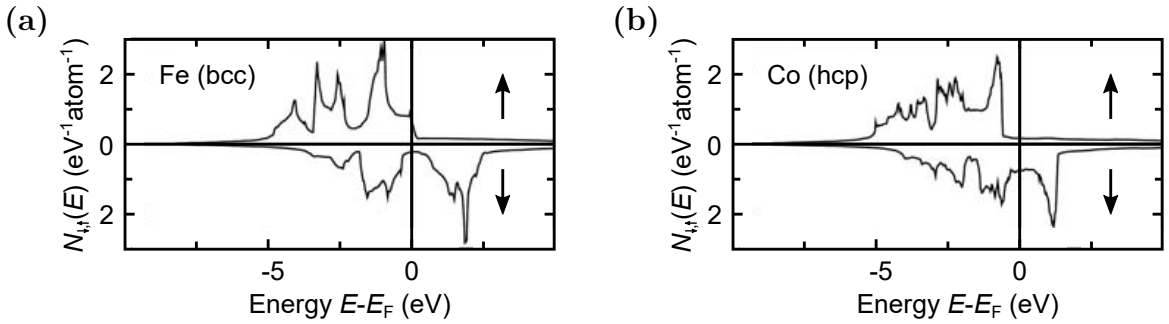

Figure 2.7: Calculated densities of states N for the majority (↑) and minority (↓) electrons of (a) Fe and (b) Co with respect to the energy E. The Fermi energy is denoted by E_F. The densities of states were calculated by Ivan Rungger. The figure is adapted from [86].

wave functions of the 3d electrons, leading to a parallel alignment of the spin moments. The strong direct coupling results in high Curie temperatures of, for example, $T_{C,\,Fe} = 1044\,K$ for pure Fe and $T_{C,\,Co} = 1360\,K$ for pure Co. [86]

In terms of band ferromagnetism, the high magnetic moments can be explained by the spontaneous spin splitting of the energy bands close to the Fermi level. Figure 2.7 displays calculated densities of states for the majority- and minority-spin electrons in Fe and Co. Here, unsplit sp bands are superposed by the spin-split 3d states. The magnetic moment per atom can be described with the magnetic valence model. The magnetic moment m of a 3d metal atom is then given by

$$m = (N_\uparrow - N_\downarrow)\mu_B = (2N_\uparrow - \mathcal{Z})\mu_B \ , \tag{2.10}$$

with the numbers of majority- (↑) and minority-spin (↓) valence electrons per atom N, the valence of the atom $\mathcal{Z} = N_\uparrow + N_\downarrow$, and μ_B denoting the Bohr magneton. The magnetic valence is defined as $\mathcal{Z}_m = 2N_{d,\uparrow} - \mathcal{Z}$, with $N_{d,\uparrow}$ denoting the number of majority-spin d electrons per atom. The magnetic moment of the atom can then be rewritten as

$$m = (\mathcal{Z}_m + 2N_{sp,\uparrow})\mu_B \ , \tag{2.11}$$

with $2N_{sp,\uparrow}$ describing the number of unpolarized electrons in the 4 sp band (with typical values of $0.6 \lesssim 2N_{sp,\uparrow} \lesssim 0.7$). The average magnetic moment $\langle m \rangle$ of any strong FM 3d metal alloy based on Fe, Co, and Ni can then be estimated by replacing $\mathcal{Z}_m$ with its weighted average $\langle \mathcal{Z}_m \rangle$ over all atoms in the alloy

$$\langle m \rangle = (\langle \mathcal{Z}_m \rangle + 2N_{sp,\uparrow})\mu_B \ . \tag{2.12}$$

The magnetic valence of Fe $\mathcal{Z}_{m,\,Fe} = 10 - 8 = 2$ would therefore lead to an average atomic moment of $\langle m_{Fe} \rangle \approx 2.6\mu_B$, whereas for Co the magnetic valence of $\mathcal{Z}_{m,\,Co} = 10 - 9 = 1$ would lead to an average magnetic moment of $\langle m_{Co} \rangle \approx 1.6\mu_B$, assuming $2N_{sp,\uparrow} \approx 0.6$. Thus,

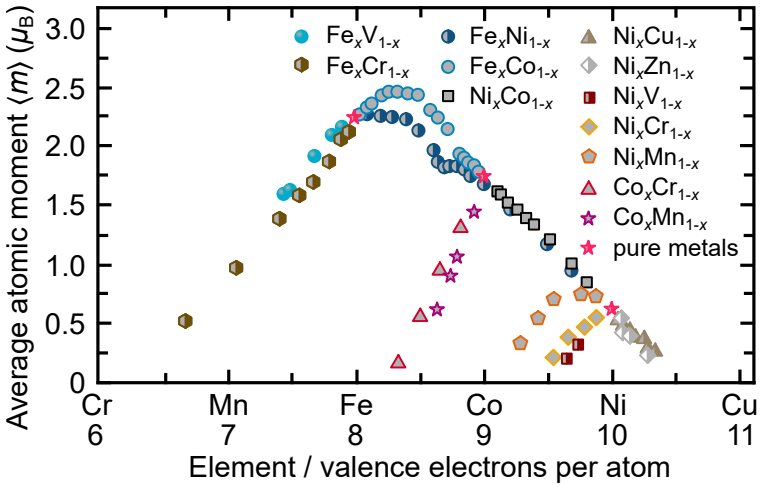

Figure 2.8: The displayed Slater-Pauling curve shows the average atomic moment in dependence on the number of the 3d and 4s valence electrons for binary 3d transition metal alloys. The figure is adapted from [86].

the magnetic valence model clearly overestimates the experimentally found average atomic moment of Fe ($\langle m_{\mathrm{Fe}} \rangle \approx 2.2 \mu_{\mathrm{B}}$ [158]), whereas it leads to a good estimation of the atomic moment in Co. The reduction of $\langle m_{\mathrm{Fe}} \rangle$ is due to Fe being a weak ferromagnet (with the 3d↑ band only partially filled, see figure 2.7a), rather than a strong ferromagnet (with the 3d↑ band pushed completely below E_{F}) as is the case for Co (see figure 2.7b) and Ni. Theoretical calculations [161, 162] and experimental studies [160, 167] showed that the average Fe atomic moment is increased in the vicinity of Co atoms. This leads to the mentioned maximum in the saturation magnetic moment of $\mathrm{Co}_x\mathrm{Fe}_{1-x}$ alloys for $0.2 \leq x \leq 0.4$. The Slater-Pauling plot (named after Slater and Pauling due to their pioneering works on magnetic 3d metal alloys [168, 169]) displayed in figure 2.8 shows a comparison of the average magnetic moments per atom of different binary 3d transition metal alloys with respect to their valence electrons per atom.

2.6 Amorphous ferrimagnetic rare earth-transition metal alloys

For a long time, it was believed that only materials with a long-range crystalline order can exhibit a spontaneous magnetization. However, since the mid of the 20$^{\mathrm{th}}$ century, many different amorphous material systems have been found to exhibit a magnetic order. [170, 171] An interesting class within these amorphous magnetic materials are the FI rare earth (RE)-3d transition metal (TM) alloys. These alloys allow the tuning of the magnetic properties like the magnetic anisotropy, the coercivity, the saturation magnetization, as well as the compensation temperature by varying the alloy composition. [171–173]

In this section, a general introduction to the magnetic coupling in RE_xTM_{1-x} alloys (subsection 2.6.1) and the temperature dependence of the magnetization of FI RE_xTM_{1-x} alloys (subsection 2.6.2) will be given. Furthermore, the specific properties of the amorphous FI Tb_xFe_{1-x} and Gd_xFe_{1-x} thin films that were used within this work will be discussed (subsection 2.6.3).

2.6.1 Magnetic coupling of rare-earth elements with ferromagnetic 3d transition metals

The following explanations are mainly based on the article by Rhyne and McGuire [174] and the book by Trémolet de Lacheisserie *et al.* [114].

In contrast to the FM 3d transition metals, the magnetic moment of the RE elements is mainly given by the 4f electrons. Due to the strong spin-orbit coupling, the total angular momentum of an atom can be described according to Hund's rules by $J_{\mathrm{tot}} = |L - S|$ for light RE elements with a half- or less than half-filled 4f shell and by $J_{\mathrm{tot}} = |L + S|$ for heavy RE elements with a more than half-filled 4f shell. The 4f electrons are localized close to the atomic nucleus and shielded by the 5s, 5p, 5d, and 6d valence electrons. Therefore, no direct interatomic coupling between the 4f electrons is possible. However, an indirect coupling via the 5d and 6d valence electrons that are spin-polarized by the 4f electrons occurs. As this coupling is relatively weak compared to the direct exchange coupling in FM 3d transition metals, the magnetic ordering temperatures of pure RE elements are below room temperature (e.g., $T_{\mathrm{C,\,Gd}} = 293\,\mathrm{K}$ [175], $T_{\mathrm{C,\,Tb}} = 237\,\mathrm{K}$ [176]).

In RE_xTM_{1-x} alloys, an interatomic exchange coupling between the magnetic moments of the RE and TM atoms occurs due to a hybridization of the TM 3d electronic states with the RE 5d states. A schematic of this hybridization is shown in figure 2.9a. In this schematic picture, it is assumed that an RE "impurity" is embedded in a FM TM matrix. The RE 5d band is energetically higher than the TM 3d band. However, a part of the 3d states of TM atoms surrounding the RE atom is transferred to the RE 5d states. This hybridization is stronger for smaller energy differences between the bands. The energy difference between the TM 3d↓ band and the RE 5d↓ states is smaller than between the TM 3d↑ band and the RE 5d↑ states. Thus, the 3d↓–5d↓ hybridization is stronger compared to the 3d↑–5d↑ hybridization, leading to an effectively antiparallel coupling between the TM 3d and the RE 5d spins. The intraatomic parallel coupling between the RE 5d and the RE 4f spins results in an antiparallel coupling between the TM 3d spins and the RE 4f spins. This coupling mechanism is strong compared to the indirect coupling in pure RE elements, and therefore high ordering temperatures can be observed for certain RE_xTM_{1-x}-based systems. As for light RE elements (e.g., Pr, Nd, Sm) the coupling between the spin and orbital momentum is antiparallel, the coupling between the TM and RE magnetic moments is

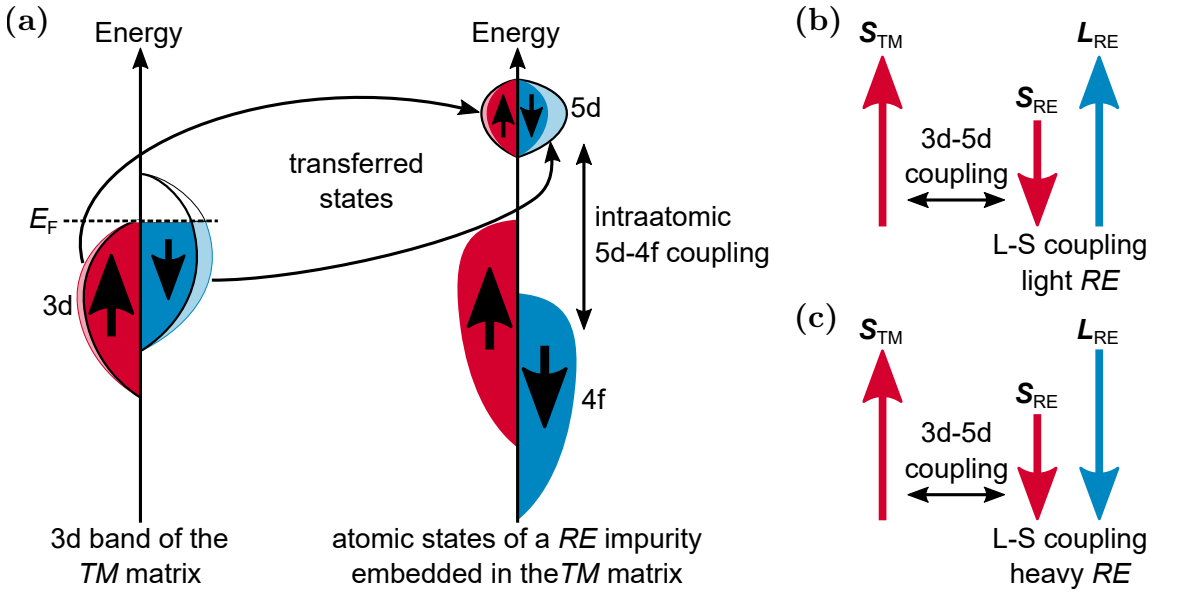

Figure 2.9: Coupling of the magnetic moments in RE_xTM_{1-x} alloys. (a) schematically shows the hybridization of the 5d atomic electron states of a RE impurity, which is embedded in a 3d TM matrix, with the 3d electronic bands of the TM matrix. (b) and (c) display the coupling of the TM and RE spin and orbital moments for light and heavy RE elements, respectively. The figures are adapted from [114].

parallel (see figure 2.9b). Among the class of these ferromagnetic RE_xTM_{1-x}-based magnetic materials are high moment permanent magnets such as $Nd_2Fe_{14}B$ [177], and Sm_2Co_{17} [178]. For heavy RE elements (e.g., Gd, Tb, Dy), the parallel coupling between the RE spin and orbital momentum leads to an antiparallel coupling of the TM and RE magnetic moments (see figure 2.9c). Therefore, these materials are ferrimagnets with RE and TM magnetic sublattices.

2.6.2 Temperature dependence of the magnetization

In general, the temperature dependence of the RE magnetic sublattice in a FI RE_xTM_{1-x} alloy is stronger compared to the TM magnetic sublattice due to the weaker exchange coupling between the RE magnetic moments. Figure 2.10 schematically shows the temperature dependence of the magnetization of the RE and TM magnetic sublattices as well as the resulting net magnetization M_{net} for FI RE_xTM_{1-x} alloys with different RE content x. For RE rich samples (a), M_{net} is RE-dominated for all temperatures up to the Curie temperature T_C. Samples with a medium RE content (b) can show a magnetic compensation point at the temperature T_{comp}. Here, M_{net} switches from a RE-dominated state for $T < T_{\text{comp}}$ to a TM-dominated state for $T_{\text{comp}} < T < T_C$. For low RE contents (c) M_{net} is TM-dominated for all temperatures up to T_C.

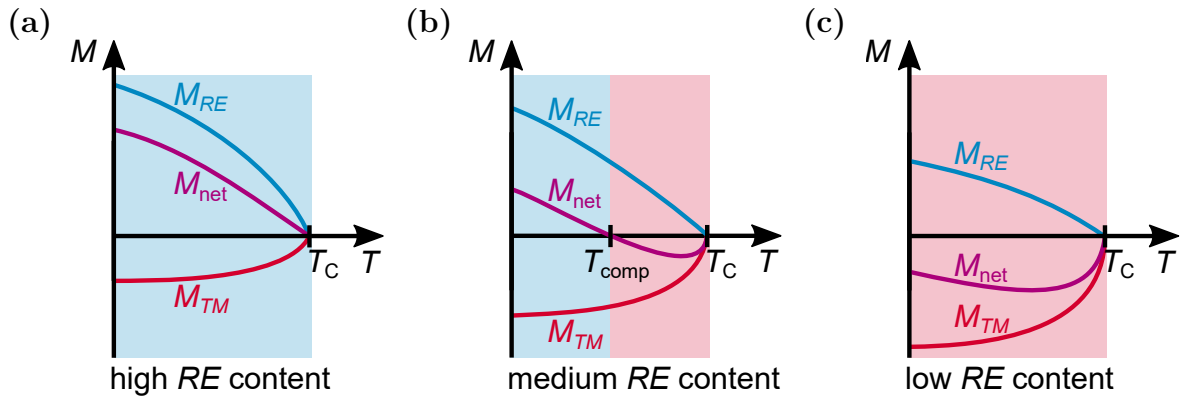

Figure 2.10: Schematic of the magnetization M of the RE (blue, positive values) and TM (red, negative values) magnetic sublattices in FI RE_xTM_{1-x} alloys in dependence on the temperature T. M_{net} describes the net magnetization. The Curie temperature is denoted with T_{C}. For the case of high RE contents x, displayed in (a), M_{net} is RE-dominated at all temperatures up to T_{C}. For medium RE contents (b) M_{net} is dominated by the RE magnetic sublattice up to the compensation temperature T_{comp} whereas it is TM-dominated for $T_{\mathrm{comp}} < T < T_{\mathrm{C}}$. For low RE contents, M_{net} is TM-dominated at all temperatures $T < T_{\mathrm{C}}$. The figures are based on [86].

2.6.3 Magnetic properties of amorphous Tb_xFe_{1-x} and Gd_xFe_{1-x} alloys

For Tb_xFe_{1-x} and Gd_xFe_{1-x} alloys with low RE content ($0.105 \leq x \leq 0.333$) four stable crystalline phases (Tb_2Fe_{17}, Tb_6Fe_{23}, $TbFe_3$, $TbFe_2$, and $GdFe_2$, $GdFe_3$, Gd_6Fe_{23}, Gd_2Fe_{17}) can be achieved for bulk material by cooling down from the liquid phase. [179–181] However, all Tb_xFe_{1-x} and Gd_xFe_{1-x} alloys investigated in this work were thin layers deposited by magnetron co-sputtering from elemental targets at room temperature (see section 4). It is well known that for this preparation method, the alloys are in a stable amorphous state at room temperature, as the kinetic energies of the deposited particles and thermal fluctuations in the films are not sufficient to allow the diffusion that is necessary to form a crystalline film. [172, 174, 182–184] Annealing of the films at temperatures $T \gtrsim 500\,\mathrm{K}$ leads to the formation of crystalline phases (Vittoria *et al.* [185] reported the crystallization of a 0.85 µm thick $GdFe_2$ film at $T = 723\,\mathrm{K}$; Sato *et al.* [186] found crystallization temperatures $490\,\mathrm{K} < T < 520\,\mathrm{K}$ for 1 µm thick Tb_xFe_{1-x} films with varying compositions).

As for this work, the samples were not heated up above the crystallization temperatures, the following discussion will focus on the properties of thin amorphous alloy films.

Magnetic order and anisotropy

Amorphous materials usually do not exhibit a long-range structural or chemical order. Due to this disorder, the local environment ("crystal field") is different for each atom, leading to varying single-site anisotropies. The magnetic order can be described by a competition between the local single-site anisotropies and exchange interactions, which describe the cou-

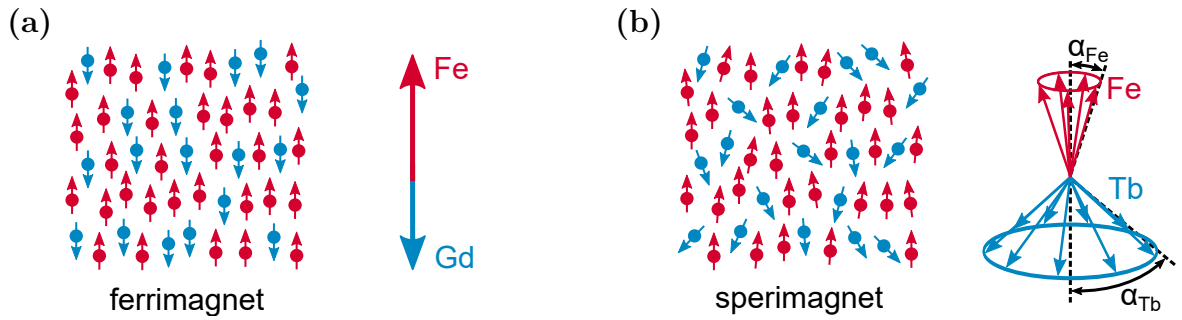

Figure 2.11: Alignment of the *RE* (blue) and Fe (red) magnetic moments in RE_xFe_{1-x} alloys. (a) displays the collinear ferrimagnetic order in amorphous Gd_xFe_{1-x} alloys, whereas in (b), the sperimagnetic order in Tb_xFe_{1-x} is shown. The averaged distributions of the Tb and Fe magnetic moments are described by the fanning cones with the angles α_{Tb} and α_{Fe}. The figures are based on [187] and [188].

pling between the magnetic moments of atoms in different positions. [171, 187, 189] For an amorphous system with two magnetic sublattices, the coupling can be described by the Hamiltonian [187]

$$\mathcal{H} = -\sum_i D_{a_i} S^2_{z,\,a_i} - \sum_j D_{b_j} S^2_{z,\,b_j} - \sum_{a,a'} J_{aa'} \boldsymbol{S}_a \cdot \boldsymbol{S}_{a'} - \sum_{a,b} J_{ab} \boldsymbol{S}_a \cdot \boldsymbol{S}_b - \sum_{b,b'} J_{bb'} \boldsymbol{S}_b \cdot \boldsymbol{S}_{b'} \ . \quad (2.13)$$

D_{a_i}, D_{b_i} describe the local (single site) anisotropy and $S_{z,\,a_i}$, $S_{z,\,b_i}$ the spin parallel to the magnetic easy axis of the atoms a_i and b_j of the two magnetic sublattices. $J_{aa'}$, $J_{bb'}$, and J_{ab} denote the exchange interactions between the spins $\boldsymbol{S}_a$, $\boldsymbol{S}_{a'}$, $\boldsymbol{S}_b$, and $\boldsymbol{S}_{b'}$. The magnetic order of the system depends on the strength and sign of the exchange interactions. Dominant exchange interactions with respect to the single-site anisotropies lead to a collinear FM or FI alignment of the magnetic moments. This is the case for Gd_xFe_{1-x} alloys, which exhibit a ferrimagnetic order (see figure 2.11a). [171, 187] However, systems with strong single-site anisotropies exhibit a non-collinear so-called sperimagnetic alignment of the magnetic moments. This is the case for Tb_xFe_{1-x} alloys, which show a distribution of both the Fe as well as the Tb magnetic moments (see figure 2.11b). [187–190] The averaged distributions of the Fe and Tb magnetic moments can be described by the so-called "fanning cones" with the angles α_{Tb} and α_{Fe}. The stronger interatomic magnetic exchange coupling with respect to the single-site anisotropies between the Fe magnetic moments compared to the Tb magnetic moments leads to a larger distribution of the Tb magnetic moments compared to the Fe moments ($\alpha_{Tb} > \alpha_{Fe}$). The Fe fanning cones in Tb_xFe_{1-x} alloys can be directly measured by Mössbauer spectroscopy using ^{57}Fe ions. [191–193] For alloys with Tb content $0.1 \leq x \leq 0.5$, Ruckert *et al.* [193] reported Fe fanning cone angles $21° \lesssim \alpha_{Fe} \lesssim 29°$ that are almost independent of the temperature T (for $20\,K \leq T \leq 300\,K$) and of the film thickness t (for $50\,nm \leq t \leq 190\,nm$). In contrast to α_{Fe}, a strong temperature dependence of α_{Tb} has been observed for $10\,K \leq T \leq 300\,K$. [194] Hebler *et al.* [188] also observed a strong decrease in α_{Tb} with increasing film thickness t for $t \lesssim 30\,nm$ in Tb_xFe_{1-x} alloys with $0.15 \leq x \leq 0.38$. This

leads to stronger contribution of the Tb magnetic sublattice to the net magnetization for higher film thicknesses. [188]

Amorphous Tb_xFe_{1-x} and Gd_xFe_{1-x} thin films exhibit an out-of-plane magnetic easy axis in a certain composition range. [172, 173, 183, 184] The origin of this perpendicular magnetic anisotropy can be attributed to a short-range chemical order that is induced by the film growth. [195–197] Several different effects leading to an anisotropy in the local atomic environment like a structural column formation [198], surface-induced ordering [199, 200], and pair ordering due to selective resputtering [201–203] have been proposed. These short-range orderings can lead to magnetoelastic [204, 205] and dipolar contributions [206, 207] to the magnetic anisotropy, as well as to a contribution due to interactions with the local crystal field on the *RE* sites [203].

Especially for sputtered Tb_xFe_{1-x} thin films, atomic pair ordering seems to play a dominant role. It has been shown that the next neighbor distances and coordination numbers for Tb-Tb, Fe-Fe, and Tb-Fe pairs are different for the in-plane and out-of-plane direction. [203, 205, 208, 209] Hufnagel *et al.* [208] and Harris *et al.* [203] reported an increased number of Tb-Fe pairs along the growth (out-of-plane) direction for sputtered films. The observed preferred out-of-plane orientation of the magnetic moments for a certain composition range can be accordingly explained by the interaction of the Tb 4f orbital, which has a disk-like shape [190], with the local crystal field. [210] In contrast to that, studies by Prados *et al.* [209] and Hernando *et al.* [205] showed a preferred Tb-Fe pair alignment in the film plane. Hernando *et al.* [205] attribute the perpendicular magnetic anisotropy to an interaction of the Tb 4f electron clouds with positive Fe ions, whereas Prados *et al.* [209] propose that the perpendicular magnetic anisotropy is caused by magnetostatic interactions between the Tb-Fe pairs. The dominating contribution to the anisotropy is, therefore, most likely depending on the film preparation method as well as on the layer thickness. Mimura *et al.* [172] observed an out-of-plane magnetic easy axis for 900 nm thick Tb_xFe_{1-x} in a composition range $0.15 < x < 0.28$.

For Gd_xFe_{1-x} films, the weak spin-orbit coupling of Gd ($L = 0$) that is caused by the 5d electrons results in a less pronounced single-ion anisotropy contribution (compared to Tb in Tb_xFe_{1-x} alloys). [211] Therefore, most probably, the main contribution to the perpendicular magnetic anisotropy is given by dipolar interactions or for thinner film thicknesses by a magneto-elastic anisotropy. [204, 212–214] An out-of-plane magnetic easy axis can be observed in a narrow composition range close to the magnetic compensation point, where the thin film shape anisotropy contribution is sufficiently small.

The perpendicular magnetic anisotropy of both, Gd_xFe_{1-x} and Tb_xFe_{1-x} films can be reduced in a controlled manner by noble gas ion implantation [212] or annealing [205, 208].

Magnetic compensation point and Curie temperature

As described in subsection 2.6.2 the net magnetization of FI RE_xTM_{1-x} alloys can be dominated by either the TM or the RE magnetic sublattices depending on the composition and temperature. Figure 2.12 shows the saturation magnetization with respect to the temperature of Gd_xFe_{1-x} and Tb_xFe_{1-x} alloys deposited by evaporation with different rare-earth content x. For the Gd_xFe_{1-x} alloys, a magnetic compensation temperature close to 300 K can be observed for $x = 0.255$. For the Tb_xFe_{1-x}, alloys a magnetic compensation temperatures of approximately 340 K and 385 K can be observed for rare-earth contents of $x = 0.243$ and $x = 0.271$. Mimura *et al.* [184] reported magnetic compensation temperatures between 100 K and 360 K for sputtered Gd_xFe_{1-x} films (with thicknesses $1.20\,\mu m \leq t \leq 1.39\,\mu m$) with $0.23 \lesssim x \lesssim 0.27$ and compensation temperatures between 180 K and 330 K for sputtered Tb_xFe_{1-x} films (with thicknesses $0.72\,\mu m \leq t \leq 0.96\,\mu m$) with $0.195 \lesssim x \lesssim 0.22$. However, as described above, especially for thin Tb_xFe_{1-x} films the compensation temperature has been shown to be strongly dependent on the film thickness. [188]

The Curie temperatures reported by Mimura *et al.* [184] for Gd_xFe_{1-x} with $0.15 \leq x \leq 0.35$ are in the range of $420\,K \leq T_{C,\,GdFe} \leq 500\,K$. For Tb_xFe_{1-x} with $0.12 \leq x \leq 0.47$ they reported Curie temperatures of $340\,K \leq T_{C,\,TbFe} \leq 420\,K$. For higher RE contents, the Curie

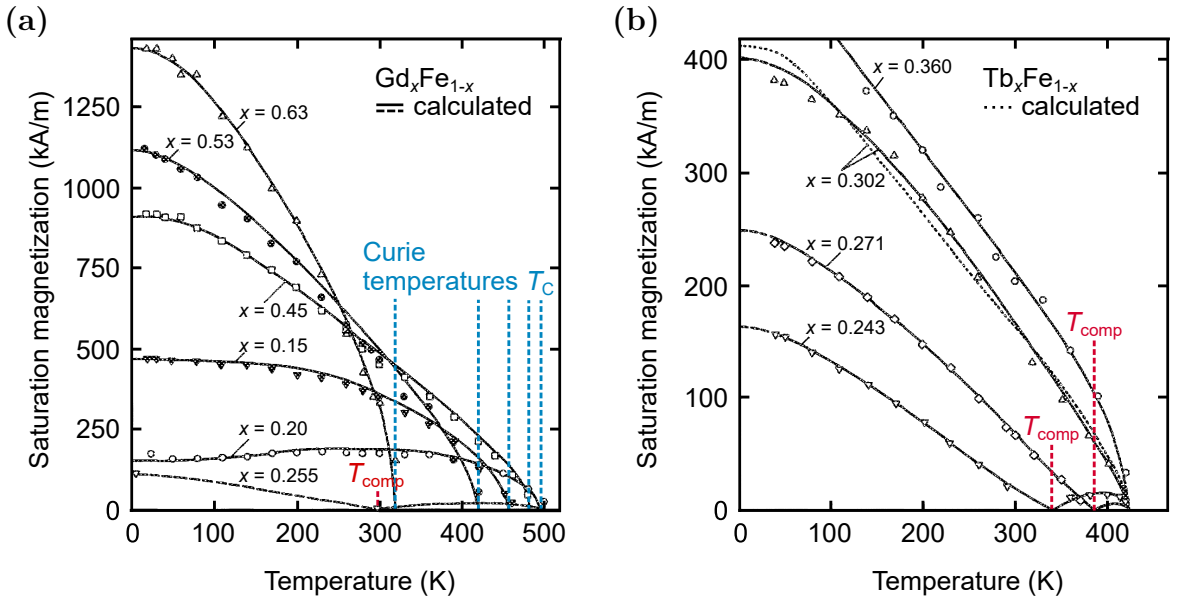

Figure 2.12: Saturation magnetization M_S in dependence on the temperature of (a) Gd_xFe_{1-x} and (b) Tb_xFe_{1-x} alloys with different rare-earth content x, reported by Hansen *et al.* [173]. The M_S values of the Gd_xFe_{1-x} alloys with $x < 0.255$ are dominated by the Fe magnetic sublattice, for $x > 0.255$ M_S is Gd-dominated. For $x = 0.255$ a magnetic compensation temperature T_{comp} close to room temperature (marked in red) can be observed. The Curie temperatures T_C are marked with the dashed blue lines. The M_S values of the Tb_xFe_{1-x} alloys with $x > 0.271$ are dominated by the Tb magnetic sublattice. For $x = 0.243$ and $x = 0.271$ a compensation point above room temperature can be observed (marked in red). The figures are adapted from [173].

temperatures strongly decrease with increasing RE content (see also the curves for $x \geq 0.45$ in figure 2.12a). [173]

Fanning cone compression and spin reorientation transitions

At high applied magnetic fields, the configuration of the magnetic moments in Tb_xFe_{1-x} films is determined by the interaction of the fanning cones with the applied field. For samples with a Tb-dominated net magnetization, a compression of the Tb fanning cone leads to an increase in the magnetization at high applied magnetic fields (see figure 2.13a). [188, 215] Close to the magnetic compensation point, the sperimagnetic configuration leads to satellite hystereses (see figure 2.13b) that are caused by irreversible spin reorientation transitions, so-called spin-flops [215]. A detailed discussion on the magnetization reversal of Tb_xFe_{1-x} films with different compositions at varying temperatures can be found in [215]. Also in the FI Gd_xFe_{1-x} films, spin-flop transitions at high applied magnetic fields can lead to increasing net magnetizations (see figure 2.13c). [212]

In the context of this work, the configuration of the magnetic moments at high applied magnetic fields is especially important for the estimation of the effective magnetic anisotropy from $M(H)$ loops that is discussed in detail in subsection 5.4.3.

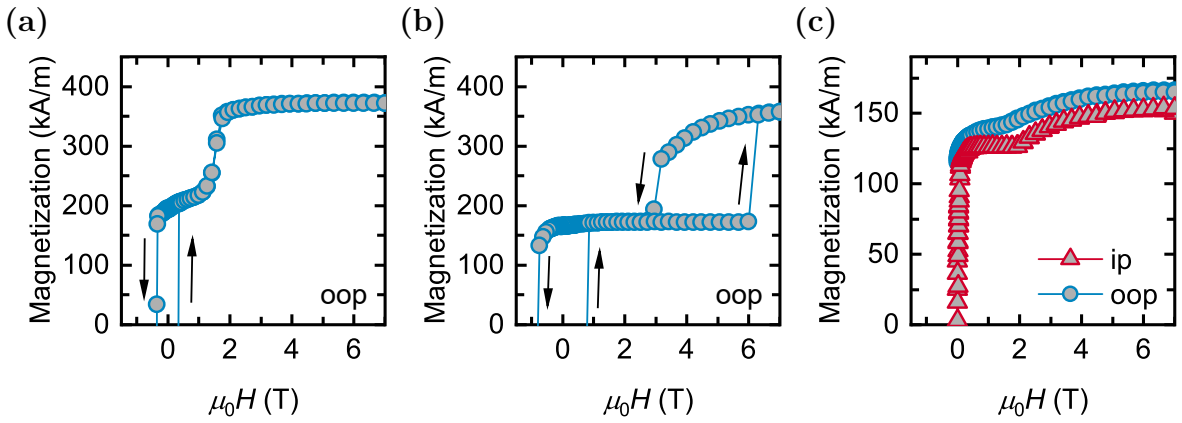

Figure 2.13: Excerpts of room-temperature $M(H)$ hysteresis loops of (a) a *sub.*/Pt(5 nm)/$Tb_{0.40}Fe_{0.60}$(20 nm)/Co(2 nm) sample measured in out-of-plane direction, (b) a *sub.*/Pt(5 nm)/$Tb_{0.22}Fe_{0.78}$(20 nm)/Si_3N_4(5 nm) sample measured in out-of-plane direction, and (c) a *sub.*/Pt(5 nm)/$Gd_{0.25}Fe_{0.75}$(20 nm)/Si_3N_4(5 nm) sample measured in in-plane and out-of-plane direction. The black arrows mark the field sweep direction.

CHAPTER 3

Laser-induced ultrafast magnetization dynamics

A promising way to manipulate the magnetic order in a material on a very short time scale is given by the use of optical pulses. The breakthrough experiment that opened the way for the emerging research field of ultrafast laser-induced magnetization dynamics was done by Beaurepaire *et al.* [216] in 1996. In time-resolved magneto-optical Kerr effect measurements performed on a thin Ni film after excitation by 620 nm laser pump pulses with a pulse duration of 60 fs, they could show that the Kerr signal drastically drops within less than 1 ps and recovers on a larger time scale. The short demagnetization time gave evidence for the direct interaction of excited, so-called hot electrons with the spin system without the involvement of the lattice, as electron-phonon interactions happen on a time scale of several picoseconds [217–219]. Since then, numerous studies on ultrafast magnetization dynamics have been performed. Besides investigations on the ultrafast demagnetization of different FM [220–225] and FI [223, 226] thin films, also laser-induced all-optical magnetization switching in different FI [188, 227–231] and FM [232–236] systems has been demonstrated. Furthermore, studies on the emission of THz radiation caused by ultrafast demagnetization [223, 237–239], as well as on the generation of ultrafast spin currents [240–242] have been performed. The fundamental studies on ultrafast magnetization dynamics also opened the way for the development of spintronic THz emitters [81], on which the main focus of this work is centered. However, despite the large variety of experimental results, there are still many open questions regarding the underlying microscopic mechanisms. Detailed reviews on laser-induced ultrafast magnetization dynamics are given, for example, in [243–246].

In the following, a short introduction to the ultrafast demagnetization of magnetic materials after excitation with short laser pump pulses will be given (section 3.1) and the emission of THz radiation directly caused by ultrafast demagnetization will be explained (section 3.2). Furthermore, the concept of spintronic THz emitters will be introduced, and a summary of the properties of spintronic THz emitters and the current stage of development will be given (section 3.3).

3.1 Laser-induced ultrafast demagnetization

The following explanations are based on the review papers by Kirilyuk *et al.* [243] and Walowski *et al.* [245] and on the book chapter by Carva *et al.* [246].

The processes that happen when a system is excited with a short optical laser pulse can be described with the phenomenological three-temperature model. [216] In this model, the electrons, the spins, and the lattice are described as separate reservoirs that are characterized by their heat capacities c_{el}, c_{sp}, c_{lat} and their temperatures T_{el}, T_{sp}, T_{lat}, respectively. The reservoirs are connected by different interactions. Figure 3.1a shows a schematic of the interactions with respect to the time scale for a FM system that is excited with a femtosecond laser pulse. The evolution of the temperatures with respect to the time τ in that model can be described by three coupled differential equations [216]:

$$\begin{aligned} c_{\mathrm{el}}\frac{\partial T_{\mathrm{el}}}{\partial \tau} &= -G_{\mathrm{el-lat}}(T_{\mathrm{el}}-T_{\mathrm{lat}}) - G_{\mathrm{el-sp}}(T_{\mathrm{el}}-T_{\mathrm{sp}}) + P(\tau)\ , \\ c_{\mathrm{sp}}\frac{\partial T_{\mathrm{sp}}}{\partial \tau} &= -G_{\mathrm{el-sp}}(T_{\mathrm{sp}}-T_{\mathrm{el}}) - G_{\mathrm{sp-lat}}(T_{\mathrm{sp}}-T_{\mathrm{lat}})\ , \\ c_{\mathrm{lat}}\frac{\partial T_{\mathrm{lat}}}{\partial \tau} &= -G_{\mathrm{el-lat}}(T_{\mathrm{lat}}-T_{\mathrm{el}}) - G_{\mathrm{sp-lat}}(T_{\mathrm{lat}}-T_{\mathrm{sp}})\ , \end{aligned} \tag{3.1}$$

where $P(\tau)$ describes the optical input. The coupling coefficients $G_{\mathrm{el-sp}}$, $G_{\mathrm{el-lat}}$, and $G_{\mathrm{sp-lat}}$ are phenomenological parameters that represent the strength of the interactions between the reservoirs and are strongly dependent on the material. The time evolution of the temperatures calculated for the demagnetization of a Ni film [216] is displayed in figure 3.1b. The processes leading to the demagnetization can be understood in the following way: (i) The laser beam hits the sample and creates electron-hole pairs (hot electrons). (ii) A relaxation of the electronic and the spin system at elevated temperatures T_{el} and T_{sp} takes place. In this time regime, incoherent processes lead to the demagnetization. The spin temperature T_{sp} is defined as the temperature corresponding to the achieved magnetization in an equilibrium $M(T)$ curve. (iii) For longer delay times (after the laser excitation), the spin and electronic excitations decay via interactions with the lattice.

However, the underlying microscopic processes are still under debate. [246] The spin angular momentum conservation leads to the necessity of an ultrafast dissipation channel for the spin angular momentum. Therefore, different mechanisms that allow spin flips of excited electrons, such as an Elliott-Yafet-type of phonon scattering [248, 249], spin flip Coulomb scattering [250], laser-induced spin flips [251, 252], or relativistic quantum electrodynamic processes [247] have been proposed. A different explanation approach is given by the spin-dependent transport of laser-excited electrons [240, 241, 253] that can lead to the generation of ultrafast spin-polarized charge currents and will be discussed in detail in subsection 3.3.1.

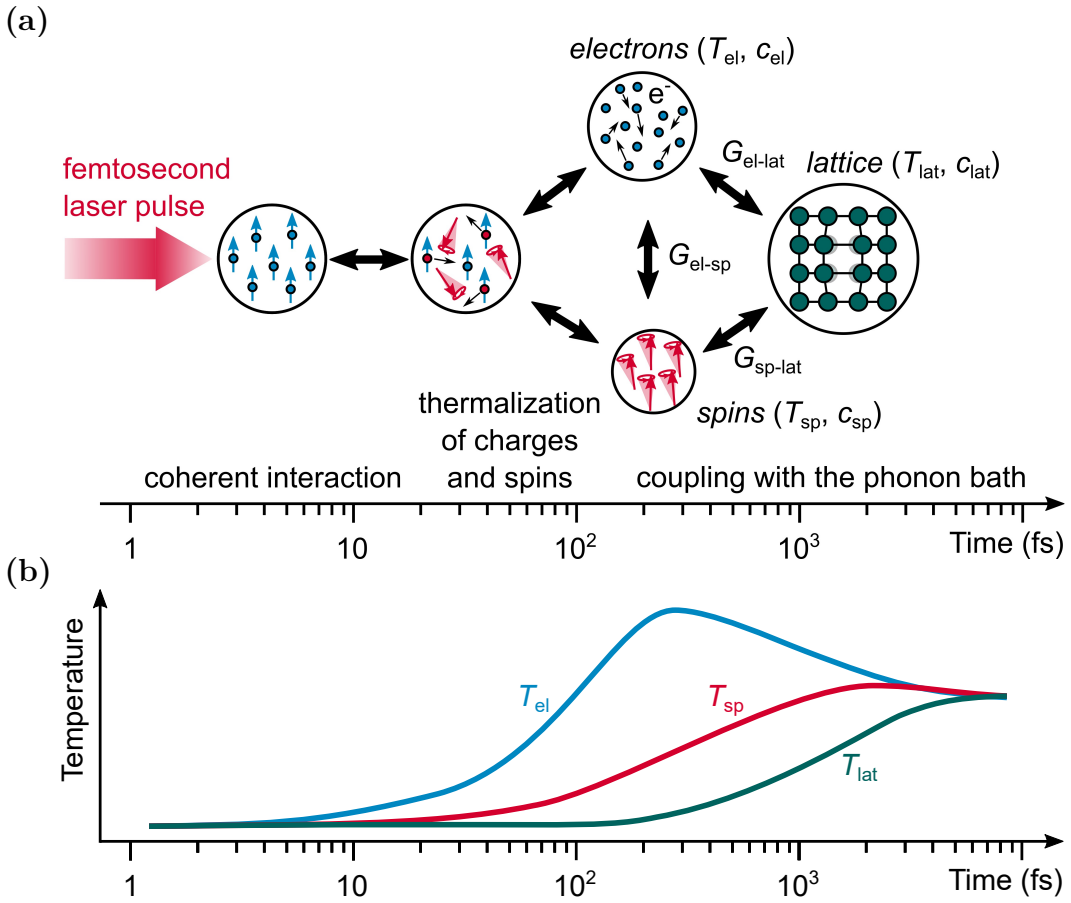

Figure 3.1: Time evolution of (a) the laser driven interactions and (b) the temperatures of the three reservoirs T. Subfigure (a) is adapted from [247] and [245]. In (b) the calculated temperatures for the laser-induced demagnetization of a Ni film, presented in [216] are plotted on a logarithmic scale for a gaussian laser pump pulse with a duration of 100 fs centered at the time $\tau = 100$ fs.

3.2 Terahertz emission directly caused by ultrafast demagnetization

As mentioned in the introduction, the ultrafast laser-induced demagnetization of thin magnetic films has been shown to lead to the emission of electromagnetic radiation in the THz frequency regime. The first experiments, were performed by Beaurepaire *et al.* in 2004 [237] on 30 nm thick Ni films. Since then, THz spectroscopy studies on different magnetic 3d transition metals (Fe [239, 254], Co [223, 238, 239], Ni [239], NiFe [255]) and rare earth-3d transition metal alloys [223], have been published and the measured THz signals have been directly compared with time-resolved magnetization measurements [223, 238]. The emission of the THz electric field can be interpreted with regard to the classical Maxwell theory as an excitation of elementary magnetic dipoles in the film, resulting in a time-varying magneti-

zation. [237] In the far field, the emitted electric field propagating in the y-direction can be described as [237]:

$$E_{\mathrm{x}}(\tau) \sim \frac{\partial^2 M_{\mathrm{z}}(\tau)}{\partial \tau^2} \ , \tag{3.2}$$

where E_{x} is the x-component of the electric field and M_{z} the magnetization in z-direction. The polarization of the THz radiation has been shown to be perpendicular to the magnetization direction [223, 237, 238, 255] and independent of the polarization of the pump laser pulse [237]. With regard to the results presented in this work, it is important to keep in mind that for all of the discussed spintronic THz emitter systems also a contribution to the THz signal caused by ultrafast demagnetization is expected. A discussion of this contribution for *sub.*/Pt(5 nm)/$\mathrm{Gd}_x\mathrm{Fe}_{1-x}$(20 nm)/$\mathrm{Si_3N_4}$(5 nm) spintronic emitter systems is presented in chapter 8.

3.3 Spintronic terahertz emitters

The concept of spintronic THz emitters was first proposed by Kampfrath *et al.* [81] in 2013. The most basic spintronic THz emitters are bilayers consisting of a FM layer and a NM layer, usually with a high spin Hall angle. Typical film thicknesses are on the order of a few nanometers. Figure 3.2 displays a schematic emitter system and the processes that lead to the emission of THz radiation. Excitation of such a bilayer with a short optical laser pulse on the order of 10 to 100 fs leads to the generation of an ultrafast spin-polarized charge current with the density $\boldsymbol{J}_{\mathrm{s}}$ [240, 242, 256] that flows from the FM layer toward the NM layer. In the NM layer, the spin-polarized electrons are deflected due to effects related to the spin-orbit coupling that leads to a transverse charge current pulse with the density $\boldsymbol{J}_{\mathrm{c}}$. For most spintronic THz emitter systems, the spin-to-charge current conversion is attributed to the inverse spin Hall effect [257]. As all these processes happen on the time scale of a few picoseconds, the charge current $\boldsymbol{J}_{\mathrm{c}}$ leads to the emission of electromagnetic radiation in the THz frequency regime. The processes leading to the THz emission will be discussed in more detail in the subsections 3.3.1–3.3.3. Furthermore, an overview of the properties of spintronic THz emitters in general and some recent developments in this research field will be given in subsection 3.3.4.

3.3.1 Generation of ultrafast spin currents

The first experiments demonstrating the laser-excited transport of spin angular momentum were carried out by Malinowski *et al.* [253] in 2008 with $[\mathrm{Co/Pt}]_n/\mathrm{Ru}/[\mathrm{Co/Pt}]_n$ multilayer systems, indicating the importance of this process for the ultrafast demagnetization. More direct measurements of laser-induced ultrafast spin currents were performed by Melnikov *et al.* [256]

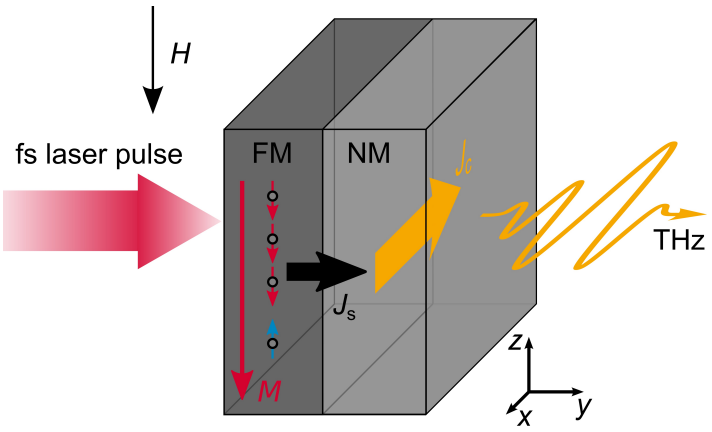

Figure 3.2: Schematic of a spintronic THz emitter. Excitation of a FM/NM bilayer leads to the formation of a spin-polarized charge current $\boldsymbol{J}_\mathrm{s}$ from the FM toward the NM layer. The red and blue arrows denote the direction of the magnetic moment of the majority- and minority-spin electrons, respectively. In the NM layer, the electrons are deflected due to the inverse spin Hall effect in different directions according to their spin and therefore form a transverse charge current $\boldsymbol{J}_\mathrm{c}$ that leads to the emission of THz radiation. The figure is adapted from [82].

in Fe/Au systems and by Rudolf *et al.* [242] in Ni/Ru/Fe trilayers, demonstrating that the spin currents reach their maximum within a few hundred fs after the optical excitation. Afterward, the systems relax back to an equilibrium state on the ps time scale. The exact relaxation times depend on the used materials. A theoretical approach was given by Battiato *et al.* [240, 241] with the proposed concept of a superdiffusive spin current generation in FM 3d transition metals. A schematic displaying the laser-induced generation of superdiffusive spin currents in a FM/NM bilayer is shown in figure 3.3. By absorption of a near-infrared ($\approx 800\,\mathrm{nm}$, $\approx 1.55\,\mathrm{eV}$) photon, an electron in the d band can be lifted to an excited state above the Fermi level E_F. It is assumed that the excitation process is spin-conserving. In a magnetized FM layer, the excited majority-spin electrons have mainly an sp-like character with higher velocities and lifetimes compared to the minority-spin electrons that are excited in d-like states with smaller velocities and shorter lifetimes. [258] For iron, the velocities of the excited electrons with an energy of $E - E_\mathrm{F} = 1.5\,\mathrm{eV}$ are on the order of $v_{\downarrow,\,\mathrm{Fe}} \approx 0.75 \cdot 10^6 \mathrm{m/s}$ for majority-spin and $v_{\uparrow,\mathrm{Fe}} \approx 0.07 \cdot 10^6 \mathrm{m/s}$ for minority-spin electrons and the respective lifetimes are $\tau_{\downarrow,\,\mathrm{Fe}} \approx 7\,\mathrm{fs}$ and $\tau_{\uparrow,\,\mathrm{Fe}} \approx 5\,\mathrm{fs}$. [258] Therefore, the relative difference in the inelastic mean free paths of excited majority-spin and minority-spin electrons by a factor of ≈ 15 is mainly caused by the different velocities. In contrast to that, the relative difference of the inelastic mean free paths of excited majority-spin and minority-spin electrons in nickel is by a factor of ≈ 3 smaller compared to Fe and mainly dominated by the difference in the lifetimes rather than by the velocities. [258] The excited electrons are assumed to move in random directions until they undergo an elastic or inelastic scattering event (for example, with other electrons, phonons, or impurities). In an inelastic scattering event with another electron, a part of the energy will be transferred to this electron, leading to its excitation. As the mean

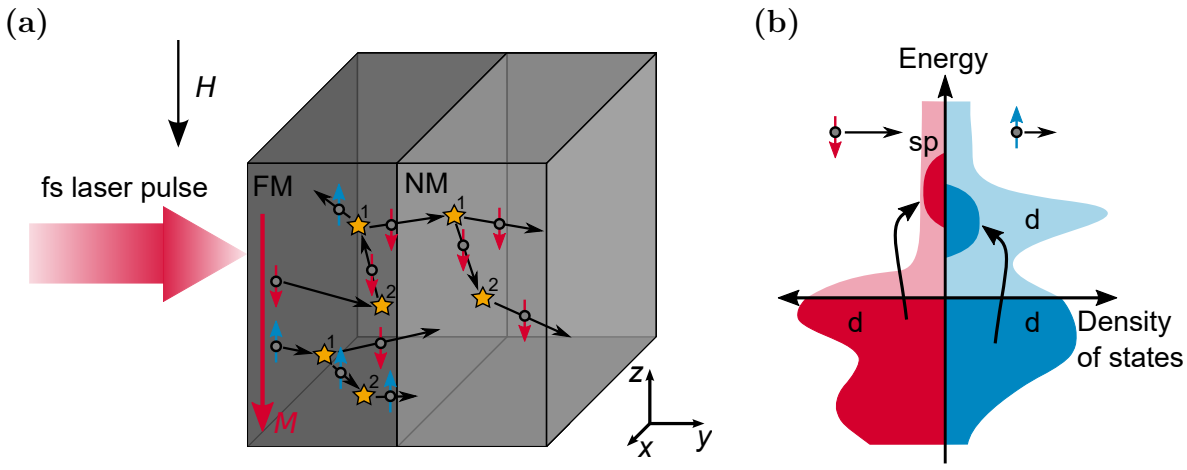

Figure 3.3: (a) illustrates the motion of laser-excited electrons on the femtosecond timescale in a FM/NM bilayer for an applied magnetic field $\boldsymbol{H}$. The red and blue arrows denote the direction of the magnetic moment of the majority- and minority-spin electrons, respectively. After the laser excitation, the hot electrons move in a random direction until they undergo elastic (1) or inelastic (2) scattering events (marked with the yellow stars) that lead to deflections in different directions. Inelastic scattering events also lead to the excitation of other electrons above the Fermi level. Some of the hot electrons also cross the FM/NM interface. The higher velocities and lifetimes of excited majority-spin electrons compared to the minority-spin electrons lead to the generation of a spin current from the FM toward the NM layer. (b) shows a schematic of the bandstructure close to the Fermi level (at the x-axis) for the laser excitation of a magnetized Fe layer. Slow majority-spin d electrons (red) are excited into fast sp-like states, whereas the minority-spin electrons (blue) are promoted to slow d-like states above the Fermi level. (a) is adapted from [240] and [241], (b) is based on [81].

free path of the electrons of a few nanometers [258, 259] usually is several orders of magnitude smaller than the laser spot size ($\approx$ mm), only a movement in the y-direction is considered. For sufficiently thin FM/NM bilayers, some of the electrons will cross the interface to the NM layer. Due to the different transport properties of the excited majority-spin and minority-spin electrons, statistically, more majority-spin electrons will move into the NM layer, resulting in a superdiffusive spin-polarized charge current $\boldsymbol{J}_\mathrm{s} = \boldsymbol{J}_{\mathrm{s}\downarrow} - \boldsymbol{J}_{\mathrm{s}\uparrow}$ from the FM toward the NM layer, and consequently to a temporary demagnetization of the FM layer. $\boldsymbol{J}_{\mathrm{s}\downarrow}$ and $\boldsymbol{J}_{\mathrm{s}\uparrow}$ denote the charge current densities caused by the majority- and minority-spin electrons, respectively. The spin-polarized charge current $\boldsymbol{J}_\mathrm{s}$ will be referred to as "spin current" within this work.

The concept of superdiffusive spin transport was first used in 2013 by Kampfrath *et al.* [81] to explain the spintronic THz emission in FM/NM bilayers. More recently, Nenno *et al.* [260, 261] applied the approach to Boltzmann transport calculations to model the spin transport and the resulting THz radiation in FM/NM samples. Besides the discussed superdiffusive spin transport, also a laser-induced heat gradient in the y-direction can cause a contribution to the spin current due to the spin(-dependent) Seebeck effect (SSE) [262–265]. However, recent studies by Sasaki *et al.* [266] and Rouzegar *et al.* [267] strongly indicate that the SSE only plays a minor role in metallic FM/NM layer stacks and Rouzegar *et al.* [267] also

demonstrated that the ultrafast demagnetization and the ultrafast spin transport share the same driving force. Nevertheless, laser excitation of non-metallic yttrium iron garnets leads to ultrafast pure (magnonic) spin currents driven by the SSE. [268]

3.3.2 Spin-to-charge current conversion

Some of the key aspects in the emerging field of spintronics are the generation, manipulation, and detection of spin currents. [269] In this regard, relativistic spin-orbit interactions that give rise to a coupling between spin and charge currents in conducting materials are of great importance. [270] Especially the different spin-dependent Hall effects [271, 272] that describe the spin-to-charge current conversion and vice versa in bulk material are widely used for spintronic devices. Also, material systems with Rashba interfaces that allow spin-to-charge current interconversions by the Rashba effect and inverse Rashba-Edelstein effect (IREE) [273, 274] gained a lot of interest. [275] In contrast to the (bulk) spin-dependent Hall effects, the IREE is a pure interface effect. A prototype Rashba system is the Ag/Bi interface. [276, 277] However, it is still under debate whether the spin-to-charge current conversion in that system can really be attributed to the IREE or to the inverse spin Hall effect. [278] As the IREE is expected to play a minor role in the material systems investigated in this work, this subsection will focus on the diverse spin-dependent Hall effects. However, these are still complex up-to-date research topics. Therefore, only a short introduction describing some of the key aspects will be given here. The interested reader is referred to the review article by Hoffmann *et al.* [271], on which this subsection is mainly based on. Other detailed reviews on the topic are given in [272, 279, 280].

In contrast to the classical Hall effect [281], the spin-dependent Hall effects describe the generation of transversal spin currents from charge currents and vice versa without the application of external magnetic fields. In figure 3.4 schematics of the spin-dependent Hall effects are displayed.

The anomalous Hall effect [280, 283] displayed in (a) has its origins back at the end of the 19^{th} century in experiments carried out by Hall [283]. It describes the transversal deflection of electrons in a FM or FI material depending on their spin when a charge current with the density $\boldsymbol{J}_\text{c}$ is applied. Due to the different amounts of majority and minority-spin electrons in a magnetized FM or FI material that contribute to $\boldsymbol{J}_\text{c}$, this leads to a transversal spin-polarized charge current with the density $\boldsymbol{J}_\text{s}^\text{AHE}$ and therefore to the accumulation of spin-polarized electrons on the sample edges. Thus, a transversal voltage drop can experimentally be measured.

The spin Hall effect displayed in (b) describes the same effect in non-magnetic metals or semiconductors. When a charge current is applied, electrons with opposing spins are deflected in opposite transversal directions. This leads to a pure transversal spin current $\boldsymbol{J}_\text{s}^\text{SHE}$ and

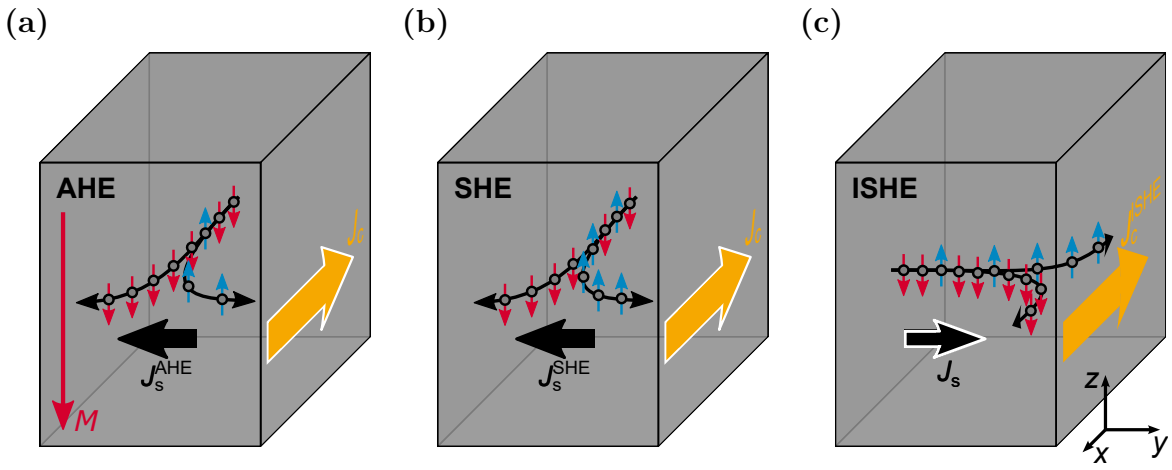

Figure 3.4: Illustration of the spin-dependent Hall effects. The arrows representing the initially applied currents are marked with white frames. The red and blue arrows denote the direction of the magnetic moment of the electrons. The anomalous Hall effect (AHE) shown in (a) describes the spin-dependent deflection of electrons when a charge current $\boldsymbol{J}_\mathrm{c}$ is applied to a FM or FI material with the magnetization $\boldsymbol{M}$. This leads to the transversal spin current $\boldsymbol{J}_\mathrm{s}^\mathrm{AHE}$. As $\boldsymbol{J}_\mathrm{c}$ is spin-polarized in an FM or FI layer, $\boldsymbol{J}_\mathrm{s}^\mathrm{AHE}$ describes a spin-polarized charge current. The spin Hall effect (SHE) displayed in (b) describes the same effect in a non-magnetic metal. As $\boldsymbol{J}_\mathrm{c}$ is not spin-polarized here, the resulting $\boldsymbol{J}_\mathrm{s}^\mathrm{SHE}$ is a pure spin current. The inverse spin Hall effect (ISHE) describes the conversion of a pure spin or a spin-polarized charge current $\boldsymbol{J}_\mathrm{s}$ that is applied to a non-magnetic or ferromagnetic metal into a charge current $\boldsymbol{J}_\mathrm{c}^\mathrm{ISHE}$. (c) displays the ISHE for a spin-polarized charge current $\boldsymbol{J}_\mathrm{s}$ that is applied to a non-magnetic metal. The different amounts of incoming majority-spin and minority-spin electrons that are deflected in opposite directions lead to the transverse charge current $\boldsymbol{J}_\mathrm{c}^\mathrm{ISHE}$. The figures are adapted from [282].

therefore to a spin accumulation at the transversal sample edges. In contrast to the anomalous Hall effect, no charge accumulation takes place, and consequently, also no transversal voltage drop can be measured. The spin Hall effect has been theoretically predicted by Dyakonov and Perel [284] in 1971. However, it took more than 30 years until the effect could be experimentally observed by Kato *et al.* [285] and Wunderlich *et al.* [286] in 2004. The spin current density can be described by [282]:

$$\boldsymbol{J}_\mathrm{s}^\mathrm{SHE} = \theta_\mathrm{sh}\left(-\frac{\hbar}{2e}\right)\boldsymbol{J}_\mathrm{c}\times\boldsymbol{\sigma}\ , \tag{3.3}$$

with the reduced Planck constant $\hbar$, the elementary charge e, and the spin polarization $\boldsymbol{\sigma}$. The spin Hall angle θ_sh is a material-dependent factor that describes the magnitude of deflection of the electrons. Depending on the material, θ_sh can take positive (e.g., in Pt, Pd, Au) or negative (e.g., in Ta, W, Mo) values. [271]

The inverse spin Hall effect has first been experimentally observed in 2006 by Saitoh *et al.* [257]. It describes the spin-dependent deflection of electrons when a pure spin current or a spin-polarized charge current is applied to non-magnetic or FM material. [282] A schematic of the

inverse spin Hall effect for the case of a spin-polarized charge current $\boldsymbol{J}_\mathrm{s}$ that is applied to a NM layer is shown in (c). The incoming spin-polarized electrons are deflected according to their spin in opposite directions perpendicular to the direction of $\boldsymbol{J}_\mathrm{s}$, leading to the charge current $\boldsymbol{J}_\mathrm{c}^\mathrm{ISHE}$. The charge current density can be described by [282]:

$$\boldsymbol{J}_\mathrm{c}^\mathrm{ISHE} = \theta_\mathrm{sh} \left(-\frac{2e}{\hbar} \right) \boldsymbol{J}_\mathrm{s} \times \boldsymbol{\sigma} \ . \tag{3.4}$$

Different microscopic mechanisms that can lead to the spin-dependent deflection of the electrons and, therefore, to the spin-dependent Hall effects have been discussed in the literature. In general, it can be distinguished between extrinsic contributions that are caused by scattering events at impurities [287–289] and an intrinsic contribution that leads to the deflection of the electrons in between the scattering events [290]. The three main mechanisms that can contribute to the spin-dependent Hall effects are schematically shown in figure 3.5.

The intrinsic deflection displayed in (a) can be described by an additional contribution to the velocity of the electrons perpendicular to $\boldsymbol{J}_\mathrm{c}$, that is given by the cross product of the electric field $\boldsymbol{E}$ giving rise to $\boldsymbol{J}_\mathrm{c}$ and the so-called Berry curvature. [279, 290] The contribution is proportional to the spin-orbit polarization at the Fermi level, and therefore, following Hund's rule, it is expected to be positive for transition metals with more than half-filled d bands and negative for transition metals with less than half-filled d bands. [271]

The spin skew scattering displayed in (b) is caused by an effective magnetic field gradient within the scattering plane that is based on spin-orbit coupling at an impurity in a crystal. This leads to a net force toward or away from the scattering center, depending on the spin direction. [288] The spin Hall angle caused by spin skew scattering is independent of the impurity concentration and tends to dominate for high-purity samples at low temperatures. [271] As the effect depends on the contrast between the spin-orbit coupling of the host and impurity, it is expected to be large for light element impurities embedded in heavy element hosts and vice versa. [271, 291]

The side jump scattering shown in (c) is caused by a spin-dependent acceleration and deceleration of the electrons during scattering events at an impurity, caused by spin-orbit interaction. For repeated scatterings, this leads to transverse displacements of the electrons. [289] This contribution is usually small compared to the two other mechanisms. [292]. However, as it is proportional to the number of impurities, it may become important for samples with high impurity concentrations. [293]

A detailed summary on the spin Hall angles of different materials is given in [271]. For the THz emitter systems investigated in this work, Pt ($+1.2\% \leq \theta_{\mathrm{sh,\,Pt}} \leq +11\%$ [271, 294, 295]) and W ($-33\% \leq \theta_{\mathrm{sh,\,W}} \leq -7\%$ [296]) were chosen as NM layers with large spin Hall angles.

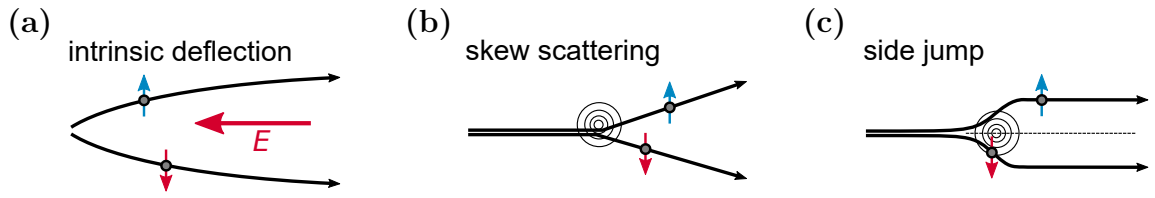

Figure 3.5: Illustration of the main mechanisms that can contribute to the spin-dependent Hall effect. (a) shows an intrinsic deflection of electrons due to an anomalous velocity perpendicular to the electric field. The anomalous velocity is related to the Berry phase curvature. (b) displays the asymmetric skew scattering of electrons at an impurity due to an effective spin-orbit coupling. (c) shows a side jump scattering at an impurity that is caused by a spin-dependent acceleration and deceleration upon approaching and leaving the impurity. The figure is adapted from [280].

3.3.3 Outcoupling of the terahertz radiation

The first description of the emitted radiation in the THz frequency regime by spintronic systems was given by Kampfrath *et al.* [81] and later on modified by Seifert *et al.* [82, 297], on which the following explanations are based. The diameter of the pump laser beam for most of the experiments shown in this work had a full width half maximum of 4 mm. Therefore, it is large compared to the thicknesses of the spintronic layer stacks (3.5 nm $\leq t \leq$ 20 nm) and a plane-wave propagation of the THz electric field along the y-axis can be assumed (see figure 3.2). The emitted electric field $\boldsymbol{E}(y,\omega)$ generated by the charge current density $\boldsymbol{J}_\mathrm{c}(\omega)$ is polarized along the x-axis ($\boldsymbol{E}||\boldsymbol{J_c}$). Therefore, the following equations are written without using a vector notation. In the frequency domain $E(y,\omega)$ can be described by the wave equation [298]

$$(\partial_y^2 + k^2(y,\omega))E(y,\omega) = Z_0\omega J_\mathrm{c}(\omega)/\mathrm{i}c \ , \tag{3.5}$$

with the vacuum impedance $Z_0 = 377\,\Omega$, the vacuum speed of light c and the wave vector $k(y,\omega)$. It is assumed that the emitter system with the thickness t is placed at the position $y = 0$ in between an infinite substrate half space ($y < 0$) with the refractive index n_1 and an infinite air half space ($y > t$) with the diffraction index $n_2 \approx 1$. The wave vector can then be described by $k^2(y,\omega) = k_0^2(y,\omega) + \Delta(k^2)(y,\omega)$, with the wave vector $k_0(y,\omega) = n(y,\omega)\omega/c$ of the system without the spintronic layers and the perturbation $\Delta(k^2)(y,\omega)$ describing the influence of the spintronic metal films. $k_0(y,\omega)$ is given by $k_0(\omega) = n_1\omega/c$ for $y < 0$ and $k_0(\omega) = n_2\omega/c$ for $y > t$. The perturbation $\Delta(k^2)(y,\omega)$ can be described by $\Delta(k^2)(y,\omega) = \mathrm{i}Z_0\sigma(y,\omega)\omega/c$ with the electrical conductivity of the spintronic layer stack $\sigma(y,\omega)$. Equation 3.6 can be analytically solved for a thin emitter system ($k(y,\omega)t \ll 1$) by using a Green's function (the interested reader is referred to [81, 82, 298]) resulting in the emitted electric field directly behind the spintronic films [82]

$$E(\omega) = -Z(\omega)J_\mathrm{c}(\omega) \ , \tag{3.6}$$

in which the impedance $Z(\omega)$ is described by

$$\frac{1}{Z(\omega)} = \frac{n_1(\omega) + n_2(\omega)}{Z_0} + \int_0^t \sigma(y,\omega)\mathrm{d}y \ . \tag{3.7}$$

Taking into account the spin-to-charge current conversion by the ISHE described in the previous subsection (see equation 3.4) and including the influence of the laser pump pulse absorption and the spin relaxation length in the NM layer, equation 3.6 can be modified for a laser-excited FM/NM bilayer to [297]

$$E(\omega) \sim C(\omega) \left(\frac{2e}{\hbar}\right) \theta_{\mathrm{sh}} J_{\mathrm{s}}(\omega) \lambda_{\mathrm{rel}} \ , \tag{3.8}$$

with the spin current density J_{s} (propagation in y-direction and polarization in z-direction), the spin Hall angle θ_{sh} of the NM layer and the relaxation length of the spin current within the NM layer λ_{rel}. Multiple reflections at the interfaces of the spintronic layers can be neglected due to the small spin relaxation lengths on the order of 1 nm. All sample parameters that are not directly connected to the spintronic properties are included in the formula [297]

$$C(\omega) = \frac{A/t}{(n_1(\omega) + n_2(\omega))/Z_0 + \int_0^t \sigma(y,\omega)\mathrm{d}y} = \frac{A}{t} Z(\omega) \ , \tag{3.9}$$

with A/t describing fraction of the laser pump pulse that is absorbed by the spintronic layers. The function $C(\omega)$ is called emission efficiency within this work.

The THz signals are emitted from the NM layer in the direction of the substrate and the capping layer. In most of the THz spectroscopy experiments performed for this work, the emitters were excited from the capping-layer side. Due to multiple reflections of the emitted THz radiation and the excitation laser at the substrate-air interface as well as on the interface between the substrate and the spintronic layer stack, several time-delayed echo signals can be detected in the experiments. However, as these will not be further discussed in this work, the interested reader is referred to the PhD thesis of Dr. Robert Schneider [299].

3.3.4 Properties of spintronic terahertz emitters and current developments

Since the development of the spintronic THz emission concept in 2013, numerous studies on the properties and on the optimization of the emitters have been performed in the last few years. Besides the possibility of an easy and cost-efficient preparation by magnetron sputter deposition (see chapter 4), spintronic emitters have been demonstrated to be scalable in size [74] and can even be fabricated on flexible substrates [300]. In the following, an overview of the properties of spintronic emitter systems and recent developments in the field will be given. Detailed reviews of the topic can also be found in [68, 301–305].

Polarization and spectrum of the emitted terahertz radiation

The polarization of the emitted THz radiation is parallel to the charge current $\boldsymbol{J}_\mathrm{c}$ and therefore perpendicular to the spin current $\boldsymbol{J}_\mathrm{s}$ and the polarization $\boldsymbol{\sigma}$ of the spin-polarized electrons that contribute to $\boldsymbol{J}_\mathrm{s}$. In soft magnetic 3d transition metal films, the spin polarization of the contributing electrons is proportional to the magnetization $\boldsymbol{M}$. Thus, the direction of the charge current can be described by $\boldsymbol{J}_\mathrm{c} \sim \theta_\mathrm{sh} \boldsymbol{J}_\mathrm{s} \times \boldsymbol{M}/|\boldsymbol{M}|$. Consequently, the polarization of the emitted THz radiation of FM/NM bilayers can be controlled by changing the magnetization direction of the FM layer with an applied magnetic field within the sample plane [83, 306] and the THz amplitude follows the $M(H)$ loop for different applied magnetic fields H [306]. Furthermore, inverting the layer stack (or exciting the emitter from the opposite side) leads to an opposite direction of $\boldsymbol{J}_\mathrm{s}$ and therefore to an inversion of the THz signal. [81, 82, 300] In contrast to that, THz radiation that is caused by the ultrafast demagnetization of the FM layer is independent of the inversion of the layer stack. Therefore, experiments with different excitation direction can be used to prove the spintronic origin of the emitted THz radiation of a sample. Figure 3.6a shows the THz electro-optic signals (see section 5.6 for details on

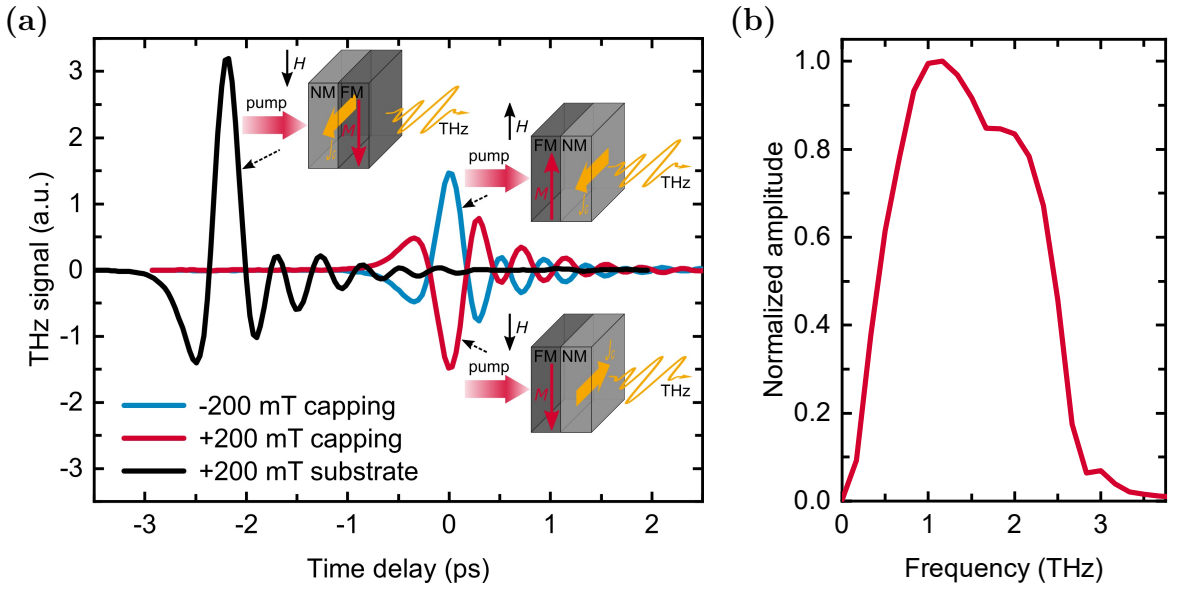

Figure 3.6: Room-temperature THz emission spectroscopy results (see section 5.6 for information measurement technique) of a *sub.*/Pt(5 nm)/Fe(20 nm)/Si_3N_4(5 nm) sample. The change in the delay time upon reversing the sample stems from different propagation of THz radiation and the excitation laser through the substrate. (a) shows the THz electro-optic signal for laser excitation from the capping-layer side with applied magnetic fields $\mu_0 H = +200\,\mathrm{mT}$ and $\mu_0 H = -200\,\mathrm{mT}$ and for excitation from the substrate side with $\mu_0 H = +200\,\mathrm{mT}$. (b) displays the corresponding normalized frequency spectrum (excitation through the capping layer, $\mu_0 H = +200\,\mathrm{mT}$) determined by Fourier transformation. Note that the bandwidth is limited by the used 1 nm ZnTe detector crystal of the THz spectroscopy setup to frequencies below 3 THz. The real bandwidth of spintronic emitters exceeds 10 THz. [81, 82] The THz spectroscopy measurements were performed by Dr. Robert Schneider at the University of Münster.

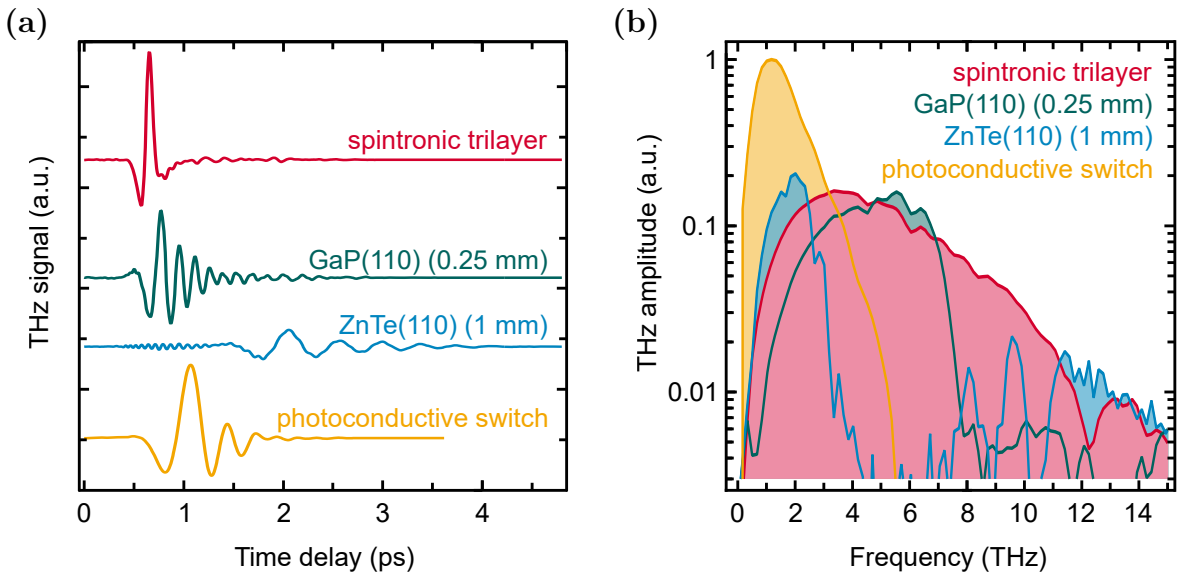

Figure 3.7: THz emission of a thickness-optimized W(2 nm)/$Co_{0.4}Fe_{0.4}B_{0.2}$(1.8 nm)/Pt(2 nm) spintronic trilayer THz emitter in comparison to the emission of GaP(110)(0.25 mm) and ZnTe(110)(1 mm) crystals as well as of a photoconductive switch. (a) displays the THz signals and (b) the corresponding frequency spectra. The figures are adapted from [82].

the measurement technique) of a Pt/Fe sample for different excitation directions and applied magnetic fields. The corresponding frequency spectrum for excitation from the capping-layer side is displayed in figure 3.6b. Besides, the polarization can also be turned by 180° by using a NM material with an opposite sign of the spin Hall angle θ_{sh}. [81, 82, 300]

Recently, also the polarization control of the spintronic THz emission by applying a magnetic field along the magnetically hard axis of a magnetic layer with a uniaxial in-plane magnetic anisotropy and using the spin-reorientation transition has been shown. [307, 308] By using piezoelectric substrates and suitable magnetic layers with a high magnetoelastic anisotropy contribution, the magnetization direction, and therefore also the polarization of the THz radiation, can also be varied by the application of a voltage to the substrate that leads to an in-plane tensile strain in the magnetic films. [309] Furthermore, it has been demonstrated that the magnetization direction and, therefore, the THz polarization can be switched by sufficiently high laser pump fluences under small applied magnetic fields. [310] Also, the adjustability of the chirality, azimuthal angle, and ellipticity of the spintronically emitted THz radiation by non-uniform applied magnetic field distributions has been demonstrated. [84, 311] The polarization can further be modulated by applying time-dependent magnetic fields. [312]

The frequency spectrum of spintronic emitter systems is dependent on the transport properties of the excited spin-polarized electrons and, therefore, on the used materials [81]. Furthermore, the amplitude is influenced by the duration of the laser pump pulse. [260, 261] Several studies also showed that the THz spectra can be tuned by using patterning tech-

niques. [83, 313, 314] Another method for the efficient tuning of the spectra that has been presented by Wang *et al.* [315] is to use multiple laser excitation pulses with varying time delays. Seifert *et al.* [82] showed that an optimized spintronic emitter system can cover a frequency range from 1 to 30 THz. In contrast to other THz emitter systems, the frequency spectra of spintronic emitters are gap-free. Figure 3.7 displays a comparison of the signal and the corresponding frequency spectrum of an optimized spintronic THz emitter (details on the optimization are discussed in the following paragraphs) with GaP(110)(0.25 mm) and ZnTe(110)(1 mm) crystals as well as a photoconductive switch. Chen *et al.* [316] demonstrated that a hybrid photoconductive-spintronic emitter system can be used to unite the advantages of the two emitter concepts. Furthermore, Nandi *et al.* [317] showed that antenna structures can be employed to optimize THz outcoupling and frequency range of spintronic emitters.

Influence of the pump laser wavelength, fluence, and polarization

So far, for most of the studies, Ti:sapphire lasers with a wavelength of 800 nm were used. The transport properties of the laser-excited electrons are dependent on the wavelength of the excitation laser. However, first studies with different excitation wavelengths ranging from 400 to 1550 nm showed little influence of the wavelength on the emitted THz spectra and on the emission amplitude. [318–320] The reason for these findings is that not only the directly laser-excited electrons contribute to the spin current, but also electrons that are excited by scattering with so-called first-generation electrons. [318] As the electron-electron scattering lifetimes significantly decrease for high energies, the first-generation electrons will partially transfer their energy to secondary electrons. The intermediate-energy electrons will then contribute to $\boldsymbol{J}_\mathrm{s}$. For higher wavelengths, these intermediate-energy electrons can be directly excited by the laser. Therefore, the emitted THz radiation is mainly dependent on the total energy that is transferred to the system by the laser pulse rather than by the excitation wavelength. In contrast to that, Adam *et al.* [306] stated that the THz amplitude can be significantly increased if an excitation wavelength of 400 nm is used instead of 800 nm. However, their measurements for the different pump wavelengths were performed with strongly different laser pump powers and, therefore, lack comparability.

Different studies showed that for small laser pump fluences, the THz amplitude increases linearly with the pump fluence until it saturates for high pump fluences. [74, 81–83, 297, 300, 318, 321–323]

Furthermore, as expected for an emission due to the ISHE, the THz radiation of spintronic emitters has been demonstrated in several studies to show a negligible influence on the polarization of the laser pump pulse [81, 82, 300, 321, 324].

Dependence on the materials, layer thicknesses, and NM/FM interface

Several studies investigated the material dependence of spintronic emitters by comparing the THz emission of different combinations of FM [82, 83, 266, 300, 325] and NM [82, 300, 321] materials in NM/FM bilayer systems. For the NM layer, the emission amplitude mainly scales with the spin Hall angle θ_{sh}. Therefore, so far Pt layers provide the highest THz signals of materials with $\theta_{\mathrm{sh}} > 0$ whereas W provides the strongest signals for $\theta_{\mathrm{sh}} < 0$. Regarding the FM layer, the main factors to gain high THz amplitudes are an efficient spin current generation and a small conductivity. So far, the highest signals have been achieved with $\mathrm{Co}_x\mathrm{Fe}_{1-x}\mathrm{B}_{0.20}$ layers [82, 266]. Figure 3.8 shows a comparison of the THz emission amplitudes of FM/NM bilayers with different FM and NM materials reported by Seifert *et al.* [82].

Besides the investigations on FM/NM bilayers, also some studies using FI rare earth-transition metal alloys instead of FM layers have been performed. [297, 326, 327] Huisman *et al.* [326] and Chen *et al.* [327] demonstrated that the emitted THz signal of laser-excited FI/NM bilayers with $\mathrm{Gd}_{0.25}(\mathrm{Fe}_{0.875}\mathrm{Co}_{0.125})_{0.75}$ or $\mathrm{Gd}_x\mathrm{Co}_{1-x}$ FI layers is mainly caused by the Co and Fe 3d electrons. However, Huisman *et al.* also showed an indication of a contribution of spin-polarized Gd electrons of the $\mathrm{Gd}_{0.25}(\mathrm{Fe}_{0.875}\mathrm{Co}_{0.125})_{0.75}$ layer to the THz signal. [326] In this work at hand, a similar behavior has been shown for $\mathrm{Tb}_x\mathrm{Fe}_{1-x}$ (see chapter 7) and $\mathrm{Gd}_x\mathrm{Fe}_{1-x}$ (see chapter 8) alloys. Recently, Qui *et al.* [328] demonstrated that also antiferromagnetic NiO layers can be used for the generation of ultrafast spin currents in AFM/NM spintronic THz emitter systems.

The dependence of the emitted radiation on the layer thicknesses has been investigated in different FM/NM emitter systems. [82, 83, 300, 321–323, 329, 330] Studies with fixed NM thicknesses and varying FM layer thicknesses t_{FM} showed maximum signals for 0.6 nm $\leq$

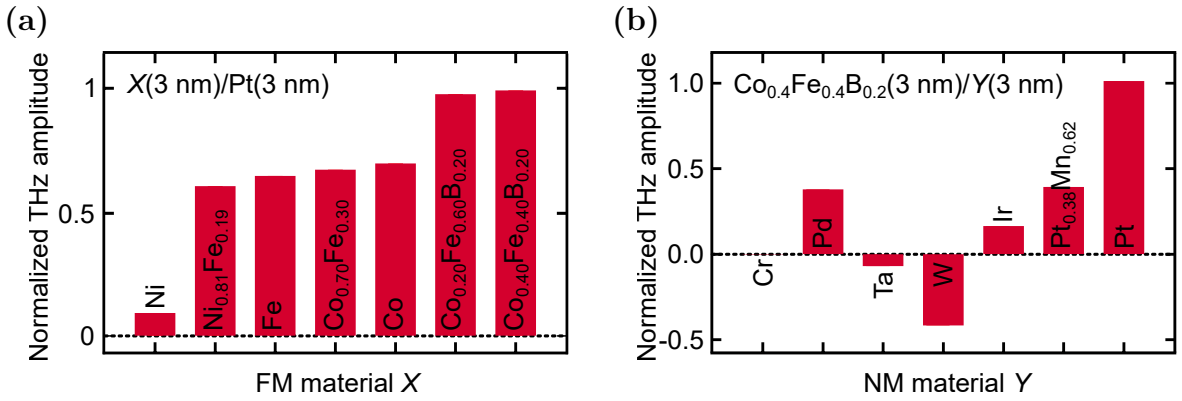

Figure 3.8: Comparison of the THz emission of various FM/NM bilayer spintronic THz emitters. (a) shows the dependence of the emitted THz amplitude on the FM material X in a *sub.*/X(3 nm)/Pt(3 nm) system, whereas (b) displays the dependence of the amplitude on the NM material Y in a *sub.*/$\mathrm{Co}_{0.4}\mathrm{Fe}_{0.4}\mathrm{B}_{0.2}$(3 nm)/$Y$(3 nm) bilayer. The negative amplitude values correspond to NM materials with $\theta_{\mathrm{sh}} < 0$. The figures are adapted from [82].

$t_{\mathrm{FM}} \leq 3\,\mathrm{nm}$. [83, 300, 322, 329] Strongly decreasing signals for smaller t_{FM} can be attributed to the loss of the magnetic order. [322] For higher thicknesses, the signals decrease again, a finding that can be attributed to the dependence of the emitted THz radiation on the electrical conductivity (see equation 3.9). For the NM layer, the thickness dependence is closely related to the relaxation length λ_{rel} of the spin current in the NM material. [82, 83, 297, 322, 323, 330] Seifert *et al.* [330] demonstrated that for Pt, W, and $Cu_{0.8}Ir_{0.2}$ NM layers, the λ_{rel} values of the THz spin currents agree well with spin relaxation lengths measured by DC experiments. The thickness dependence of the emitted THz electric field can be qualitatively described by $E \sim \tanh(t_{\mathrm{NM}}/2\lambda_{\mathrm{rel}})$. [82, 322]. As for the FM layers, the impedance of the layer stack becomes dominant for higher thicknesses. For Pt, the most prominent NM material in spintronic emitter systems, different studies observed maxima of the emitted THz amplitudes for thicknesses in the range of $2\,\mathrm{nm} \leq t_{\mathrm{Pt}} \leq 6\,\mathrm{nm}$. [83, 300, 322, 323, 330]

Furthermore, several studies investigated the influence of the FM/NM interface on the emitted THz radiation. [260, 322, 324, 329–331]. Torsyan *et al.* [322] and Nenno *et al.* [260] showed that the THz amplitude of Fe/Pt emitter systems is significantly increased for epitaxially grown layers compared to polycrystalline growth. Nenno *et al.* explain these results by the reduced defect density and, therefore, a larger electron-defect scattering lifetime for the epitaxial growth. Moreover, Li *et al.* [324] demonstrated that the THz emission of Co/Pt emitters can be increased by a factor of 4.2 by the introduction of a $Pt_{0.75}Co_{0.25}(1\,\mathrm{nm})$ interlayer. A theoretical study by Lu *et al.* [332] suggested that additional spin filter layers between the FM and NM layers might be used to improve the THz emission amplitudes. Recently, Gueckstock *et al.* [331] demonstrated that besides the bulk ISHE, interfacial skew scattering at imperfections at the FM/NM interface can lead to a significant spin-to-charge current conversion in systems with NM layers that show a weak bulk spin-orbit coupling.

Spintronic multilayer emitter stacks

Besides spintronic bilayer emitters, also several multilayer emitter stacks have been proposed. Seifert *et al.* [82] demostrated that a thickness-optimized $W(2\,\mathrm{nm})/Co_{0.4}Fe_{0.4}B_{0.2}(1.8\,\mathrm{nm})/Pt(2\,\mathrm{nm})$ system can be used as a highly efficient broadband THz emitter (see figure 3.7). The working principle of the emitter is displayed in figure 3.9a. The laser pump pulse leads to the formation of the spin currents $\boldsymbol{J}_{\mathrm{s}}$ from the FM layer toward the neighboring NM layers. As NM layers, two materials with opposite spin Hall angles θ_{sh}, for example W and Pt are used. Due to the opposite signs of θ_{sh}, the spin currents $\boldsymbol{J}_{\mathrm{s}}$ are transformed via the ISHE into charge currents $\boldsymbol{J}_{\mathrm{c}}$ with the same direction, following $\boldsymbol{J}_{\mathrm{c}} \sim \theta_{\mathrm{sh}} \boldsymbol{J}_{\mathrm{s}} \times \boldsymbol{M}/|\boldsymbol{M}|$. Therefore, both charge currents $\boldsymbol{J}_{\mathrm{c}}$ contribute constructively to the emitted THz radiation.

Likewise, FM 1/NM/FM 2 trilayer systems with opposite magnetization directions of the two FM layers can be used (see figure 3.9b). Here, the two spin currents $\boldsymbol{J}_{\mathrm{s}}$ contribute construc-

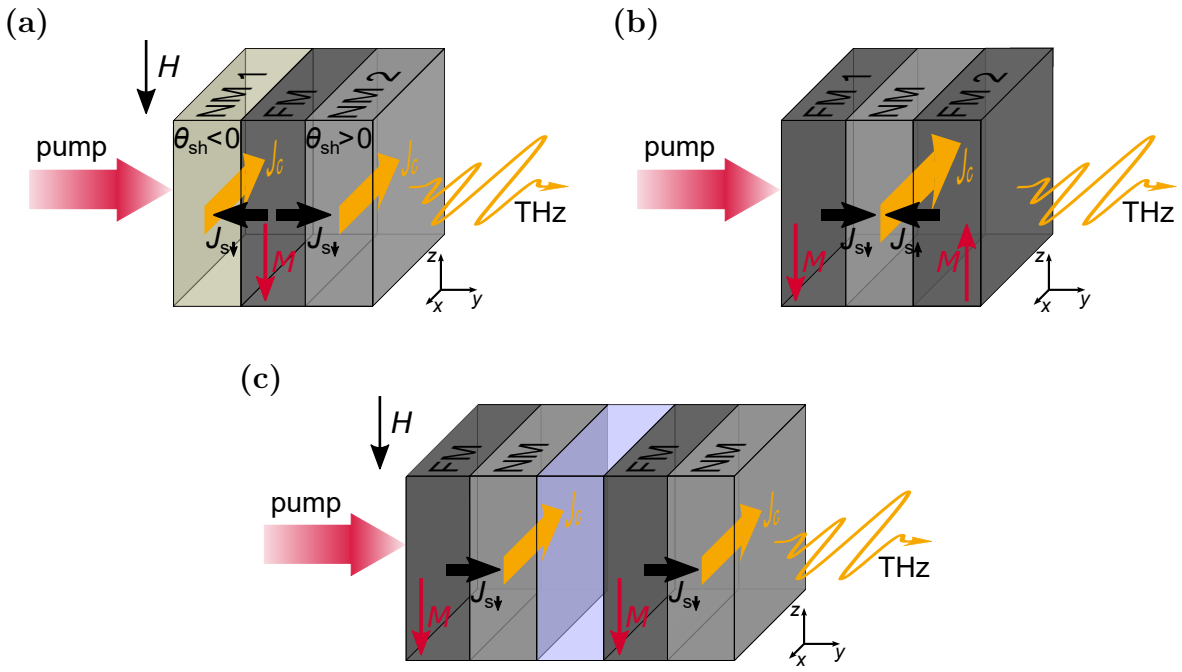

Figure 3.9: Emitter concepts of different multilayer spintronic emitter stacks. (a) shows a trilayer emitter system with a FM layer in the middle and NM layers with opposite spin Hall angles θ_{sh} on each side of the FM layer. Due to the opposite signs of θ_{sh} of NM 1 and NM 2, the two spin currents $\boldsymbol{J}_s$ lead to charge currents $\boldsymbol{J}_c$ with the same direction that contribute constructively to the emitted THz radiation. (b) displays a trilayer emitter system with a NM layer in the middle and two FM layers with opposite magnetization directions on each side of the NM layer. Due to the opposite magnetization directions of FM 1 and FM 2, the spin currents $\boldsymbol{J}_s$ contribute constructively to $\boldsymbol{J}_c$ leading to a high THz signal. (c) displays a stacked bilayer emitter system consisting of two FM/NM bilayers that are separated by an insulating interlayer and contribute constructively to the emitted THz radiation. (a) is adapted from [82], (c) is adapted from [83].

tively to $\boldsymbol{J}_c$, leading to a high THz signal. However, for the usually used thin layer thicknesses on the order of a few nm the FM layers with an in-plane magnetic easy axis typically have very small coercivities and the magnetizations of FM 1 and FM 2 will align parallel to an applied magnetic field. One option to realize an antiparallel magnetization alignment is to use antiferromagnetic interlayer exchange coupling (see subsection 2.4.2). Recently, Zhang *et al.* [333] and Ogasawara *et al.* [334] demonstrated that synthetic antiferromagnets with Ru or Ir interlayers show a high THz signal in their antiparallel ground state when no external magnetic field is applied, whereas the signal is low for the parallel magnetization alignment in high applied magnetic fields. However, the NM interlayers in the synthetic antiferromagnets cannot be optimized for the use as an efficient THz emitting NM layer, as only certain materials of a suitable thickness allow for the necessary antiferromagnetic RKKY coupling between the two FM layers.

In this work, two other concepts that can be used to achieve an antiparallel relative magnetization alignment are presented. In chapter 9 an emitter system that uses an antiparallel

alignment of the Fe magnetic sublattices of FI Gd_xFe_{1-x} layers with different Gd content x is presented. The usage of a spin valve AFM/FM/NM/FM system in which one of the FM layers is exchange biased by an AFM layer is presented in chapter 10.

Another concept that can be used to increase the THz emission amplitude is to use stacked bilayers that are separated by insulating layers. The concept is displayed for two stacked bilayers in figure 3.9c. As the layer thicknesses are thin compared to the wavelengths of the THz radiation, the charge currents $\boldsymbol{J}_\mathrm{c}$ contibute constructively. In 2016, Yang *et al.* [83] demonstrated the concept with thickness-optimized Fe/Pt bilayers that were separated by insulating MgO layers. They achieved the highest amplitudes for a $[\mathrm{Pt}(2\,\mathrm{nm})/\mathrm{Fe}(1\,\mathrm{nm})/\mathrm{MgO}(2\,\mathrm{nm})]_n$ system with three repetitions. Furthermore, Feng *et al.* [335] showed that high THz emission amplitudes can be achieved by (NM 1/FM/NM 2)–dielectric photonic crystals.

CHAPTER 4

Sample preparation by magnetron sputter deposition

All thin film samples discussed in this work were prepared by magnetron sputtering, which is a thin film deposition technique. Due to the high deposition rates that can be achieved, as well as the possibility to fabricate large-area samples, this technique is not only of interest for fundamental research but also widely used in commercial applications. [336] A short overview of the technique and some device-specific characteristics will be given in the following.

Sputtering is a physical vapor deposition technique that has its origin in the middle of the 18^{th} century when the improving vacuum technologies and researches on gas glow discharges lead to the invention of the technique. [337] A detailed historical description of the development from the very beginning to state-of-the-art sputtering techniques can be found in [338]. The sputtering process is based on highly energetic gas ions that are accelerated toward a target material. The gas ions hit the target surface and sputter parts of the material. The sputtered atoms then settle on a substrate material and form a film. However, the deposition rates in such a conventional sputtering chamber are rather low, and gas pressures on the order of 10^{-2} mbar are necessary to stabilize a gas plasma. [339] In the late 1970s, these disadvantages were overcome by the invention of magnetron sputtering. [340] Here, a magnetic field parallel to the target surface is applied in order to control the electron movement by the acting Lorentz force and therefore confine the gas plasma. In that way, higher plasma densities close to the target can be achieved, which allow for the use of lower gas pressures on the order of 10^{-3} mbar. Therefore, higher deposition rates can be achieved. The magnetrons are usually placed in an ultra-high vacuum chamber.

A schematic of a magnetron is shown in figure 4.1. A high voltage is applied between the anode and the cathode in order to form a gas plasma by glow discharge with the working gas that is introduced to the chamber. For non-reactive sputtering, usually noble gases are used, whereas, for reactive sputtering, atmospheres containing reactive gases like oxygen or nitrogen are applied. The gas ions are accelerated toward the target that serves as the cathode if a metallic material is used. The gas ions partially transfer their energy to neutral sputtering gas atoms. Both, accelerated neutral gas atoms, as well as a part of the gas ions,

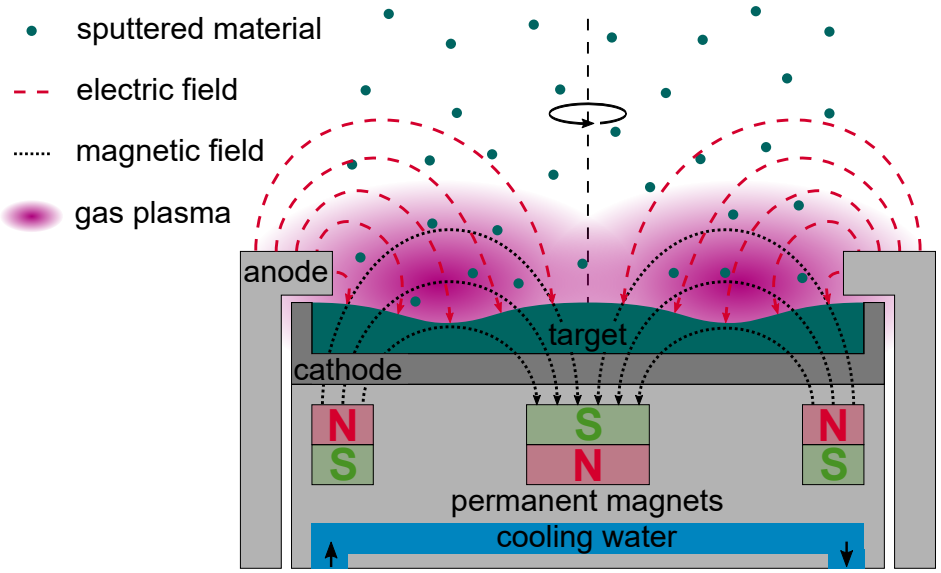

Figure 4.1: Schematic cross-section view on a magnetron during a sputtering process. The magnetron is rotationally symmetric. The dashed black line marks the axis of rotation.

collide into the target. This leads to the emission of sputtered atoms but also of secondary electrons. The electrons are accelerated by the high voltage and also contribute to the plasma by ionizing neutral gas atoms. The sputtered atoms can move freely, settle down on the substrate (*sub.*) material that is placed next to the magnetron and form a film. The kinetic energy impact of the sputtered atoms on the substrate, and therefore the film growth can be adjusted by the working gas pressure and also by the applied voltage. Besides the mobility of the incoming atoms on the surface of the substrate, also the resputtering has to be considered. The rates for the resputtering of previously deposited materials from the substrate are significantly lower than the original sputter rates. However, they are strongly dependent on the binding energies of the deposited materials. Thus, the resputtering can have an impact on the local order of sputtered alloys, such as for the Tb_xFe_{1-x} and Gd_xFe_{1-x} alloys investigated in the chapters 7–9. Further control parameters are the material and temperature of the substrate. The choice of suitable parameters is strongly dependent on the geometry of the used sputtering chamber. The permanent magnets which are placed underneath the target material are arranged in order to apply a magnetic field that localizes the gas plasma in a torus above the target material. Figure 4.1 displays a balanced magnet configuration [339] where the strength of the outer magnet poles is similar to the pole in the middle of the magnetron. Even higher growth rates can be achieved by using an unbalanced magnet configuration where some of the magnetic field lines point toward the substrate. [339] By using radio frequency (RF) sputtering with frequencies in the MHz range instead of direct current (DC) sputtering, also insulating materials can be deposited by this technique. [336]

All the films prepared for this work were sputtered with a magnetron sputtering system from Bestec (project number 450) with eight magnetrons, each of which can be run with either

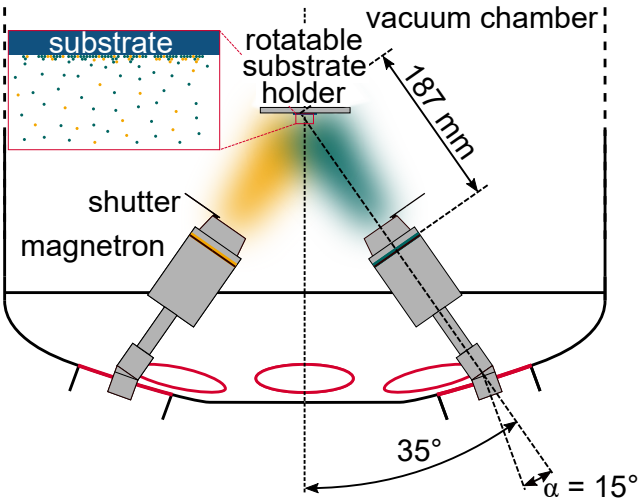

Figure 4.2: Schematic cross-section view of the Bestec 450 sputter chamber with two exemplarily shown magnetrons (the red circles mark the positions of the chamber openings for three of the other six magnetrons). The sputtering angle α can be adjusted according to the size of the substrate. The figure is based on engineering drawings of the Bestec sputter chamber [341].

a DC or a RF power supply. The magnetrons are positioned in a circle with equal distance from each other and are designed for the use of planar targets with a diameter of 5.08 cm (2 in). Each of the magnetrons is provided with a shutter. The substrates are placed on a rotatable, heatable holder with a diameter of 10.16 cm (4 in) in the middle of the circle above the magnetrons that can also be covered by a shutter. A schematic cross-section of the magnetron configuration in the Bestec sputter chamber for two exemplary magnetrons that are placed opposite each other is displayed in figure 4.2. The film depositions take place under ultra-high vacuum conditions with a chamber base pressure $p_{\mathrm{ch}} \leq 8.5 \cdot 10^{-8}$ mbar. The distance between the magnetrons and the substrate is 187 mm for a sputtering angle α of 15°. The angle α of the magnetrons can be adjusted between $-10°$ and $+20°$ according to the size of the substrates to achieve homogeneous films. Furthermore, different sputtering angles for the magnetrons involved in the co-sputtering of alloys can be used to achieve strongly different sputtering rates of the used materials. The magnet configuration of four of the magnetrons in the Bestec system can be adjusted by replacing the center magnet of the magnetron with a nonmagnetic material, which is necessary for the sputtering of FM materials. Further information about the Bestec sputter chamber can be found in the instruction manual [342].

For this work, different series of single or multilayer samples with varying compositions and film thicknesses were prepared. All depositions were performed at room temperature. For all materials except Si_3N_4, argon (5.0) was used as the working gas, with a sputtering pressure of $p_{\mathrm{Ar}} = 3.5\,\mu$bar. For the deposition of Si_3N_4, a mixture consisting of 96% argon (5.0) and 4% nitrogen (5.0) served as the sputter gas and a sputtering pressure $p_{\mathrm{Ar,N}} = 1.5\,\mu$bar was used. All target materials were pre-sputtered (sputtering with closed magnetron shutters)

before the depositions to get rid of thin oxide films or other contaminations on the target surfaces. To ensure the homogeneity of the films, the substrates (*sub.*) were rotated during the sputtering process with a frequency of $0.5\,\mathrm{s}^{-1}$. The sputtering rates were calibrated before the depositions using a quartz balance that was placed in the same position where the substrate holder was later on during the depositions. The Co_xFe_{1-x} alloys of the samples discussed in chapter 6 as well as the Tb_xFe_{1-x} and Gd_xFe_{1-x} layers of the samples that are discussed in chapters 7–9 were deposited by co-sputtering from elemental targets. The sputter rates ϕ are defined as the deposited thickness t in the time τ. By assuming that the sputtered materials have the bulk values for their densities ρ, and by neglecting resputtering effects, the sputter rates for a desired composition of an alloy X_xY_{1-x} can be calculated by the following equation:

$$\frac{\phi(X)}{\phi(Y)} = \frac{x}{1-x}\frac{A_\mathrm{u}(X)\rho(Y)}{A_\mathrm{u}(Y)\rho(X)}\ , \tag{4.1}$$

with A_u denoting the atomic masses of the materials X and Y. The desired layer thickness of the alloy is then achieved by adjusting the sputter time τ:

$$\tau = \frac{t}{\phi(X)+\phi(Y)}\ . \tag{4.2}$$

Especially for the co-sputtering of alloys it is important to verify the compositions and thicknesses after the depositions which was done in this work by Rutherford backscattering spectroscopy (see section 5.1) and by energy dispersive X-ray spectroscopy (see section 5.2).

A full list of the samples used in this work with the applied sputter parameters can be found in appendix A.1.

CHAPTER 5

Measurement techniques and data processing

5.1 Rutherford backscattering spectroscopy

Rutherford backscattering spectroscopy (RBS) is a non-destructive measurement technique that is based on the interaction of highly energetic low-mass gas ions with the atoms of the sample. For thin film samples, it offers information about the present elements, their concentration, and their depth distribution. Here a short introduction to the technique, mainly following the books by Ohring [343] and Verma [344] and the review article by Feldman and Poate [345], as well as an example of a measurement that was done for this work will be presented.

Figure 5.1 shows a schematic of the geometry in a RBS measurement device. Low-mass gas ions (usually $^4He^+$ or $^4He^{++}$) are accelerated toward the sample with energies in the MeV range. The light ions can penetrate up to a few microns into the film or substrate of the sample and cause negligible sputtering of the surface atoms. The loss of kinetic energy of the ions is mainly caused by electronic excitation of the sample atoms. Some of the ions, however, come close enough to the nuclei of the sample atoms to be scattered by the Coulomb repulsion between the ion and the nucleus (Rutherford scattering). A part of these backscattered gas ions can be measured with a detector that is typically placed at an angle of 170°.

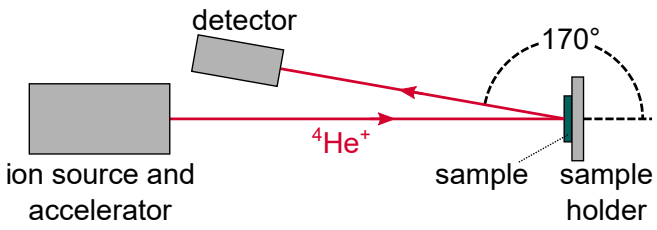

Figure 5.1: Schematic geometry of a typical RBS setup. Accelerated light ions (typically $^4He^+$ or $^4He^{++}$) are elastically scattered at a sample and measured with a detector that is typically located at an angle of 170°.

For an elastic scattering process of an incoming ion with the atomic mass $A_{\mathrm{u},0}$ and the energy E_0 at a target atom at the surface of a sample, it can be shown by energy and momentum conservation that the energy of the ion after the scattering process $E_{\mathrm{scattered}}$ is given by [343]:

$$E_{\mathrm{scattered}} = \left(\frac{(A_{\mathrm{u,\,target}}^2 - A_{\mathrm{u},0}^2 \sin^2\theta)^{1/2} + A_{\mathrm{u},0}\cos\theta}{A_{\mathrm{u},0} + A_{\mathrm{u,\,target}}} \right)^2 E_0 =: K_{\mathrm{target}} E_0 \ , \tag{5.1}$$

with $A_{\mathrm{u,\,target}}$ denoting the atomic mass of the target atom and the scattering angle θ. K_{target} is called the kinematic factor. If the gas ions and their energy E_0 are selected, for a particular scattering angle θ, K_{target}, and therefore the energy of the scattered ion is just dependent on the atomic mass of the target atom. The scattering can happen not only at the surface of the layer but also at any point within the sample. The energy loss rate $-\frac{\mathrm{d}E}{\mathrm{d}s}$ of the ions due to electronic excitation can be described by the Bethe-Bloch equation [346, 347]. However, for thin film systems with layer thicknesses in the nm range and energies in the MeV range, the energy loss of the incoming ions with energy E_0 while penetrating the film $-\left(\frac{\mathrm{d}E}{\mathrm{d}s}\right)_{E_0}$ is approximately constant. A schematic of the scattering events in a Rutherford backscattering experiment with $^4\mathrm{He}^+$ ions that happen in a thin alloy film consisting of the elements X and Y is shown in figure 5.2. Ions with the energy E_0 hit the film at $s = 0\,\mathrm{nm}$. Most of the ions penetrate the film and lose their energy in a linear behavior. However, a part of the ions is scattered close to the surface. These scattered ions have the energy E_1, which is dependent on the target atom (X or Y). The scattering can happen at any film depth s up to the film thickness t. To generalize equation 5.1 for a scattering process at the depth s, the energy E_0

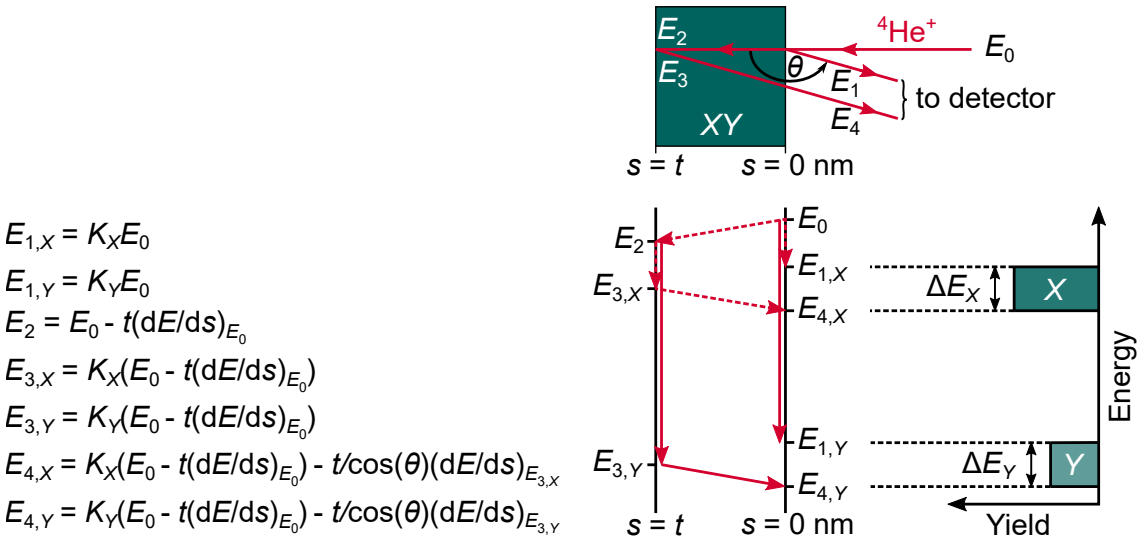

Figure 5.2: Schematic of a Rutherford backscattering experiment on a thin alloy film consisting of the materials X and Y with incoming $^4\mathrm{He}^+$ particles under an incident angle $\alpha = 0°$. The figure is based on [348] and [343].

of the incident ion has to be replaced by:

$$E_s = E_0 - \frac{s}{\cos\alpha}\left(\frac{\mathrm{d}E}{\mathrm{d}s}\right)_{E_0} \ , \tag{5.2}$$

with α denoting the incident angle of the incoming ion. The energy E_{det} of the scattered ion outside the target material on the detector side can then be derived by modification of equation 5.1:

$$E_{\mathrm{det}} = K_{\mathrm{target}}\left(E_0 - \frac{s}{\cos\alpha}\left(\frac{\mathrm{d}E}{\mathrm{d}s}\right)_{E_0}\right) - \frac{s}{\cos\theta}\left(\frac{\mathrm{d}E}{\mathrm{d}s}\right)_{E_{\mathrm{scattered}}} \ . \tag{5.3}$$

The first part of the equation describes the energy of a particle just after the scattering event at depth s, whereas the second part describes the energy loss of the ion caused by the passage through the target material after the scattering event. Thus, a variation of the depth δs causes a variation of the energy δE_{det}. The minimum energies E_{det} that occur for scattering events that happen at depths s close to the film thickness t are denoted with E_4 in figure 5.2, the energies of such an ion just before and after the scattering events are denoted with E_2 and E_3, respectively. ΔE_X and ΔE_Y denote the energy regions (limited by E_1 and E_4) for which ions scattered at the materials X and Y can be measured with the detector. The depth resolution of the experiment is therefore determined by the energy resolution of the detector as well as by the stopping power $\frac{\mathrm{d}E}{\mathrm{d}s}$ and the geometry of the experiment. The number of scattering events for a particular sort of target atoms is given by its scattering cross-section σ_{c}. For Rutherford scattering processes, the differential cross-section $\frac{\mathrm{d}\sigma_{\mathrm{c}}}{\mathrm{d}\Omega}$ can be described by [344]:

$$\frac{\mathrm{d}\sigma_{\mathrm{c}}}{\mathrm{d}\Omega} = \left(\frac{Z_0 Z_{\mathrm{target}} e^2}{8\pi\epsilon_0 E_0 \sin^2\theta}\right)^2 \frac{\left(\sqrt{1-\left(\frac{A_{\mathrm{u},\,0}}{A_{\mathrm{u,\,target}}}\sin\theta\right)^2}+\cos\theta\right)^2}{\sqrt{1-\left(\frac{A_{\mathrm{u},\,0}}{A_{\mathrm{u,\,target}}}\sin\theta\right)^2}} \ , \tag{5.4}$$

with the solid angle Ω and the atomic numbers of the incoming ion Z_0 and the target atom Z_{target}. Taking this into account, the number of detected ions $\mathrm{d}Q_X$ (which is given by the area under a measured peak) for a sort of target atom X in a thin film system is given by [344]:

$$\mathrm{d}Q_X = Q\Delta\Omega\frac{\mathrm{d}\sigma_{\mathrm{c},\,X}(E_0)}{\mathrm{d}\Omega}\frac{n_X\Delta t}{\cos\alpha} \ , \tag{5.5}$$

with the detector solid angle $\Delta\Omega$, the number of incident particles Q, and the effective layer thickness $\frac{\Delta t}{\cos\alpha}$, with the incident angle α. n_X is the number of target atoms per unit volume, which is given by

$$n_X = N_{\mathrm{A}}\rho_X / A_{\mathrm{u},\,X} \ , \tag{5.6}$$

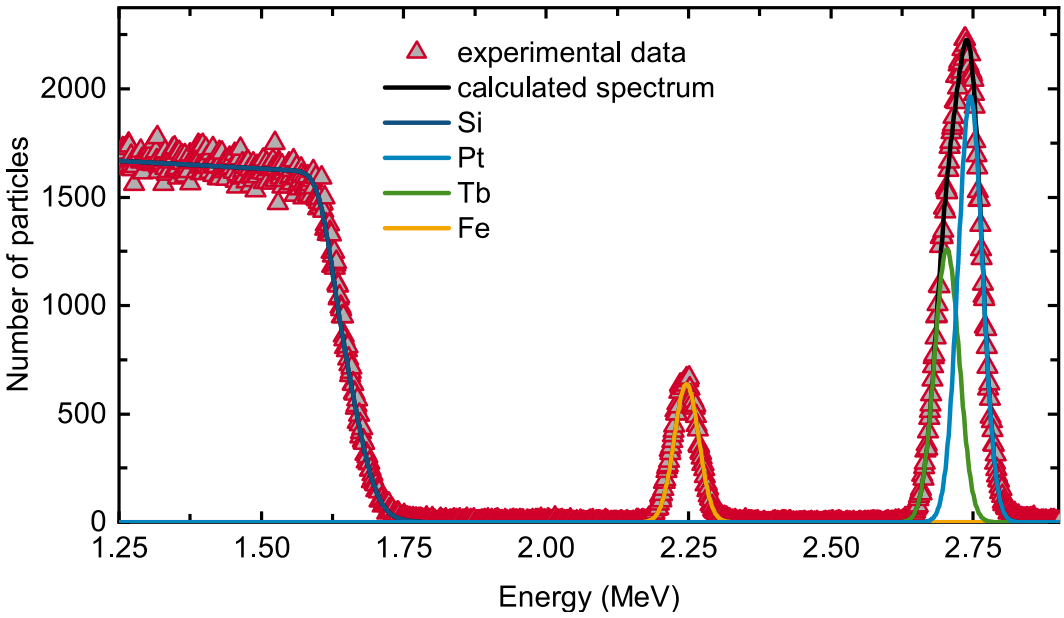

Figure 5.3: Evaluated Rutherford backscattering spectrum of a $Si/SiO_2(100\,nm)/Pt(5\,nm)/Tb_{0.26}Fe_{0.74}(20\,nm)/Si_3N_4(5\,nm)$ sample measured with He^{++} ions with an initial energy of 3 MeV, an incident angle of 7°, and a detector angle of 170°. The red triangles show the experimental data and the black line displays the calculated spectrum. The colored lines show the contributions of the different elements to the calculated spectrum.

with the Avogadro constant N_A, the mass density ρ_i, and the atomic weight $A_{u,i}$. Therefore, by fitting a measured spectrum, the thicknesses of each sublayer as well as the compositions of alloy films can be derived. However, the densities ρ_i of the sputtered materials have to be known for the evaluations. For thin films and especially for alloys, the assumptions for the densities might lead to rather large errors in the film thicknesses as the densities in these thin layers often deviate from the bulk values. Further details on the technique can be found in [344].

All RBS measurements for this work were performed with a tandem ion accelerator system by High Voltage Engineering Europa B.V. at an incident angle of 7° and a detector angle of 170°. The accelerator allows energies of up to 6 MeV if $^4He^{++}$ ions are used. The data evaluation has been done with the program SIMNRA [349, 350] (version 6.03). By fitting the measured RBS spectra, the areal densities for the elements have been evaluated. Figure 5.3 shows an example of a measured RBS spectrum of a $Si/SiO_2(100\,nm)/Pt(5\,nm)/Tb_{0.26}Fe_{0.74}(20\,nm)/Si_3N_4(5\,nm)$ sample and the calculated spectra from which the deviations from the nominal values were derived. For this example, the composition of the Tb_xFe_{1-x} alloy shows a deviation of $\Delta x = -0.02$ from the nominal value. The film thicknesses show deviations from the nominal value of -10% for the $Tb_{0.26}Fe_{0.74}$ layer and of -18% for the Pt layer.

5.2 Energy-dispersive X-ray spectroscopy

Energy-dispersive X-ray spectroscopy (EDX) is a non-destructive measurement technique that is based on the detection of the characteristic X-ray spectrum of a sample. For thin film samples, the technique can be used to gain information about the film compositions and layer thicknesses. A short introduction to the technique based on [351] and [352] will be given in the following.

Excitation of inner-shell electrons of a sample to a high energy level leads to the emission of characteristic X-rays, as the hole in the inner shell is filled by an electron from a higher orbital (see figure 5.4a). The energy of the emitted photon depends on the shell from which the photoelectron is emitted as well as on the shell in which the replacement electron has its origin (see figure 5.4b). As the energy of these characteristic X-rays is element-specific, the elements

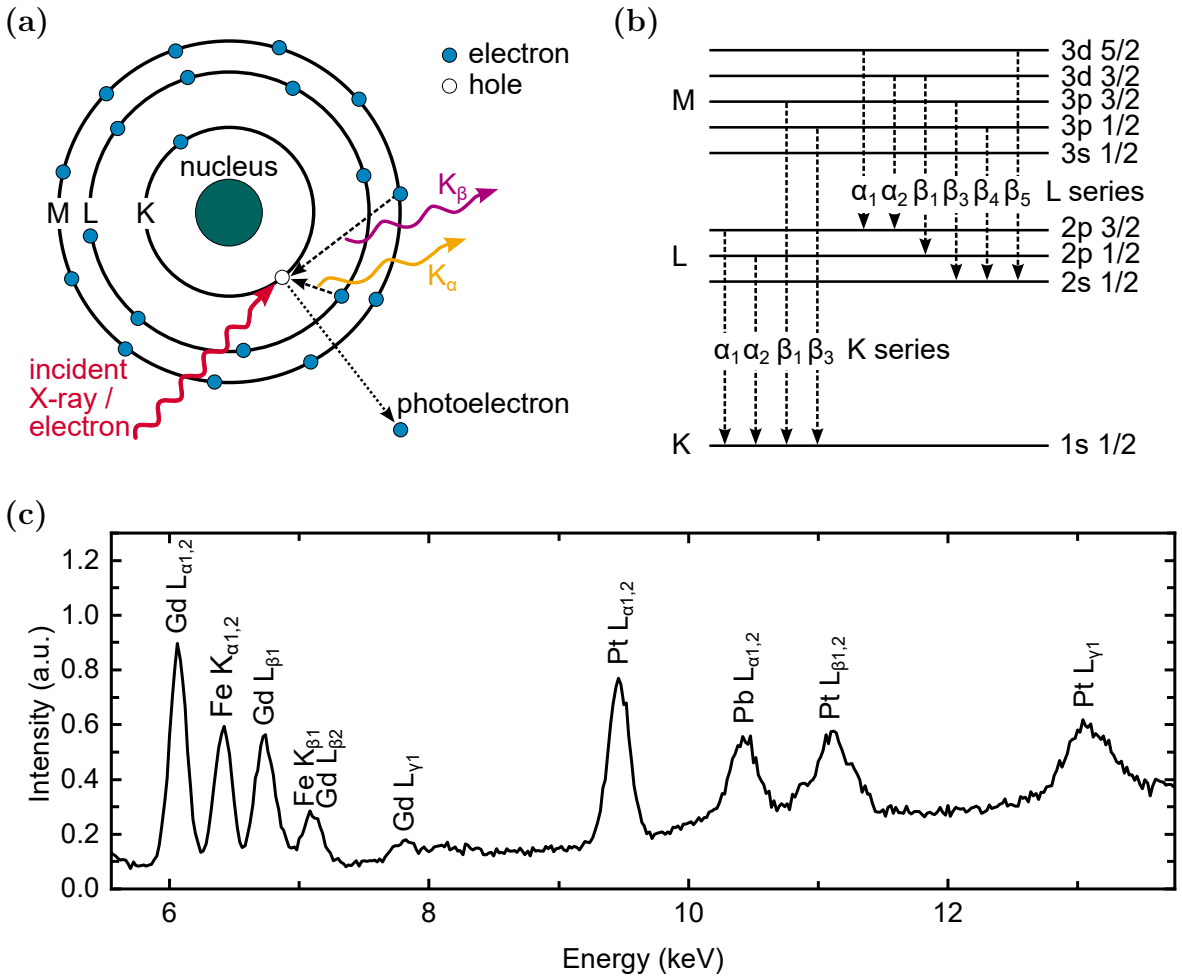

Figure 5.4: (a) Illustration of the generation of characteristic X-rays and (b) the relationship between the energy levels of the electrons and the generated characteristic X-rays (excerpt of the K and L series in the Siegbahn notation). (c) Measured EDX spectrum of a *sub.*/Pt(5 nm)/$Gd_{0.6}Fe_{0.4}$(20 nm)/Si_3N_4(5 nm) sample. The Pb $L_{\alpha1,2}$ peak is caused by the shielding of the device. (a) is adapted from [352], (b) is based on [351].

of a sample can be identified by the peak energies of the emitted photon spectra. Figure 5.4c shows an exemplary EDX spectrum of a *sub.*/Pt(5 nm)/$Gd_{0.6}Fe_{0.4}$(20 nm)/Si_3N_4(5 nm) sample. The contents of the different elements in the sample can be analyzed from the integrated peak intensities. Details on the necessary data evaluation can be found, for example, in [351] or [352]. For the excitation of the photoelectrons, either X-rays or electrons can be used. The excitation with electrons is often used as an additional analysis technique for transmission or scanning electron microscopes. Here, the technique can be used for space-resolved measurements to get elemental mappings or line scans of specific regions on the sample. The EDX detection limit for a standard specimen has been estimated to be about 1 at.%. [351]. However, in practical use, the errors of the calculated element contents depend on the fitting of the peaks and on the applied background correction and can exceed this detection limit even for measurements with a good signal-to-noise ratio.

For this work, a Shimadzu EDX-720-P energy-dispersive fluorescence X-ray spectrometer with a rhodium tube (Rh-$K_{\alpha 1}$: 20.2 keV) for the generation of the excitation X-rays was used to determine the compositions and layer thicknesses of the *sub.*/Pt(5 nm)/Gd_xFe_{1-x}(20 nm)/Si_3N_4(5 nm) samples discussed in chapter 8. The software of the device (PCEDX-E version 1.12 [353]) was used to fit of the measured spectra and calculate the compositions and thicknesses. For the data evaluation, the Gd L_α, the Fe K_α, and the Pt L_α peaks were used. Additionally, EDX mappings and line scans of selected samples were measured by transmission and scanning electron microscopy.

5.3 Magneto-optical Kerr effect magnetometry

The magneto-optical Kerr effect (MOKE) describes the magnetization-dependent change of the polarity of light reflected by a magnetic sample. [354] Therefore, MOKE measurements offer the possibility of fast optical measurements of magnetic hysteresis loops. Furthermore, MOKE measurements can be used in pump-probe setups for investigations on ultrafast laser-induced magnetization dynamics. [216] However, no absolute values of the magnetic moments can be determined. At the chair Experimental Physics IV (EP IV) in Augsburg, a polar MOKE (P-MOKE) measurement setup that can be used to gain information on the out-of-plane magnetic properties was available. For the spintronic THz emitters investigated in this work, measurements of the in-plane magnetization of the samples are of specific interest. Thus, only a few additional MOKE measurements were performed, mainly to better estimate the impact of some of the superconducting quantum interference device-vibrating sample magnetometry measurement artifacts. Therefore, this method will not be explained in detail here, and the interested reader is referred to [355, 356] for further information on the technique.

However, it should be noted that the sensitivity of the Kerr signals is dependent on the wavelength of the used laser. In the P-MOKE setup at EP IV a laser with a wavelength of 632.8 nm ($\approx$ 1.5 eV) was applied. With this wavelength, mainly the Fe electrons of the RE_xFe_{1-x} alloys investigated in this work can be excited and therefore contribute to the Kerr signal. Thus, the resulting hysteresis loops are element specific for Fe. For the comparison of MOKE measurements with the results gained by other techniques, it is furthermore important to keep in mind that the used measurement setup gives information on the area of the laser spot on the sample and not about the whole sample area. Therefore, the technique is insensitive to measurement artifacts that arise from the sample edges (see subsection 5.4.2). Moreover, the method is rather surface sensitive and limited to the penetration depth of the laser light.

Besides the P-MOKE measurements done in Augsburg, extreme ultraviolet (EUV) transversal MOKE (T-MOKE) measurements on selected Pt/Tb_xFe_{1-x} samples (see chapter 7) have been performed by Henrike Probst in the group of Prof. Stefan Mathias at the University of Göttingen. The high harmonic generation [357] light source of the EUV T-MOKE setup allows for energy-resolved measurements between 24 eV and 72 eV. Theoretically, element-specific information on the magnetic properties of Tb_xFe_{1-x} samples in in-plane direction could be obtained by measurements of the Fe $M_{2,3}$ absorption edge at approximately 52.6 eV–55.0 eV [358–362] (excitation of 2p electrons into the spin split 3d band) and the Tb O_2 absorption edge at approximately 28.7 eV [363] (excitation of $5p_{1/2}$ electrons into the spin split 5d band). However, only Fe magnetic signals could be resolved for the measured samples. The EUV T-MOKE measurement setup is described in detail [362].

5.4 Superconducting quantum interference device-vibrating sample magnetometry

Superconducting quantum interference devices (SQUID) are the most sensitive magnetic flux and field detectors, reaching quantum-limited field resolutions of 10^{-17} T. [364] As the technique is already well described in literature, only a short overview of the basic working principle of a SQUID in the used SQUID-vibrating sample magnetometer (SQUID-VSM) measurement setup, based on [100, 364–366], will be given in subsection 5.4.1. In subsection 5.4.2, the focus will be set on occurring device-specific measurement errors and sample-specific measurement artifacts and their treatment within this work. Subsection 5.4.3 describes the determination method for the effective magnetic anisotropy using SQUID-VSM measurements.

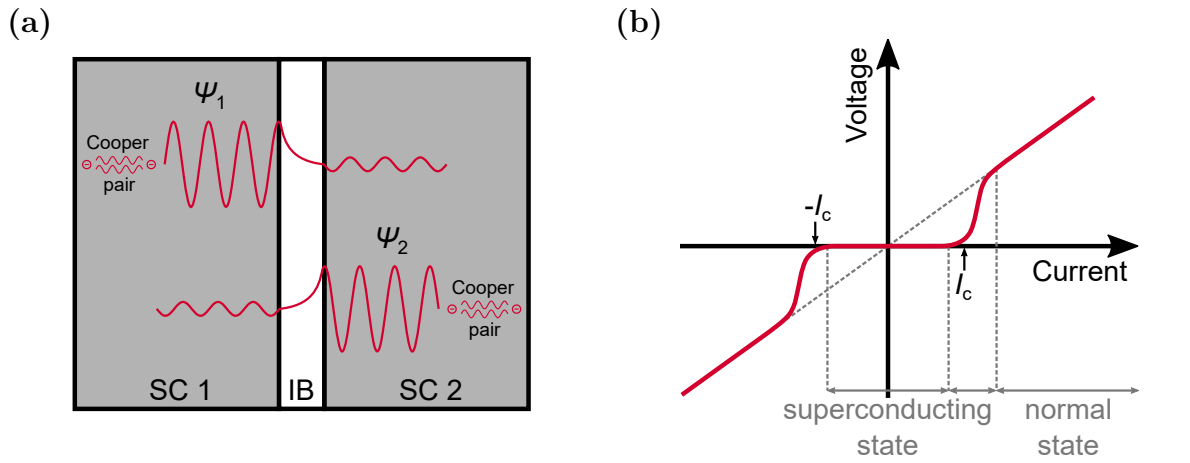

Figure 5.5: (a) shows a schematic of Josephson contact consisting of the two superconductors SC 1 and SC 2 that are separated by a sufficiently thin insulating barrier (IB) that allows the tunneling of Cooper pairs with the macroscopic wave functions Ψ_1 and Ψ_2, respectively. (b) shows a characteristic $V(I)$ curve of a Josephson junction. Up to a critical current I_c, the voltage drop at the junction is $V = 0$. An ideal Josephson contact would show a sharp transition from the superconducting to the normal conducting state at I_c. However, real devices show the smoother transition displayed here. (a) is adapted from [364] and [366], (b) is based on [364].

5.4.1 Working principle

A SQUID consists of a superconducting ring with one (AC-SQUID) or two parallel (DC-SQUID) Josephson contacts. These are thin non-superconducting tunnel barriers between two superconducting materials. The fundamental effects on which the function of a SQUID is based are the flux quantization in a superconducting ring [367, 368] and the Josephson effect [369, 370]. The flux quantization states that the magnetic flux Φ in a superconduction loop can only take values that are multiples of the flux quantum $\Phi_0 = h/2e \approx 2.068 \times 10^{-15}\,\mathrm{Wb}$ [367, 368], with h denoting the Planck constant. The Josephson effect describes the Cooper pair tunneling through a Josephson junction, which is based on the overlap of the macroscopic wavefunctions Ψ_1 and Ψ_2 of the Cooper pairs on either side of the tunnel barrier. Figure 5.5a shows a schematic of a Josephson junction. Due to the Cooper pair tunneling, the voltage V across the junction remains zero up to a critical current I_c. The two fundamental equations describing the Josephson effect are [100]:

$$I = I_c \sin\delta = I_c \sin(\theta_2 - \theta_1) \tag{5.7}$$

and

$$\frac{\partial\delta}{\partial t} = -\frac{2e}{\hbar}V \ . \tag{5.8}$$

I describes the electrical current flowing through the junction and δ represents the phase difference of the macroscopic wave functions Ψ_1 and Ψ_2 of Cooper pairs with the phases θ_1

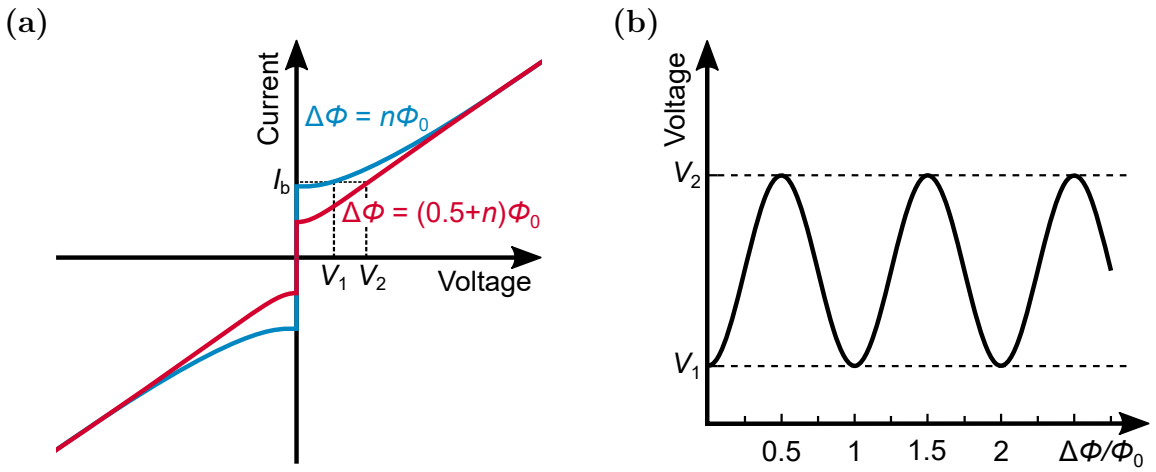

Figure 5.6: (a) $I(V)$ curves of a SQUID for applied magnetic fluxes $\Delta\Phi = n\,\Phi_0$ and $\Delta\Phi = (0.5{+}n)\,\Phi_0$. When a fixed bias current I_b is applied, the voltage changes periodically between the values V_1 and V_2 with a period of 0.5 Φ_0. (b) corresponding $V(\Phi)$ curve. The figures are based on [365] and [366].

and θ_2 in the superconducting materials on the two sides of the Josephson contact, respectively. Figure 5.5b shows the characteristic $V(I)$ curve of a Josephson contact. A constant non-zero voltage V across the junction results in an oscillating current I, a phenomenon that is known as the AC Josephson effect [371], which will not be discussed here in detail.

It can be shown that the flux quantization in a superconducting ring with two Josephson junctions can also be represented by the phase differences δ_1 and δ_2 of the macroscopic wave functions of Cooper pairs across the two Josephson junctions [366]:

$$\delta_2 - \delta_1 = 2\pi\frac{\Phi}{\Phi_0} = 2\pi\frac{\Delta\Phi + LI_\mathrm{s}}{\Phi_0}\,, \tag{5.9}$$

where $\Phi = \Delta\Phi + LI_\mathrm{s}$ describes the total magnetic flux penetrating the loop, with an externally applied flux $\Delta\Phi$, the self-inductance L of the loop, and the screening current I_s. Without an applied external flux, the phase differences δ_1 and δ_2 take the identical value δ_0. The screening current can be described as the difference between the currents I_1 and I_2 flowing through the two Josephson junctions: $I_\mathrm{s} = (I_1 - I_2)/2$. By applying Kirchhoff's law, the total current flowing through the loop can be written as $I_\mathrm{tot} = I_1 + I_2$. According to equation 5.7, for two identical Josephson contacts with the same critical current I_c, the critical current for the case of zero voltage loss for the whole SQUID loop $I_\mathrm{c,tot}$ can be written as:

$$I_\mathrm{c,tot} = I_1 + I_2 = I_\mathrm{c}\,(\sin\delta_1 + \sin\delta_2) = 2I_\mathrm{c}\sin\delta_0\cos\left(\pi\frac{\Phi}{\Phi_0}\right), \tag{5.10}$$

with $\delta_0 = (\delta_1 + \delta_2)/2$. The magnetic flux can be expressed as:

$$\frac{\Phi - \Delta\Phi}{\Phi_0} = \frac{LI_\mathrm{s}}{\Phi_0} = \frac{LI_\mathrm{c}(\sin\delta_1 - \sin\delta_2)}{\Phi_0} = \beta_\mathrm{L}\cos\delta_0\sin\left(\pi\frac{\Phi}{\Phi_0}\right), \tag{5.11}$$

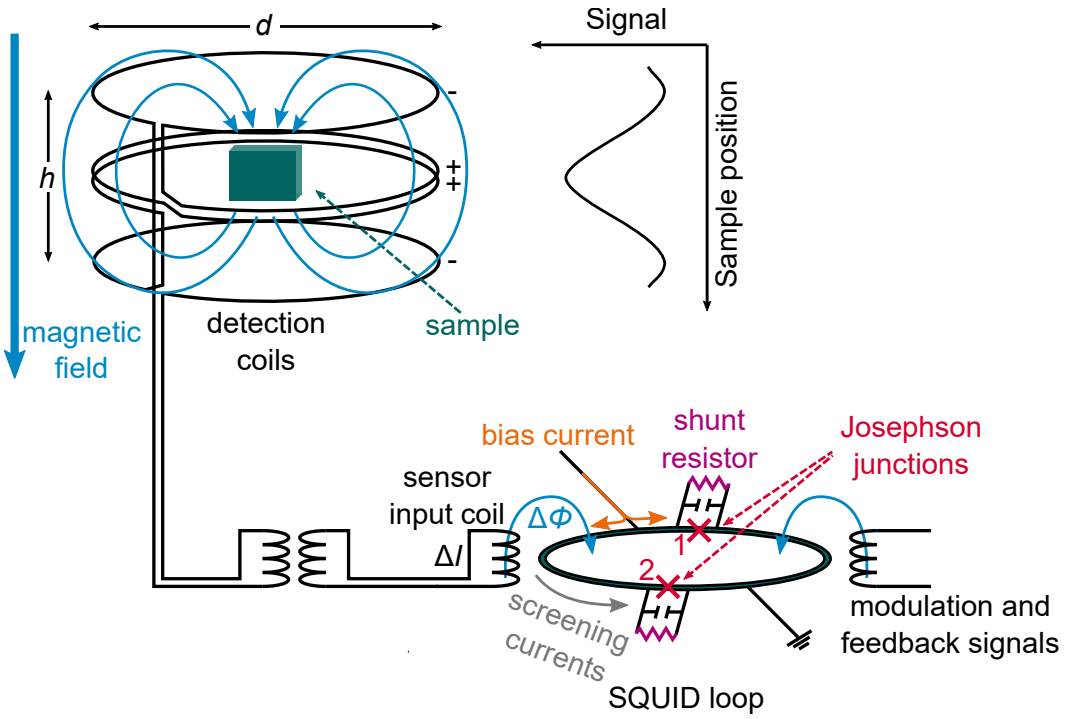

Figure 5.7: Simplified schematic of the detection setup of the DC-SQUID used for this work (without the entire feedback and amplification electronics). In the MPMS3 system, a second-order gradiometer coil setup with a coil diameter d of 17 mm and a height h of 8 mm is applied. The figure is based on [364] and [372].

with the inductance parameter $\beta_L = 2LI_c/\Phi_0$. For small inductance values $\beta_L \approx 0$ consequently $\Phi \approx \Delta\Phi$. Thus, the critical current $I_{c,tot}$ shows a cosinusoidal dependence on the applied flux $\Delta\Phi$ with maxima for $\Delta\Phi = 2n\Phi_0$, with the integer n. Figure 5.6a shows exemplary $I(V)$ curves of a DC-SQUID for $\Delta\Phi = n\Phi_0$ and $\Delta\Phi = (0.5 + n)\Phi_0$, representing the maxima and the minima cases of $I_{c,tot}$. When an external bias current I_b is fixed to a value slightly higher than I_c, the voltage changes periodically between the values V_1 and V_2 with the period of the flux quantum Φ_0 (see figure 5.6b). Using feedback electronics, the SQUID can be locked at a fixed point at the $V(\Delta\Phi)$ curve. By monitoring the feedback current, the magnetic flux $\Delta\Phi$ can be measured.

The measurements for this work were done with a Magnetic Properties Measurement System (MPMS3) by Quantum Design, a SQUID-VSM in which a DC-SQUID is applied. The MPMS3 allows measurements at temperatures between 1.8 K and 1000 K at external magnetic fields $\mu_0 H$ of up to 7 T. [372, 373] A schematic picture displaying the main elements of the detection setup is shown in figure 5.7. The (magnetic) sample is vibrated in between the detection coils in which an electrical current is induced. It should be mentioned here that the current is nulled by the feedback electronics, which are not fully displayed in the picture. The MPMS3 uses a second-order derivative axial gradiometer, as it is sketched in the figure. The DC-SQUID is inductively coupled to the detection coils and serves as a highly sensitive

current to voltage converter. For small samples, the induced signal shows approximately the plotted dependence on the sample position. An external magnetic field can be applied by a superconducting solenoid (not displayed). To allow the maximum sensitivity, all coils and wires have to be superconducting to avoid current losses. The resistive shunts at each of the Josephson junctions eliminate hysteretic behavior in the $I(V)$ curves of the Josephson contacts. [365]

It should be emphasized here that figure 5.7 only shows the main elements that are necessary to understand the basic functionality of a DC-SQUID in a SQUID-VSM. In modern SQUID magnetometers, complex feedback and amplification electronics are applied to increase the signal-to-noise ratio. Detailed descriptions of these are given in [364–366]. More details regarding the MPMS3 system can be found in the user manual [372].

5.4.2 Measurement errors and artifacts

Despite the high accuracy of the SQUID-VSM, there are several device- and sample-specific measurement errors and artifacts that have to be taken care of. An overview of some of the challenges concerning SQUID magnetometry measurements of nanomagnetic samples is given in [374].

Sample geometry

The detection coils have a diameter $d = 17\,\mathrm{mm}$ and a height of $h = 8\,\mathrm{mm}$. As only the magnetic flux lines that are not closed within the detection coils are detected, the measured signal depends on the sample geometry. Therefore, the MPMS3 is calibrated with a cylindrical, paramagnetic palladium reference sample with a diameter of 2.8 mm and a length of 3.8 mm. For samples with a different geometry and especially for thin film samples, this leads to a systematic error in the measured magnetic moment depending on the sample size and the sample orientation, but also on the sample vibration amplitude. However, for small samples, the diameter of the coils is still relatively large compared to the sample size. Figure 5.8a shows calculated correction values for square-shaped thin film samples with different edge lengths and vibration amplitudes taken from an application note on the MPMS3 provided by Quantum Design [375]. The values represent the magnetic moment correction factors for the sample plane aligned along the external magnetic field, which will be referred to as the in-plane geometry and for the sample plane aligned perpendicular to the external magnetic field, which will be referred to as the out-of-plane geometry. All thin film samples measured in this work were approximately square, with edge lengths between 3 mm and 4 mm. According to [375], the expected error for the sample vibration amplitude of 5 mm that was used for all measurements presented in this work is close to zero for out-of-plane measurements and between +10% and +15% for in-plane measurements. Figure 5.8b shows magnetization val-

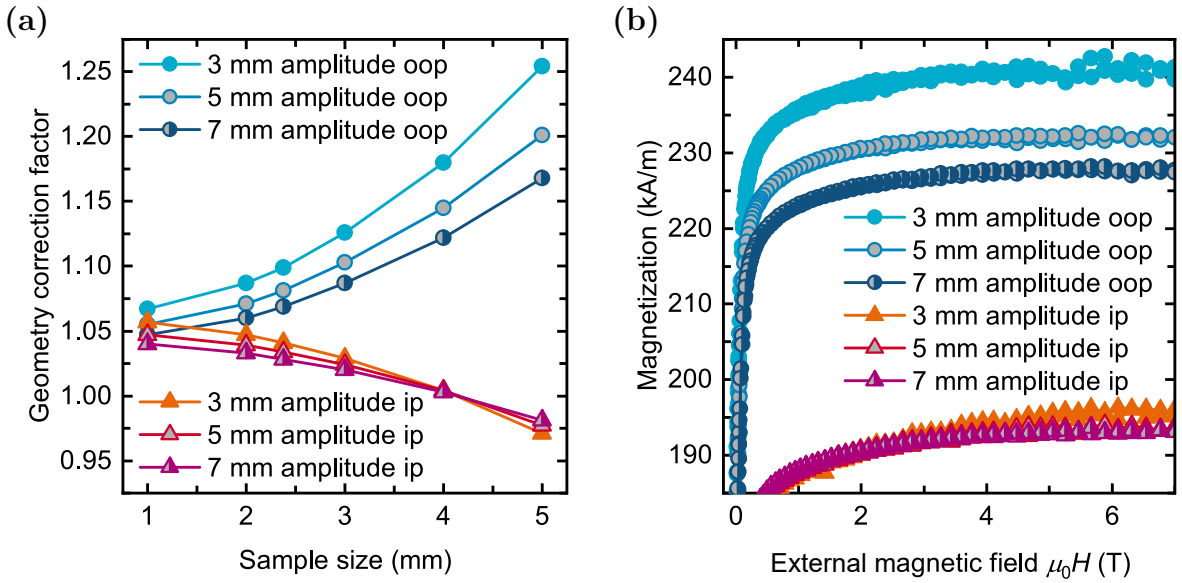

Figure 5.8: (a) displays the correction factor for different measurement vibration amplitudes for the MPMS3 system in dependence on the sample size. The displayed values are calculated values for square thin film samples with the sample size value as edge lengths that were provided by Quantum Design in an application note [375]. (b) shows magnetization values for a *sub.*/Pt(5 nm)/$Gd_{0.15}Fe_{0.85}$(20 nm)/Si_3N_4(5 nm) measured with different vibration amplitudes in in-plane and out-of-plane geometry.

ues of an approximately rectangular *sub.*/Pt(5 nm)/$Gd_{0.15}Fe_{0.85}$(20 nm)/Si_3N_4(5 nm) sample with edge lengths of 3.4 mm and 4.3 mm measured in dependence on the external magnetic field for vibration amplitudes of 3 mm, 5 mm, and 7 mm in in-plane and out-of-plane geometry. The magnetization values for the measurements performed in in-plane geometry show almost no dependence on the vibration amplitude. The measurements performed in out-of-plane geometry show between 18% (7 mm amplitude) and 24% (3 mm amplitude) higher results compared to the in-plane values. Therefore, the measurements show the same trend as the calculations [375] presented in figure 5.8a. However, the difference between the two measurement directions is slightly higher than expected. For an exact correction of this error, the shape of each sample would have needed to be measured and implied in the calculations described in [375]. Therefore, as the absolute magnetization values of the samples only play a minor role in the following discussion of the results of this work, no correction of the sample geometry effects has been applied. Nevertheless, this error has to be kept in mind for all presented $M(H)$ loops.

Sample position

Another additional error can be caused by the position of the sample with respect to the detection coils. The samples are centered to the position for which the maximum magnetic moment is detected. Especially for samples with a low moment, a guiding field has to be

applied for the centering. In this case, the substrate, the glue (used to fix the sample on the in-plane sample holder), or the asymmetries of the straws that are used as out-of-plane sample holders also contribute to the signal used for the centering procedure. This, along with other possible contaminations of the holder, might lead to errors in the sample center position, resulting in lower measured magnetic moments. However, if the centering is done correctly, the error is rather small compared to the other errors. Even when a small vibration amplitude of only 2 mm is used, the resulting magnetic moment error is only 2% for a vertical offset of 0.5 mm. [376]

Normalization of the magnetic moment by the film volume or area

All the values of the magnetic moments presented in this work were either normalized by the volume of the magnetic films for samples with only one magnetic layer or by the area of the magnetic films for samples with more than one magnetic layer. The area of the samples was measured using an optical microscope. For the film thicknesses, either values measured by RBS or the nominal values were used. Assuming an error of up to 5% for the sample area and an error for the film thickness of up to 15%, estimated from RBS and EDX measurements, this gives rise to an additional unknown error for the magnetization values of up to 20%. However, for most of the samples, this error will be smaller than the estimated maximum error. This error is independent of the measurement direction (in-plane or out-of-plane).

For the normalization with the sample volume, an additional error occurs due to the magnetic moment induced in the Pt seed layers by the magnetic proximity effect. [116–118] As for the normalization, only the thickness of the magnetic layers was used, the resulting magnetization values are systematically overestimated. With regard to this work, especially for the Pt/Co_xFe_{1-x} (chapter 6) and the $Pt/Gd_{0.3}Fe_{0.7}$ (section 9.2) bilayer systems this error might be significantly large.

Magnetic field error

As the magnetic field values in the MPMS3 software are calculated from the net current passing through the magnetic coils, an error in the field caused by magnetic flux trapped inside the solenoid of up to $\approx 4\,\mathrm{mT}$ might appear. [377] This field error is strongly dependent on the history of the magnet and is largest for small magnetic fields. For soft magnetic samples for which these errors are of specific importance, one option to reduce the error is to first oscillate the magnet from high field values (e.g., 7 T) to zero and then only measure in a small field range. Another method that reduces the error even more, is to use the "reset magnet" command of the MPMS3 software, which heats up the coils to above the critical temperature of the superconductor. However, a small error still remains, and these two methods are only possible for measurements within a small field range. Therefore, for

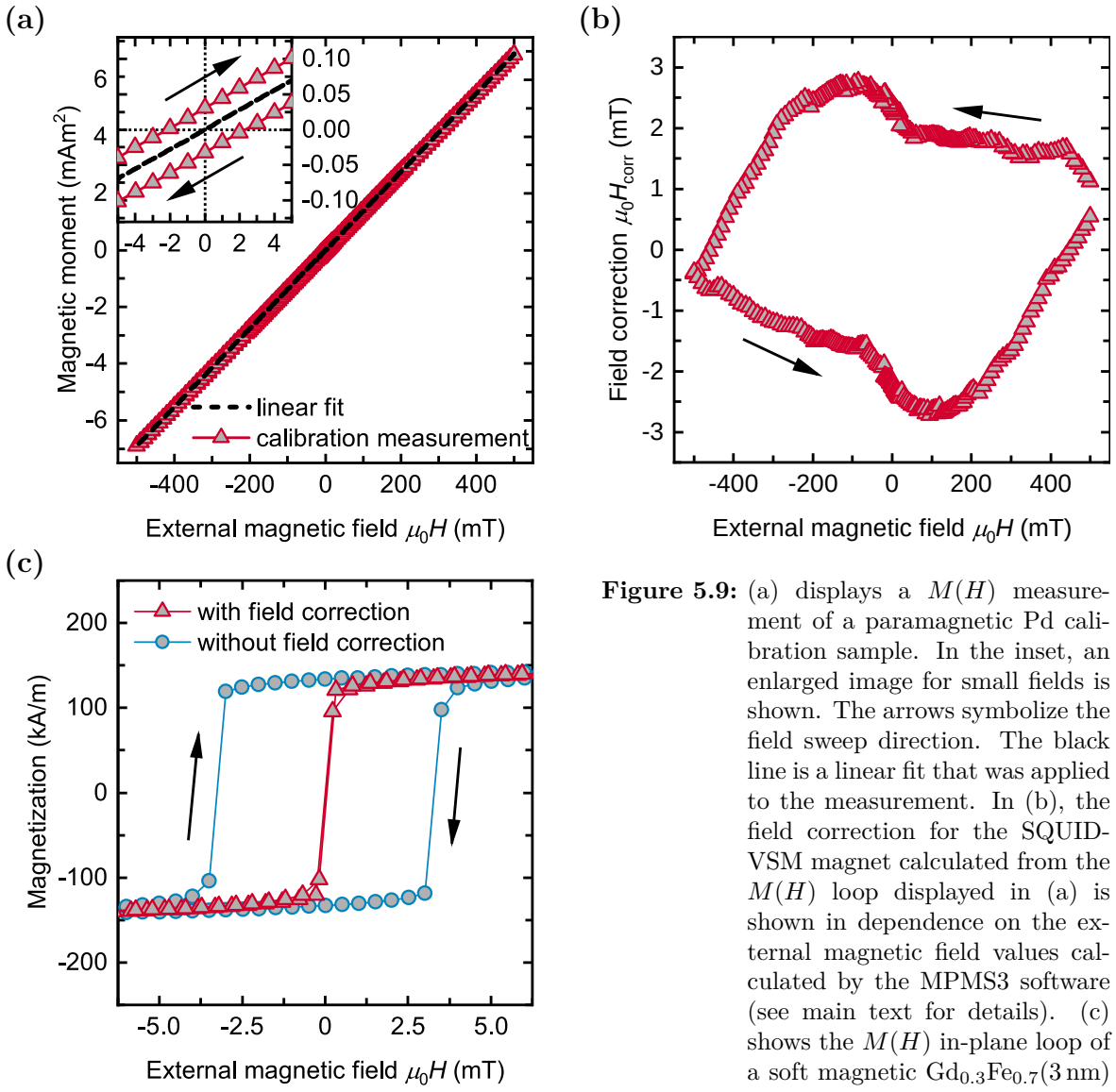

Figure 5.9: (a) displays a $M(H)$ measurement of a paramagnetic Pd calibration sample. In the inset, an enlarged image for small fields is shown. The arrows symbolize the field sweep direction. The black line is a linear fit that was applied to the measurement. In (b), the field correction for the SQUID-VSM magnet calculated from the $M(H)$ loop displayed in (a) is shown in dependence on the external magnetic field values calculated by the MPMS3 software (see main text for details). (c) shows the $M(H)$ in-plane loop of a soft magnetic $Gd_{0.3}Fe_{0.7}$(3 nm) film with and without correction of the applied magnetic field.

all $M(H)$ curves measured for this work, the field values were corrected by using calibration measurements. Figure 5.9a shows a calibration measurement of a cylindrical paramagnetic palladium calibration sample provided by Quantum Design. As the signal of the calibration sample is purely paramagnetic, the hysteresis (see inset of figure 5.9a) stems from the magnetic field error of the values calculated by the MPMS3 software. To correct the magnetic field values, a linear fit is applied to the calibration measurement. The difference of the magnetic field $H_{exp}(M_{exp})$ for the measured magnetic moment M_{exp} to the magnetic field $H_{fit}(M_{exp})$ corresponding to the linear fit at the same magnetic moment is used as the field correction H_{corr} for the applied magnetic field. Figure 5.9b shows the field correction values H_{corr} derived from the calibration measurement shown in figure 5.9a. For all measured magnetization loops, the field correction was applied by subtraction of H_{corr} from the field

values given by the MPMS3 software. Figure 5.9c displays the in-plane $M(H)$ loop of a soft magnetic *sub.*/Pt(3 nm/$Gd_{0.3}Fe_{0.7}$(3 nm)/Si_3N_4(5 nm) sample (measured in the field range from 7 T to −7 T) with (red triangles) and without (blue circles) application of the described field correction method. The clearly unphysical magnetization switching behavior of the uncorrected curve is caused by the wrong values of the external magnetic field. It is important to note that for all loops with different field steps, and therefore also a different history of the SQUID-VSM magnet, appropriate calibration measurements with the same field steps have to be performed.

Para-/diamagnetic background

In addition, the measured $M(H)$ loops of FM or FI samples show additional para- or diamagnetic contributions caused by the substrate, the sample holder, and the glue that is used to fix the samples onto the in-plane sample holders. In order to evaluate the magnetic properties of magnetic layers, it is necessary to subtract that para-/diamagnetic background. As the background follows a linear dependence on the magnetic field, the background can be linearly fitted for high applied magnetic fields, for which the FM or FI moments are in a saturated state. The linear fit can then be subtracted from the measured loop (see figure 5.10a). However, this method can only be applied for samples that show a clearly saturated magnetic state. Especially for the investigated Tb_xFe_{1-x} films (see chapter 7), for certain compositions (and temperatures), the samples cannot be saturated in the hard axis direction. The background subtraction, therefore, only gives a rough estimation as the paramagnetic background will be overestimated or the diamagnetic background underestimated. This leads to smaller magnetization values. Also, spin-flop transitions in FI samples (see out-of-plane loop in figure 5.10a) can make the fitting of the background challenging, especially if the transition overlaps with the main hystereses. Furthermore, for magnetic films with Curie temperatures close to or below the measurement temperature, it cannot be distinguished between the background signal and the signal of the magnetic film. One method to overcome these problems would be to measure pure substrates without the magnetic film system and subtract the results from the measurements of the samples with the magnetic film system. In this work, that was done for $M(T)$ measurements, for which high guiding fields were needed (for example, in sections 8.5 and 9.3). However, the background signal is different for all the samples due to slightly different sample sizes but also due to different contributions from the glue that was used to mount the samples for in-plane measurements as well as asymmetries in the straws that were used as sample holders for the out-of-plane measurements. These contributions can hardly be estimated. Therefore, despite the noted disadvantages, the background of all $M(H)$ loops presented in this work was corrected with linear fits.

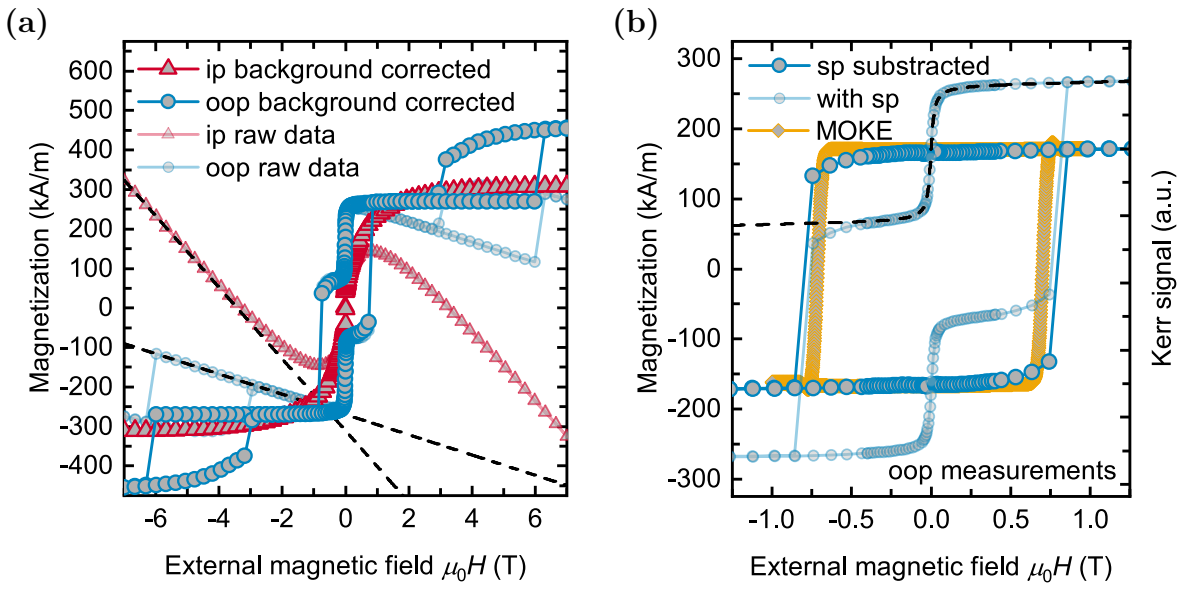

Figure 5.10: Magnetic hysteresis loops of a *sub.*/Pt(5 nm)/$Tb_{0.22}Fe_{0.78}$(20 nm)/Si_3N_4(5 nm) sample. In (a), the measured SQUID-VSM raw magnetization loops (already normalized with the sample volume), as well as the background-corrected loops, are plotted for in-plane and out-of-plane geometry. The dashed lines mark the linear fit functions that were applied to subtract the diamagnetic background. (b) displays magnetic hysteresis curves measured by SQUID-VSM and MOKE magnetometry in out-of-plane geometry. The background-corrected SQUID-VSM loops with the soft magnetic phase (with sp) and with the soft magnetic phase subtracted (sp subtracted) are plotted with blue circles. The dashed black line is the arctan function that was used to fit the soft magnetic phase. The orange diamonds represent a MOKE reference measurement of the same sample. The soft phase is absent here.

Magnetic soft phase

Especially for samples with rare earth-transition metal alloys or multilayers that have a low net magnetization, a soft magnetic phase can often be observed in SQUID-VSM $M(H)$ loops. This soft magnetic phase can be attributed to edge effects due to the sample preparation and can be reduced by cutting the samples on all edges or especially by using masks during the sputtering process. [378] However, it is sometimes not possible to completely avoid that soft magnetic phase. As it is only visible in SQUID-VSM measurements and not by spatially more localized methods such as MOKE measurements, it is treated as a measurement artifact in this work. Therefore, the soft phase is fitted with an arctan function [379] and subtracted from the loops for all samples where it can be clearly differentiated from the loop. Figure 5.10b shows an exemplary comparison of out-of-plane hysteresis loops of a *sub.*/Pt(5 nm)/$Tb_{0.22}Fe_{0.78}$(20 nm)/Si_3N_4(5 nm) sample magnetic measured by MOKE magnetometry and SQUID-VSM. The small transparent blue circles show the uncorrected SQUID-VSM loop, where a strong soft magnetic phase can be observed. The bigger, non-transparent blue circles display the SQUID-VSM loop with the soft phase subtracted. The dashed black line shows the arctan function that was used to fit the soft phase. The orange

diamonds show a MOKE loop for the sample in which the soft phase is not visible. The difference in the coercivities between the SQUID-VSM and the MOKE loops can be explained by local variations of the film composition and by local defects, as different pieces of the sample were used for the two measurement techniques. Furthermore, different measurement times in the MOKE and the SQUID-VSM setup can lead to the varying coercivities.

Influence of the measurement speed

All SQUID-VSM $M(H)$ loops were measured in a field stabilized mode. After sweeping the magnetic field to the desired value, the magnet is first stabilized at that value, and afterward, the sample is vibrated for 4 s with a frequency of 14 Hz, and the value of the magnetic moment is calculated as an average. Therefore, each data point takes several seconds to record. The coercivity of magnetic materials shows a time dependence due to the thermally-assisted reversal of magnetic domains, which is dependent on the material and on the size of the investigated structures. [380] As a direct consequence, the measured magnetization $M(H)$ loops are dependent on the measurement speed. When the applied magnetic field H is swept faster, the measured coercivity will appear larger.

To estimate the impact of the measurement speed on the SQUID-VSM hysteresis loops of the investigated Pt/Tb_xFe_{1-x} samples (see chapter 7), out-of-plane MOKE hysteresis measurements with different sweeping rates of the external magnetic field were performed for exemplary samples. Figure 5.11 shows the slopes of the MOKE hysteresis loops for a *sub.*/Pt(5 nm)/$Tb_{0.22}Fe_{0.78}$(20 nm)/Si_3N_4(5 nm) sample in the magnetic field range in which the reversal of the magnetic moments takes place. The measurements were performed in a field sweep mode with an integration time of 500 ms. The current sweep rates applied to the electromagnet of the P-MOKE setup were varied from 1 mA/s to 500 mA/s, resulting in magnetic field sweep rates of approximately 0.06 mT/s to 25.40 mT/s. With increasing sweep rates the coercivity increases from $\mu_0 H_c = 0.54$ mT (measured with 0.06 mT/s) to $\mu_0 H_c = 0.63$ mT (measured with 25.40 mT/s).

The SQUID-VSM $M(H)$ loops for this work were measured with different resolutions/measurement speeds depending on the region of the external applied magnetic fields. Usually, around $\mu_0 H = 0$ mT a higher resolution was used to allow for the correction of the soft magnetic phase described above. For the Pt/Tb_xFe_{1-x} and Pt/Gd_xFe_{1-x} series, the used average field sweep rates (estimated from the time that was necessary to measure the field regions with the used field stabilized measurement mode) were approximately as follows:

Magnetic field region:	Field sweep rate:
$400\,\text{mT} \leq \mu_0 H \leq 7\,\text{T}$	6.1 mT/s
$50\,\text{mT} \leq \mu_0 H \leq 400\,\text{mT}$	1.0 mT/s
$0\,\text{mT} \leq \mu_0 H \leq 50\,\text{mT}$	0.2 mT/s

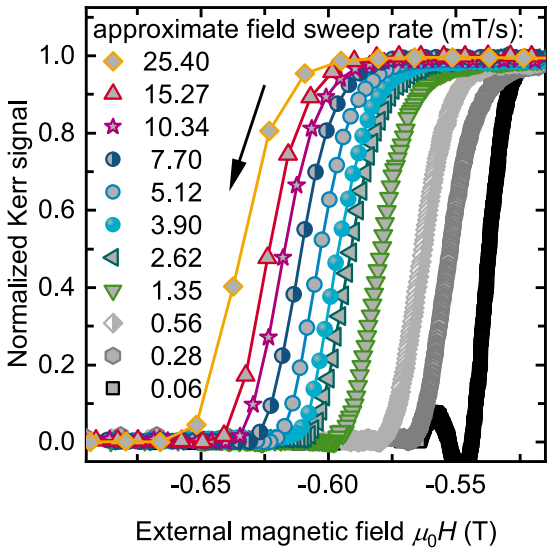

Figure 5.11: P-MOKE measurements of a *sub.*/Pt(5 nm)/$Tb_{0.22}Fe_{0.78}$(20 nm)/Si_3N_4(5 nm) sample recorded with different magnetic field sweep rates. The black arrow denotes the measurement direction.

Therefore, the coercivities determined by SQUID-VSM measurements are expected to be overestimated, especially for samples with coercivities $\mu_0 H_c > 400\,\mathrm{mT}$.

5.4.3 Estimation of the effective magnetic anisotropy

The amorphous Tb_xFe_{1-x} (see chapter 7) and Gd_xFe_{1-x} (see chapter 8) thin films that were investigated for this work have an out-of-plane magnetic easy axis for a certain range of the rare-earth content x. In order to systematically characterize this behavior, an estimation of the effective magnetic anisotropy energy density K_{eff} using SQUID-VSM $M(H)$ loops has been done for all of these samples. The steps that were performed for this estimation (especially to remove the hystereses of the $M(H)$ loops) will be explained in the following on a measurement of a *sub.*/Pt(5 nm)/$Tb_{0.24}Fe_{0.76}$(20 nm)/Si_3N_4(5 nm) sample. Figure 5.12a shows the background and soft-phase-corrected hysteresis loops measured in in-plane and out-of-plane direction. The solid black lines are first-order splines that were used to interpolate the curves. For the following steps, it is necessary that the absolute magnetization values strictly increase from the minimum. Therefore, starting from the minimum, values that were smaller than the previous ones were deleted in order to deal with minor fluctuations in the SQUID-VSM loops. The black line in figure 5.12b shows the splines after performing that step. Afterward, the curves were inverted, and again spline interpolations with the same magnetization values were calculated for the in-plane and out-of-plane direction for both field sweep directions. Then, the average of the values for the two field sweep directions (spline 1 and spline 2) was calculated (see figure 5.12c). In the last step, the curves were inverted again, and the curves measured in in-plane and out-of-plane direction were normalized to the same

M_S value. For all samples, the M_S values of the magnetic easy axis direction were taken for the normalization. Then, the area between the curves in the first quadrant of the graph was calculated and used as an estimation of the effective magnetic anisotropy K_{eff}. The curves in comparison to the original data points are plotted in figure 5.12d.

There are several errors that make the estimation rather rough for some of the samples. First, there are several errors due to the spline interpolations and also due to the treatment of data points for which the absolute value of the magnetization is not strictly in-

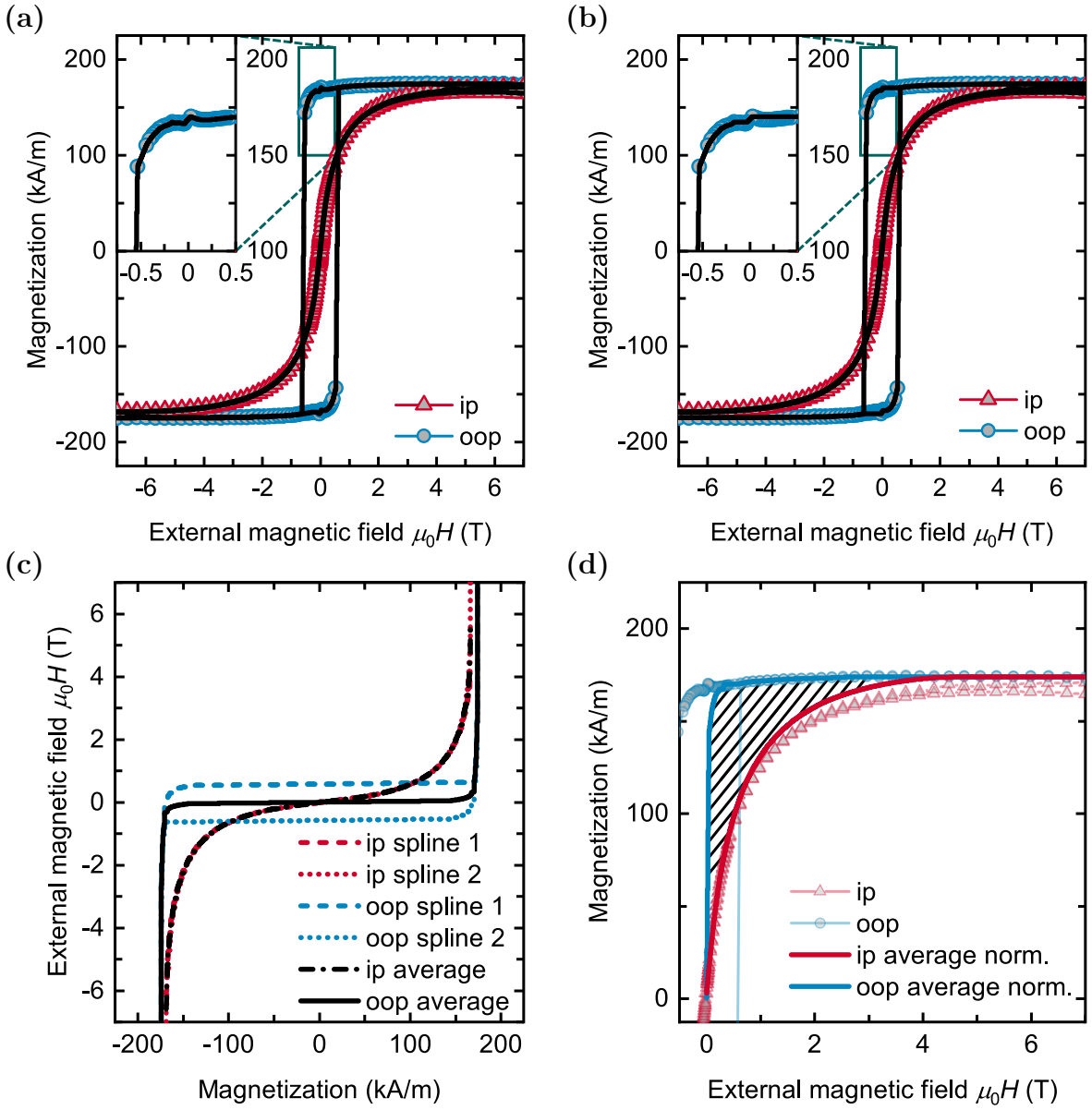

Figure 5.12: (a)–(d) show the different steps that were performed to estimate the effective anisotropy energy density K_{eff} of a *sub.*/Pt(5 nm)/$Tb_{0.24}Fe_{0.76}$(20 nm)/Si_3N_4(5 nm) sample. Details are described in the main text. The solid lines in (a) and (b) show the used spline interpolations of the loops. The area between the two curves that was used as the estimation of K_{eff} is marked with the black shading in (d).

creasing from the minimum. However, these are small compared to the errors caused by unsaturated samples and the normalization of the in-plane and out-of-plane loops to the same maximum. For samples where the saturation is not reached for the hard magnetic axis, the estimation only gives a lower limit for the anisotropy. Therefore, the anisotropy is strongly underestimated for some samples (see, for example, the SQUID-VSM $M(H)$ loops of a *sub.*/Pt(5 nm)/$Tb_{0.20}Fe_{0.80}$(20 nm)/Si_3N_4(5 nm) sample shown in appendix A.3, figure A.8g). As described above, the curves were normalized to the M_S value of the easy axis for all curves. For some of the samples, the difference between the in-plane and out-of-plane M_S values is rather large and can hardly be explained by the SQUID-VSM errors noted above. In such cases, a large error of M_S can be assumed that is directly reflected in the K_{eff} values. Furthermore, the samples with an out-of-plane easy axis generally have higher M_S values due to the measurement geometry (see subsection 5.4.2). One option to overcome some of the problems regarding errors due to the normalization is to compare K_{eff}/M_S values instead of K_{eff}. For some of the FI samples, a further challenge is the treatment of spin-flop transitions and the fanning cone compression in Tb_xFe_{1-x} samples (see subsection 2.6.3). In such cases, all magnetization values for applied magnetic fields within the region of the spin-flop transition or the fanning cone compression have been set to the saturation magnetization M_S of the FI state for the estimation of K_{eff}. However, for some samples, no clearly saturated magnetization state is reached for applied fields below the spin-flop transition field (see, for example, the SQUID-VSM $M(H)$ loops of the *sub.*/Pt(5 nm)/$Gd_{0.25}Fe_{0.75}$(20 nm)/Si_3N_4(5 nm) sample shown in appendix A.4, figure A.11e), which leads to an additional error, as M_S is underestimated in this case and the exact slope of the loop is unknown.

5.5 Four-point resistivity measurements

Four-point resistivity measurements are used to determine absolute values of specific resistivities. The technique was initially proposed by Wenner [382] in 1915 and adopted for semi-

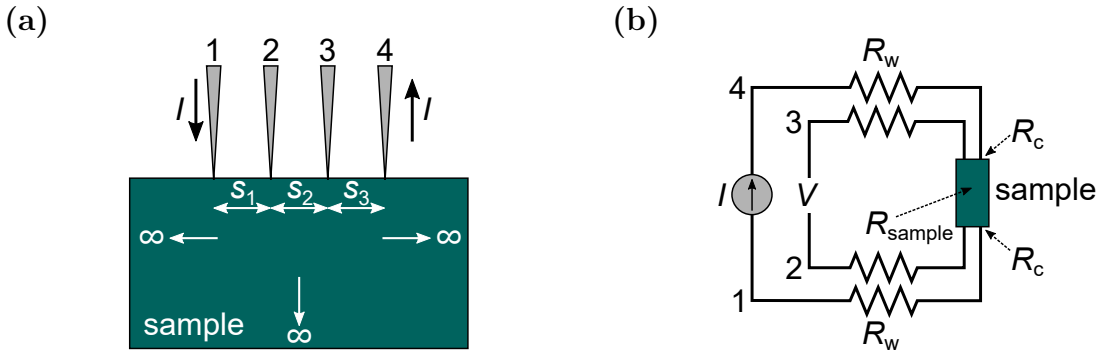

Figure 5.13: Schematic of a four-point resistivity measurement setup. (a) shows the probe geometry, and in (b), an equivalent circuit diagram for the measurement is displayed. The figures are adapted from [381].

conductor wafer resistivity measurements by Valdes [383] in 1954. Here, a short introduction to the technique following the book by Schroder [381] will be given.

Figure 5.13 shows (a) a schematic of a four-point resistivity measurement setup and (b) an equivalent circuit diagram for the measurement. Four measurement contacts are typically arranged on a line with equal probe spacings. A current I is applied between the contacts 1 and 4, and the voltage V is measured between the contacts 2 and 3. The total resistance R_t is given by:

$$R_\mathrm{t} = \frac{V}{I} = 2R_\mathrm{w} + 2R_\mathrm{c} + R_\mathrm{sample} \ , \tag{5.12}$$

with the wire resistances R_w, the contact resistances R_c, and the sample resistance R_sample. Due to the high input impedance of the voltmeter (on the order of $10^{12}\,\Omega$), the voltage drops across R_w and R_c are negligibly small for the voltage measurement circuit, and thus the measured voltage drop is essentially the voltage drop across the sample. The specific resistance ρ of the sample is given by [383]:

$$\rho = \frac{2\pi}{1/s_1 - 1/(s_1+s_2) - 1/(s_2+s_3) + 1/s_3}\frac{V}{I} \ . \tag{5.13}$$

For equally spaced probes ($s_1 = s_2 = s_3 =: s$) equation 5.13 reduces to:

$$\rho = 2\pi s\frac{V}{I} \ . \tag{5.14}$$

However, equation 5.14 is only valid for infinite sample dimensions. For thin conducting layers with thicknesses $t \ll s$ that are sandwiched in between two insulating layers, a correction factor

$$F = \frac{t/s}{2\ln(2)} \tag{5.15}$$

has to be applied. [383] According to equations 5.14 and 5.15, the specific resistance of a thin conducting layer is given by:

$$\rho = F2\pi s\frac{V}{I} = \frac{\pi t}{\ln(2)}\frac{V}{I} \ . \tag{5.16}$$

Another additional error arises for small lateral sample dimensions with respect to the probe spacings s. The measurement setup that was used for this work has a probe spacing s of 1.3 mm. For the used rectangular sample sizes of approximately 1.5 cm in length and 1 cm in width, the systematic error is on the order of 10%. [381] Measurements that have been performed with the probes aligned parallel or perpendicular to the long sample side or diagonal across the sample showed only small deviations of less than 3% from each other. An additional non-systematic error of up to 20% arises from errors in the film thicknesses that

are directly reflected in the resistivity values (see equation 5.16). All measurements shown in this work were measured with an applied current I of 1 mA.

5.6 Terahertz time-domain spectroscopy

All THz spectroscopy results presented in this work were measured by Dr. Robert Schneider and Jannis Bennsmann in the group of Prof. Rudolf Bratschitsch at the University of Münster. Nevertheless, a short introduction to the used THz emission spectroscopy measurement setup will be given here, as the focus of this work was set on the development of spintronic THz emitter systems, and therefore this is one of the key techniques that was used for this work. Detailed reviews on the used measurement setups can be found in the PhD thesis of Dr. Robert Schneider [299].

Figure 5.14 shows a schematic of a room-temperature THz-TDS setup that was used for this work. The beam of a linearly polarized, pulsed (1 kHz) laser with a center wavelength of 810 nm and a pulse duration τ_{probe} of 60 fs is split into a pump and a probe pulse using a beam splitter, with 90% and 10% of the intensity, respectively. The pump pulse excites the sample, which is placed in between the poles of an electromagnet (room-temperature setup) or within a cryostat in the magnetic field of NdFeB permanent magnets (low-temperature setup). The external magnetic field is aligned perpendicular to the pump pulse, along the sample plane. The emitted THz radiation is guided through the parabolic mirrors PM1–3 onto the (110) ZnTe detector crystal with a thickness of 1 mm. In between, a 1 mm thick Si wafer reflects the partly transmitted laser pump pulse to a beam block. The probe pulse is spatially overlaid with the THz radiation on the detector crystal. The THz signal is detected by electro-optic sampling [385, 386]. The electric field of THz radiation causes a change in the refraction index of the detector crystal due to the Pockels effect [387], which is proportional to the electric field of the THz signal. This leads to a change of the probe pulse from an initially linear polarization to an elliptical polarization, which is measured with a photodiode detector. As the duration of the probe pulse τ_{probe} is short compared to the period of the THz radiation, the emitted THz pulse can be scanned by varying the delay time. The detectable bandwidth is dependent on τ_{probe} as well as on the properties of the used detector crystal [388–390]. For the used 1 mm thick ZnTe detector crystal, the bandwidth is limited to frequencies below 3 THz. To avoid absorption losses of the THz radiation due to water, most of the experiments were carried out in a dry nitrogen atmosphere.

It should be mentioned here that in all studies shown in this work, the THz electro-optic signals $S(\tau)$ were analyzed. In the frequency domain, $S(\omega)$ is connected to the THz electric

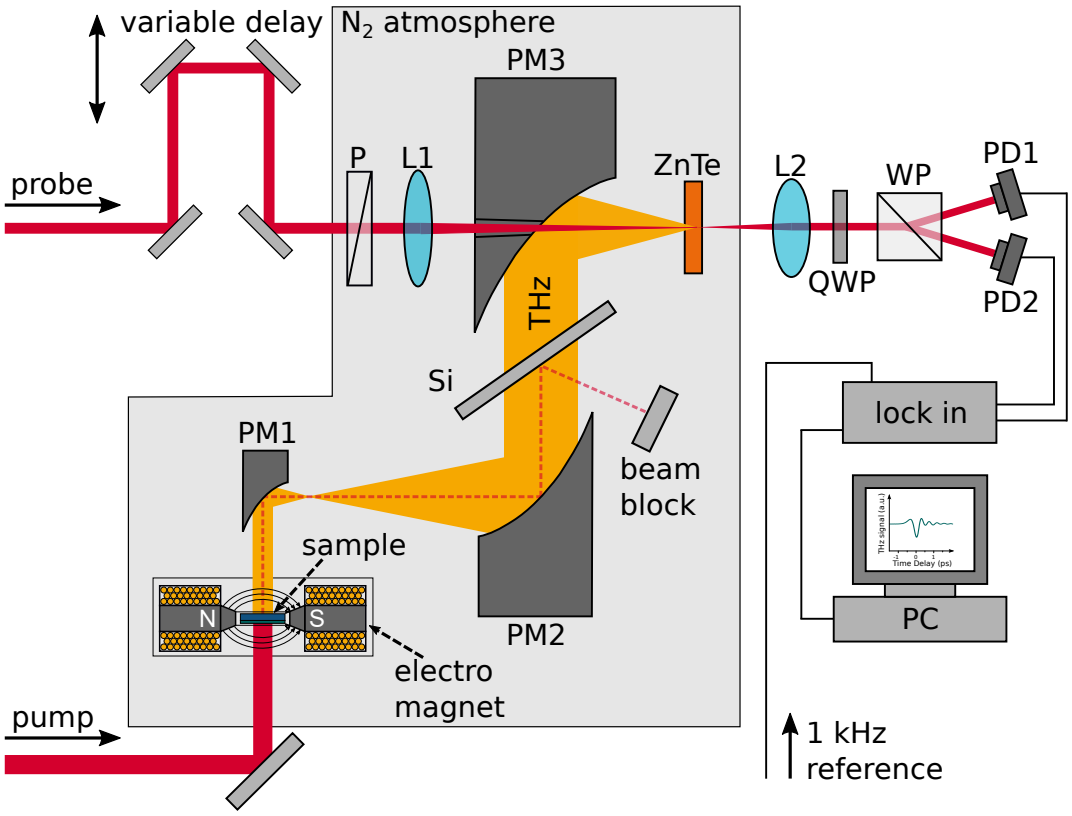

Figure 5.14: Schematic of a room-temperature THz emission spectroscopy setup. P: polarizer, PM1–3: off-axis parabolic mirror, Si: 1 mm thick silicon wafer, ZnTe: 1 mm thick (110) zinc telluride crystal, QWP: quarter-wave plate, WP: Wollaston prism, PD1,2: photodiode, and L1,2: plano-convex lenses. The figure is adapted from [384] and [299].

field directly behind the sample $E(\omega)$ by a transfer function $H(\omega)$ that accounts for the detection process and the propagation of the THz pulse to the electro-optic crystal [81]:

$$S(\omega) = H(\omega)E(\omega) \ . \tag{5.17}$$

However, as the same detection setup was used for all measurements, the electro-optic signals can be used to compare the THz emission characteristics of different samples. Furthermore, it should be noted that for the 1 kHz repetition rate of the used pump laser system, the investigated samples are expected to be in the same ground state before each excitation pulse, as the relaxation times of the electron and spin systems are on the order of picoseconds. [245]

For the determination of the complex conductivities of the samples, a THz transmission setup was used. Here, a spintronic Pt(3 nm)/Fe(1.5 nm)/W(3 nm)/Si_3N_4(5 nm) emitter system that was sputtered on a 1 mm thick Si wafer with a diameter of 10.16 cm (4 in) served as a high power broadband THz emitter. By measuring the transmission of the THz radiation through a sample and by comparison with measurements of the substrates that serve as a reference, the complex conductivities of the film systems can be determined. Details on this setup, as

well as on the determination of the complex conductivities in the THz regime, can also be found in the PhD thesis of Dr. Robert Schneider [299].

CHAPTER 6

Spintronic Pt/Co_xFe_{1-x} terahertz emitters

As described in section 2.5, soft magnetic Co_xFe_{1-x} alloys with Co content $0.2 \lesssim x \lesssim 0.4$ are well known for their high saturation magnetization, reaching values up to $M_S \approx 1900\,kA/m$ that result from an increased spin polarization of the 3d electrons compared to pure Fe and pure Co. [158] Therefore, Co_xFe_{1-x} alloys are promising candidates for the use as effective spin current generating FM layers in FM/NM spintronic THz emitters. However, despite the unique properties of Co_xFe_{1-x} alloys, by the time this study was done, only one work on the THz emission of an exemplary $Co_{0.7}Fe_{0.3}(3\,nm)/Pt(3\,nm)$ bilayer [82] had been published. Recently, Sasaki *et al.* [266] reported on the effect of different Co contents in annealed $(Co_xFe_{1-x})_{0.8}B_{0.2}/Ta$ bilayers on the spintronic THz emission, demonstrating the influence of the sample magnetization on the spin current generation.

The aim of the study presented in this chapter was to systematically investigate the composition dependency of the spintronic THz emission of Pt/Co_xFe_{1-x} bilayers with respect to the magnetic properties. Pt is well known for its large spin Hall angle ($+1.2\% \leq \theta_{sh} \leq +11\%$ [271, 294, 295]) and its suitability for the use in spintronic THz emitter systems [82, 300] and therefore has been chosen as THz emitting NM layer. Besides the composition dependence, also the influence of the layer thicknesses on the emitted THz radiation and a thickness-optimized composition series have been investigated. For the latter, also the composition-dependent efficiency to inject spin currents into the Pt layer has been estimated based on measurements of the pump beam absorption, the electrical conductivity in the THz frequency regime, and the THz emission amplitude. Additionally, the thickness-optimized bilayers were applied for $[Pt/Co_{0.3}Fe_{0.7}/Si_3N_4]_n$ stacked bilayer emitters with varying repetitions n.

The results were achieved in collaboration with Dr. Robert Schneider, Jannis Bensmann, Dr. Steffen Michaelis de Vasconcellos, and Prof. Rudolf Bratschitsch from the University of Münster. The studies on the thickness dependency, the thickness-optimized series, and the stacked bilayers are published in [391].

6.1 Pt(5 nm)/Co_xFe_{1-x}(3 nm) composition series

As a starting point, a composition series of *sub.*/Pt(5 nm)/Co_xFe_{1-x}(5 nm)/Si_3N_4(5 nm) samples with varying Co content $0 \leq x \leq 1$ has been prepared. The aim of this study was to measure the magnetization and THz emission in dependence on the Co content and check the results for a correlation between the magnetization and the THz emission amplitude.

6.1.1 Sample preparation and structural characterization

All samples were prepared by magnetron sputter deposition at room temperature. The Co_xFe_{1-x} layers were deposited by co-sputtering from elemental targets. Pt, Co, and Fe were deposited by DC sputtering. The Si_3N_4 layers, which serve as a capping to prevent the spintronic layers from oxidation, were deposited by RF sputtering from a stoichiometric compound target (see chapter 4 for details on the sample preparation). Each layer system was prepared on a 500 µm thick Al_2O_3(0001) substrate, polished on both sides, for the THz spectroscopy experiments as well as, for cost reasons, on a 525 µm thick p-doped Si(100) substrate with a 100 nm thick thermally oxidized SiO_2 layer on which all other measurements of the structural and magnetic properties have been performed.

The Pt layers show a similar polycrystalline growth on both substrates (see appendix A.2, figures A.1a and A.1b for transmission electron microscope (TEM) bright-field images of *sub.*/ Pt(3 nm)/Fe(3 nm)/Si_3N_4(5 nm) reference samples grown on Al_2O_3 and Si/SiO_2 substrates). Therefore, also a similar growth of the Co_xFe_{1-x} and consequently similar magnetic properties are expected for both substrates. Thus, the magnetic properties measured on the samples grown on Si/SiO_2 substrates can be directly compared to the THz emission results measured on the samples grown on Al_2O_3 substrates.

To investigate the compositions of the Co_xFe_{1-x} films and layer thicknesses, RBS measurements have been performed on all samples. Figure 6.1 shows the results with respect to the nominal Co content x_{cal}. For all samples, the measured Co contents x_{RBS} are smaller than the nominal values. The deviations from x_{cal} become larger with increasing Co content up to 5% for $x_{\mathrm{cal}} = 0.8$ (see figure 6.1a). The thickness of the Co_xFe_{1-x} layers systematically decreases with increasing Co content from 3.2 nm for pure Fe to 2.5 nm for pure Co (see figure 6.1b). Therefore, most likely, the Co sputter rates were slightly lower than the calibrated values. The Pt layer thicknesses are in the range from 5.0–5.3 nm for all samples except the one with $x_{\mathrm{cal}} = 0.3$, for which the measured thickness is only 4.4 nm (see figure 6.1c). This particular sample was the only one that was deposited on a different day, as it was part of the thickness series described in section 6.2. The film thicknesses and compositions measured by RBS are used for the following discussion.

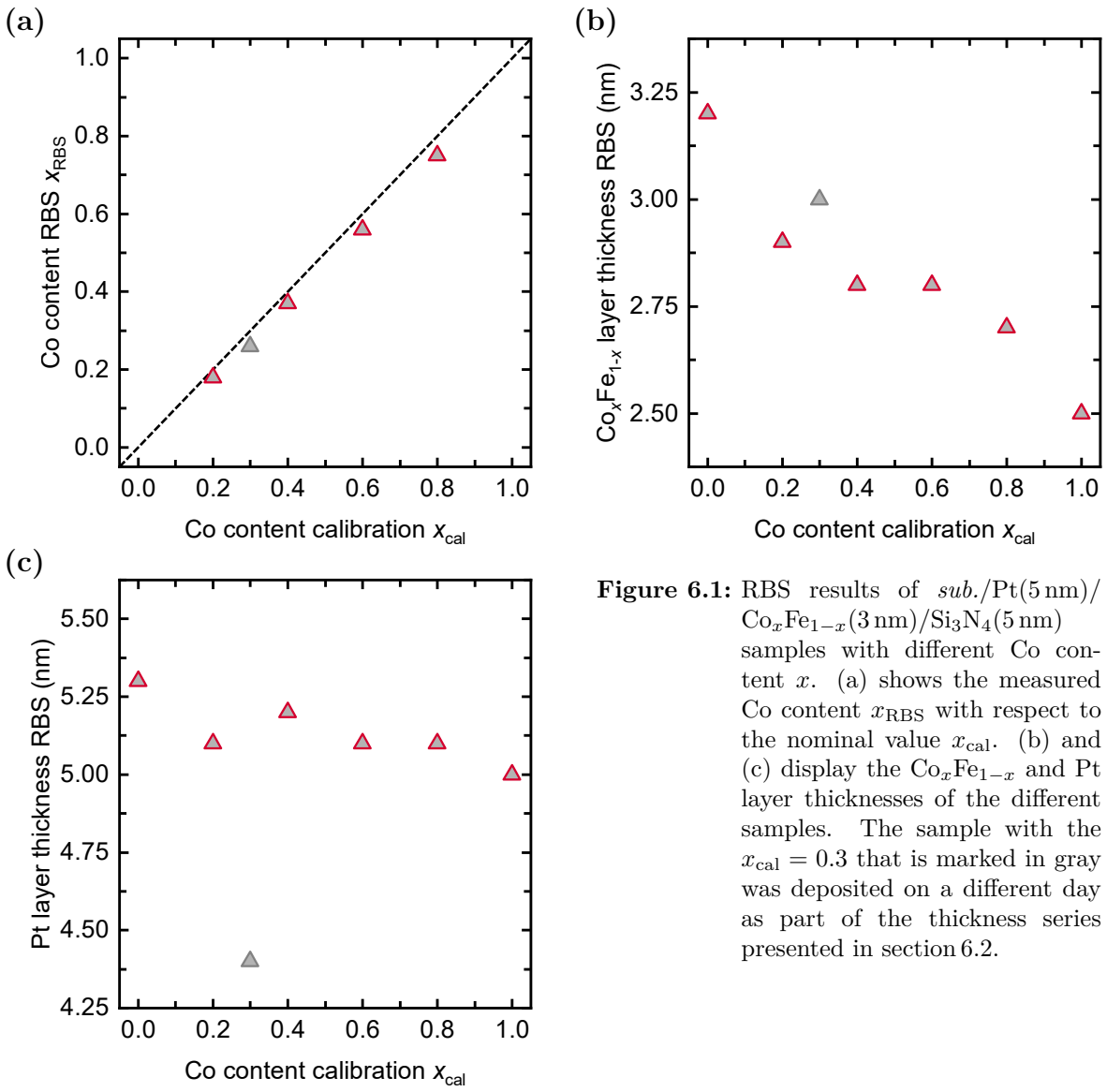

Figure 6.1: RBS results of *sub.*/Pt(5 nm)/Co_xFe_{1-x}(3 nm)/Si_3N_4(5 nm) samples with different Co content x. (a) shows the measured Co content x_{RBS} with respect to the nominal value x_{cal}. (b) and (c) display the Co_xFe_{1-x} and Pt layer thicknesses of the different samples. The sample with the $x_{cal} = 0.3$ that is marked in gray was deposited on a different day as part of the thickness series presented in section 6.2.

6.1.2 Magnetization and terahertz emission results

For all samples, room-temperature SQUID-VSM $M(H)$ loops have been measured in in-plane and out-of-plane direction, revealing an in-plane magnetic easy axis. The loops are displayed in appendix A.2, figure A.2. Additionally, THz emission spectroscopy measurements were performed. All THz spectroscopy experiments shown in this chapter were carried out by Dr. Robert Schneider and Jannis Bensmann at the University of Münster with the measurement setup described in section 5.6. The measurement geometry, which was used for all THz emission spectroscopy experiments shown in this chapter, is displayed in figure 6.2. As described in detail in section 3.3, the excitation of electrons in the FM Co_xFe_{1-x} layer above the Fermi level leads to a superdiffusive spin current $\boldsymbol{J}_s$ from the FM toward the nonmagnetic Pt layer, in which $\boldsymbol{J}_s$ is converted via the inverse spin Hall effect into a transverse charge

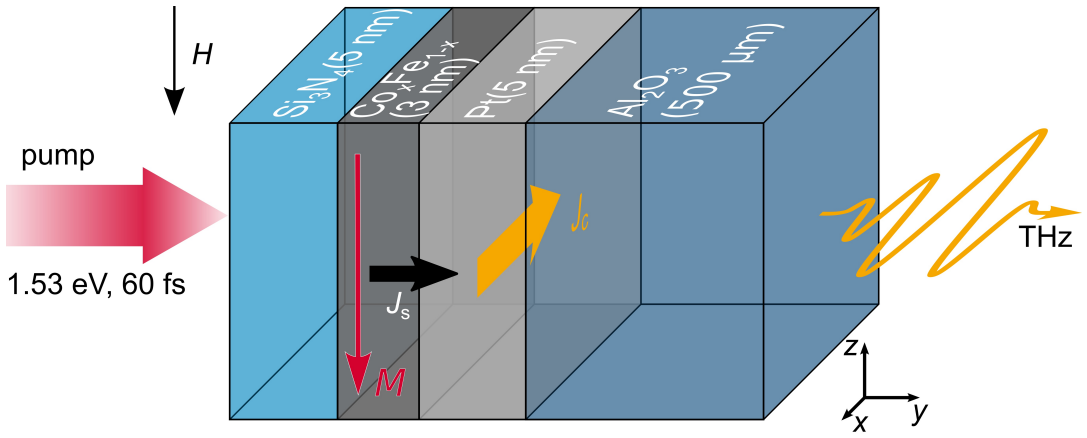

Figure 6.2: Illustration of the layer stacking and the excitation geometry that was used for the THz emission spectroscopy measurements performed on the *sub.*/Pt(5 nm)/Co_xFe_{1-x}(3 nm)/Si_3N_4(5 nm).

current $\boldsymbol{J}_c$, that leads to the emission of electromagnetic radiation in the THz frequency regime. For the investigated Pt/Co_xFe_{1-x} systems, it is expected that both, spin-polarized Co and Fe 3d electrons contribute to the spin currents $\boldsymbol{J}_s$ and therefore to the emission of THz radiation, as the 3d bands in both materials are energetically located close to the Fermi level (see figure 2.7 for the calculated densities of states for majority- and minority-spin electrons in Fe and Co).

Figure 6.3 displays (a) the in-plane magnetization values for an applied magnetic field $\mu_0 H = 200\,\mathrm{mT}$ and the saturation magnetization measured with an applied field $\mu_0 H = 7\,\mathrm{T}$ and (b) the THz root mean square (RMS) signals measured at an applied magnetic field of $\mu_0 H = 200\,\mathrm{mT}$ with a laser pump fluence $\Phi = 0.75\,\mathrm{mJ/cm^2}$ in dependence on the Co content x. The THz waveforms are almost similar for all samples (see appendix A.2, figure A.3 for the THz signals and the corresponding frequency spectra). The THz RMS amplitudes and the magnetization values show a similar qualitative composition dependence with a maximum at $x = 0.37$. Compared to the Fe/Pt sample, the magnetization of the sample with $x = 0.37$ is increased by $\approx 27\%$, whereas the THz RMS signal is increased by $\approx 22\%$. However, for the THz amplitudes, the maximum can be observed in a broader composition region ($0.18 \leq x \leq 0.37$). Furthermore, despite the lower saturation magnetization, the pure Pt/Co sample shows a slightly increased ($\approx 4\%$) THz signal compared to the pure Pt/Fe sample. Similar results have been reported by Seifert *et al.* [82] for Pt(3 nm)/Fe(3 nm) and Pt(3 nm)/Co(3 nm) samples. This can be explained by a different dependence on the laser pump fluence, as the THz amplitude of the Pt/Co sample increases more strongly with the pump fluence than the Pt/Fe sample (see appendix A.2, figure A.4 for the pump fluence dependence of the samples with pure Fe and Co as well as the sample with $x = 0.37$). The pump fluence dependence, as well as the other factors that play a role in the emitted THz radiation, will be discussed in more detail for the thickness-optimized composition series

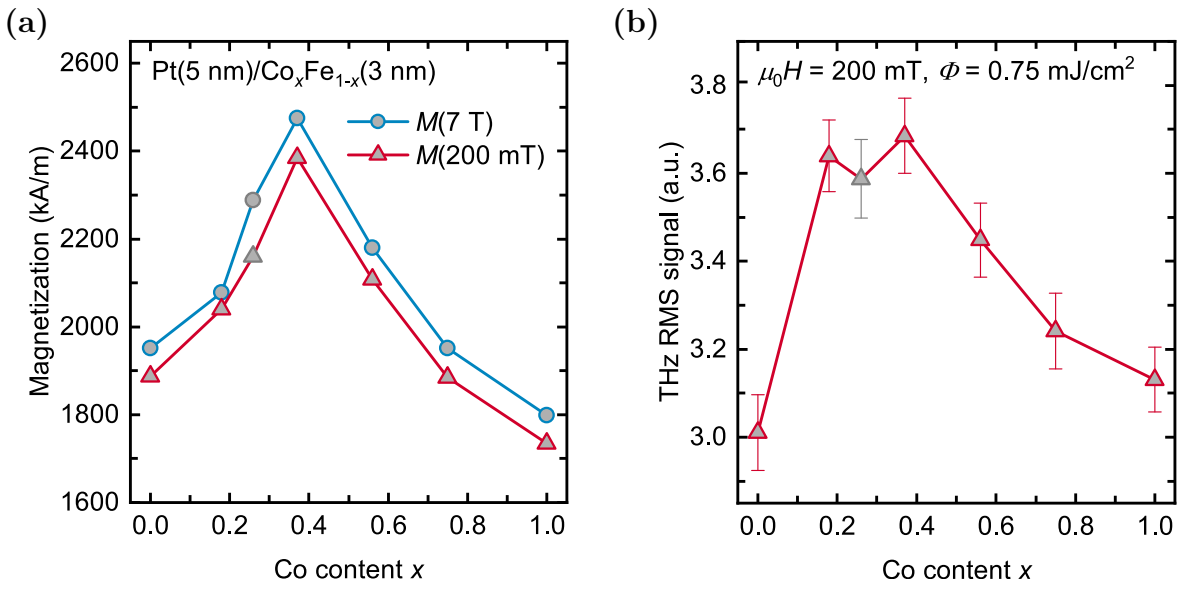

Figure 6.3: (a) shows the magnetization values of *sub.*/Pt(5 nm)/Co_xFe_{1-x}(5 nm)/Si_3N_4(5 nm) samples with different Co content x measured at applied magnetic fields $\mu_0 H = 200$ mT (red triangles) and $\mu_0 H = 7$ T (blue circles) that were taken from room temperature SQUID-VSM in-plane loops (shown in appendix A.2, figure A.2). (b) displays the THz RMS amplitudes measured at room temperature with a pump fluence $\Phi = 0.75\,\mathrm{mJ/cm^2}$ and an applied magnetic field $\mu_0 H = 200$ mT. The error bars represent the statistical errors of the RMS values and an additional statistical error of 1.8% that is caused by small variations in the mounting of the different samples. The sample with $x = 0.3$, which has a slightly smaller Pt layer thickness compared to the other samples, is marked in gray.

in section 6.3. The saturation magnetizations clearly exceed the values reported in literature. [158] This can be explained by the normalization of the measured magnetic moments to the volume of the Co_xFe_{1-x} layers, for which the thicknesses measured by RBS have been used. Thus, the additional magnetic moments that are induced in the Pt layers by the magnetic proximity effect [116–118] have been neglected. These induced moments in the Pt layer close to the interface of Pt/Fe as well as Pt/Co bilayers are on the order of 0.6–0.7 μ_B per Pt atom. [117, 118] The averaged value of an induced moment of 0.3 μ_B per Pt atom within the first 1.1 nm from the Fe/Pt interface reported by Kuschel *et al.* [118] for a Fe(9.1 nm)/Pt(3.1 nm) bilayer would therefore lead to an additional contribution to the magnetization on the order of 110 kA/m. For the sputtered layers investigated in this work, a strong intermixing of the Co_xFe_{1-x} layers with the Pt is expected (see transmission electron microscope EDX mappings of *sub.*/Pt(3 nm)/Fe(3 nm)/Si_3N_4(5 nm) reference samples in appendix A.2, figures A.1c–A.1f). The intermixing can lead to induced magnetic moments in a larger thickness area and therefore explain the high magnetization values. As the magnetic moments induced in a Pt layer by Fe and Co layers are expected to be almost similar [117, 118], only an offset in the magnetization values, which is independent of the Co content, is expected. The spin-polarized Pt electrons could also contribute to the spin current $\boldsymbol{J}_s$, as a decreasing spin polarization of the Pt electrons with increasing distance from the Fe layer is

expected. This would lead to a higher THz amplitude and maybe also to a change in the signal shape. However, this contribution is expected to be independent of the Co content x.

Please note that the THz RMS amplitudes shown in figure 6.3b cannot be directly compared to the RMS amplitudes presented in the following sections, as these measurements were carried out almost two years later under slightly different conditions of the measurement setup.

6.2 Pt(t_{Pt})/$Co_{0.3}Fe_{0.7}$(3 nm) and Pt(5 nm)/$Co_{0.3}Fe_{0.7}$(t_{CoFe}) thickness series

A Co content of $x = 0.3$ has been chosen for two additional thickness series in order to optimize the Pt as well as the $Co_{0.3}Fe_{0.7}$ layer thickness for a high THz amplitude. Therefore, *sub.*/Pt(t_{Pt})/$Co_{0.3}Fe_{0.7}$(3 nm)/Si_3N_4(5 nm) samples with Pt layer thicknesses 1 nm $\leq t_{Pt} \leq$ 5 nm as well as *sub.*/Pt(5 nm)/$Co_{0.3}Fe_{0.7}$(t_{CoFe})/Si_3N_4(5 nm) samples with $Co_{0.3}Fe_{0.7}$ layer thicknesses 0.5 nm $\leq t_{CoFe} \leq$ 3 nm have been prepared as described in subsection 6.1.1. In contrast to the composition series described above, for some of these thin film systems, no compositions or layer thicknesses could be obtained experimentally. Therefore, the nominal values were used for the following discussion.

Figure 6.4 shows the THz RMS signals for all samples measured with a pump fluence $\Phi = 0.75\,\mathrm{mJ/cm^2}$ and an applied magnetic field $\mu_0 H = 200\,\mathrm{mT}$. For the $Co_{0.3}Fe_{0.7}$ layer thickness,

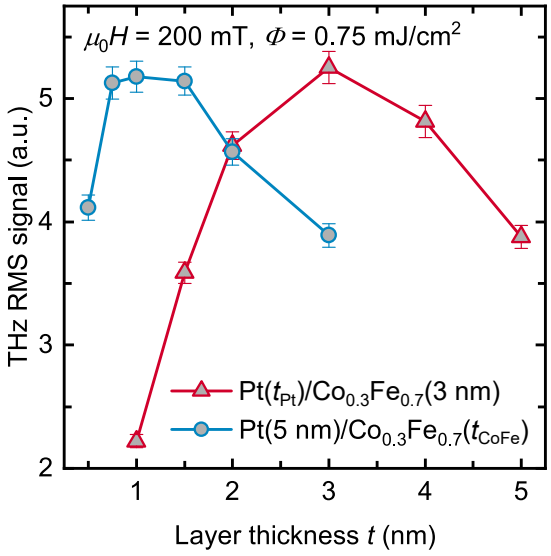

Figure 6.4: THz RMS signals of *sub.*/Pt(t_{Pt})/$Co_{0.3}Fe_{0.7}$(3 nm)/Si_3N_4(5 nm) and *sub.*/Pt(3 nm)/$Co_{0.3}Fe_{0.7}$(t_{CoFe})/Si_3N_4(5 nm) samples with varying layer thicknesses t measured with a pump fluence $\Phi = 0.75\,\mathrm{mJ/cm^2}$ and an applied magnetic field $\mu_0 H = 200\,\mathrm{mT}$ at room temperature. The error bars represent the statistical errors of the RMS values and an additional statistical error of 1.8% that is caused by small variations in the mounting of the different samples.

a broad maximum at 0.75 nm $\leq t_{CoFe} \leq$ 1.5 nm can be observed. The results are therefore comparable to the optimal FM film thicknesses 0.6 nm $\leq t_{FM} \leq$ 3 nm [83, 300, 322, 329] that were reported for different FM materials. For the Pt layer, a maximum of the THz RMS signal can be observed for $t_{Pt} = 3$ nm. This thickness value also agrees with other Pt thickness studies of spintronic THz emitters in the literature that report the maximum THz amplitude for Pt thicknesses ranging from 2 nm to 6 nm. [83, 300, 322, 323, 330] The rather large differences in these values can be caused by the different sample preparation methods, the used FM materials, and especially also by varying overall layer thicknesses of the investigated layer stacks.

6.3 Thickness-optimized Pt(2.5 nm)/Co_xFe_{1-x}(1 nm) composition series

Taking into account the results of the thickness study, a *sub.*/Pt(2.5 nm)/Co_xFe_{1-x}(1 nm)/Si_3N_4(5 nm) composition series with optimized layer thicknesses was prepared as described in subsection 6.1.1. Also, for this series, no compositions or layer thicknesses could be obtained experimentally. Therefore, the nominal values were used for the following discussion and the error in the layer thicknesses is assumed to be ±10%.

6.3.1 Magnetic properties

SQUID-VSM $M(H)$ measurements were carried out in in-plane and out-of-plane geometry. The $M(H)$ loops that are displayed in appendix A.2, figure A.5, reveal an in-plane magnetic easy axis for all samples. Figure 6.5a shows the in-plane magnetization values for an applied field $\mu_0 H = 200$ mT and the saturation magnetization M_S measured at $\mu_0 H = 7$ T. Despite the expected overestimation due to the negligence of the induced magnetic moments in the Pt layer for the normalization with the film thickness, in contrast to the composition series with thicker layers, the observed magnetization values are significantly smaller than the bulk values. The maximum, for which an increase in the magnetization of $\approx$ 17% compared to the Pt/Fe sample ($x = 0$) is obtained, can be observed for $x = 0.5$. Furthermore, the sample with pure Co ($x = 1$) shows a higher saturation magnetization than the sample with pure Fe ($x = 0$). This can be explained by a stronger temperature dependence of the Fe compared to the Co magnetization for very thin films that is caused by a weaker interatomic exchange coupling of the atomic moments in Fe. To investigate the dependence of the magnetization on the temperature T, field cooled and zero-field cooled in-plane $M(T)$ measurements have been carried out on the samples with $x = 0$, $x = 0.5$, and $x = 1$ in the following way: For the ZFC curves, the samples were cooled down in zero field from 400 K to 10 K, and the magnetization was subsequently recorded in a temperature sweep mode (10 K/min) with an

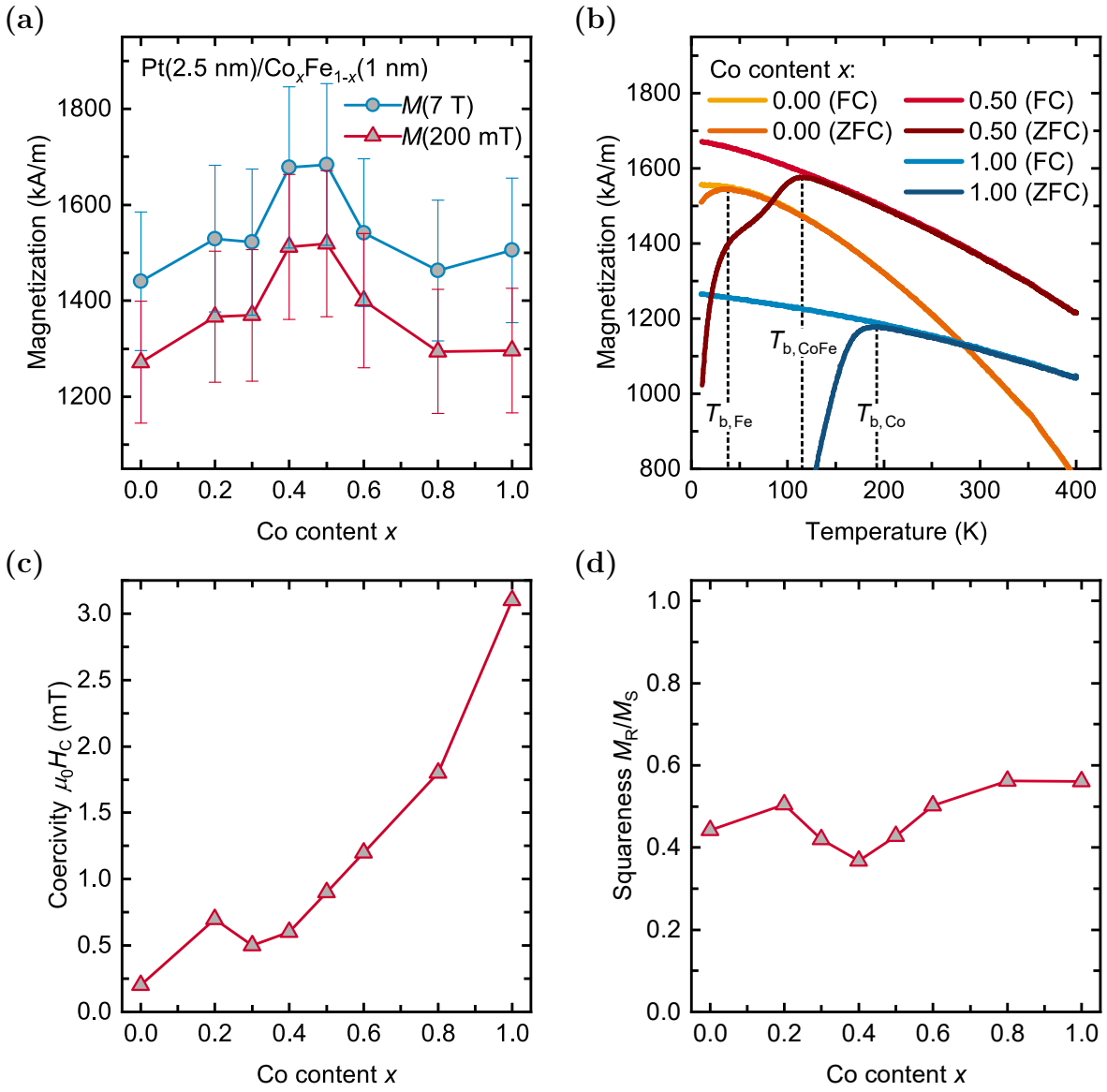

Figure 6.5: SQUID-VSM results of *sub.*/Pt(2.5 nm)/Co_xFe_{1-x}(1 nm)/Si_3N_4(5 nm) samples with different Co contents x. (a) shows the magnetization for an in-plane applied magnetic field $\mu_0 H = 200\,\mathrm{mT}$ and $\mu_0 H = 7\,\mathrm{T}$ in dependence on x measured at room temperature. The error bars represent the error of the film thickness of 10%. (b) displays the magnetization of samples with $x = 0$, $x = 0.5$, and $x = 1$ measured for increasing temperatures from 10 K to 400 K at an applied in-plane magnetic field of $\mu_0 H = 10\,\mathrm{mT}$. The measurements were performed in field-cooled (FC) and zero-field-cooled (ZFC) mode. (c) and (d) display the coercivity H_C and the squareness M_R/M_S in dependence on the Co content x at room temperature.

applied in-plane magnetic field $\mu_0 H = 10\,\mathrm{mT}$ while warming up to 400 K. For the FC curve, the sample was cooled down from room temperature to 10 K in an applied in-plane magnetic field $\mu_0 H = 10\,\mathrm{mT}$. Then, the magnetization was recorded while warming up to 400 K with the magnetic field still applied. The results are displayed in figure 6.5b. All samples show at least a partially superparamagnetic state at room temperature, which is indicated

by the different behavior of the ZFC and FC curves at low temperatures. The blocking temperatures T_b (marked with the dashed lines) increase with rising Co content. The results agree well with investigations of thin Fe [109–111] and Co [112] films by Shiratsuchi *et al.* that also showed superparamagnetic behavior for film thicknesses below 3 nm. The observed superparamagnetism of the samples also explains the lower M_S values compared to the bulk material. Nevertheless, all samples are in an almost saturated magnetic state for the applied field $\mu_0 H = 200\,\mathrm{mT}$ that was used for the THz emission spectroscopy experiments. The coercivity of the samples systematically increases with rising Co content (see figure 6.5c). The ratio between the magnetic remanence M_R and M_S, the so-called squareness, takes values between 0.37 and 0.56, with a local minimum for $x = 0.4$ (see figure 6.5d).

6.3.2 Terahertz emission results

The THz RMS amplitudes measured with a laser pump fluence $\Phi = 0.75\,\mathrm{mJ/cm^2}$ in dependence on the Co content are shown with the red triangles in figure 6.6. Also, for this series, only a minor influence of the Co content on the THz waveforms can be observed (see appendix A.2, figure A.6 for the THz signals and the corresponding frequency spectra). Similar to the magnetization, the THz amplitude shows a broad maximum. However, the maximum appears at a slightly higher Co content, $x = 0.6$, for which an increase of $\approx 46\%$ compared to the sample with pure Fe ($x = 0$) can be observed. Furthermore, the sample with pure Co

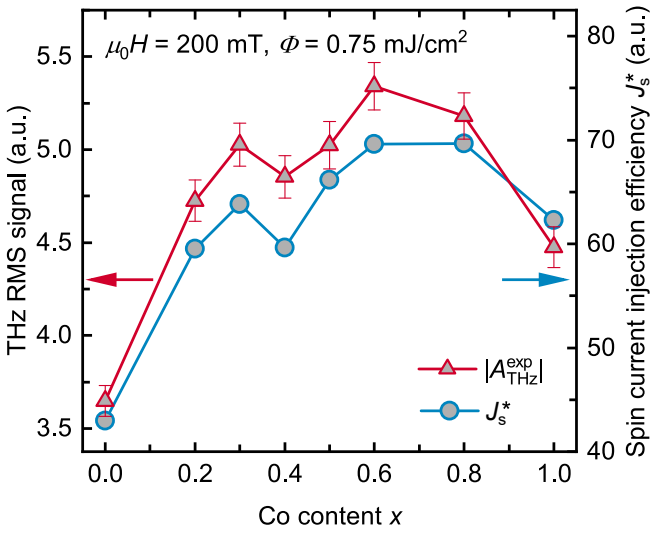

Figure 6.6: THz RMS signals (red triangles) of *sub.*/Pt(2.5 nm)/Co_xFe_{1-x}(1 nm)/Si_3N_4(5 nm) samples with different Co content x measured at room temperature with an applied magnetic field $\mu_0 H = 200\,\mathrm{mT}$ and a laser pump fluence $\Phi = 0.75\,\mathrm{mJ/cm^2}$. The error bars represent the statistical errors of the RMS values and an additional statistical error of 1.8% that is caused by small variations in the mounting of the different samples. The blue circles display the efficiency J_s^* to inject spin currents into the Pt layer.

($x = 1$) shows a significantly higher ($\approx 23\%$) THz amplitude compared to the sample with pure Fe.

As described in equations 3.8 and 3.9 in subsection 3.3.3, the emitted THz radiation depends on several sample properties. Therefore, the different parameters that contribute to equation 3.8 have been measured or estimated to characterize the samples further. The relaxation length λ_{rel} of the spin current within the Pt layer, the spin Hall angle of the Pt layer $\theta_{\mathrm{sh,\,Pt}}$, and the layer thicknesses are assumed to be approximately constant for all samples. The complex frequency-dependent electrical conductivities in the low THz regime $\sigma_{\mathrm{THz}}(x, \omega)$ were determined by ultrafast transient THz spectroscopy measurements that were performed by Dr. Robert Schneider (see [299] for details on the measurement setup). The electrical conductivity was found to be almost independent of the frequency in the whole measurement range up to 3 THz, with a vanishing imaginary part. Therefore, the average of the real part in the frequency range from 0.78 to 2.5 THz was used as $\sigma_{\mathrm{THz}}(x)$. Figure 6.7a shows the THz conductivity, as well as the corresponding impedance Z in dependence of x. For the calculation of Z, the values of the vacuum impedance $Z_0 \approx 377\,\Omega$, the total layer thickness $t = t_{\mathrm{Pt}} + t_{\mathrm{CoFe}} = 3.5\,\mathrm{nm}$ as well as the refractive indices at 1 THz of the substrate $n_{\mathrm{Al_2O_3}} = 3.07$ [299], and nitrogen $n_{\mathrm{N_2}} = 1.00$ were applied. The impedance Z shows a slight, almost linear decrease of 16% from $x = 0$ to $x = 1$. The transmission T and reflection R for the 1.53 eV pump laser pulses, which were used for the THz emission spectroscopy, were also measured by Dr. Robert Schneider (see [299] for the used measurement setup). The absorption A was calculated by

$$A = 1 - R - T \; . \tag{6.1}$$

The results are shown in figure 6.7b. The absorption $A = (43.0 \pm 1.5)\%$ is approximately constant for all samples.

Using the measured THz emission amplitudes $|A_{\mathrm{THz}}^{\mathrm{exp}}(x)|$, the efficiency to inject a spin current from the Co_xFe_{1-x} into the Pt layer $J_{\mathrm{s}}^{*}(x)$ can be estimated in dependence on the Co content x according to equation 3.8 by

$$J_{\mathrm{s}}^{*}(x) \sim \frac{|A_{\mathrm{THz}}^{\mathrm{exp}}(x)|}{A(x)Z(x)} \; . \tag{6.2}$$

For the estimation, it is assumed that the spin-to-charge current conversion takes place only in the Pt layer and therefore is independent of x. Furthermore, the THz signal that is directly generated by the ultrafast demagnetization of the Co_xFe_{1-x} layer (see section 3.2) is assumed to be small compared to the THz signal generated by the inverse spin Hall effect. To prove the validity of this assumption, *sub.*/Co_xFe_{1-x}(1 nm)/Si_3N_4(5 nm) (with $x = 0, 0.3, 0.6, 1$) samples without a Pt layer were investigated. The THz emission amplitude of all these samples was measured to be less than 0.6% compared to the *sub.*/Fe(1 nm)/Pt(2.5 nm)/Si_3N_4(5 nm)

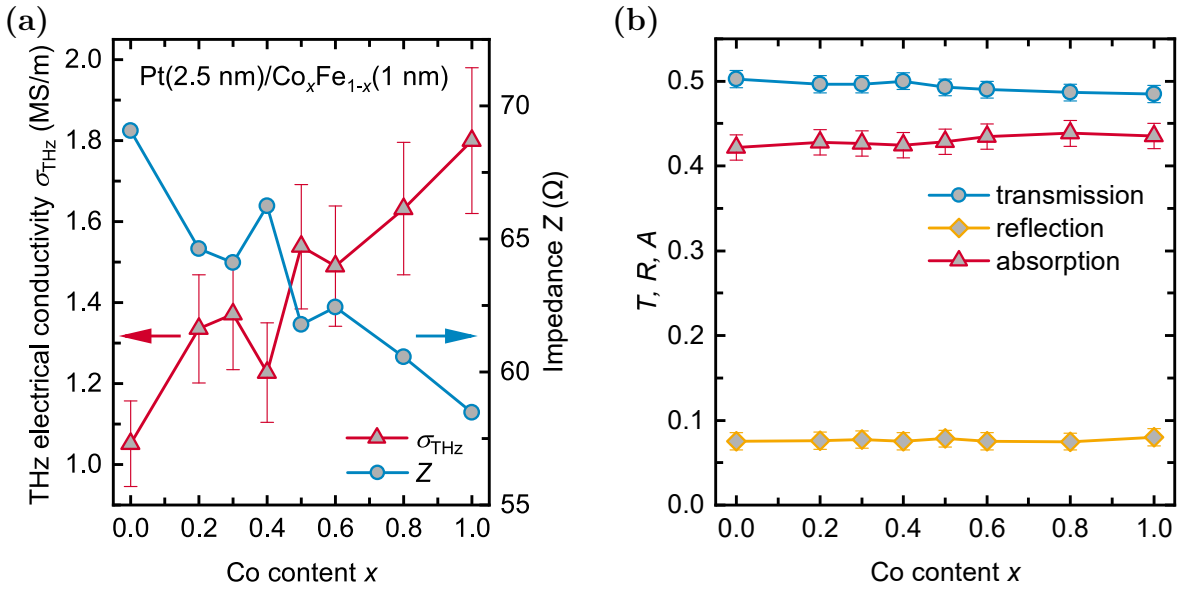

Figure 6.7: (a) shows the room-temperature electrical conductivity in the THz frequency regime σ_{THz} as well as the impedance Z of *sub.*/Pt(2.5 nm)/Co_xFe_{1-x}(1 nm)/Si_3N_4(5 nm) samples in dependence on the Co content x. The error bars mainly represent the 10% error of the film thicknesses. (b) displays the measured transmission T, reflection R, and the calculated absorption A of the 1.53 eV pump laser pulse in dependence on x.

sample. Therefore, for the Pt/Co_xFe_{1-x} bilayer series, the THz emission by ultrafast demagnetization is on the order of the measurement uncertainty. The extracted values of $J_s^*(x)$ represent a convolution of the magnitude of the spin current launched in the Co_xFe_{1-x} layer and possible interface effects, such as a reflection of the spin current or a loss of spin polarization due to scattering of electrons at the interface that also might show a dependence on x. The results are shown in figure 6.6 (blue circles). The values of $J_s^*(x)$ mainly follow the THz amplitudes, as $Z(x)$ only shows a weak dependence on x, and $A(x)$ is almost constant for all x.

In order to further investigate the dependence of the THz emission on the laser pump fluence Φ, measurements with different Φ were carried out for all samples. Figure 6.8a shows the THz RMS amplitudes of all samples measured with four different pump fluences Φ, normalized to the sample with pure Fe ($x = 0$), in dependence on x. The pump fluence dependence of the THz RMS amplitudes of four selected samples ($x = 0, 0.3, 0.6, 1$) for $0.075\,\mathrm{mJ/cm^2} \leq \Phi \leq 1.5\,\mathrm{mJ/cm^2}$ is displayed in figure 6.8b. The RMS signals of all samples show a concave dependence on the pump fluence. Though, for pump fluences $\Phi < 0.75\,\mathrm{mJ/cm^2}$, the samples with high Co content show a stronger increase in the THz amplitude with rising pump fluence compared to samples with small Co content. For $\Phi > 0.75\,\mathrm{mJ/cm^2}$ an increase in the pump fluence does not affect the relative composition dependence of the THz amplitudes (see figure 6.8a). However, further investigations that are beyond the scope of this work are necessary to clarify the origin of the observed pump fluence dependence.

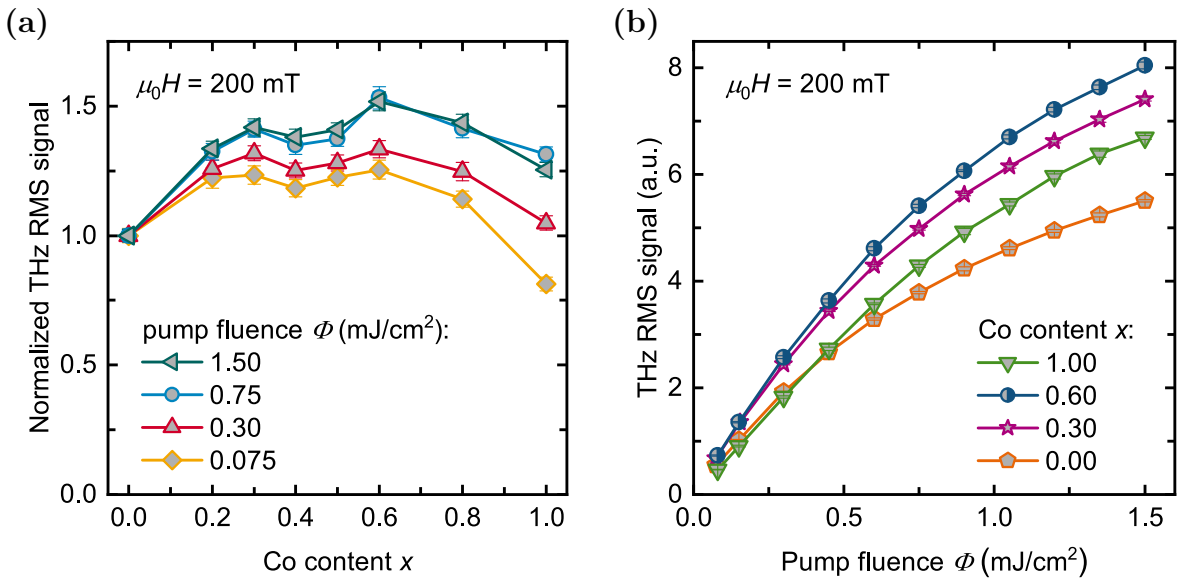

Figure 6.8: Pump fluence dependency of *sub.*/Pt(2.5 nm)/$Co_xFe_{1.x}$(1 nm)/Si_3N_4(5 nm) samples with different Co content x measured at room temperature with an applied magnetic field $\mu_0 H = 200\,\mathrm{mT}$. (a) shows the THz RMS amplitudes of all investigated samples for four selected pump fluences, normalized to the THz emission of the sample with pure Fe ($x = 0$). (b) displays the THz RMS amplitudes as a function of the pump fluence for four selected samples ($x = 0, 0.3, 0.6, 1$). The error bars represent the statistical errors of the RMS values.

6.4 Stacked bilayer emitters

Additionally to the bilayer emitters described above, a *sub.*/[Pt(2.5 nm)/$Co_{0.3}Fe_{0.7}$(1 nm)/Si_3N_4(5 nm)]$_n$ multilayer series with varying repetitions $1 \leq n \leq 5$ was prepared in the same way as described in subsection 6.1.1. The aim of this study was to boost the THz amplitude in the same way as demonstrated by Yang *et al.* [83] for *sub.*/[Pt(2 nm)/Fe(1 nm)/MgO(2 nm)]$_n$ samples (see also subsection 3.3.4). Figure 6.9 shows the THz RMS signals for this sample series in comparison with *sub.*/[Pt(2.5 nm)/$Tb_{0.1}Fe_{0.9}$(1 nm)/Si_3N_4(5 nm)]$_n$, and *sub.*/[Pt(5 nm)/$Ni_{0.81}Fe_{0.19}$(3 nm)/Si_3N_4(5 nm)]$_n$ stacked bilayer emitters. The highest THz emission amplitude is achieved for $n = 2$, for which an increase of 36% compared to the single bilayer can be observed. The slightly increased THz signal of the sample with $n = 1$ compared to the composition series shown in figure 6.6 can be explained by small variations in the sample preparation. With an increasing number of layer stacks n, the THz radiation generated in the first layers experiences more and more reflections at the interfaces to the subsequent layers. The absorption of the pump laser beam, however, becomes gradually more significant with increasing repetitions n. Therefore, in the layers close to the substrate, more electrons are excited, leading to a higher spin current density. These two effects lead to the observed maximum for $n = 2$. [83] The multilayers with $Tb_{0.1}Fe_{0.9}$ show a behavior similar to the $Co_{0.3}Fe_{0.7}$ series. For the series with 3 nm thick $Ni_{0.81}Fe_{0.19}$ and 5 nm thick Pt, the THz amplitudes gradually decrease with increasing repetition numbers n. Here,

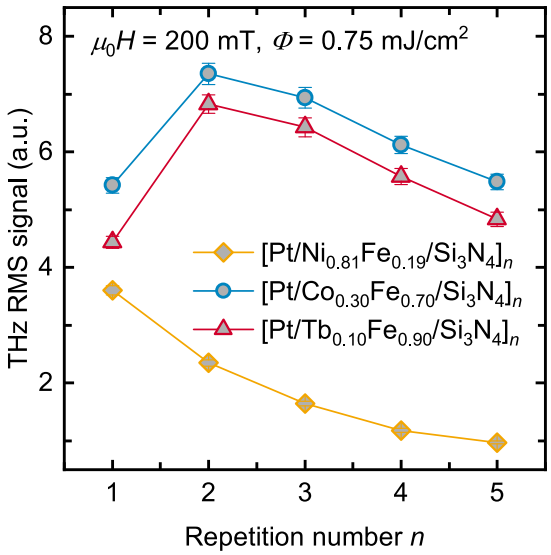

Figure 6.9: THz RMS amplitudes of *sub.*/[Pt(2.5 nm)/$Co_{0.3}Fe_{0.7}$(1 nm)/Si_3N_4(5 nm)]$_n$, *sub.*/[Pt(2.5 nm)/$Tb_{0.1}Fe_{0.9}$(1 nm)/Si_3N_4(5 nm)]$_n$, and *sub.*/[Pt(5 nm)/$Ni_{0.81}Fe_{0.19}$(3 nm)/Si_3N_4(5 nm)]$_n$ stacked bilayer spintronic THz emitters in dependence on the repetition number n. The measurements were done at room temperature with an applied magnetic field $\mu_0 H = 200$ mT and a laser pump fluence $\Phi = 0.75$ mJ/cm^2. The error bars represent the statistical errors of the RMS values and an additional statistical error of 1.8% that is caused by small variations in the mounting of the different samples.

the absorption and reflection effects described above dominate due to the increased layer thicknesses. A comparison of the THz emission of the *sub.*/[Pt/$Co_{0.3}Fe_{0.7}$/Si_3N_4]$_n$ and *sub.*/[Pt/$Tb_{0.1}Fe_{0.9}$/Si_3N_4]$_n$ systems with other spintronic THz emitters, which is displayed in section 9.4, figure 9.8, shows that the THz amplitudes of the stacked bilayers are comparable to other efficient emitter systems.

6.5 Summary

In this study, the composition-dependent THz emission characteristics of spintronic Pt/Co_xFe_{1-x} bilayers were investigated with respect to their magnetic properties. The layer thicknesses were optimized with regard to the THz emission amplitude to 1 nm for the Co_xFe_{1-x} and 2.5 nm for the Pt layer. It was shown that the THz emission only weakly depends on the Co content, indicating that laser-excited spin-polarized Fe and Co electrons contribute in a similar way to a spin current that is launched toward the Pt layer, where it becomes converted into a charge current via the inverse spin Hall effect, which leads to the emission of THz radiation. The magnetization and the THz emission amplitude show a maximum at slightly different Co contents x. For the thickness-optimized bilayers, a maximum increase in the THz emission amplitude of $\approx 46\%$ compared to the Pt/Fe sample and $\approx 19\%$ compared to the Pt/Co sample could be observed for a Co content $x = 0.6$. The magnetization showed a maximum increase of $\approx 19\%$ compared to the Pt/Fe sample and

$\approx 17\%$ compared to the Pt/Co sample for a Co content $x = 0.5$. The composition-dependent efficiency J_s^* to inject spin currents into the Pt layer has been estimated based on the THz emission amplitudes, the laser pump pulse absorption, and the THz electrical conductivity. J_s^* has been shown to mainly follow the THz amplitude. Furthermore, the dependence of the THz emission on the laser pump fluence Φ has been investigated, revealing a stronger increase in the THz emission with rising Φ for samples with high Co content for $\Phi < 0.75\,\mathrm{mJ/cm^2}$. In addition, stacked bilayer $[Pt/Co_{0.3}Fe_{0.7}/Si_3N_4]_n$ emitters were prepared to increase the THz emission amplitude further. A maximum increase in the THz emission amplitude of 36% could be achieved for $n = 2$.

CHAPTER 7

Spintronic Pt/Tb_xFe_{1-x} terahertz emitters

The focus of many previous studies on spintronic THz emitters was set on the optimization of the used layer stacks. [82, 83, 300] However, by the time this study was done, only a few works on the use of FI layers in spintronic THz emitter systems had been published. [297, 326] Furthermore, these works only investigated exemplary samples and did not present systematic studies on ferrimagnets with different magnetic properties. The aim of the study presented in this chapter was to fill this gap and investigate bilayers of amorphous FI Tb_xFe_{1-x} films with varying Tb content $0 \leq x \leq 1$ combined with a nonmagnetic Pt layer. As described in detail in subsection 2.6.3, the Tb_xFe_{1-x} films offer a great variety of magnetic properties depending on the film composition and thickness. Thus, the material is an ideal candidate for investigating the influence of the sample magnetic properties on the THz emission characteristics. Also, for this study, Pt has been chosen as NM layer due to its large spin Hall angle ($+1.2\% \leq \theta_{\mathrm{sh}} \leq +11\%$ [271, 294, 295]) and its suitability for the use in spintronic THz emitter systems [82, 300]. THz emission spectroscopy as well as magnetic measurements with different applied magnetic fields and temperatures have been performed to characterize the samples. It could be shown that mainly the spin-polarized Fe 3d electrons contribute to the emitted THz signal and that the THz amplitude mainly follows the in-plane magnetization of the Fe magnetic sublattice. A phenomenological model has been developed for a qualitative description of the THz emission amplitude in dependence on the Tb content x.

The results were achieved in collaboration with Dr. Robert Schneider, Dr. Steffen Michaelis de Vasconcellos, Dr. Richard Heming, and Prof. Rudolf Bratschitsch from the University of Münster. The room-temperature results are predominantly published in [384].

7.1 Sample preparation and structural characterization

Two series of *sub.*/Pt(5 nm)/Tb_xFe_{1-x}(20 nm)/*cap.* samples with Tb content $0 \leq x \leq 1$ were prepared by magnetron sputtering at room temperature (see chapter 4 for details). For the first series, Co layers with a thickness of 2 nm that are expected to oxidize in air to form

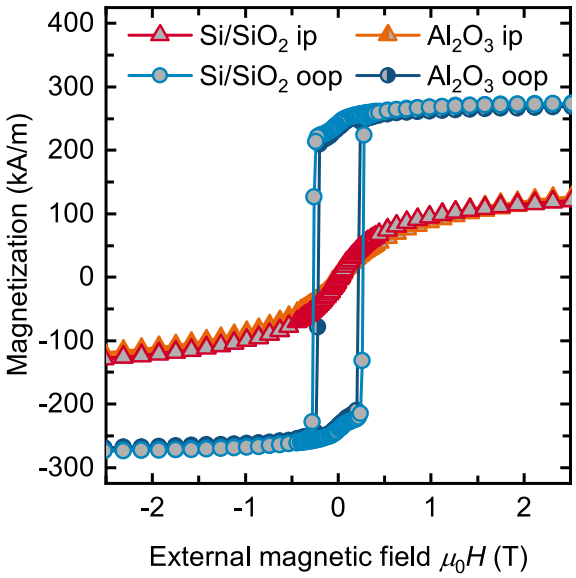

Figure 7.1: Comparison of room-temperature in-plane and out-of-plane SQUID-VSM $M(H)$ loops of *sub.*/Pt(5 nm)/$Tb_{0.2}Fe_{0.8}$(20 nm)/Si_3N_4(5 nm) samples with either 500 µm thick Al_2O_3(0001) substrates or 525 µm thick Si(100) substrates with a 100 nm thick thermally oxidized SiO_2 layer.

CoO [392] served as capping layers (*cap.*). As the thin Co layer showed an influence on the magnetic and THz emitting properties of the samples, a second series with Si_3N_4 capping layers of 5 nm thickness was prepared and investigated later on. In SQUID-VSM measurements that were performed after more than two years, the samples with Si_3N_4 capping layer still showed similar results as the measurements that were done directly after the deposition. However, the samples with Co capping showed a degradation of the magnetic properties. Here, the net magnetization values of the films were found to be more Fe-dominated. This can be explained by a higher level of oxidation of Tb in the TbFe alloys compared to the Fe. Therefore, for the Co series, only measurements that were performed within a few months after the deposition were used for this work. DC sputtering was used for the deposition of the Pt and Co layers. The Tb_xFe_{1-x} alloys were deposited by co-sputtering from elemental targets with either DC or RF sources, depending on the composition of the layers. For the Si_3N_4 layers, RF sputtering from a stoichiometric compound target was applied. The samples were prepared on 500 µm thick Al_2O_3(0001) substrates, polished on both sides for the THz spectroscopy experiments, as well as on 525 µm thick p-doped Si(100) substrates with a 100 nm thick thermally oxidized SiO_2 layer on which all other measurements were performed. Exemplary SQUID-VSM measurements of *sub.*/Pt(5 nm)/$Tb_{0.2}Fe_{0.8}$(20 nm)/Si_3N_4(5 nm) samples deposited on the different substrates showed only a minor influence of the substrate on the magnetic properties of the system (see figure 7.1). This can be attributed to the Pt seed layers that protect the Tb_xFe_{1-x} layers from reacting with the substrate. The Pt layers show a similar polycrystalline growth on both substrates (see appendix A.2, figure A.1 for transmission electron microscope images of *sub.*/Pt(3 nm)/Fe(3 nm)/Si_3N_4(5 nm) samples grown on Al_2O_3

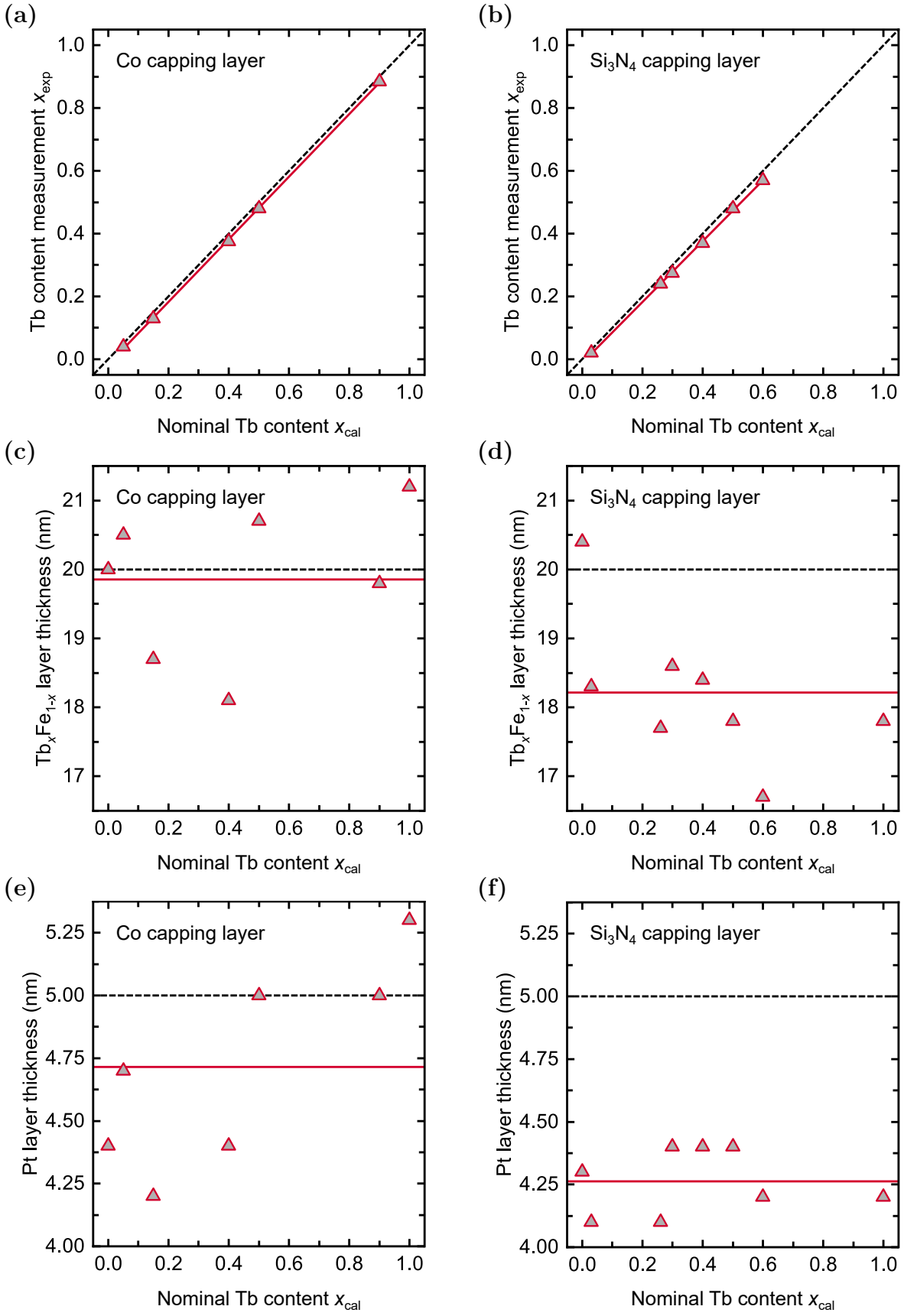

Figure 7.2: Extracted Tb contents and layer thicknesses from RBS measurements of the *sub.*/ Pt(5 nm)/Tb_xFe_{1-x} series with (a, c, d) Co(2 nm) and (b, d, f) Si_3N_4(5 nm) capping layers. The dashed black lines represent the nominal values. The red lines are (a, b) linear fits and (c–f) average values.

and Si/SiO_2 substrates). It should be mentioned here that the samples included in the two series were not sputtered in one run but deposited on different days between September 2017 and January 2018 and, therefore, with slightly different sputter conditions (see appendix A.1 for a list of sputtered samples). Therefore, for each of the sputter days, at least for one of the samples, RBS measurements were carried out to check the stoichiometry of the alloys and the layer thicknesses. Figure 7.2 displays the RBS results for the two sample series with respect to the nominal Tb content x_{cal}. For the film compositions shown in the subfigures (a) and (b), linear fits were applied to the derived values (red curve) to gain better visibility of general trends. Compared to the nominal values (dashed black curve), the measurements systematically reveal slightly smaller Tb contents x_{exp} of up to -0.025 for the series with Co capping layer and -0.03 for the series with Si_3N_4 capping layer. For the Pt and Tb_xFe_{1-x} film thicknesses displayed in the subfigures (c) to (f), the average values were calculated (red lines). For all layers, the average film thicknesses are smaller than the nominal values (dashed black lines). However, for the series with Si_3N_4 capping layer, the thicknesses show a more systematic general trend toward smaller film thicknesses compared to the series with Co capping layer. The deviations of the Pt layer thicknesses from the nominal values are up to 18% for the series with Co capping and up to 16% for the series with Si_3N_4 capping. For the Tb_xFe_{1-x} layer thicknesses, the deviations from the nominal values are up to 9.5% (Co series) and 16.5% (Si_3N_4 series).

As the deviations from the nominal values are small and rather unsystematic (especially for the layer thicknesses of the Co series), and RBS measurements were performed only on several samples, the nominal values for the thicknesses and compositions are used for the following discussions.

7.2 Magnetic properties

For both series, SQUID-VSM $M(H)$ and $M(T)$ measurements were carried out to determine the magnetic properties of the Tb_xFe_{1-x} films in dependence on the Tb content x. The $M(H)$ loops of the series with Co and Si_3N_4 capping layer are displayed in appendix A.3, figures A.7 and A.8, respectively.

Figure 7.3 shows the estimations for the effective magnetic anisotropy at room temperature that were derived from the $M(H)$ loops measured in in-plane and out-of-plane direction by the method described in subsection 5.4.3. The effective magnetic anisotropy K_{eff} is displayed in (a), whereas (b) shows the values of K_{eff} divided by the saturation magnetization M_{S} of the samples. Both series show comparable results. For small Tb contents $x \leq 0.15$, the magnetic shape anisotropy K_{shape} dominates K_{eff} due to the high M_{S} of the samples, leading to an in-plane magnetic easy axis (EA). For $0.2 \leq x \leq 0.5$, the lower M_{S} leads to a decrease in K_{shape}, and the short-range chemical order in the films leads to an out-of-plane magnetic

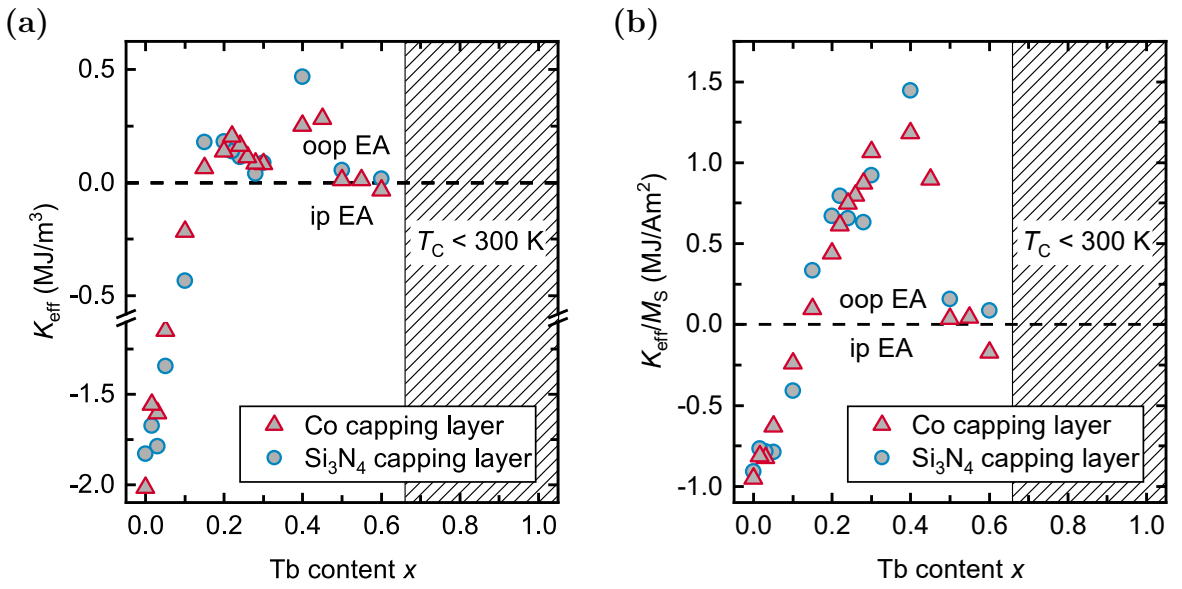

Figure 7.3: Effective magnetic anisotropy K_{eff} of *sub.*/Pt(5 nm)/$\mathrm{Tb}_x\mathrm{Fe}_{1-x}$(20 nm)/*cap.* samples with Co(2 nm) (blue circles) and $\mathrm{Si_3N_4}$(5 nm) (red triangles) capping layers in dependence on the Tb content x, derived from room-temperature SQUID-VSM $M(H)$ loops. (a) shows K_{eff}, whereas (b) displays K_{eff} divided by the respective saturation magnetization M_{S}. The shaded area marks the composition region for which the $\mathrm{Tb}_x\mathrm{Fe}_{1-x}$ layers are clearly paramagnetic at room temperature, and therefore no K_{eff} values could be determined. For the sample with $x = 0.26$ of the $\mathrm{Si_3N_4}$ capping layer series, the coercivity in out-of-plane direction is above 7 T. Thus, no K_{eff} value could be determined for this sample.

easy axis (see subsection 2.6.3 for more details). For higher Tb contents $x > 0.5$, the samples gradually become paramagnetic, and therefore the anisotropy vanishes. In the K_{eff} values (a), a local minimum at about $0.26 \leq x \leq 0.3$ can be observed, close to the room-temperature compensation composition. This is an expected behavior due to the small M_{S} values of these samples. However, despite the low K_{eff} values, the out-of-plane alignment is still strongly preferred, as can be seen in the K_{eff} values divided by M_{S}, shown in (b). $K_{\mathrm{eff}}/M_{\mathrm{S}}$ increases up to the maximum at $x = 0.4$ with rising Tb content x. It should be noted here again that the errors for the estimation of K_{eff} (see subsection 5.4.3 for details) are rather large for some of the samples. Especially for samples exhibiting a compensation point close to room temperature and for samples with high Tb content, which are close to the paramagnetic state at room temperature, significant errors of $K_{\mathrm{eff}}/M_{\mathrm{S}}$ are expected.

Figure 7.4 shows the $M(T)$ curves for samples with different Tb content x. For the results shown in (a) and (b), the measurements were performed in out-of-plane direction, whereas for the curves shown in (c) and (d), the external field was applied in in-plane direction, following the respective magnetic easy axis. For all of the shown measurements, the samples were first saturated at room temperature at $\mu_0 H = 7$ T and then cooled down to 40 K with the field still applied. The measurements were subsequently carried out in a temperature sweep mode (10 K/min) with small applied guiding fields from 40 K to 340 K or 400 K for the out-of-plane

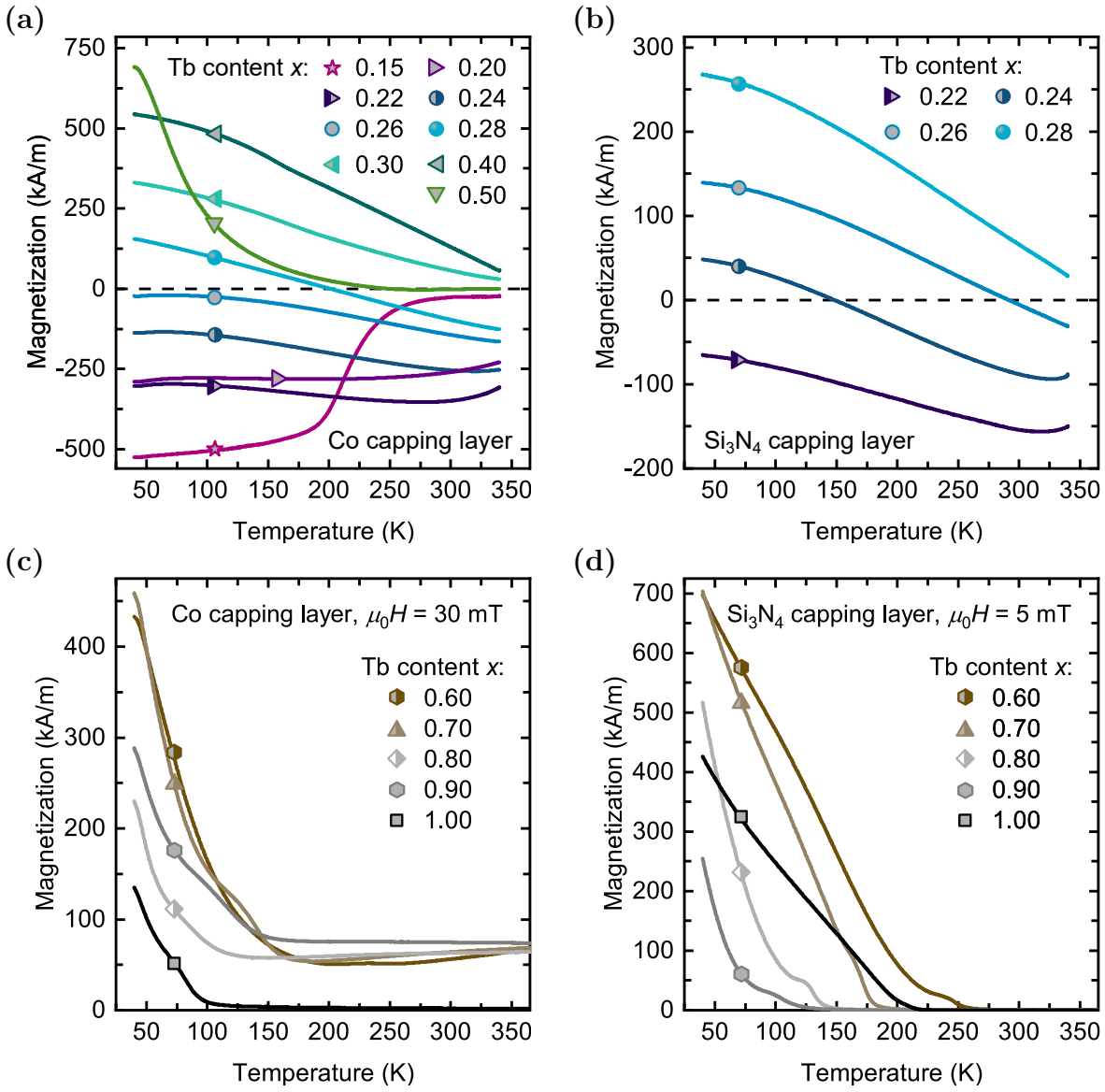

Figure 7.4: $M(T)$ curves of *sub.*/Pt(5 nm)/Tb_xFe_{1-x}(20 nm)/*cap.* samples with (a) Co(2 nm) and (b) Si_3N_4(5 nm) capping layers measured in out-of-plane direction with small guiding fields $\mu_0 H < 5$ mT. The samples were first saturated at room temperature with an external magnetic field of 7 T. Afterward, the samples were cooled down to 40 K (or 5 K for the sample with $x = 0$). The applied magnetic field was then reduced to the guiding field value, and the magnetization was recorded while heating the sample up to 340 K in a temperature sweep mode (10 K/min). Positive magnetization values denote net magnetizations that are dominated by the Tb magnetic sublattice, whereas negative values represent Fe-dominated net magnetizations. The dashed lines mark the compensated magnetic states. (c) and (d) display in-plane $M(T)$ curves that were measured in a similar way as the out-of-plane curves up to 400 K, with guiding fields of $\mu_0 H = 30$ mT and $\mu_0 H = 5$ mT for the Co and Si_3N_4 capping layer series, respectively.

or in-plane direction, respectively. For the out-of-plane measurements, no guiding fields were applied, and therefore an effective field $\mu_0 H \approx -4.5$ mT was present caused by trapped fluxes in the superconducting magnet of the MPMS3 (see section 5.4.2). For the measurements in

in-plane direction, guiding fields of 30 mT and 5 mT were applied for the series with Co and Si_3N_4 capping, respectively. Positive magnetization values represent Tb-dominated net magnetizations, whereas negative values represent Fe-dominated net magnetizations. The out-of-plane measurements in figures 7.4a and 7.4b show a compensation point for the sample with $x = 0.28$ at $T_{comp} \approx 201\,K$ of the Co series and for the samples with $x = 0.24$ at $T_{comp} \approx 148\,K$ and $x = 0.26$ at $T_{comp} \approx 292\,K$ of the Si_3N_4 series. The Tb contents x for which a magnetic compensation point can be observed are slightly higher (about 0.02 for the series with Co capping and 0.04 for the series with Si_3N_4 capping) compared to the values reported in [215] and [188] for 20 nm and 19 nm thick films, respectively. The deviation from the literature values could be explained by the used nominal composition values that were slightly larger than the values measured by RBS. However, also different film growth parameters or small variations in the film thicknesses [188] might have led to deviations in the compensation point. The higher x values for which a compensation point can be observed in the series with Co capping compared to the series with Si_3N_4 capping can be explained by a remaining magnetic moment of the Co capping layers that have not been fully oxidized to CoO by the time the measurements were performed (the measurements were performed within a few weeks after the sample preparation). This agrees well with a study by Gan *et al.* [392] on the oxidation of thin Co layers in air, in which they observed that after one month, approximately 1.2 nm of a Co film were oxidized. The Co magnetic moments couple parallel to the Fe moments and therefore shift the composition region where the moment is Tb-dominated to higher x values. For the sample with $x = 0.15$ in figure 7.4a, a change of the magnetic easy axis from out-of-plane at low temperatures to in-plane at higher temperatures can be observed. The sample with $x = 0.5$ becomes gradually paramagnetic at increasing temperatures, and therefore the coercivity becomes small. This is reflected in the reduced magnetic moment in the $M(T)$ curve. The in-plane $M(T)$ curves of the samples with $x \geq 0.6$ that are displayed in figures 7.4c and 7.4d were performed to get an estimation for the Curie temperature T_C of the samples. However, only for the series with Si_3N_4 capping, displayed in figure 7.4d, a clear dependence of T_C on x can be observed. Here, the pure Tb layer shows a T_C of about 215 K. For $x = 0.9$, the smallest T_C of about 130 K can be found that successively increases with decreasing x. For the samples with Co capping shown in 7.4c, a remaining magnetization of about 70 kA/m that is almost similar for all x values can be observed at high temperatures for all samples except the pure Tb layer. This magnetization can be attributed to the remaining magnetic moment of the Co capping and is also observable in the room-temperature $M(H)$ loops in appendix A.3, figure A.7. The pure Tb sample shows a T_C value that is comparable to the sample with $x = 0.9$ of the series with Si_3N_4 capping. This might be an indication of a strong intermixing between the Co capping layer and the Tb layer.

7.3 Room-temperature electrical and optical properties

As shown in subsection 3.3.3, equation 3.9, the THz emission efficiency $C(\omega)$ of a spintronic THz emitter is dependent on the absorption of the used pump laser A, the thickness of the spintronic layer stack t, and on the electrical conductivity in the THz frequency regime $\sigma_{\mathrm{THz}}(\omega)$. Thus, in order to investigate the THz emission efficiency of samples with different Tb content x, the necessary parameters have been determined.

The transmission T and reflection R of the 1.53 eV laser pump pulses, which were later on used for the THz emission spectroscopy, were measured by Dr. Robert Schneider at the University of Münster (see [299] for the used measurement setup), and the absorption A was calculated by equation 6.1. The results for the two series are shown in figure 7.5. Both series show a similar behavior. The reflection decreases for rising Tb contents x, whereas the transmission increases with rising x. The absorption is constant within the errors for all samples and takes a value of 0.31 ± 0.03.

By the time this study was performed, no setup to determine the electrical conductivities of the samples in the THz regime was available. Therefore, the DC conductivities $\sigma_{\mathrm{DC}}(x) = \int_0^t \sigma_{\mathrm{DC}}(x,y)\mathrm{d}y$ were determined with the four-point resistivity measurement setup described in section 5.5 and used as an approximation for the conductivities in the low THz frequency regime $\sigma_{\mathrm{THz}}(x,\omega) = \int_0^t \sigma_{\mathrm{THz}}(x,\omega,y)\mathrm{d}y$. The results for the samples with varying x are shown in figure 7.6a. For small x, the conductivities show a strong decrease with increasing x, whereas the curve flattens for higher x. The assumption that the DC electrical conductivities

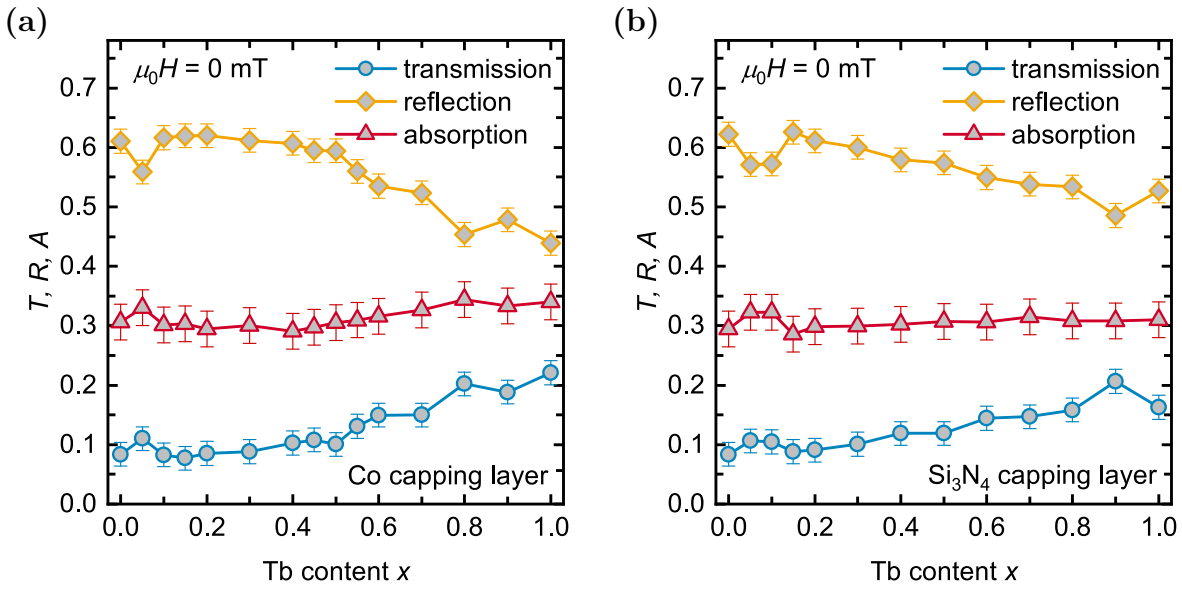

Figure 7.5: Transmission T, absorption A and reflection R of the 1.53 eV pump laser in *sub.*/ Pt(5 nm)/Tb_xFe_{1-x}(20 nm)/*cap.* samples measured at room temperature with respect to the Tb content x for the series with (a) Co(2 nm) and (b) Si_3N_4(5 nm) capping layers.

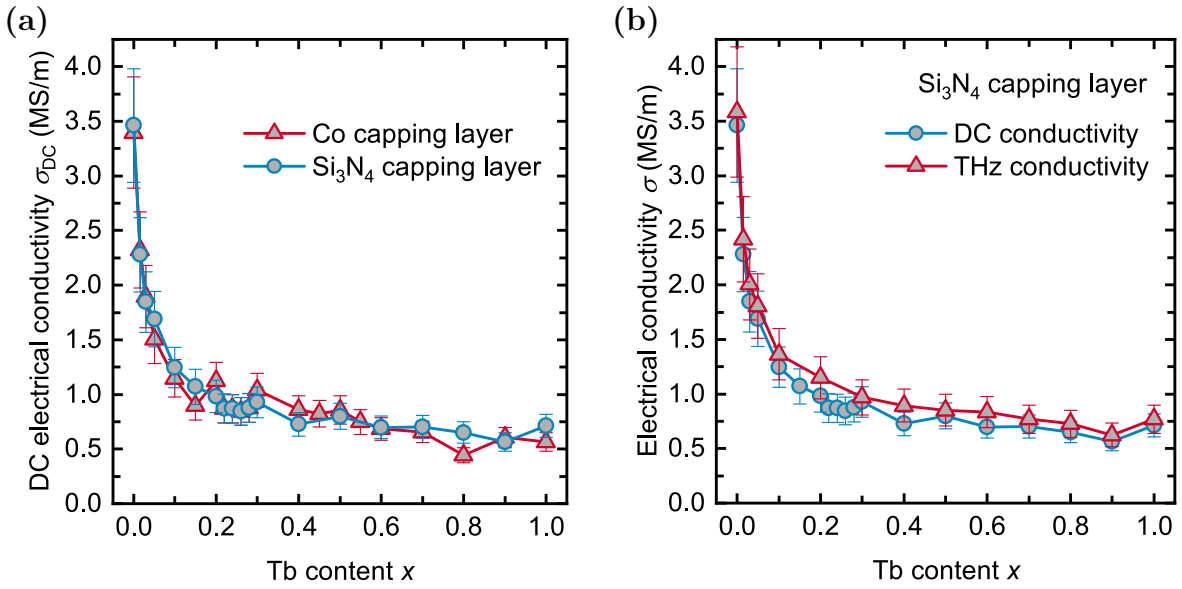

Figure 7.6: (a) shows the DC electrical conductivities σ_{DC} of *sub.*/Pt(5 nm)/Tb_xFe_{1-x}(20 nm)/*cap.* samples with Co(2 nm) and Si_3N_4(5 nm) as capping layer measured at room temperature with respect to Tb content x. The error bars are calculated from the maximum uncertainty of the film thicknesses that is assumed by RBS measurements to be ±15%. (b) displays a comparison of the DC conductivities with results from time-resolved THz emission spectroscopy measurements for the series with Si_3N_4(5 nm) capping layer. Also, for the THz conductivities, the error bars are mainly derived from the assumed uncertainty of the film thicknesses.

are comparable to the complex frequency-dependent electrical conductivities in the low THz regime was later on proved by time-resolved THz transmission spectroscopy experiments that were performed by Dr. Robert Schneider (see [299] for details on the measurement setup). In the frequency range from 0.5 to 2.5 THz, the samples show constant real and imaginary (for $x > 0$) conductivities. As the imaginary parts are negligibly small compared to the real parts, the average values of the real parts for the frequency range from 0.78 to 2.5 THz were used for a comparison with the DC conductivities that is displayed in figure 7.6b. The results show that the electrical conductivities in the low THz regime agree well with the DC values.

As the absorption of the laser pump pulses as well as the thickness of the spintronic layer stack $t = t_{Pt} + t_{TbFe}$ is approximately constant for all samples, the THz emission efficiency $C(x, \omega)$ given in equation 3.9 is proportional to the sample impedance $Z(x, \omega)$, which is approximately independent on the wavelength:

$$C(x,\omega) \sim Z(x,\omega) \approx Z(x) \approx \frac{1}{(n_1 + n_2)/Z_0 + \sigma_{DC}(x) \cdot t} \,, \tag{7.1}$$

with the vacuum impedance $Z_0 = 377\,\Omega$ and the refraction indices $n_1 \approx 3.07$ of the Al_2O_3 substrate at 1 THz [299] and $n_2 \approx 1.00$ of nitrogen. The impedance Z is displayed in figure 7.7 in dependence on x. For small Tb contents, the impedance, and therefore, the THz emission efficiency strongly increases with rising x.

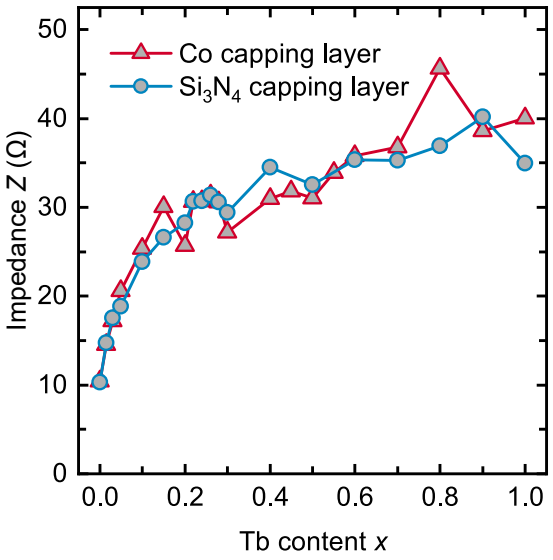

Figure 7.7: Room-temperature impedance Z of *sub.*/Pt(5 nm)/Tb_xFe_{1-x}(20 nm)/*cap.* samples with Co(2 nm) and Si_3N_4(5 nm) capping layers *cap.* in dependence on the Tb content x.

7.4 Room-temperature terahertz emission results

For both sample series, THz emission spectroscopy measurements with varying external magnetic fields were performed by Dr. Robert Schneider using the measurement setup described in section 5.6. The used measurement geometry is displayed in figure 7.8. As described in detail in section 3.3, the excitation of electrons in the magnetic layer above the Fermi level leads to the formation of a superdiffusive spin current $\boldsymbol{J}_\mathrm{s}$ from the magnetic Tb_xFe_{1-x} layer toward the non-magnetic Pt layer, in which $\boldsymbol{J}_\mathrm{s}$ is converted by the inverse spin Hall effect into a transverse charge current $\boldsymbol{J}_\mathrm{c}$, which leads to the emission of electromagnetic radiation in the THz frequency regime. For the investigated FI Pt/Tb_xFe_{1-x} system, spin-polarized Tb and Fe electrons as well as Pt electrons that are spin-polarized due to the magnetic proximity effect could theoretically contribute to the spin currents $\boldsymbol{J}_\mathrm{s}$ and therefore to the emission of THz radiation. However, the spin-polarized 4f electrons of the Tb that give rise to the magnetic moment of the Tb magnetic sublattice are localized close to the atomic nucleus. These electrons are energetically about 2.23 eV below the Fermi level [393] and therefore cannot be efficiently excited by the 1.53 eV pump laser. In contrast to that, the spin-polarized 3d electrons of Fe are energetically located close to the Fermi level (see section 2.5, figure 2.7a) and therefore are expected to give a strong contribution to $\boldsymbol{J}_\mathrm{s}$. Nevertheless, due to the hybridization of the Fe 3d with the Tb 5d electrons in Tb_xFe_{1-x} alloys (see subsection 2.6.1), also a small contribution of the Tb 5d electrons to the signal is expected. The influence of excited Pt electrons that are spin-polarized due to the magnetic proximity effect on $\boldsymbol{J}_\mathrm{s}$ is expected to be small compared to the contribution of the Fe 3d electrons and therefore is neglected in the following discussion. Furthermore, the influence of emitted THz radiation that is caused directly by the ultrafast demagnetization of the magnetic films is assumed to

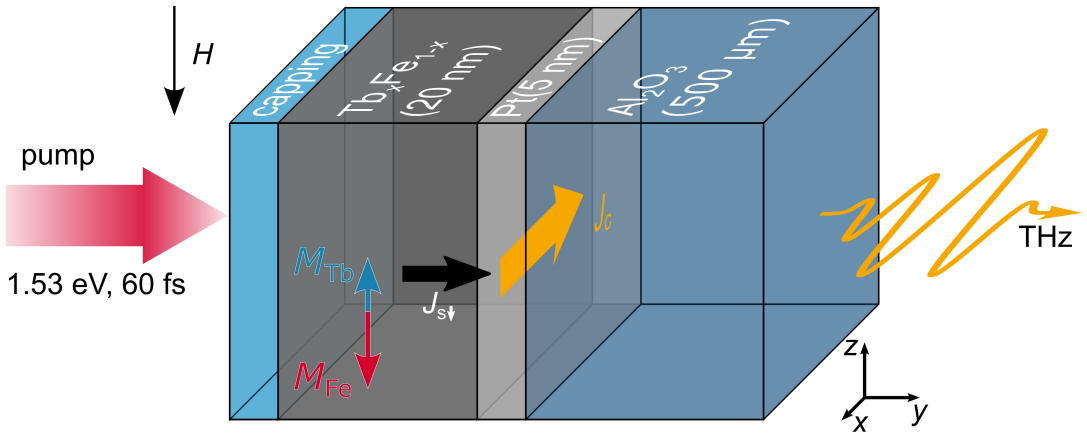

Figure 7.8: Illustration of the excitation geometry that was used for the THz emission spectroscopy measurements performed on the *sub.*/Pt(5 nm)/Tb_xFe_{1-x}(20 nm)/*cap.* samples with Co(2 nm) and Si_3N_4(5 nm) capping layers.

be negligibly small. For the Pt/Gd_xFe_{1-x} samples discussed in chapter 8, this contribution has been investigated in detail. In that study, only for the pure Pt/Fe sample a significant contribution of $\approx 14\%$ to the emitted signal caused directly by the ultrafast demagnetization has been found.

7.4.1 Composition dependence of the terahertz electro-optic signal

Figure 7.9 shows the normalized THz electro-optic signals of selected samples with different Tb content x for the two series, measured with a pump fluence $\Phi = 0.75\,\mathrm{mJ/cm^2}$ and an applied magnetic field $\mu_0 H = 200\,\mathrm{mT}$. For low Tb contents $x \leq 0.3$, a similar signal shape can be observed for the different samples. The sample with $x = 0.4$ of the Co series shows a more dispersive signal shape. An inversion of the signals compared to the Fe/Pt bilayer can be observed for $0.45 \leq x \leq 0.55$ (Co series) and $0.4 \leq x \leq 0.6$ (Si_3N_4 series). For the Co series, the signal shape of the samples with high Tb content $x \geq 0.6$ is again similar to the samples with low Tb content ($x \leq 0.3$). For the Si_3N_4 series, the samples with $x \geq 0.7$ are completely paramagnetic at room temperature. Therefore, the measured signals are small. However, also for these samples, the measured signals are again inverted compared to the samples with $0.4 \leq x \leq 0.6$.

The inversions of the signals can be explained by a significantly higher contribution of spin-polarized Fe electrons to $\boldsymbol{J}_\mathrm{s}$ compared to the Tb electrons. As described in subsection 3.3.4, the charge current in the Pt layer that causes the THz signal is described by $\boldsymbol{J}_\mathrm{c} \sim \theta_\mathrm{sh} \boldsymbol{J}_\mathrm{s} \times \boldsymbol{M}/|\boldsymbol{M}|$. However, for the systems with the FI Tb_xFe_{1-x} layers, $\boldsymbol{M}/|\boldsymbol{M}|$ describes the magnetization direction of the Fe magnetic sublattice, as the Fe electrons are expected to give the dominant contribution to $\boldsymbol{J}_\mathrm{s}$. A change from a net magnetization that is dominated by the Fe magnetic sublattice for samples with low Tb content to a magnetic state that

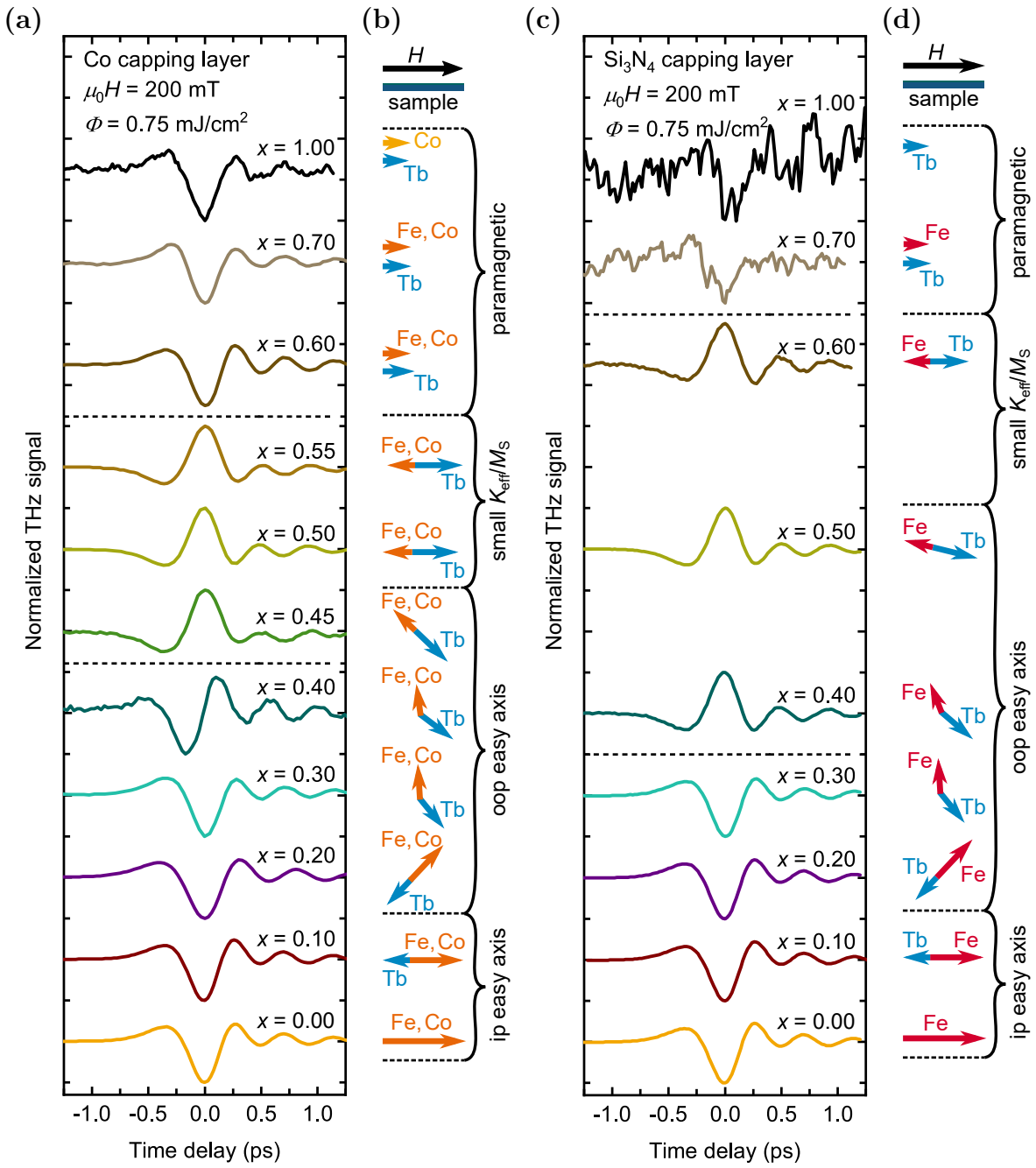

Figure 7.9: THz electro-optic signals of *sub.*/Pt(5 nm)/Tb_xFe_{1-x}(20 nm)/*cap.* samples with (a) Co(2 nm) and (b) Si_3N_4(5 nm) capping layers with respect to the Tb content x. The signals were normalized to the maximum of their absolute values to allow for comparison between the signal shapes. The signals were measured at room temperature with a pump fluence $\Phi = 0.75\,\mathrm{mJ/cm^2}$ and an applied magnetic field $\mu_0 H = 200\,\mathrm{mT}$. The dashed black lines mark the composition region for which an inversion of the signals compared to the Pt/Fe bilayer can be observed.

is dominated by the Tb magnetic sublattice for higher Tb contents, therefore, leads to an inversion of $\boldsymbol{M}/|\boldsymbol{M}|$ when saturated in an applied magnetic field and consequently to the observed inverted THz signal. A similar behavior was also found for the FI Pt/Gd_xFe_{1-x}

emitter systems that are discussed in chapter 8 [394] as well as for Pt/Gd_xCo_{1-x} [327] and $Pt/Gd_{0.25}(Fe_{0.875}Co_{0.125})_{0.75}$ [326] emitters. For the samples with high Tb content x, the Tb_xFe_{1-x} are either paramagnetic with a FM contribution of the Co capping layer or fully paramagnetic for the series with Si_3N_4 capping. Therefore, the Tb, Fe, and Co magnetic moments are aligned along the applied field. Consequently, the THz signal is inverted again.

The first inversion of the signals (for increasing Tb content) would be expected to correlate with the magnetic compensation point discussed in section 7.2. However, it can be observed at slightly higher Tb contents. To understand this behavior and especially to clarify whether the non-inverted THz signals of samples with Tb content slightly above the magnetic compensation composition are really caused by the Fe 3d electrons or by the Tb 5d electrons, energy-resolved EUV T-MOKE measurements [362] were carried out by Henrike Probst in the group of Prof. Stefan Mathias at the University of Göttingen. The sample with $x = 0.1$, which has a clearly Fe-dominated net magnetization, and the sample with $x = 0.3$, which shows a Tb-dominated net magnetization but a still non-inverted THz signal, of the Si_3N_4 capping layer series have been chosen for these measurements. Figures 7.10a and 7.10b show the magnetic signals with respect to a Fe reference sample. The asymmetries are calculated as the difference between the spectra measured for the applied magnetic field in positive and negative direction displayed in figures 7.10c–7.10e. Unfortunately, the high harmonic closest to the aluminum L_3 edge at 72.7 eV that is used for the energy calibration of the used EUV T-MOKE setup [362] is not observable for the Tb_xFe_{1-x} samples due to the low reflectivity of the samples (see figures 7.10d and 7.10e). Therefore, the measured spectra might be shifted by a multiple of the energy difference between two harmonics. The shown spectra are plotted for the two most probable energy calibrations (red and blue curves). For the Fe reference sample, the highest harmonic below the aluminum L_3 edge at 72.7 eV is observable (see figure 7.10c) and used for an exact energy calibration. In the region of the Fe $M_{2,3}$ absorption edge at approximately 52.6 eV–55.0 eV [358–362], a peak in the magnetic signal can be observed for all samples. The observed peaks of all samples, including the Fe reference sample, are at slightly lower energies compared to the literature values. Despite the varying shapes observed for the different samples, the peaks most probably reflect the Fe magnetic signal. As the peak is clearly inverted for the samples with $x = 0.1$ and $x = 0.3$, the magnetization direction of the Fe magnetic sublattice is also inverted for the two samples, and accordingly, the Fe magnetic moments of the sample with $x = 0.3$ are aligned antiparallel to the applied magnetic field. The Tb O_2 absorption edge at an energy of 28.7 eV [363] did not give rise to a measurable magnetic asymmetry signal (not shown).

The EUV T-MOKE measurements give a strong indication that Fe electrons cannot be the source of the observed non-inverted THz signal of the sample with $x = 0.3$. Thus, the THz signals of the samples with $0.28 < x \leq 0.4$ of the Co capping series and $0.26 \leq x < 0.4$ of the Si_3N_4 series might be caused by spin-polarized Tb 5d electrons. As shown in figure 7.3, the

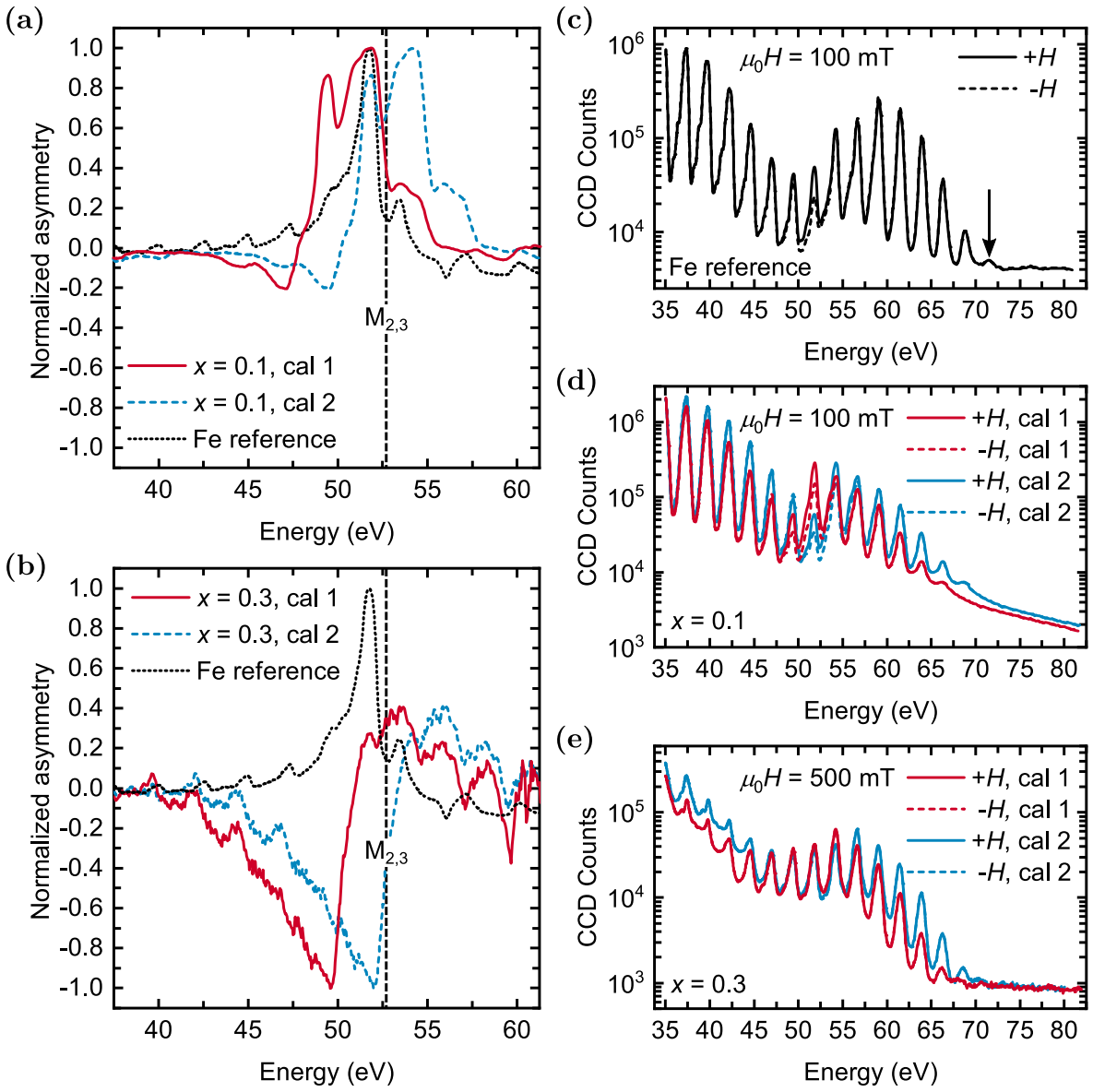

Figure 7.10: Energy-resolved room-temperature EUV T-MOKE results of *sub.*/Pt(5 nm)/Tb_xFe_{1-x}(20 nm)/Si_3N_4(5 nm) samples with $x = 0.1$ and $x = 0.3$. (a) and (b) display the difference in the spectra measured for in-plane magnetic fields applied in positive and negative direction in comparison to the results of a Fe reference sample for the samples with $x = 0.1$ and $x = 0.3$, respectively. The signals are normalized to their respective maximum. The dashed black lines in (a) and (b) mark the value of the Fe $M_{2,3}$ binding energy presented in [358]. (c)–(e) show the spectra of the Fe reference sample, and the samples with $x = 0.1$ and $x = 0.3$ measured with positive ($+H$, solid lines) and negative ($-H$, dashed lines) applied magnetic fields. The arrow in (c) marks the highest visible harmonic that is used for the energy calibration. The red (cal 1) and blue (cal 2) curves display the two most probable energy calibrations for the measurements. An external magnetic field $\mu_0 H = 100\,\mathrm{mT}$ was applied for measurements of the Fe reference and the sample with $x = 0.1$, whereas $\mu_0 H = 500\,\mathrm{mT}$ was used for the sample with $x = 0.3$.

samples with $0.2 \leq x < 0.5$ exhibit an out-of-plane magnetic easy axis with high $K_{\mathrm{eff}}/M_{\mathrm{S}}$. Therefore, the applied in-plane magnetic field $\mu_0 H = 200\,\mathrm{mT}$ is not sufficient to reach a sat-

urated magnetic state. The strong magnetic anisotropy could, due to the large distribution of the Tb magnetic moments, cause a stronger alignment of the Tb magnetic moments along the applied in-plane magnetic field and therefore lead to a canted state between the Fe and Tb magnetic moments. As a result, the few spin-polarized Tb 5d electrons might contribute stronger to $\boldsymbol{J}_\mathrm{s}$ in the discussed composition region than the spin-polarized Fe 3d electrons. Schematics showing the average magnetization alignments of the Fe and Tb magnetic sublattices in this scenario are displayed in figures 7.9b and 7.9d for the Co and Si_3N_4 capping layer series, respectively. However, further element-specific magnetization measurements, especially of the Tb magnetic moments, which are beyond the scope of this work, would be necessary to confirm or falsify this explanation.

7.4.2 Dependence of the terahertz amplitude on the applied magnetic field

Besides the signal shapes, also the dependence of the emitted THz radiation on the applied magnetic field has been investigated. Figures 7.11 and 7.12 show the THz peak-to-peak amplitude as well as the in-plane magnetization in dependence on the applied magnetic field for the Co series. The results for the Si_3N_4 series are shown in figures 7.13 and 7.14. The THz measurements were performed from the demagnetized state for rising external magnetic fields. The $M(H)$ values were taken from the full $M(H)$ loops displayed in appendix A.3, figures A.7 and A.8, except for the samples with $x = 0.55$ and $x = 0.6$ of the Co series, for which the $M(H)$ measurements were performed from the demagnetized state at $\mu_0 H = 0\,\mathrm{mT}$ with increasing fields up to $\mu_0 H = 540\,\mathrm{mT}$. For the samples with small Tb content $x \leq 0.15$, an initial steep rise of the THz amplitude as well as of the magnetization with increasing external magnetic field followed by a saturation can be observed. The stronger applied magnetic fields lead to a higher number of spin-polarized electrons. Also, the number of excitable spin-polarized (mainly Fe) electrons close to the Fermi energy E_F is increased. Consequently, a higher spin current J_S is launched, leading to an increase in the THz amplitude. Therefore, the THz amplitude closely follows the in-plane magnetization of the sample. For sufficiently high applied fields, the maximum spin polarization is reached, and therefore the magnetization and the THz amplitude saturate. The saturation is shifted to higher magnetic fields for increasing Tb content as the perpendicular magnetic anisotropy of the samples gradually increases (see figure 7.3).

For samples with $x > 0.15$, deviations from the clear functional dependence between the THz emission and the in-plane magnetization can be observed. This can be explained by the transition from an in-plane to an out-of-plane magnetic easy axis (see figure 7.3). Furthermore, canted states between the Fe and Tb magnetic sublattices can lead to a complex dependence of the magnetization and the THz amplitude on the applied magnetic field. This becomes especially evident for the sample with $x = 0.55$ of the Co capping layer series. Figure 7.15 shows the full hysteresis loops of the THz amplitude and the magnetization of the samples

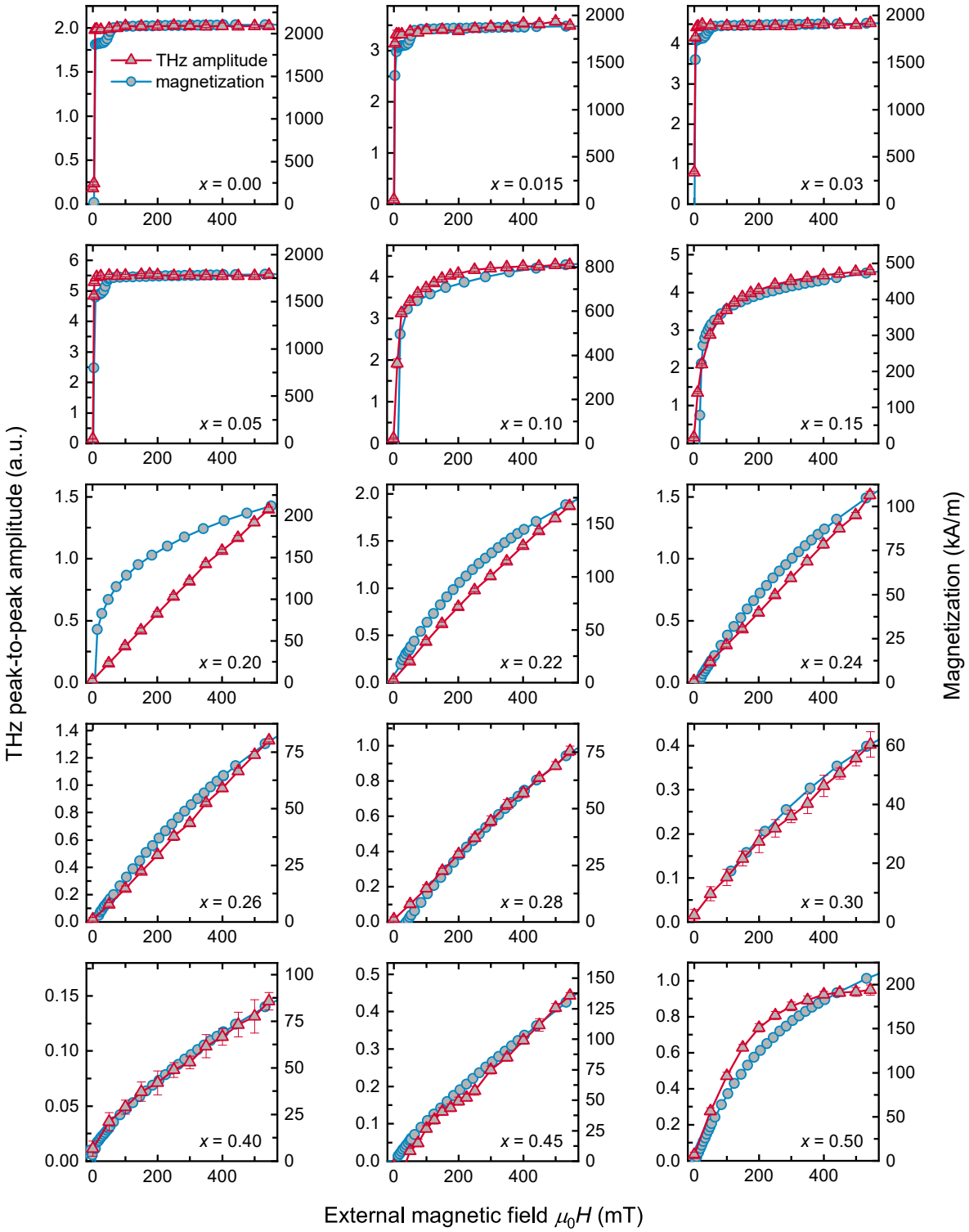

Figure 7.11: THz peak-to-peak amplitude (pump fluence $\Phi = 0.75\,\mathrm{mJ/cm^2}$) and magnetization of *sub.*/Pt(5 nm)/Tb_xFe_{1-x}(20 nm)/Co(2 nm) samples measured at room temperature in dependence on the external magnetic field. The error bars represent the statistical errors of the THz peak-to-peak amplitudes.

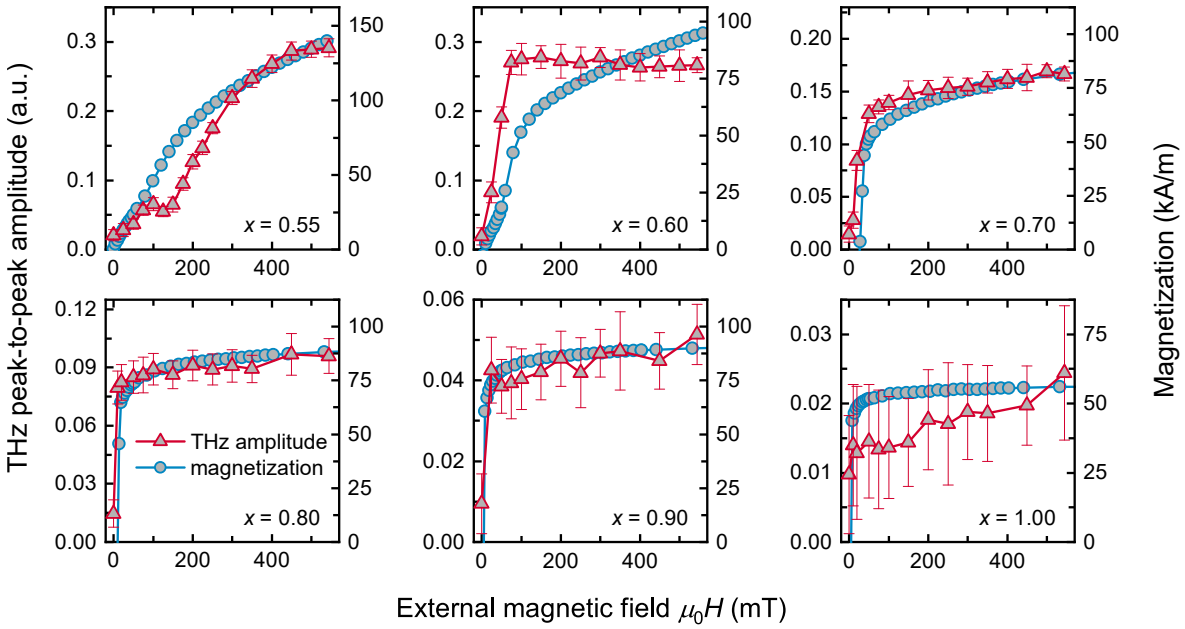

Figure 7.12: THz peak-to-peak amplitude (pump fluence $\Phi = 0.75\,\mathrm{mJ/cm^2}$) and magnetization of *sub.*/Pt(5 nm)/Tb_xFe_{1-x}(20 nm)/Co(2 nm) samples measured at room temperature in dependence on the external magnetic field. The error bars represent the statistical errors of the THz peak-to-peak amplitudes.

with (a) $x = 0.10$ and (b) $x = 0.55$. For $x = 0.10$, the loops of the THz amplitude and the magnetization have an almost identical shape. For the sample with $x = 0.55$, however, the THz amplitude shows an entirely different dependence on the applied magnetic field than the magnetization. The THz amplitude even shows an increase for decreasing applied fields in the region of small positive field values $60\,\mathrm{mT} \leq \mu_0 H \leq 120\,\mathrm{mT}$ and the inverted field dependence for increasing applied fields. Therefore, this behavior gives a strong indication for the mentioned canted state between the FI sublattices and also points to a strong magnetic field dependence of the canting. To clarify this behavior, element-specific $M(H)$ loops that are beyond the scope of this work would be needed.

For samples with high Tb content, which are paramagnetic at room temperature, the THz emission again mainly follows the in-plane magnetization. However, both absolute values, the THz amplitude as well as the magnetization, in this composition region are small.

7.4.3 Composition dependence of the terahertz amplitude

The dependence of the THz peak-to-peak amplitude on the Tb content, measured with a pump fluence $\Phi = 0.75\,\mathrm{mJ/cm^2}$ at a constant applied magnetic field $\mu_0 H = 544\,\mathrm{mT}$, is displayed in figures 7.16a and 7.16b (red triangles) for the series with Co and Si_3N_4 capping layers, respectively. Compared to the pure Pt/Fe bilayer, the THz amplitude first increases with rising Tb content x and then drastically decreases to a minimum at $x = 0.4$. For higher

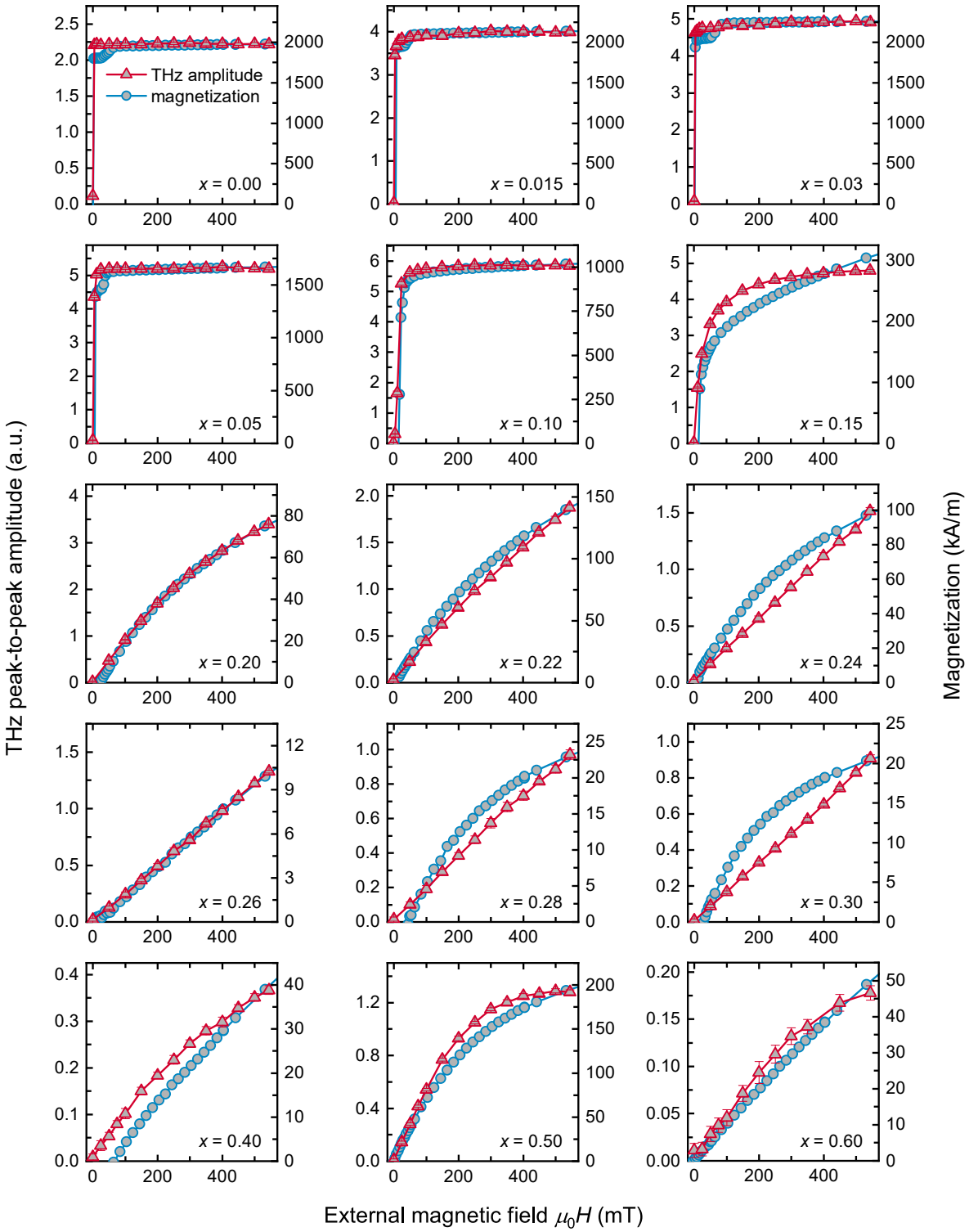

Figure 7.13: THz peak-to-peak amplitude (pump fluence $\Phi = 0.75\,\mathrm{mJ/cm^2}$) and magnetization of *sub.*/Pt(5 nm)/Tb_xFe_{1-x}(20 nm)/Si_3N_4(5 nm) samples measured at room temperature in dependence on the external magnetic field. The error bars represent the statistical errors of the THz peak-to-peak amplitudes.

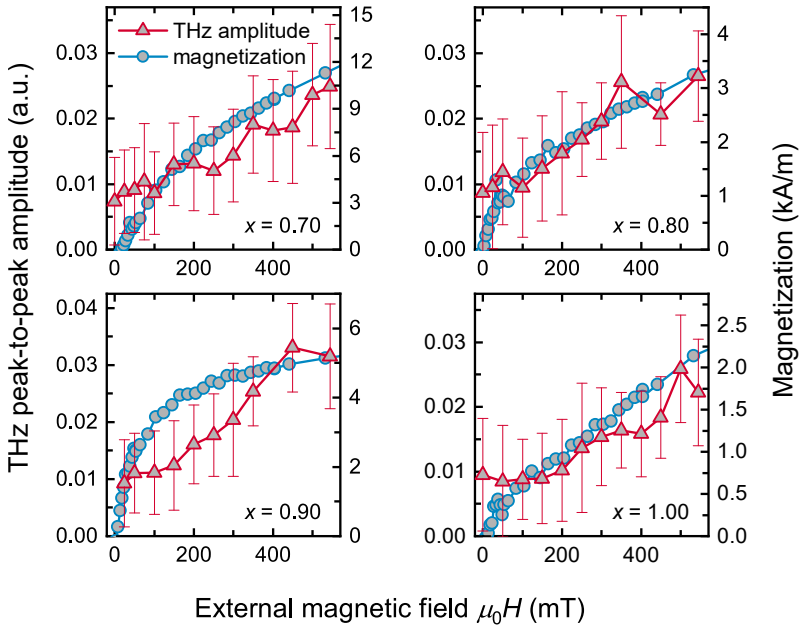

Figure 7.14: THz peak-to-peak amplitude (pump fluence $\Phi = 0.75\,\mathrm{mJ/cm^2}$) and magnetization of *sub.*/Pt(5 nm)/Tb_xFe_{1-x}(20 nm)/Si_3N_4(5 nm) samples measured at room temperature in dependence on the external magnetic field. The error bars represent the statistical errors of the THz peak-to-peak amplitudes.

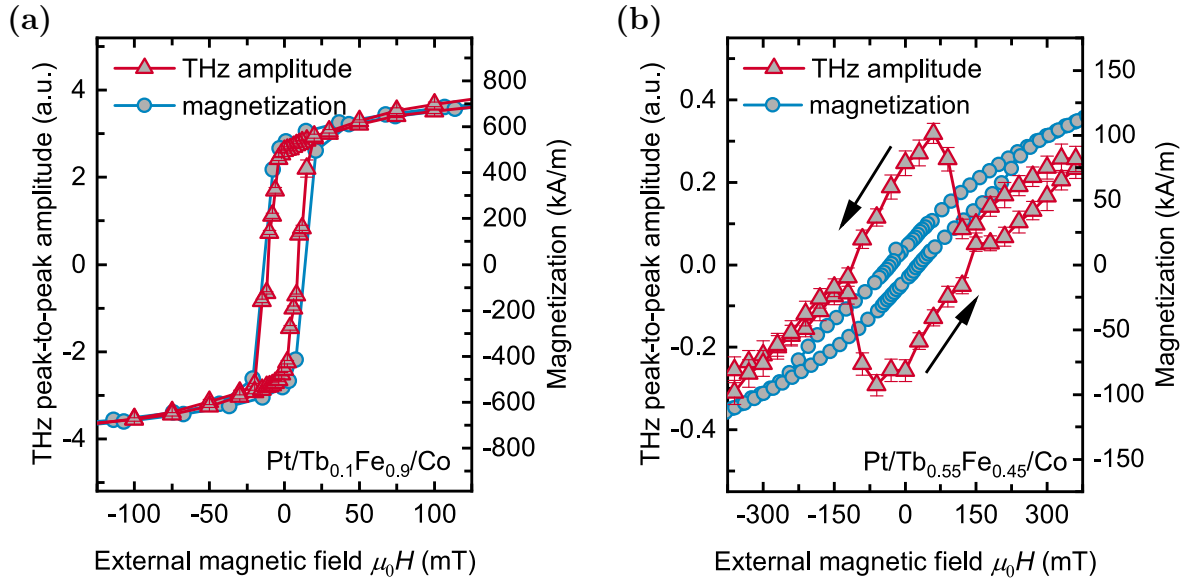

Figure 7.15: Room-temperature THz peak-to-peak signal and magnetization in dependence on the applied magnetic field of (a) *sub.*/Pt(5 nm)/$Tb_{0.10}Fe_{0.9}$(20 nm)/Co(2 nm) and (b) *sub.*/Pt(5 nm)/$Tb_{0.0.55}Fe_{0.45}$(20 nm)/Co(2 nm) samples. The black arrows show the sweep direction of the applied magnetic field. The error bars represent the statistical errors of the THz peak-to-peak amplitudes.

Tb contents, the amplitude again increases up to a local maximum at $x = 0.5$ until it gradually vanishes for $x > 0.6$.

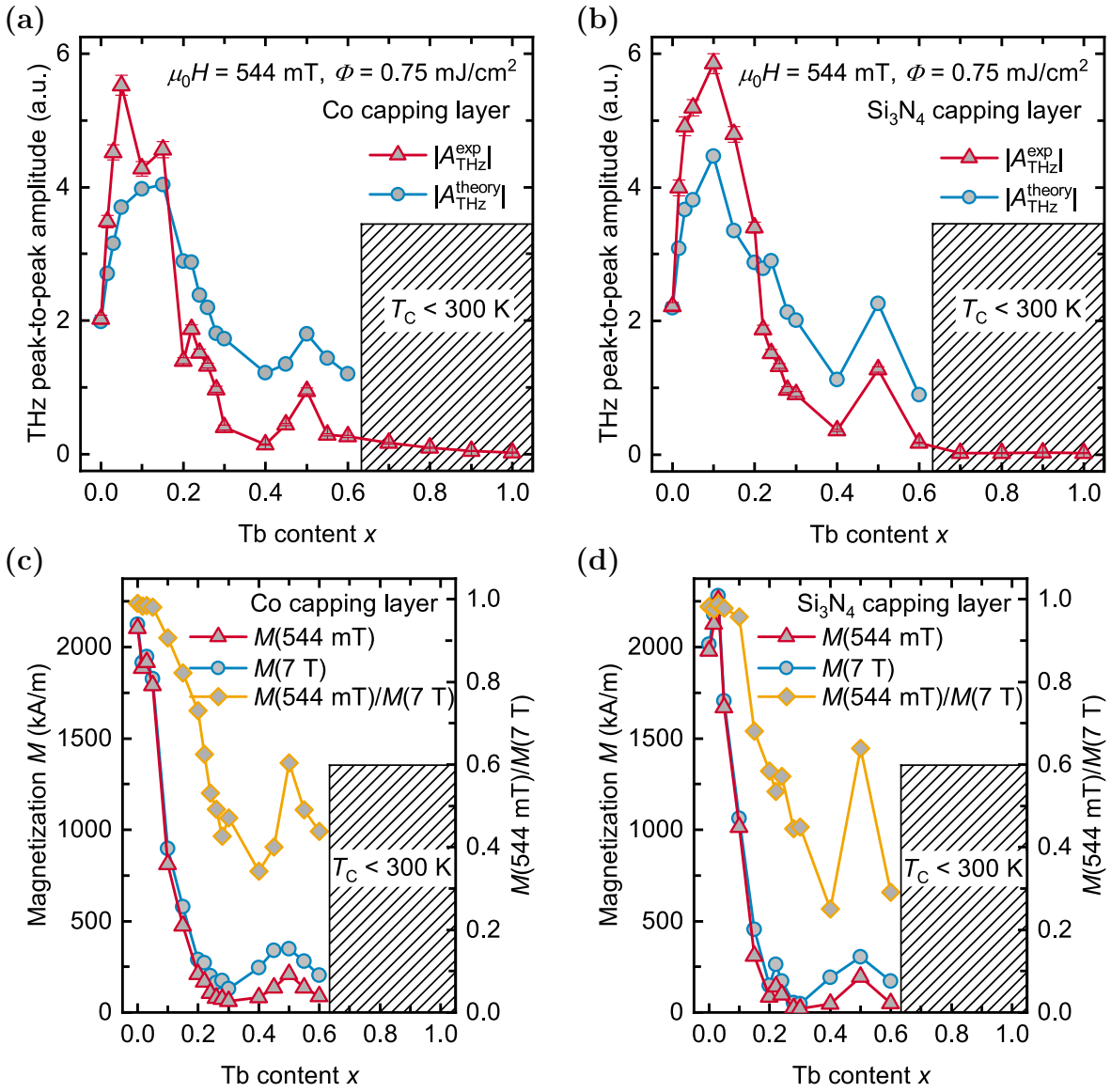

Figure 7.16: (a) and (b) show the THz amplitudes of *sub.*/Pt(5 nm)/Tb_xFe_{1-x}(20 nm)/*cap.* samples in dependence on the Tb content x of the series with Co and Si_3N_4 capping layers, respectively. The THz amplitudes $|A_{THz}^{exp}|$ (red triangles) were measured at room temperature with a pump fluence $\Phi = 0.75\,mJ/cm^2$ and an applied magnetic field $\mu_0 H = 544\,mT$. The error bars represent the statistical errors of the peak-to-peak amplitudes and an additional error of 1.8% that is caused by small variations in the mounting of the samples. The blue circles display the results of the model $|A_{THz}^{theory}|$, which is described in detail in the main text. (c) and (d) show the measured magnetization values for $\mu_0 H = 544\,mT$ and $\mu_0 H = 7\,T$ as well as $M(544\,mT)/M(7\,T)$ of the two sample series with respect to x, which were used in the model. The shaded area represents the composition region for which the Tb_xFe_{1-x} layers are in a paramagnetic state at room temperature.

This composition dependence can be understood by taking into account the different factors that play a role in the emission process. (i) The spin current J_s is mainly driven by the Fe 3d electrons and therefore directly scales with the amount of Fe $(1-x)$ in the Tb_xFe_{1-x} layer.

This leads to a linear decrease in the THz amplitude with increasing x. (ii) As discussed in the previous section, the number of excitable spin-polarized (mainly Fe) electrons also scales with the in-plane spin-polarization of electrons close to the Fermi energy E_F and is therefore connected to the in-plane magnetization of the Fe magnetic sublattice. Consequently, the THz emission amplitude is smaller for $\mathrm{Tb}_x\mathrm{Fe}_{1-x}$ layers that show a high K_eff and, therefore, cannot be magnetically saturated along the in-plane axis. (iii) As shown in section 7.3, figure 7.7, the THz emission efficiency shows a substantial increase with rising x, especially for small x, which is also reflected in the THz emission amplitude.

With regard to these aspects, a simple phenomenological model has been developed to qualitatively model the THz emission amplitude $|A_\mathrm{THz}^\mathrm{theory}(x)|$ in dependence on the Tb content x:

$$|A_\mathrm{THz}^\mathrm{theory}(x)| = \alpha \cdot Z(x) \cdot (1-x) \cdot \frac{M(x)}{M_\mathrm{S}(x)} \ . \tag{7.2}$$

The sample impedance $Z(x)$ is proportional to the THz emission efficiency $C(x,\omega)$. The number of Fe electrons is represented by the Fe content $(1-x)$. The in-plane spin-polarization close to the Fermi level E_F is approximated by $M(x)/M_\mathrm{S}(x)$, with the magnetization $M(x)$ that is measured for the in-plane magnetic field that is applied for the THz emission experiment (here $\mu_0 H = 544\,\mathrm{mT}$) and the saturation magnetization M_S, for which $M(7\,\mathrm{T})$ was used. $M(x)/M_\mathrm{S}(x)$ only gives a rough estimation of the spin polarization close to E_F, as the magnetization of the Fe and Tb magnetic sublattices might be in a canted state for some of the samples (see previous sections). Furthermore, in general, the measured net magnetization does not scale linearly with the spin-polarization close to the E_F. However, $M(x)/M_\mathrm{S}(x)$ takes into account the influence of the magnetic anisotropy of the samples that has a major influence on the number of excitable spin-polarized electrons. The values of $M(x)$, $M_\mathrm{S}(x)$, and $M(x)/M_\mathrm{S}(x)$ in dependence on the composition are shown in figures 7.16c and 7.16d for the series with Co and $\mathrm{Si_3N_4}$ capping layer, respectively. All parameters that are assumed to be independent of the composition are summarized in the proportionality factor α, including the spin Hall angle of the Pt layer $\theta_{\mathrm{sh,\,Pt}}$, the relaxation length of the spin current $\boldsymbol{J}_\mathrm{s}$ within the Pt layer $\lambda_{\mathrm{rel,\,Pt}}$, as well as interface effects. α was chosen to match the model for the sample with $x = 0$ with the measured amplitude. $|A_\mathrm{THz}^\mathrm{theory}(x)|$ is plotted in figures 7.16a and 7.16b with blue circles.

Despite the simplicity of the model, $|A_\mathrm{THz}^\mathrm{theory}|$ shows a good qualitative agreement with the measured THz amplitudes. The maximum of the amplitude for small x as well as the local minimum for $x = 0.4$ and the local maximum for $x = 0.5$ are reflected in the model. However, the model has a few drawbacks. (i) No absolute values for the THz amplitude can be estimated. $M(x)/M_\mathrm{S}(x)$ gives a good approximation for the effect of the magnetic anisotropy on the THz amplitude. However, due to the normalization to $M_\mathrm{S}(x)$, the total spin-polarization

(especially close to E_F) that is partially reflected in the absolute value of $M(x)$ is not included in the model. The total number of excitable electrons is just included by the number of Fe electrons $(1-x)$. Therefore, only a qualitative dependence of the amplitude on the Tb content x can be determined. (ii) The model cannot be applied to the paramagnetic samples ($x \gtrsim 0.6$) as no magnetic saturation can be achieved for these samples with applied magnetic fields $\mu_0 H = 7\,\mathrm{T}$. (iii) Composition-dependent interface effects are completely neglected. For example, a different level of intermixing between the Tb_xFe_{1-x} and the Pt layer occurring during the film deposition that is likely to be dependent on the Tb content x might play a role in the THz amplitudes.

7.5 Low-temperature results

Besides room-temperature measurements, also preliminary investigations on selected emitters with Si_3N_4 capping layers at low temperatures ($\approx 80\,\mathrm{K}$) have been performed. Therefore, in-plane and out-of-plane SQUID-VSM $M(H)$ loops were recorded at $T = 79\,\mathrm{K}$ (see appendix A.3, figure A.9), and the effective magnetic anisotropy K_{eff} was estimated. Figure 7.17 displays (a) K_{eff} and (b) K_{eff}/M_S. A similar behavior compared to the room-temperature results can be observed. However, the composition region with an out-of-plane magnetic easy axis is shifted toward lower Tb contents as the magnetization of the samples becomes more Tb-dominated at low temperatures. Furthermore, for all samples, the Curie temperature is clearly above 79 K (see figure 7.4d). Therefore, the samples with high Tb content are

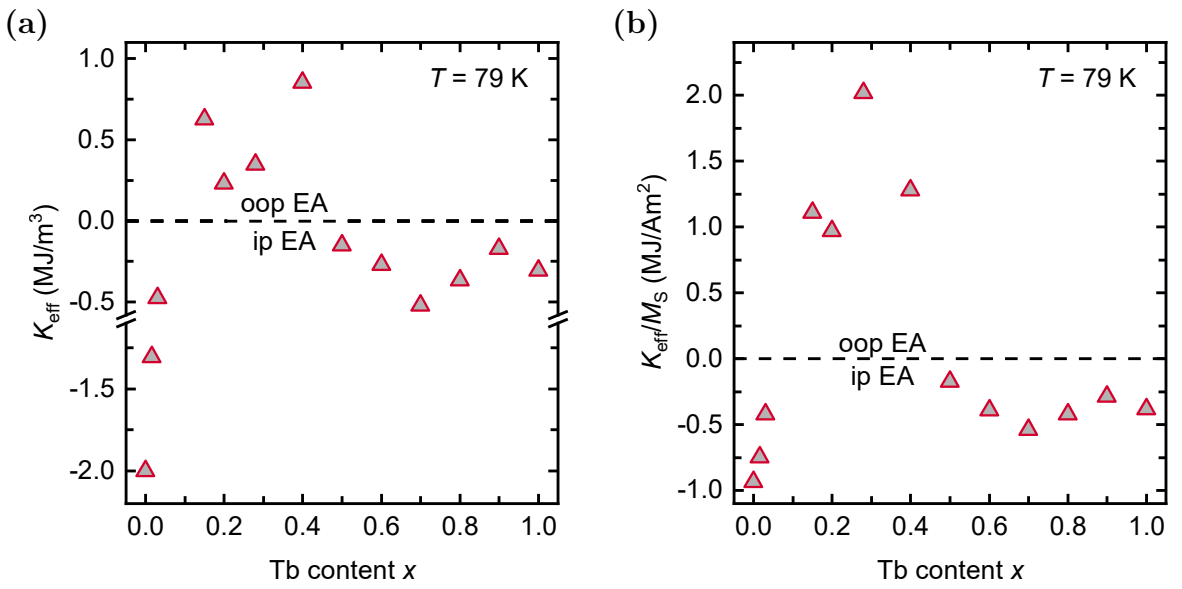

Figure 7.17: (a) shows the effective magnetic anisotropy K_{eff} of *sub.*/Pt(5 nm)/Tb_xFe_{1-x}(20 nm)/Si_3N_4(5 nm) samples at a temperature of 79 K with respect to the Tb content x. (b) displays the values of K_{eff} divided by the saturation magnetization M_S of the respective samples.

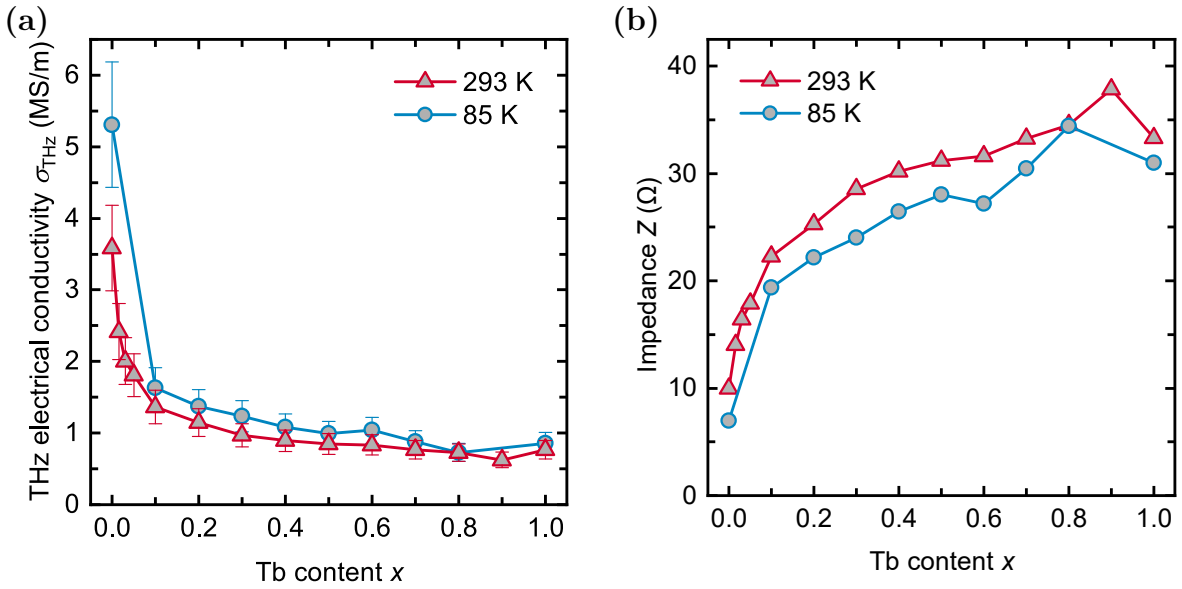

Figure 7.18: (a) shows the THz electrical conductivities (the error bars are mainly derived from the assumed uncertainty of the film thicknesses) and (b) the impedance values of *sub.*/ Pt(5 nm)/Tb_xFe_{1-x}(20 nm)/Si_3N_4(5 nm) samples measured at room temperature and 85 K with respect to the Tb content x.

in a FI (or FM, for $x = 1$) state and show an in-plane magnetic easy axis. The electrical conductivities in the THz frequency regime as well as the THz emission properties at 85 K have been determined by Dr. Robert Schneider at the University of Münster (see section 5.6 and [299] for details on the measurement setups). Figure 7.18 shows (a) the THz conductivity σ_{THz} and (b) the impedance Z in dependence on the Tb content x in comparison with the room-temperature results. A similar qualitative dependence of σ_{THz} and Z on x as for the room-temperature measurements can be observed. However, at 85 K, the conductivity of the samples is slightly increased, and accordingly, the impedance slightly decreased.
Figure 7.19 shows the low-temperature THz emission spectroscopy results, measured with a pump fluence $\Phi = 0.75\,\mathrm{mJ/cm^2}$ and an applied magnetic field $\mu_0 H = 103\,\mathrm{mT}$. Please note that the measurements were performed in air atmosphere. The shape of the measured THz signals displayed in figure 7.19a shows a comparable dependence on the Tb content x as the room-temperature results for $x \leq 0.6$ (see figure 7.9). Also, at low temperature, the signal inversion, which can be observed between the samples with $x = 0.28$ and $x = 0.4$, appears at a Tb content that is clearly above the magnetic compensation composition at 85 K, which is expected at a Tb content $x < 0.24$ (see figure 7.4b). As the samples with $x > 0.6$ change from a paramagnetic state at room temperature to a FI (or FM, for $x = 1$) state at low temperatures, the measured THz signals are significantly stronger at 85 K. Furthermore, a change of the signal shape for $x \geq 0.8$ can be observed, that is also reflected in the corresponding frequency spectra displayed in figure 7.19b as a shift toward lower frequencies. Due to the air atmosphere in which the measurements were performed, water absorption lines

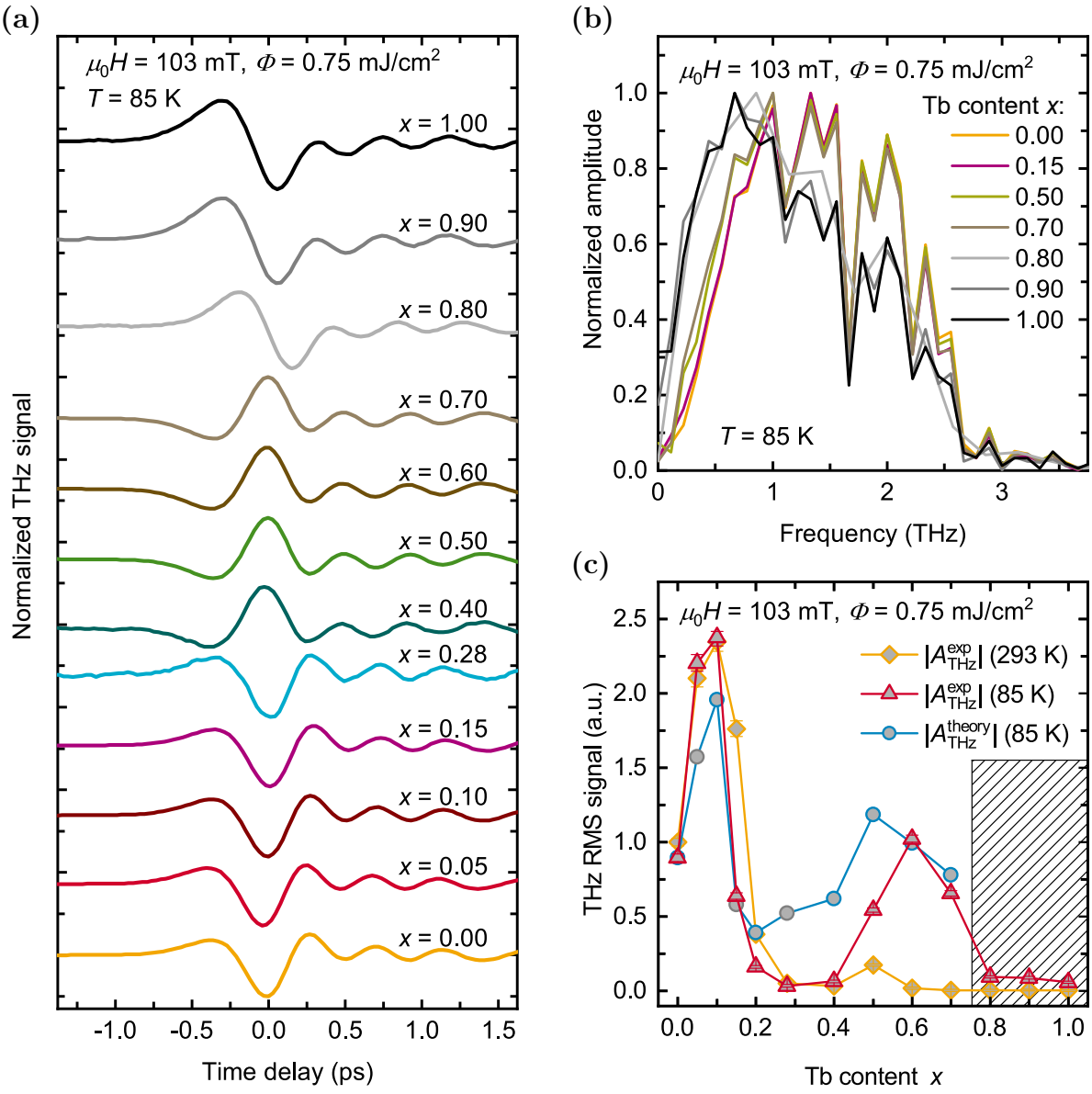

Figure 7.19: THz emission spectroscopy results of *sub.*/Pt(5 nm)/Tb_xFe_{1-x}(20 nm)/Si_3N_4(5 nm) samples, measured with a pump fluence $\Phi = 0.75\,\mathrm{mJ/cm^2}$ and an applied magnetic field $\mu_0 H = 103\,\mathrm{mT}$ at a temperature of 85 K. (a) shows the measured THz electro-optic signals for samples with different Tb content x. The signals were normalized to the maximum of their absolute values to allow for a comparison between the signal shapes. (b) displays the corresponding frequency spectra of selected samples that are also normalized to their respective maxima. (c) shows the THz RMS amplitudes $|A_{\mathrm{THz}}^{\mathrm{exp}}|$ measured at a temperature of 85 K in comparison to the room-temperature results, as well as the modeled THz amplitudes $|A_{\mathrm{THz}}^{\mathrm{theory}}|$ for 85 K. The gray circles represent values of the model for which interpolated THz conductivity values were used. The shaded area displays the compositions for which the signal shapes change significantly. The error bars represent the statistical errors of the RMS amplitudes and an additional error of 1.8% that is caused by small variations in the mounting of the samples.

are observable in the spectra. The THz amplitudes in dependence on x are displayed in figure 7.19c. As the signal shape significantly differs for samples with $x \leq 0.7$ compared to

samples with $x \geq 0.8$, the peak-to-peak amplitude, which is dependent on the signal shape, is not a good measure to compare the amplitudes of the different samples. Therefore, the THz RMS signal has been used for the comparison of the amplitudes of the different samples. The low-temperature results show a similar qualitative dependence on x as the room-temperature amplitudes. However, a few differences can be observed. (i) The strong decrease in the amplitude that is caused by the out-of-plane magnetic easy axis of the samples shifts toward lower x values, as the magnetic compensation point and, therefore, also the composition region for which the samples have an out-of-plane magnetic easy axis shifts toward lower x at 85 K. (ii) The THz amplitudes for $x > 0.4$ are strongly enhanced at low temperatures. This can be explained by a higher spin polarization at low temperatures but also by the lower values of K_{eff} compared to the room-temperature values. (iii) Especially the sample with $x = 1$ shows a significantly higher THz signal. This, as well as the change of the signal shape of the samples with $x \geq 0.8$, could indicate the influence of spin-polarized Tb electrons on the emission process. However, further investigations that are beyond the scope of this work are necessary to clarify this behavior.

Also, for the low-temperature results, the THz amplitude can be qualitatively modeled by equation 7.2, using the same assumptions as for the room-temperature results. Furthermore, it is assumed that also at low temperatures, the absorption of the laser pump pulse is independent of the Tb content x. The modeled THz amplitudes are also plotted in figure 7.19c. As the signal shape significantly changes for $x \geq 0.8$, and a stronger influence of the Tb electrons is expected for these samples, the model is not suitable for describing the amplitudes for $x \geq 0.8$. It is therefore only applied to the samples with $x \leq 0.7$. The model qualitatively agrees with the measured amplitudes. The deviations can be explained, for example, by canted states between the Fe and Tb magnetic sublattices that are not included in the model. Furthermore, it should be noted that for the samples with $x = 0.05$, $x = 0.15$, and $x = 0.28$, no electrical conductivities have been determined, and therefore linear interpolations have been used for the estimation of these values. Especially for the sample with $x = 0.05$ an overestimation of the conductivity is expected, which leads to an underestimation of the impedance and accordingly to the modeled amplitude.

7.6 Summary

In the presented study, the static magnetic properties, as well as the spintronic THz emission characteristics after excitation by femtosecond laser pulses of $\mathrm{Pt}(5\,\mathrm{nm})/\mathrm{Tb}_x\mathrm{Fe}_{1-x}(20\,\mathrm{nm})$ bilayers at room temperature, have been systematically investigated in dependence on the Tb content $0 \leq x \leq 1$. It could be shown that the emitted THz signal is mainly caused by laser-excited spin-polarized Fe 3d electrons that give rise to a spin current into the Pt layer, where it is converted into a charge current pulse by the inverse spin Hall effect, leading to the

emission of THz radiation. Therefore, the emission amplitude follows the in-plane magnetization of the Fe magnetic sublattice of the Tb_xFe_{1-x} layers that gives a rough measure of the excitable spin-polarized 3d electrons. This also leads to a composition-dependent inversion of the THz signals close to the magnetic compensation point. The composition dependence of the THz emission amplitude for an applied in-plane magnetic field $\mu_0 H = 544\,\mathrm{mT}$ could be qualitatively described by a simple phenomenological model using only the measured electrical conductivity, the absorption of the laser pump pulses, the net magnetization, and Tb content of the samples. Especially for low Tb contents $0 \leq x \leq 0.15$, the substantial decrease in the electrical conductivity with rising x has been demonstrated to cause a strong increase in the THz emission efficiency and, accordingly, the measured THz amplitude. For higher Tb contents $0.15 \leq x \leq 0.5$, the THz amplitude has been found to be intensely dependent on the magnetic anisotropy of the samples, as the applied magnetic field is not sufficient to saturate the samples in in-plane direction for samples with large effective magnetic anisotropies. Accordingly, the THz amplitude shows a local minimum at $x = 0.4$ that correlates with a maximum in the measured effective magnetic anisotropy. For $x \gtrsim 0.6$, only small THz amplitudes could be observed, as the samples were in a paramagnetic state at room temperature.

Besides the investigations at room temperature, also first measurements on selected samples at low temperatures ($T \approx 80\,\mathrm{K}$) have been performed. The THz emission of Tb-rich samples is strongly enhanced at low temperatures, as the Tb_xFe_{1-x} layers that are in a paramagnetic state at room temperature become FI (or FM, for $x = 1$) at low temperatures. For samples with $x \leq 0.7$, the composition dependence of the emitted THz radiation at low temperatures can still be qualitatively described by the model developed for the room-temperature results. However, for higher Tb contents, the THz signal significantly changes, indicating that the excitation of spin-polarized Tb electrons might give a significant contribution to the emitted signal.

At both temperatures, especially for samples with compositions close to the magnetic compensation point that also exhibit large effective magnetic anisotropies, the interpretation of the measured THz signals is challenging. The results of the magnetic and THz emission properties give a strong indication for complex canted states between the Fe and Tb magnetic sublattices. These magnetic states could be revealed by element-specific magnetic measurements of the Tb and Fe magnetic sublattices that might be the subject of future works.

The study demonstrated that the THz emission properties of FI/NM bilayer systems can be systematically tailored by varying the magnetic properties of the samples. Especially the composition-dependent inversion of the THz signal also motivated the investigations on the Pt/Gd_xFe_{1-x} emitter systems presented in the following chapter.

CHAPTER 8

Spintronic Pt/Gd_xFe_{1-x} terahertz emitters

In the study presented in this chapter, the magnetic and spintronic THz emitting properties of FI Gd_xFe_{1-x} thin films combined with Pt layers have been investigated with respect to the Gd content x. The study was a follow-up work on the investigations on the Pt/Tb_xFe_{1-x} spintronic THz emitter system presented in the previous chapter. The THz emission properties of the Pt/Gd_xFe_{1-x} system are expected to be comparable to the emitters with Tb_xFe_{1-x} alloys, as also for the Gd_xFe_{1-x} alloys, mainly the Fe electrons will be excited by the femtosecond laser pulse and therefore contribute to the THz emission process. However, in contrast to the Tb_xFe_{1-x} layers, the Gd_xFe_{1-x} films exhibit a lower effective magnetic anisotropy, and therefore, the magnetization can be saturated in the in-plane direction with smaller applied magnetic fields. Furthermore, the Gd and the Fe magnetic sublattices are expected to be more collinearly aligned. Also, for this study, Pt has been chosen as NM layer due to its large spin Hall angle ($+1.2\% \leq \theta_{\mathrm{sh}} \leq +11\%$ [271, 294, 295]). Furthermore, this also allows for a direct comparison of the THz emission properties of Gd_xFe_{1-x} layers with the Tb_xFe_{1-x} layers. THz emission spectroscopy as well as magnetic measurements with different applied magnetic fields and temperatures have been performed to characterize the samples. The phenomenological model presented in the previous chapter has been applied for a qualitative description of the THz emission amplitude in dependence on the Gd content x.

The results were achieved in collaboration with Dr. Robert Schneider, Jannis Bensmann, Dr. Steffen Michaelis de Vasconcellos, and Prof. Rudolf Bratschitsch from the University of Münster. The room-temperature results are predominantly published in [394].

8.1 Sample preparation and structural characterization

A series of *sub.*/Pt(5 nm)/Gd_xFe_{1-x}(20 nm)/Si_3N_4(5 nm) samples with varying Gd content $0 \leq x \leq 1$ was prepared by magnetron sputtering at room temperature (see chapter 4 for details). The Gd_xFe_{1-x} alloys were deposited by co-sputtering from elemental targets. DC sputtering was applied for the Pt, Fe, and Gd targets. The Si_3N_4 layers were deposited by RF sput-

tering from a stoichiometric compound target. The samples were prepared on 500 µm thick Al_2O_3(0001) substrates, polished on both sides, for the THz spectroscopy experiments as well as on 525 µm thick p-doped Si(100) substrates with a 100 nm thick thermally oxidized SiO_2 layer on which all other measurements have been performed. Also, for this series, the similar polycrystalline growth of the Pt seed layers on the different substrates (see appendix A.2, figure A.1 for transmission electron microscopy images of *sub.*/Pt(3 nm)/Fe(3 nm)/Si_3N_4(5 nm) grown on Al_2O_3 and Si/SiO_2 substrates) allows for the direct comparison of the magnetic properties measured on the layer stacks grown on Si/SiO_2 with the THz spectroscopy results measured on the films grown on Al_2O_3. The Pt also prevents the Gd_xFe_{1-x} layer from reacting with the substrate.

RBS measurements were carried out to check the composition of the alloys and the layer thicknesses. Unfortunately, only for four of the samples RBS measurements could be performed, as the RBS setup has been out of order since then. Thus, additionally, EDX measurements have been carried out on all samples. The RBS and EDX results are summarized in figure 8.1. Subfigure (a) shows the measured Gd content x_{exp}, (c) and (e) display the Gd_xFe_{1-x} and Pt layer thicknesses with respect to the nominal Gd content x_{cal} of the different samples. In order to determine the statistical error of the EDX measurements, for the sample with $x = 0.67$, the measurements were repeated 15 times under different conditions. Two series of measurements were carried out with an integration time of 100 s. For the first of these series, the measurements were repeated without varying the sample position, whereas, for the second series, the sample was removed and remounted for each measurement. Additionally, a series with a fixed sample position and an integration time of 200 s has been performed. The results of the measured Gd contents are displayed in (b). The measured layer thicknesses of the $Gd_{0.67}Fe_{0.33}$ and Pt layers are shown in (d) and (f), respectively. For all measurement series shown in (b), (d), and (f), the average values (marked with the thick colored lines) and the standard deviations (marked with the thin dashed colored lines and the arrows) were determined. Almost similar standard deviations of the measured Gd contents between 0.7% and 1.0% of the average values could be observed. The layer thicknesses show standard deviations with respect to the average values between 0.7% and 1.1% for the $Gd_{0.67}Fe_{0.33}$ layer and between 1.0% and 1.4% for the Pt layer. Variations in the sample mounting seem to have only a minor influence on the measurements. Increasing the integration time by 100 s leads to a slight reduction of the standard deviation with respect to the average values of about 0.4%. However, as the errors due to the necessary background correction and the fitting of the measured peaks are expected to clearly exceed the determined small statistical errors, an integration time of 100 s has been used for the measurements of all samples. The determined standard deviations are used for the error bars in the subfigures (a), (c), and (e). In comparison to the nominal values (dashed black curve), the EDX measurements reveal systematically higher Gd contents for all samples. The strongest deviation from the nominal value of $\Delta x = +0.097$ can be observed

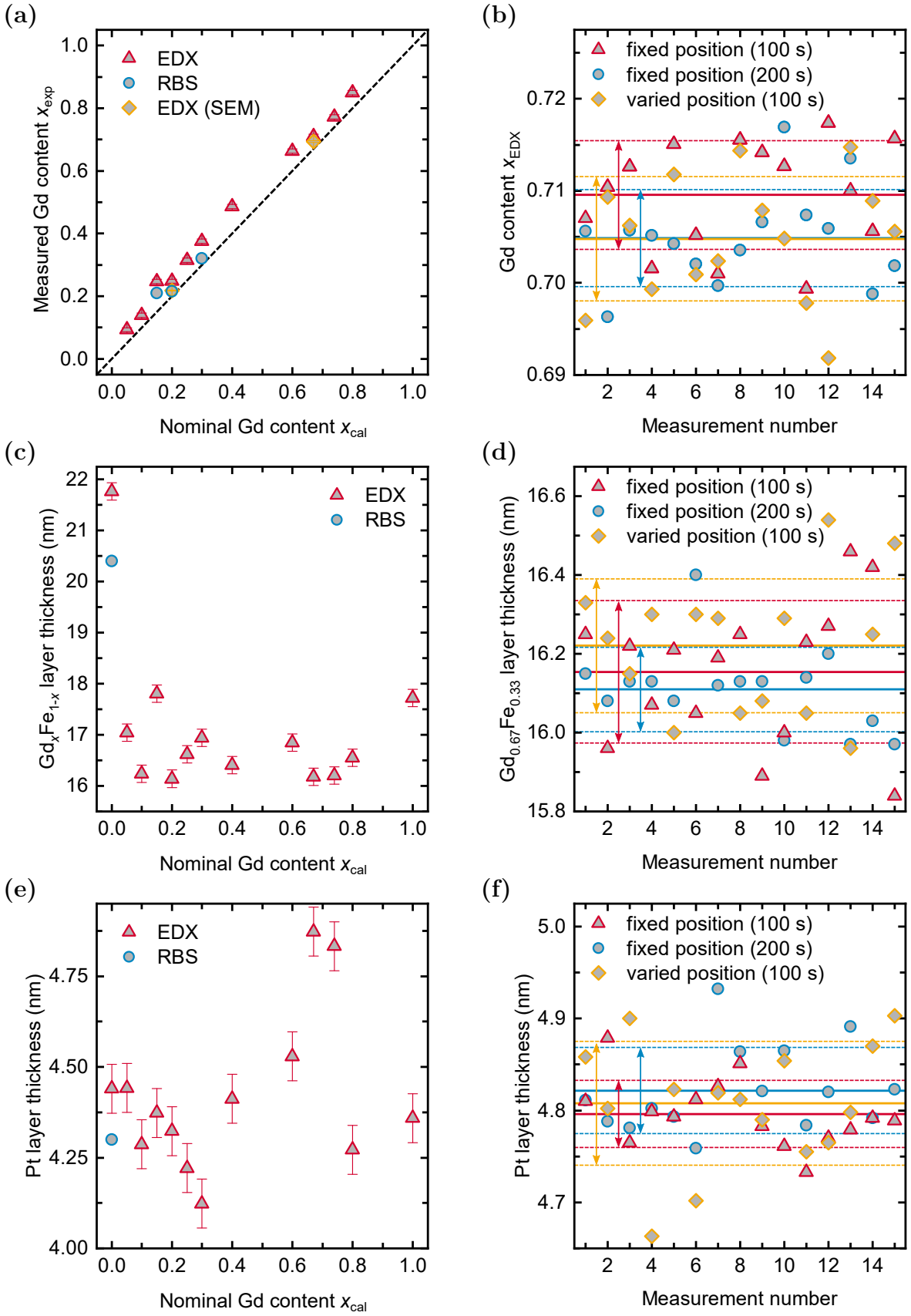

Figure 8.1: (a, c, e) EDX and RBS results of the *sub.*/Pt(5 nm)/Gd_xFe_{1-x}(20 nm)/Si_3N_4(5 nm) sample series. (b, d, f) EDX results for $x = 0.67$ of repeated measurements, performed with 100 s and 200 s integration time for fixed and varied sample positions. The average values are marked with the thick colored lines, the standard deviations, which are also used for the error bars in (a, c, e), with dashed colored lines and arrows.

for the sample with $x_{cal} = 0.15$. In contrast to the EDX measurements, the compositions measured by RBS show significantly smaller deviations from the nominal values. However, also here, the measured Gd content of the sample with $x_{cal} = 0.15$ is almost as high as for the sample with $x_{cal} = 0.2$. As the magnetization measurements that were later on carried out on this sample also gave strong indications for a significantly higher Gd content, this sample has been excluded from the following discussions. To further cross-check the EDX results, scanning electron microscope EDX line scans have been performed on the samples with $x_{cal} = 0.2$ and $x_{cal} = 0.67$ (see appendix A.4, figure A.10). The determined average composition values with their respective standard deviations are displayed in (a) with yellow diamonds. Similar to the RBS values, the Gd contents determined by scanning electron microscope EDX line scans are lower than those measured with the integrating energy-dispersive X-ray spectrometer. Thus, the Gd contents determined by integrating EDX are presumably shifted by a systematic error toward higher values. Furthermore, large variations of the Gd contents determined by the integrating EDX of up to $\Delta x \approx 0.05$ have been observed for a different energy interval used for the fitting of the peaks. Due to this sensitivity in the fitting of the peaks, further calibration measurements with other measurement techniques would be necessary to calibrate the integrating EDX device for the determination of the Gd and Fe contents. Therefore, the values can be used only for a rough quality control. The determined layer thicknesses of the Gd_xFe_{1-x} films with $x > 0$ in (c) show systematically smaller values than the nominal thicknesses. However, the layer thickness of the Gd_xFe_{1-x} layers is strongly correlated with the layer composition and therefore, also here, the errors might be large. Unfortunately, for the RBS measurements of the samples with $x_{cal} = 0.15$, $x_{cal} = 0.2$, and $x_{cal} = 0.3$, which were performed with $^4He^{++}$ particle energies of 6 MeV, no exact background correction could be performed due to multiple reflections of the $^4He^{++}$ particles in the substrate. Thus, as only for the pure Pt/Fe bilayer (that was taken from the Pt/Tb_xFe_{1-x} series) a reference value that was determined by a different technique exists, also the determined thickness values should only be used for a rough quality control of the deposition processes to determine substantial deviations within one sample series.

For the reasons mentioned above, the nominal values and not the values determined by integrating EDX are used for the following discussion, and a maximum error of the film thicknesses of ±15% is assumed.

8.2 Magnetic properties

SQUID-VSM $M(H)$ and $M(T)$ measurements were carried out to determine the magnetic properties of the Gd_xFe_{1-x} films in dependence on the Gd content x. The room-temperature $M(H)$ loops measured in in-plane and out-of-plane direction are displayed in appendix A.4, figure A.11.

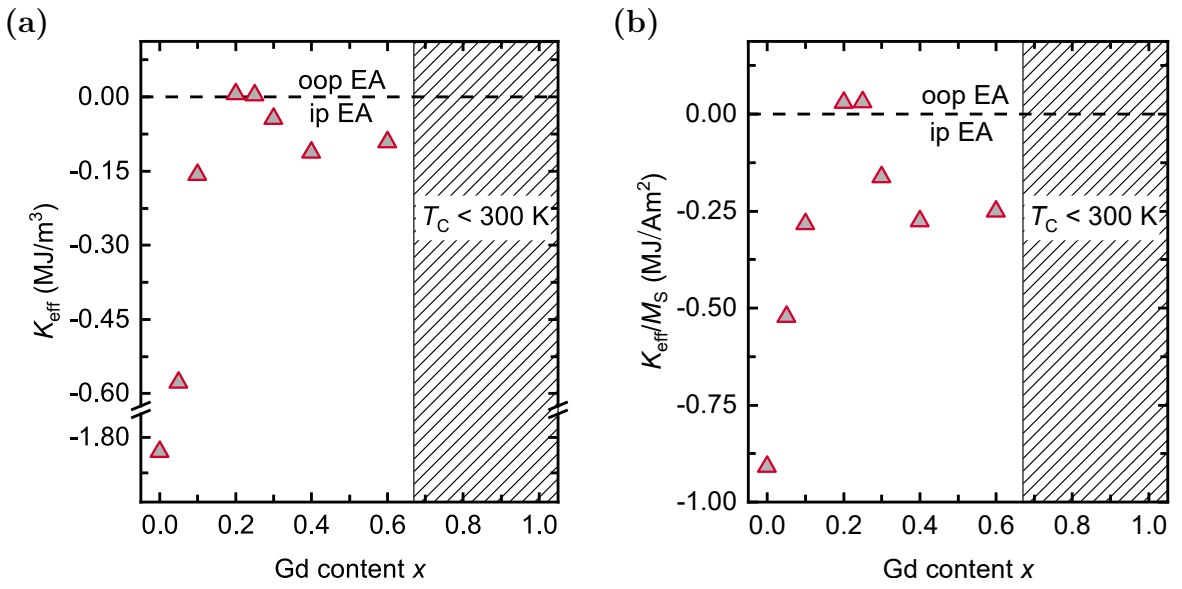

Figure 8.2: (a) shows the effective magnetic anisotropy K_{eff} of *sub.*/Pt(5 nm)/Gd_xFe_{1-x}(20 nm)/Si_3N_4(5 nm) samples at room temperature with respect to the Gd content x, calculated from $M(H)$ loops that were measured in in-plane and out-of-plane direction. The K_{eff} values divided by the saturation magnetization M_S are plotted in (b). The shaded area marks the composition region for which the Gd_xFe_{1-x} layers are clearly paramagnetic at room temperature, and therefore no K_{eff} values could be determined.

Figure 8.2 shows the estimations for the effective magnetic anisotropy at room temperature that were derived from the $M(H)$ loops by the method described in subsection 5.4.3. The effective magnetic anisotropy K_{eff} is displayed in subfigure (a), whereas (b) shows the values of K_{eff} divided by the saturation magnetization M_S of the samples. For Gd contents $x \leq 0.2$ and $x \geq 0.3$, the magnetic shape anisotropy K_{shape} dominates K_{eff} due to the high M_S of the samples, leading to an in-plane magnetic easy axis. Only for sample compositions close to the room-temperature magnetic compensation point, i.e., $x = 0.2$ and $x = 0.25$, the low M_S and consequently the small K_{shape} of the samples lead to an out-of-plane magnetic easy axis due to the short-range chemical order in the films (see subsection 2.6.3 for more details). In contrast to the Tb_xFe_{1-x} samples, even the Gd_xFe_{1-x} films that show an out-of-plane magnetic easy axis can be saturated in-plane with relatively small applied magnetic fields. The samples with $x > 0.6$ are in a paramagnetic state at room temperature, and therefore no K_{eff} values could be determined.

Figure 8.3 displays the in-plane $M(T)$ curves. Positive magnetization values are used for samples with a Gd-dominated net magnetization, and negative values for samples with a Fe-dominated net magnetization. For all of the shown measurements, the samples were first saturated at room temperature at $\mu_0 H = 7\,\text{T}$ and then cooled to 40 K (or 5 K for the samples with $x = 0$, $x = 0.67$, and $x = 0.74$) with the field still applied. The measurements were subsequently carried out after reduction of the applied magnetic field to a small guiding field value in a temperature sweep mode (10 K/min) while heating up the samples to 400 K. For the

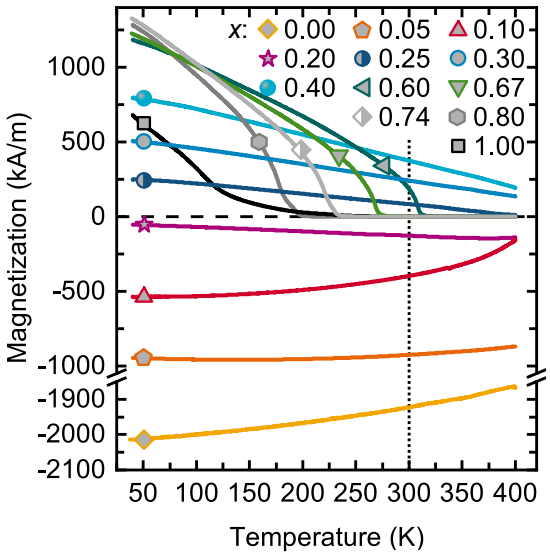

Figure 8.3: $M(T)$ curves of *sub.*/Pt(5 nm)/Gd_xFe_{1-x}(20 nm)/Si_3N_4(5 nm) samples measured in in-plane direction. The samples were first saturated at room temperature with an external magnetic field $\mu_0 H = 7$ T. Afterward, the samples were cooled down to 40 K (or 5 K, for the samples with $x = 0$, $x = 0.67$, and $x = 0.74$). The applied field was then reduced to the guiding field value, and the magnetization was recorded while heating the sample up to 400 K in a temperature sweep mode. The dashed lines mark the compensation point. For this figure, Fe-dominated magnetization values were defined as negative, Gd-dominated values as positive. The room temperature (300 K) is marked with the dotted line.

sample with $x = 0.25$, a guiding field of $\mu_0 H = 140$ mT was applied during the measurement in order to gain an in-plane alignment of the magnetic moments at all temperatures. All other measurements have been performed with smaller applied guiding fields 0 mT $\leq \mu_0 H \leq$ 10 mT. Samples with $x \leq 0.2$, show a Fe-dominated net magnetization. For $x \geq 0.25$, the Gd magnetic sublattice dominates the net magnetization. The Curie temperature T_C systematically decreases with rising Gd content. For samples with $x \leq 0.6$, T_C is above 300 K, and the samples are in a FI (or FM, for $x = 0$) state at room temperature.

8.3 Room-temperature electrical and optical properties

Also, for this sample series, the room-temperature electrical and optical properties of all samples have been measured in order to determine the THz emission efficiency $C(\omega)$ in dependence on the Gd content x.

The transmission T and reflection R of the 1.53 eV laser pump pulses, which were later on used for the THz emission spectroscopy, were measured by Dr. Robert Schneider at the University of Münster (see [299] for the used measurement setup), and the absorption A was calculated by equation 6.1. The results are shown in figure 8.4. Similar to the previously investigated Pt/Tb_xFe_{1-x} samples, slightly decreasing values of the reflection and increasing values of the

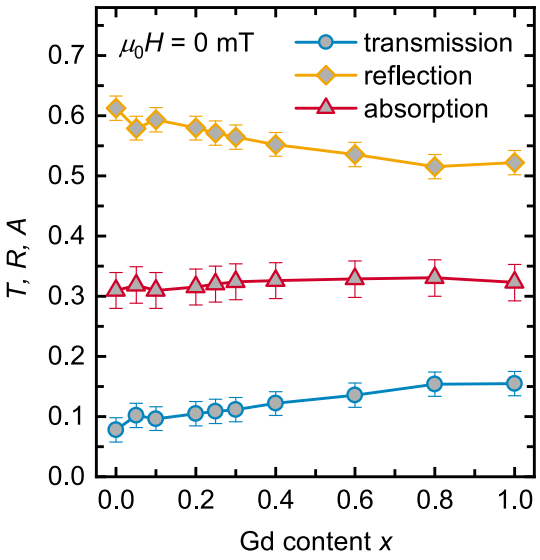

Figure 8.4: Transmission T, reflection R, and absorption A of the 1.53 eV pump laser in *sub.*/ Pt(5 nm)/Gd_xFe_{1-x}(20 nm)/Si_3N_4(5 nm) samples with different Gd content x measured at room temperature.

transmission with rising x can be observed. The absorption shows an almost constant value of approximately 0.32. The electrical conductivities of the samples in the low THz regime have been determined by time-resolved THz transmission spectroscopy experiments that were also performed at the University of Münster by Dr. Robert Schneider (see [299] for details on the measurement setup). For all samples, an almost frequency independent conductivity could be measured. Therefore, the average values over the frequency range 0.78 THz–2.5 THz are used for further discussions. Figure 8.5a shows the determined THz conductivities σ_{THz} (red triangles) in comparison to DC conductivity values σ_{DC} (gray triangles) determined by four-point resistivity measurements and the results for the Pt/Tb_xFe_{1-x} samples discussed in the previous chapter (blue circles) with respect to the rare-earth content x. The error bars mainly represent the assumed film thickness error of 15% (see section 8.1). σ_{THz} and σ_{DC} show matching values within the error range. In contrast to the Pt/Tb_xFe_{1-x} samples, the Pt/Gd_xFe_{1-x} samples show slightly lower conductivities.

As also for the Pt/Gd_xFe_{1-x} series, the absorption of the laser pump pulses, as well as the thickness of the spintronic layer stack $t = t_{\mathrm{Pt}} + t_{\mathrm{GdFe}}$, is approximately constant for all samples, the THz emission efficiency $C(x,\omega)$ given in equation 3.9 is again proportional to the sample impedance $Z(x,\omega)$, which is approximately independent of the wavelength:

$$C(x,\omega) \sim Z(x,\omega) \approx Z(x) \approx \frac{1}{(n_1+n_2)/Z_0 + \sigma_{\mathrm{THz}}(x)\cdot t}\ , \tag{8.1}$$

with the vacuum impedance $Z_0 = 377\,\Omega$ and the refraction indices $n_1 \approx 3.07$ of the Al_2O_3 substrate at 1 THz [299] and $n_2 \approx 1.00$ of nitrogen. The calculated impedance values of the

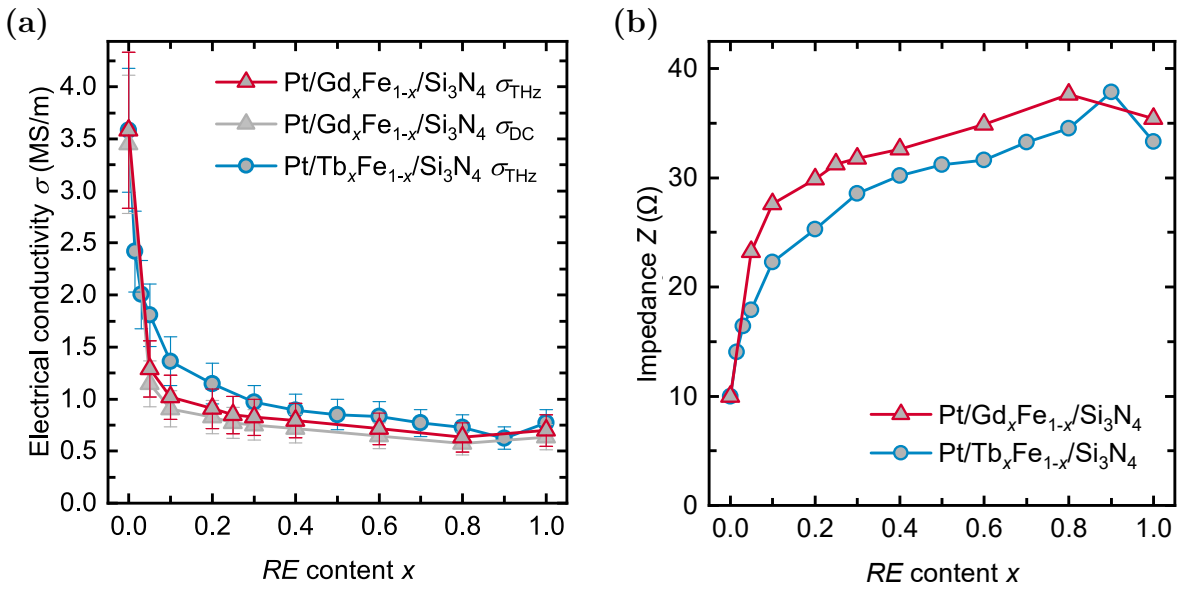

Figure 8.5: (a) shows the room-temperature electrical conductivities of the *sub.*/Pt(5 nm)/Gd_xFe_{1-x}(20 nm)/Si_3N_4(5 nm) sample series in comparison to the *sub.*/Pt(5 nm)/Tb_xFe_{1-x}(20 nm)/Si_3N_4(5 nm) series discussed in the previous chapter with respect to rare-earth content x. The error bars are mainly derived from the assumed uncertainty of the film thicknesses. (b) displays the corresponding impedance values of the samples.

Pt/Gd_xFe_{1-x} series are shown in comparison to the Pt/Tb_xFe_{1-x} series in figure 8.5b with respect to the rare-earth content x.

8.4 Room-temperature THz emission results

Also, for the Pt/Gd_xFe_{1-x} sample series, THz emission spectroscopy measurements with varying external magnetic fields were performed by Dr. Robert Schneider with the measurement setup described in section 5.6 in the measurement geometry displayed in figure 8.6. The laser excitation of electrons in the magnetic layer above the Fermi level leads to the formation of a superdiffusive spin current $\boldsymbol{J}_\mathrm{s}$ from the magnetic Gd_xFe_{1-x} layer toward the nonmagnetic Pt layer, in which $\boldsymbol{J}_\mathrm{s}$ is converted by the inverse spin Hall effect into a transverse charge current $\boldsymbol{J}_\mathrm{c}$, that leads to the emission of electromagnetic radiation in the THz frequency regime (see section 3.3). For the Pt/Gd_xFe_{1-x} emitter system, it is expected that mainly the spin-polarized Fe 3d electrons that are energetically located close to the Fermi energy E_F will contribute to $\boldsymbol{J}_\mathrm{s}$. The spin-polarized Gd 4f electrons that give the main contribution to the magnetic moment of the Gd are energetically located about 7–9 eV [395, 396] below E_F and can therefore not be efficiently heated by the 1.53 eV pump laser pulses. However, a small contribution of the Gd to $\boldsymbol{J}_\mathrm{s}$ might be given by the slightly spin split s, p, and d bands. [395]

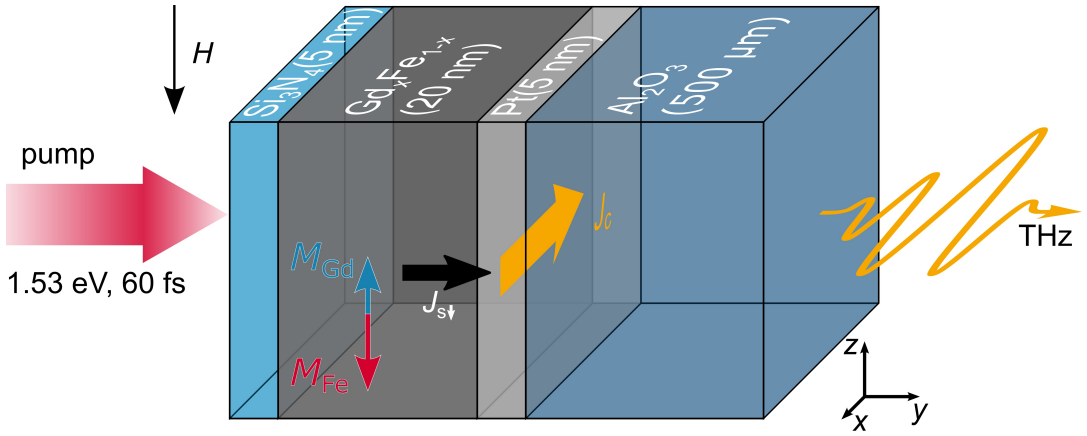

Figure 8.6: Illustration of the excitation geometry that was used for the THz emission spectroscopy measurements performed on the *sub.*/Pt(5 nm)/Gd_xFe_{1-x}(20 nm)/Si_3N_4(5 nm) sample series.

8.4.1 Composition dependence of the terahertz electro-optic signals and dependence of the THz amplitude on the applied magnetic field

Figure 8.7a shows the normalized THz signals of different samples. The corresponding frequency spectra are displayed in appendix A.4, figure A.12. Between $x = 0.2$ and $x = 0.25$ an inversion of the THz signals can be observed. In analogy to the previously discussed Pt/Tb_xFe_{1-x} emitters (see chapter 7 [384]), as well as studies on Pt/Gd_xCo_{1-x} [327] and $Pt/Gd_{0.25}(Fe_{0.875}Co_{0.125})_{0.75}$ [326] emitters, this inversion can be explained by the dominant contribution of the Fe electrons to $\boldsymbol{J}_s$. For Gd contents $x \leq 0.2$, the net magnetization is dominated by the Fe magnetic sublattice. Thus, the Fe magnetic moments are aligned parallel to the external magnetic field. For $x \geq 0.25$, the net magnetization is Gd-dominated, and consequently the Fe magnetic moments are aligned antiparallel to the applied magnetic field. As the charge current $\boldsymbol{J}_c \sim \theta_{sh}\boldsymbol{J}_s \times \boldsymbol{M}/|\boldsymbol{M}|$ and accordingly the THz signal is proportional to the magnetization direction $\boldsymbol{M}/|\boldsymbol{M}|$ of the Fe magnetic sublattice, the inversion of the THz signal is expected at the magnetic compensation point. Therefore, the results agree well with the $M(T)$ measurements shown in figure 8.3. For $x \geq 0.6$, the THz signal significantly changes. This can be attributed to a different THz generation process that is discussed in subsection 8.4.2.

Figure 8.7b shows the dependence of the THz peak-to-peak signals and the magnetization (taken from the SQUID-VSM loops displayed in appendix A.4, figure A.11) on the applied magnetic field. For all samples, the THz amplitude clearly follows the magnetization, as the in-plane alignment of the Fe magnetic moments is directly correlated with the net magnetization.

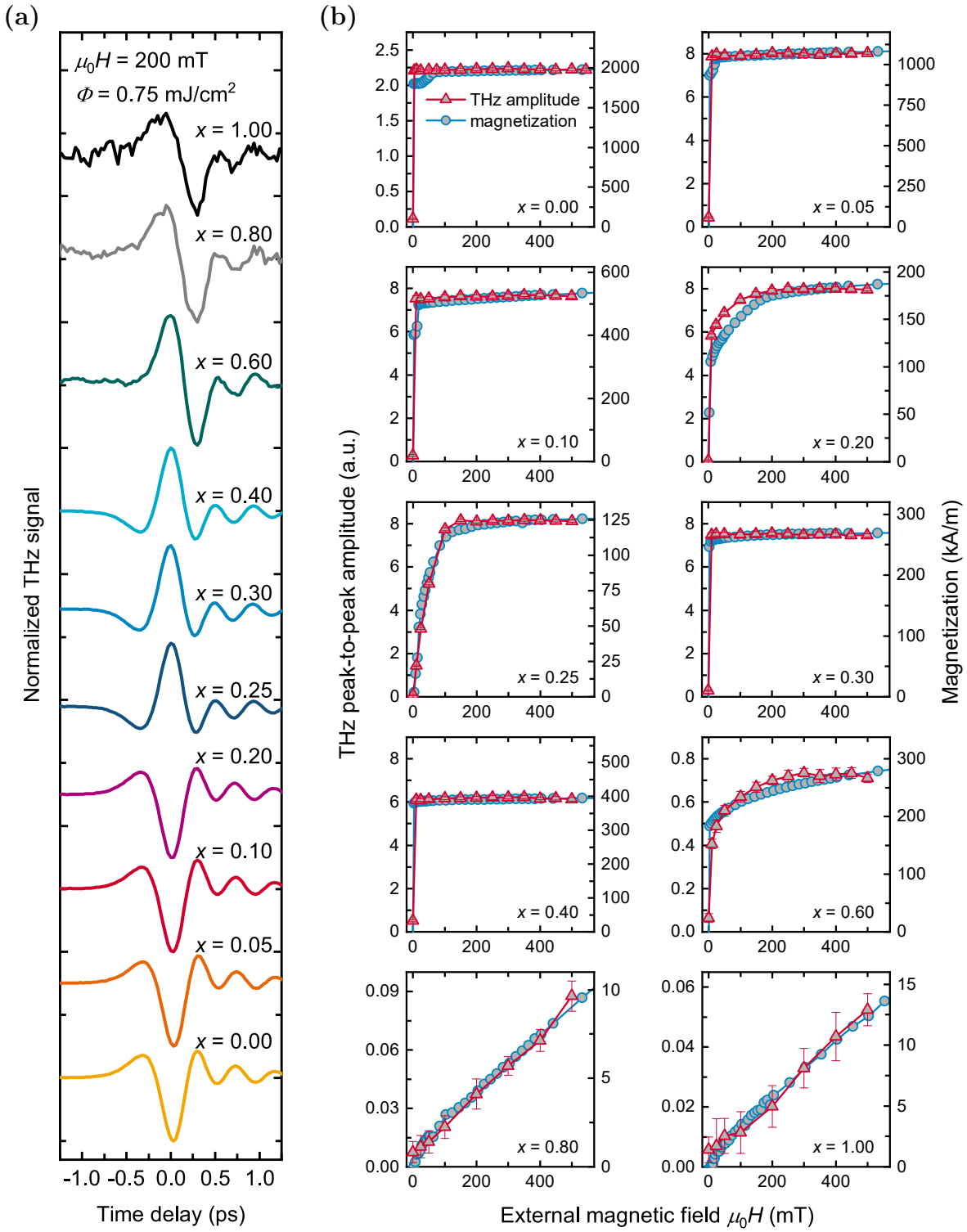

Figure 8.7: THz emission spectroscopy results of Pt(5 nm)/Gd_xFe_{1-x}(20 nm)/Si_3N_4(5 nm) samples with different Gd content x measured at room temperature with a laser pump fluence $\Phi = 0.75\,\mathrm{mJ/cm^2}$. (a) displays the normalized THz electro-optic signals measured with an applied magnetic field $\mu_0 H = 200\,\mathrm{mT}$. (b) shows the THz peak-to-peak amplitude in comparison with the magnetization in dependence on the applied magnetic field. The error bars represent the statistical errors of the RMS amplitudes.

8.4.2 Results for different excitation directions and Gd_xFe_{1-x} single-layer samples

To further investigate the signal change between $x = 0.4$ and $x = 0.6$ and the influence of THz radiation directly caused by the ultrafast demagnetization of the magnetic layers, THz emission spectroscopy measurements with different excitation geometries have been performed on the *sub.*/Pt(5 nm)/Gd_xFe_{1-x}(20 nm)/Si_3N_4(5 nm) as well as on single-layer *sub.*/Gd_xFe_{1-x}(20 nm)/Si_3N_4(5 nm) reference samples. The reference samples have been prepared similar to the bilayer samples on 500 µm thick Al_2O_3(0001) substrates by magnetron sputter deposition. The measured THz electro-optic signals of the bilayers in comparison with the reference samples are displayed in figure 8.8. All bilayer samples show a clear inversion of the THz signals for the excitation from opposite sides, indicating that the emission process is mainly driven by a spin-to-charge current conversion via a spin-dependent Hall effect. However, especially for the pure Pt/Fe bilayer ($x = 0$), the amplitude of the signal is significantly lower for the excitation from the capping-layer side. The lower signal is caused by the absorption of the THz radiation in the substrate as well as by a contribution to the signal that is caused directly by the ultrafast demagnetization of the Gd_xFe_{1-x} layer (see section 3.2). As the signal that has its origin in the ultrafast demagnetization is only dependent on the magnetization direction ($E_x \sim \frac{\partial^2 M_z(\tau)}{\partial \tau^2}$) and not on the excitation direction, this signal either adds up constructively or destructively with the signal caused by the inverse spin Hall effect in the Pt layer, depending on the excitation direction. The contributions to the signal that are not caused by the inverse spin Hall effect in the Pt layer can be estimated by the measurements on the single-layer reference samples. For $x \leq 0.4$, the signals of the single-layer samples show no inversion for excitation from the different sample sides and can therefore be attributed to the ultrafast demagnetization of the Gd_xFe_{1-x} layers. The highest signal can be observed for the sample with $x = 0$. With regard to the different emission efficiencies of the single and bilayer samples, for the Pt/Fe, the signal caused by the ultrafast demagnetization can be estimated to be approximately 14%. For increasing Gd contents ($x \leq 0.4$), this contribution decreases to less than 1.5% (i.e., below the uncertainties of the measurements). The single-layer samples with $x \geq 0.6$, however, show high signals that are inverted for the different excitation directions. Thus, ultrafast demagnetization can be excluded as the dominant THz excitation mechanism for these compositions. Depending on the Gd content x and the excitation direction, the THz peak-to-peak amplitudes of the single layers show values between 42% and 131% of the amplitudes of the respective bilayer samples. A possible scenario would be a spin-to-charge current inversion via the anomalous Hall effect in the Gd_xFe_{1-x} layers. Seifert *et al.* [397] measured an almost frequency independent anomalous Hall angle up to 40 THz of approximately 2.6% of a $Gd_{0.27}Fe_{0.73}$ sample, which agrees well with the results of DC measurements presented in previous studies [398, 399]. Zhang *et al.* [400] reported on the THz emission of different FM single layers ($Fe_{0.8}Mn_{0.2}$,

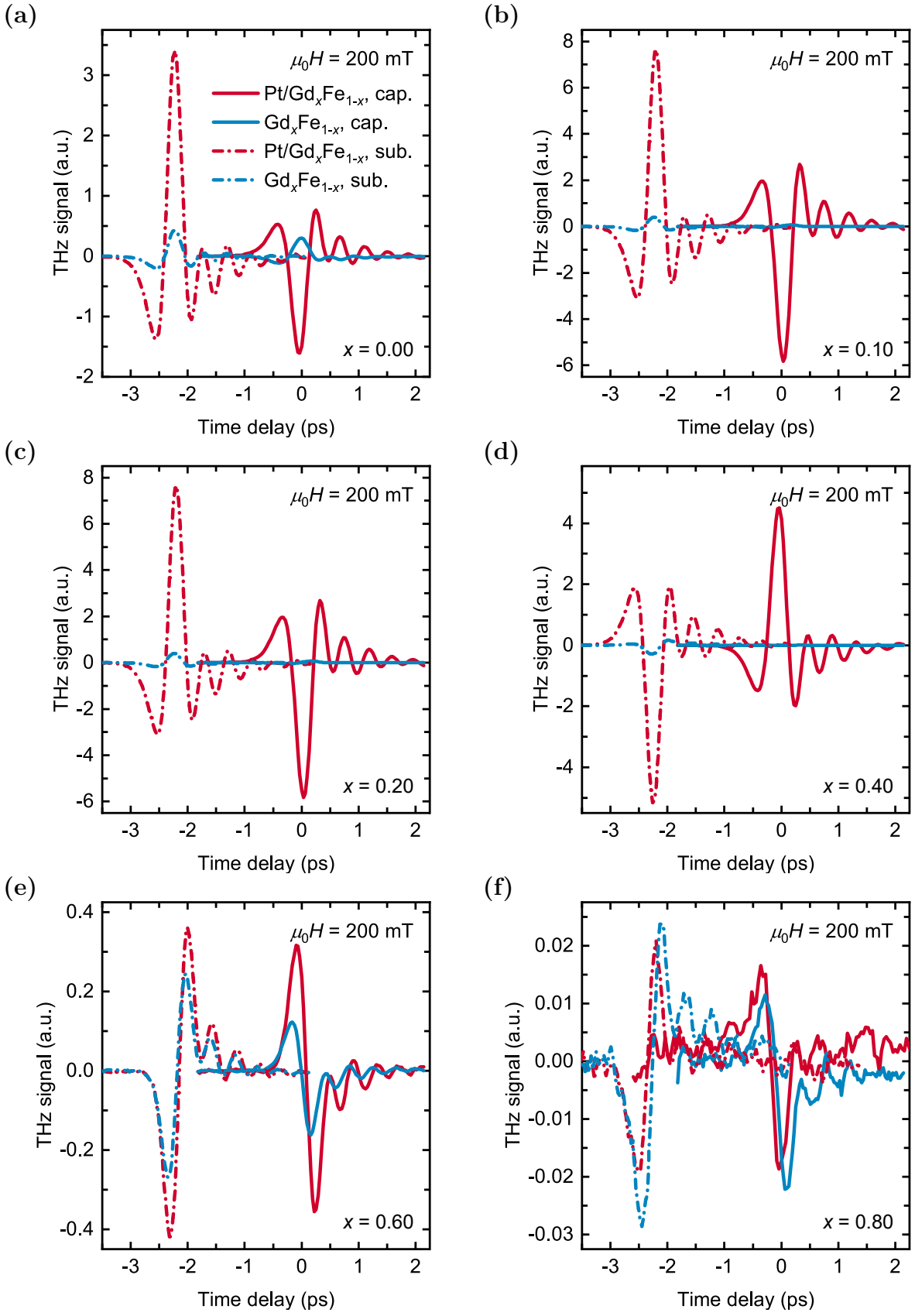

Figure 8.8: THz electro-optic signals of *sub.*/Pt(5 nm)/Gd_xFe_{1-x}(20 nm)/Si_3N_4(5 nm) (red lines) and *sub.*/Gd_xFe_{1-x}(20 nm)/Si_3N_4(5 nm) (blue lines) samples with different Gd content x, measured at room temperature with laser excitation from the substrate (sub., dashed lines) and from the capping layer (cap., solid lines) side with an in-plane applied magnetic field $\mu_0 H = 200\,\mathrm{mT}$.

$(Fe_{0.8}Mn_{0.2})_{0.67}Pt_{0.33}$, $Co_{0.2}Fe_{0.6}B_{0.2}$, $Ni_{0.8}Fe_{0.2}$) via the anomalous Hall effect. The spin current generation in that study is explained by a different interface reflectivity for the electrons at the used quartz substrate compared to the MgO capping layer. This explanation could also be applied to the Gd_xFe_{1-x} single samples on Al_2O_3 substrates with Si_3N_4 capping layers used here. However, it is puzzling that the contribution is not increased for the bilayer sample with $x = 0.8$, as the difference between the reflectivities for the electrons of the Al_2O_3 substrate and the Pt layer is expected to be enhanced compared to the difference between the substrate and the Si_3N_4 capping layer. A possibility to further investigate the emission mechanism would be to use single-layer Gd_xFe_{1-x} samples with a metallic capping layer that has a small spin Hall angle, such as, for example, Cu. In the emission scenario explained above, the strongly modified reflectivity of the excited electrons at the Gd_xFe_{1-x}/Cu interface (compared to the Gd_xFe_{1-x}/Si_3N_4 interface) would be expected to lead to an enhanced THz signal. A different reason for the generation of a spin current in the Gd_xFe_{1-x} layer could also be given by a possible composition gradient in the film growth direction. This would lead to a spin current from the more Fe-rich side toward the more Gd-rich side of the layer. Such a composition gradient could be revealed, for example, by EDX cross-section images measured by transmission electron microscopy. However, the explanation of the shown results is still an ongoing research topic and beyond the scope of this work.

8.4.3 Composition dependence of the terahertz amplitude

In analogy to the studies on Pt/Tb_xFe_{1-x} emitters, the THz emission amplitude of the Pt/Gd_xFe_{1-x} emitters has been investigated in dependence on the Gd content. The results for an applied magnetic field $\mu_0 H = 200\,\mathrm{mT}$ are shown in comparison to the results of the Pt/Tb_xFe_{1-x} series in figure 8.9a. The amplitude of the Pt/Fe sample ($x = 0$) has been corrected by subtraction of the contribution to the THz signal caused directly by the ultrafast demagnetization of the Fe layer. It should be mentioned here that, despite the clear change of the THz signals between $x = 0.4$ and $x = 0.6$, the THz peak-to-peak amplitudes have been used for the comparison of the different samples because the amplitudes of the paramagnetic samples are rather small compared to the background noise, and accordingly, the RMS amplitudes of these samples would have overestimated the real amplitudes. The Pt/Gd_xFe_{1-x} samples show higher THz amplitudes compared to the Pt/Tb_xFe_{1-x} samples. This can be explained by the higher impedance values (see figure 8.5b) and, accordingly, higher THz emission efficiencies of the Pt/Gd_xFe_{1-x} samples as well as by the smaller perpendicular magnetic anisotropies compared to the Pt/Tb_xFe_{1-x} samples. With rising Gd content, the amplitudes show a substantial increase between $x = 0$ and $x = 0.05$, followed by a plateau up to $x \approx 0.3$. This plateau in the amplitudes is caused by a competition of the increasing THz emission efficiencies with the decreasing number of excitable Fe electrons with rising Gd content. For higher Gd contents ($x \geq 0.4$), the amplitudes strongly decrease

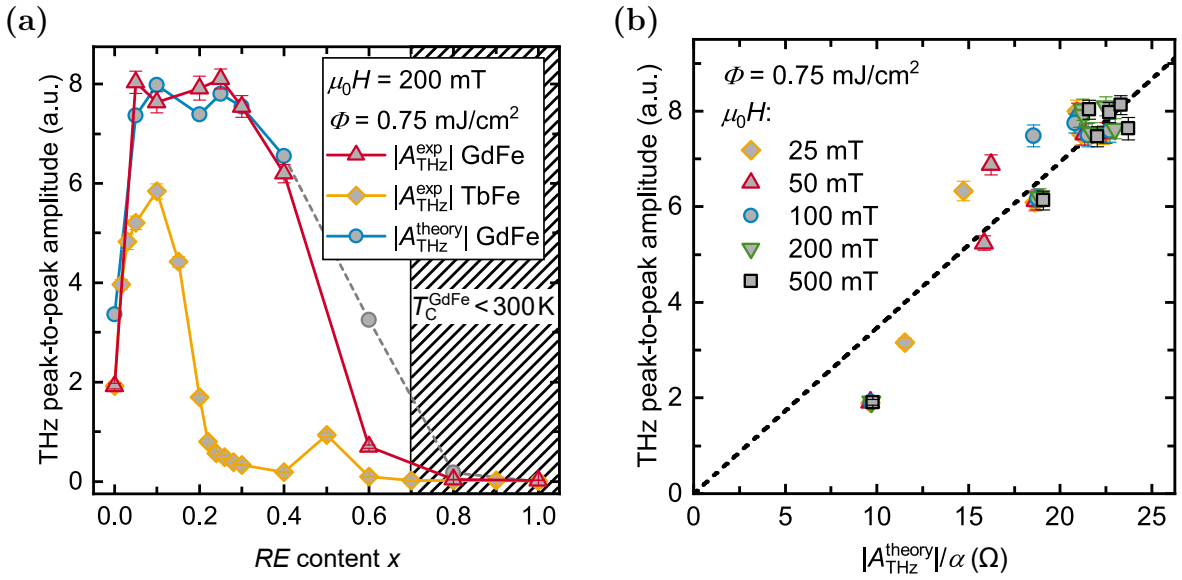

Figure 8.9: (a) shows the THz peak-to-peak amplitudes of *sub.*/Pt(5 nm)/Gd_xFe_{1-x}(20 nm)/Si_3N_4(5 nm) samples (red triangles) in comparison to *sub.*/Pt(5 nm)/Tb_xFe_{1-x}(20 nm)/Si_3N_4(5 nm) samples (yellow diamonds) in dependence on the rare-earth content x. The THz amplitudes $|A_{\mathrm{THz}}^{\mathrm{exp}}|$ were measured at room temperature with a pump fluence $\Phi = 0.75\,\mathrm{mJ/cm^2}$ and an applied magnetic field $\mu_0 H = 200\,\mathrm{mT}$. The error bars represent the statistical error of the peak-to-peak amplitudes and an additional error of 1.8% that is caused by small variations in the mounting of the samples. The blue circles display the results of the model $|A_{\mathrm{THz}}^{\mathrm{theory}}|$, described in detail in subsection 7.4.3, applied to the Pt/Gd_xFe_{1-x} sample series. For the values marked in gray, the assumptions of the model are expected to be invalid. The shaded area marks compositions for which the Curie temperature of the Pt/Gd_xFe_{1-x} samples is below 300 K. (b) displays the THz peak-to-peak amplitudes measured for samples with $x \leq 0.4$ with different applied magnetic fields H in dependence on $|A_{\mathrm{THz}}^{\mathrm{theory}}|$ divided by α. The dashed line represents a linear fit with the slope α.

due to the lower Fe contents in the samples and the lower spin polarization as the samples become more and more paramagnetic.

Also, for the Pt/Gd_xFe_{1-x} sample series, the phenomenological model described by equation 7.2, which has been developed for the Pt/Tb_xFe_{1-x} sample series (see subsection 7.4.3), can be used to model the THz amplitudes in dependence on the Gd content x. For the saturation magnetization M_{S}, the values measured with an in-plane applied field $\mu_0 H = 7\,\mathrm{T}$ were used except for the samples with $x = 0.25$ and $x = 0.3$. In these samples, a spin-flop transition leads to an increase in the magnetic moments for high applied fields. Therefore, the highest magnetization values for applied magnetic fields below the spin-flop transition were used instead, as these values represent the FI saturation state. The proportionality factor α in equation 7.2 has been determined by fitting the model to the THz peak-to-peak amplitudes of the samples with $x \leq 0.4$, as for samples with $x \geq 0.6$, most probably a different THz emission mechanism plays a major role (see the previous subsection). Values measured with different external magnetic fields H were applied for all samples. Fig-

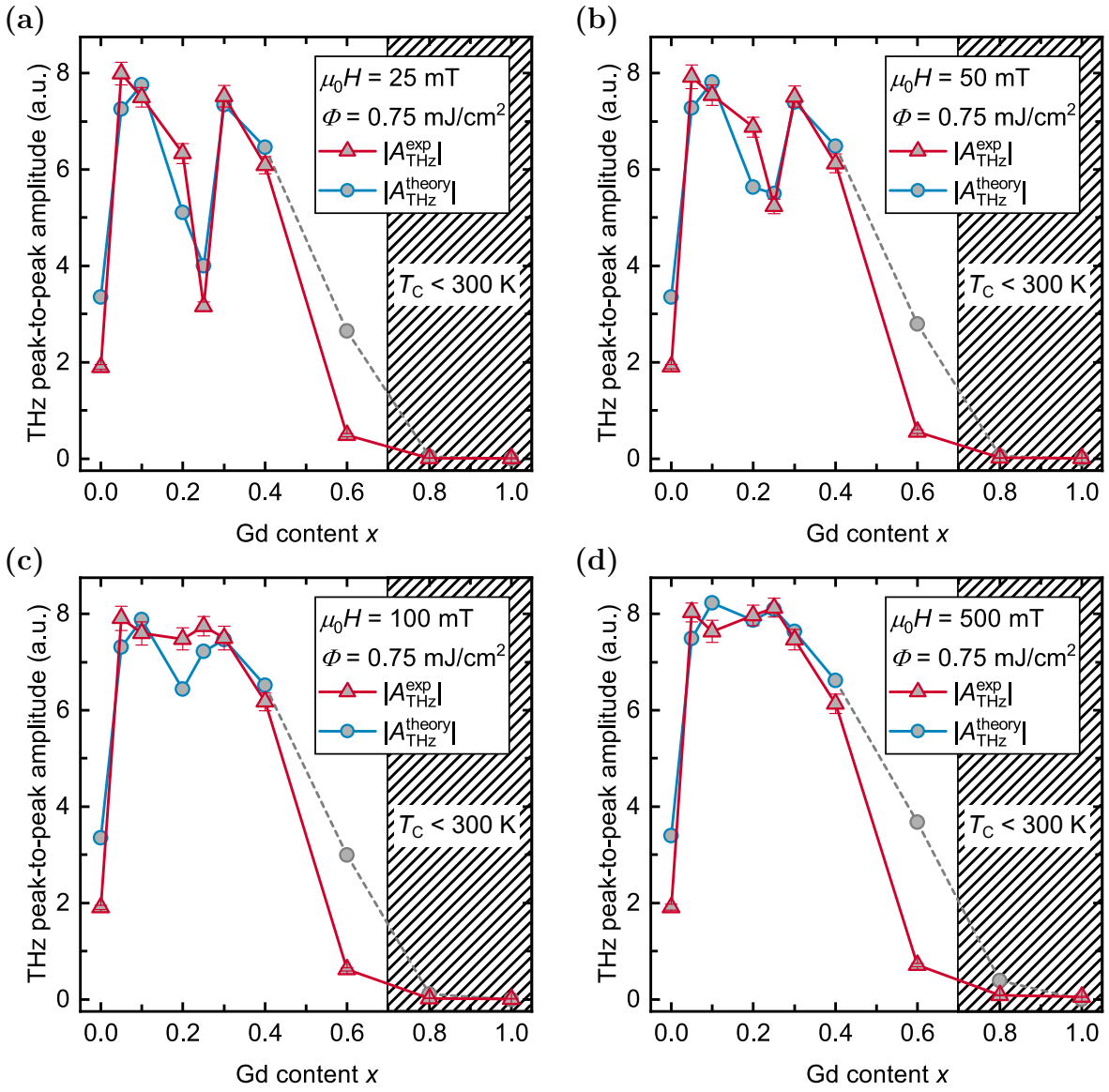

Figure 8.10: Room-temperature THz peak-to-peak amplitudes (red triangles) of *sub.*/Pt(5 nm)/Gd_xFe_{1-x}(20 nm)/Si_3N_4(5 nm) samples with respect to the Gd content x measured at different applied magnetic fields H with a laser pump fluence $\Phi = 0.75\,\mathrm{mJ/cm^2}$. The error bars represent the statistical error of the peak-to-peak amplitudes and an additional error of 1.8% that is caused by small variations in the mounting of the samples. The blue circles display the results of the model $|A_{\mathrm{THz}}^{\mathrm{theory}}|$, which is described in detail in subsection 7.4.3, applied to the Pt/Gd_xFe_{1-x} sample series. For the values marked in gray, the assumptions of the model are expected to be invalid. The shaded area marks the composition region for which the Gd_xFe_{1-x} layers are paramagnetic at room temperature.

ure 8.9b shows the THz peak-to-peak amplitudes for the used magnetic fields in dependence on $|A_{\mathrm{THz}}^{\mathrm{theory}}(x)|/\alpha = (1-x)\cdot Z(x)\cdot M(x,H)/M_{\mathrm{S}}$. The dashed line shows a linear fit that was applied to the THz amplitudes. The intercept with the THz amplitude axis was set to zero. The slope of the fit represents the proportionality factor α. The modeled values $|A_{\mathrm{THz}}^{\mathrm{theory}}|$ for an applied magnetic field $\mu_0 H = 200\,\mathrm{mT}$ are shown in figure 8.9a with blue circles. The

modeled amplitudes of samples with $x \geq 0.6$, for which the assumptions of the model are expected not to be fully valid anymore, are marked in gray.

Figure 8.10 shows the THz peak-to-peak amplitudes measured with different applied magnetic fields in comparison to the model. The model shows good agreement with the measured amplitudes for $x \leq 0.4$. For small applied magnetic fields $\mu_0 H \lesssim 100\,\mathrm{mT}$, the out-of-plane magnetic easy axis of the samples with $x = 0.2$ and $x = 0.25$ leads to a reduction of the THz amplitude, as the magnetic saturation in the in-plane direction is not reached. This feature is well resolved in the modeled values. In comparison to the Pt/Tb_xFe_{1-x} emitters, the Gd and Fe magnetic sublattices are antiparallel aligned for $\mu_0 H \leq 500\,\mathrm{mT}$ and no canted states are expected. Therefore, M/M_S gives a better approximation for the in-plane alignment of the Fe magnetic moments. For $x \geq 0.6$, the model deviates from the measured amplitudes. Here, the assumptions that the THz signal is caused only by a spin-to-charge current conversion in the Pt layer via the inverse spin Hall effect and that the spin current is only driven by the excitation of spin-polarized Fe electrons are not valid anymore.

8.5 Low-temperature results

Also, for the Pt/Gd_xFe_{1-x} series, investigations on the magnetic and THz emission properties at low temperatures have been performed. SQUID-VSM $M(H)$ loops at $T = 79\,\mathrm{K}$ were recorded in in-plane and out-of-plane direction (see appendix A.4, figure A.13), and the effective magnetic anisotropy K_{eff} has been estimated. Figure 8.11 shows (a) the K_{eff} and (b)

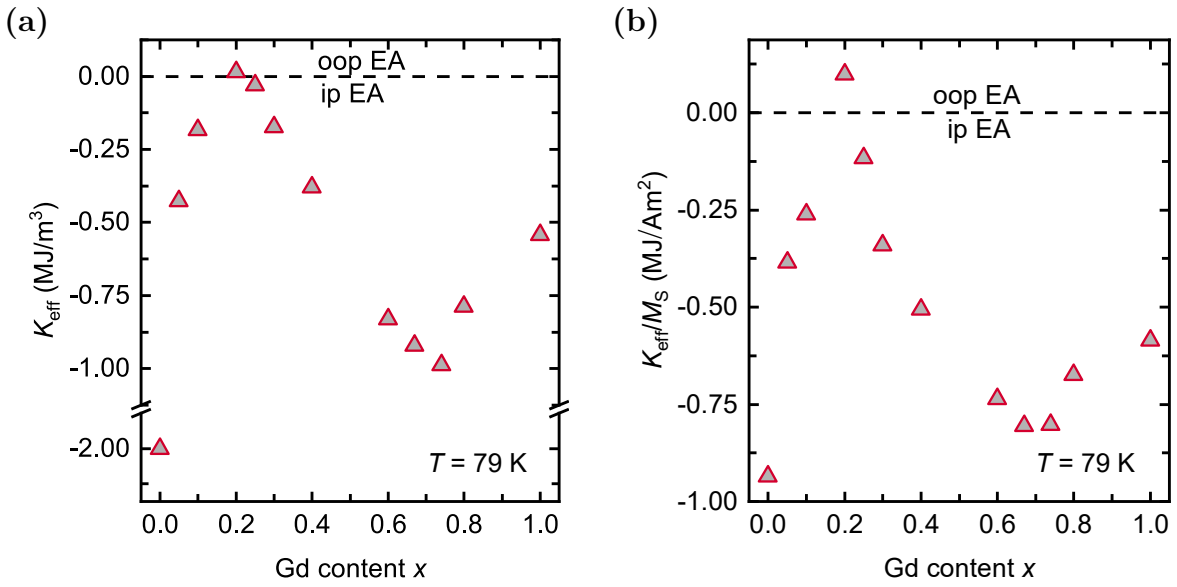

Figure 8.11: (a) shows the effective magnetic anisotropy K_{eff} of *sub.*/Pt(5 nm)/Gd_xFe_{1-x}(20 nm)/Si_3N_4(5 nm) samples at $T = 79\,\mathrm{K}$, calculated from $M(H)$ loops that were measured in in-plane and out-of-plane direction, with respect to the Gd content x. The K_{eff} values divided by the saturation magnetization M_S are displayed in (b).

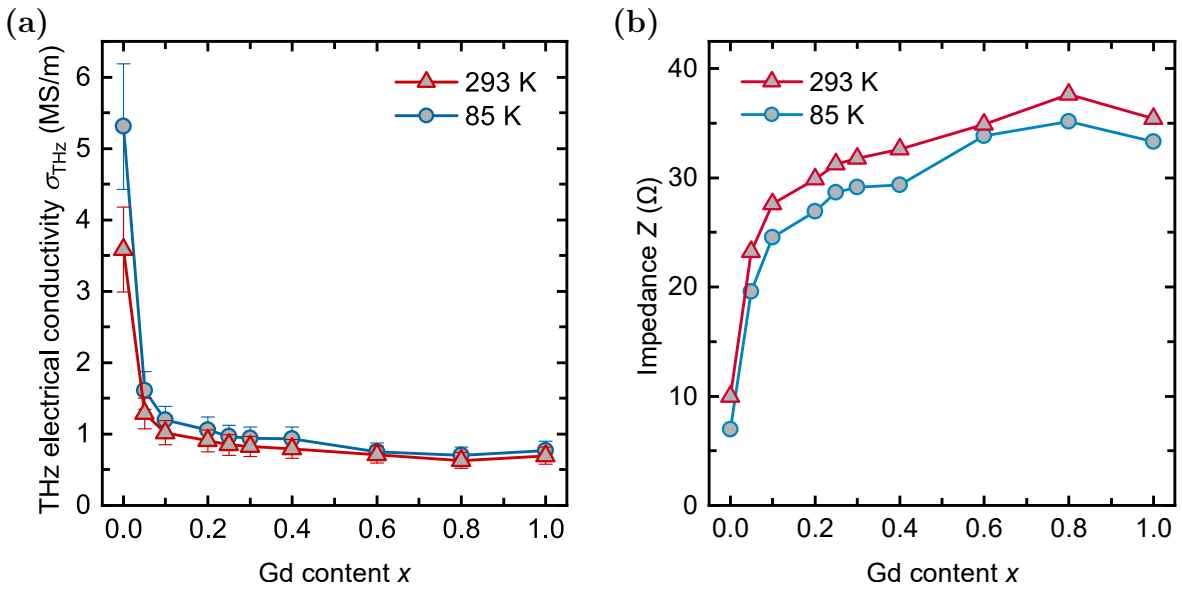

Figure 8.12: (a) shows the THz electrical conductivities (the error bars are mainly derived from the assumed uncertainty of the film thicknesses) and (b) the impedance values of *sub.*/ Pt(5 nm)/Gd_xFe_{1-x}(20 nm)/Si_3N_4(5 nm) samples measured at room temperature and 85 K with respect to the Gd content x.

the $K_{\mathrm{eff}}/M_{\mathrm{S}}$ values in dependence on the Gd content x. The Gd content x_{comp} for which the Gd_xFe_{1-x} layer is magnetically compensated shifts toward lower x with decreasing temperatures. At $T = 79\,\mathrm{K}$, only the sample with $x = 0.2$, which has the composition closest to x_{comp} and therefore the lowest M_{S}, shows an out-of-plane magnetic easy axis. The samples with high Gd content ($x \geq 0.67$), which are paramagnetic at room temperature, show a strong in-plane magnetic easy axis in their FI (or FM, for $x = 1$) state at low temperatures.

The electrical conductivities in the THz frequency regime as well as the THz emission properties at 85 K have been determined by Dr. Robert Schneider at the University of Münster (see section 5.6 and [299] for details on the measurement setups). Figure 8.12 shows (a) the THz conductivity σ_{THz} and (b) the impedance Z in dependence on the Gd content x in comparison with the room-temperature results. A similar qualitative dependence of σ_{THz} and Z on x as for the room-temperature measurements can be observed. However, at 85 K, the conductivity of the samples is slightly increased, and accordingly, the impedance slightly decreased. The absorption of the laser pump pulses has been measured to be independent on x also at $T = 85\,\mathrm{K}$ with a similar value as at room temperature (see appendix A.4, figure A.14). Therefore, also at low temperatures, the impedance $Z(x)$ is proportional to the THz emission efficiency $C(x, \omega)$. Figure 8.13 shows the low-temperature THz emission spectroscopy results, measured with a pump fluence $\Phi = 0.75\,\mathrm{mJ/cm^2}$ and an applied in-plane magnetic field $\mu_0 H = 103\,\mathrm{mT}$. The shape of the measured THz signals displayed in figure 8.13a shows a comparable dependence on the Gd content x as at room temperature. Also, at low temperatures, a signal inversion can be observed between the samples with $x = 0.2$ and $x = 0.25$,

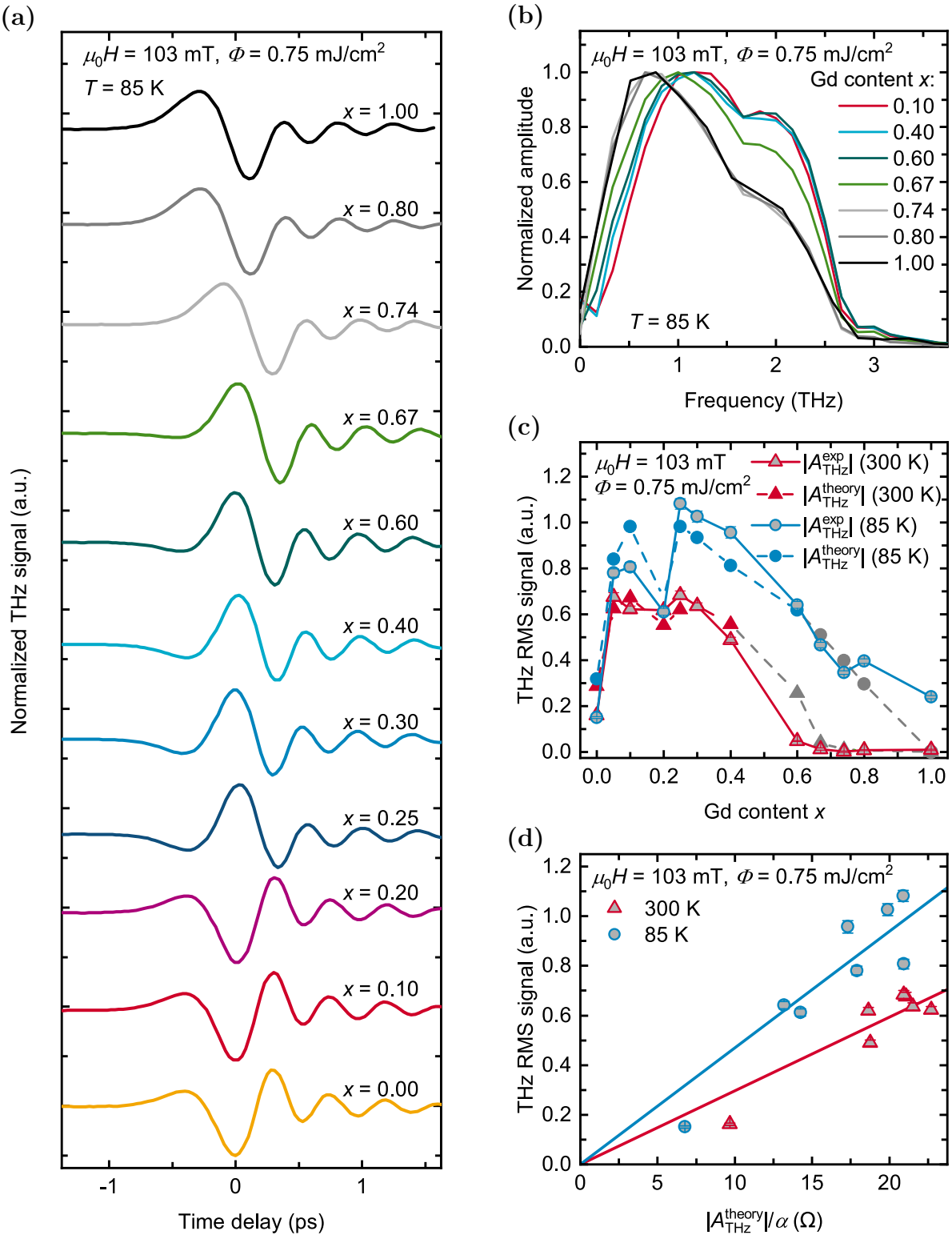

Figure 8.13: THz emission results of *sub.*/Pt(5 nm)/Gd_xFe_{1-x}(20 nm)/Si_3N_4(5 nm) samples measured at $T = 85\,\mathrm{K}$ with an applied in-plane magnetic field $\mu_0 H = 103\,\mathrm{mT}$ and a laser pump fluence $\Phi = 0.75\,\mathrm{mJ/cm^2}$. (a) shows the normalized THz electro-optic signals and (b) the corresponding frequency spectra. (c) displays the THz RMS amplitudes $|A_{\mathrm{THz}}^{\mathrm{exp}}|$ in comparison to the room-temperature measurements as well as the results of the model $|A_{\mathrm{THz}}^{\mathrm{theory}}|$ (values for which the assumptions are expected to be invalid are marked in gray). (d) shows the linear fits that were applied to determine α. The error bars represent the statistical error of the RMS signals and an additional error of 1.8% that is caused by small variations in the mounting of the samples.

which can be attributed to the magnetic compensation point (see figure 8.3). As the samples with $x > 0.6$ change from a paramagnetic state at room temperature to a FI (or FM, for $x = 1$) state at low temperatures, the measured THz signals are significantly stronger at 85 K. Interestingly, the change of the signal shape that could be observed at room temperature between $x = 0.4$ and $x = 0.6$ is shifted to slightly higher Gd contents at low temperatures. The transition appears between $x = 0.6$ and $x = 0.74$ and is also reflected in a shift toward lower frequencies in the corresponding frequency spectra shown in figure 8.13b. The THz amplitudes in dependence on x are displayed in figure 8.13c in comparison with the room-temperature results. As the signal shape significantly differs for samples with $x \leq 0.6$ compared to samples with $x \geq 0.74$, the THz RMS signals have been used for the comparison of the amplitudes of the different samples. The low-temperature results show a similar qualitative dependence on x as the room-temperature amplitudes. However, despite the lower THz emission efficiencies at $T = 85\,\mathrm{K}$ (see figure 8.12b), especially the samples with high Gd content show significantly larger amplitudes. Even the Pt/Gd sample ($x = 1$) shows a higher amplitude than the Pt/Fe sample ($x = 0$). Thus, the assumption that the THz signal is caused mainly by laser-excited Fe electrons is proven to be wrong for samples with high Gd content at low temperatures. Nevertheless, the model $|A_{\mathrm{THz}}^{\mathrm{theory}}|$ (equation 7.2) has been applied to describe the THz amplitudes measured at low temperatures, as for $x \leq 0.6$ the assumptions still seem to be justified. Therefore, the values of $M(103\,\mathrm{mT})/M_{\mathrm{S}}$ and Z measured at 79 K and 85 K, respectively, have been applied to the model. The M_{S} values of all samples were taken from the $M(H)$ loops at in-plane applied magnetic fields $\mu_0 H = 7\,\mathrm{T}$ except for the samples with $x = 0.2$ and $x = 0.25$. For these samples, the highest magnetization values for applied magnetic fields below the occurring spin-flop transition were used instead. The proportionality factor α has been derived by fitting the model to the measured amplitudes of the samples with $x \leq 0.6$ (and $x \leq 0.4$ for the room-temperature measurements). Figure 8.13d shows the THz RMS amplitudes of these samples measured at $T = 85\,\mathrm{K}$ in dependence on $|A_{\mathrm{THz}}^{\mathrm{theory}}|/\alpha$ in comparison to the amplitudes of the samples with $x \leq 0.4$ measured at room temperature. The lines display the applied linear fits. α is represented by the slope of the respective fit. At $T = 85\,\mathrm{K}$, the proportionality factor α is increased by 58% compared to the room-temperature results. This could be explained by a higher spin polarization at low temperatures that is only reflected in the model in the factor α. Furthermore, also the spin Hall angle of the Pt layer $\theta_{\mathrm{sh,\,Pt}}$ and the relaxation length of the spin current $\boldsymbol{J}_{\mathrm{s}}$ within the Pt layer $\lambda_{\mathrm{rel,\,Pt}}$ that are included in this factor could show a temperature dependence. At $T \approx 80\,\mathrm{K}$, Isasa *et al.* [295] measured an increase in $\lambda_{\mathrm{rel,\,Pt}}$ by $\approx 25\%$ compared to room temperature, whereas $\theta_{\mathrm{sh,\,Pt}}$ almost did not change within that temperature region. The results of $|A_{\mathrm{THz}}^{\mathrm{theory}}|$ for room temperature and $T = 85\,\mathrm{K}$ are plotted in figure 8.13c. The values for which the assumptions of the model are expected to be invalid are marked in gray. Also, at low temperatures, the model fits surprisingly well to the measured amplitudes up to a Gd content $x \approx 0.8$ and only strongly deviates from the measured amplitudes for the pure Gd/Fe

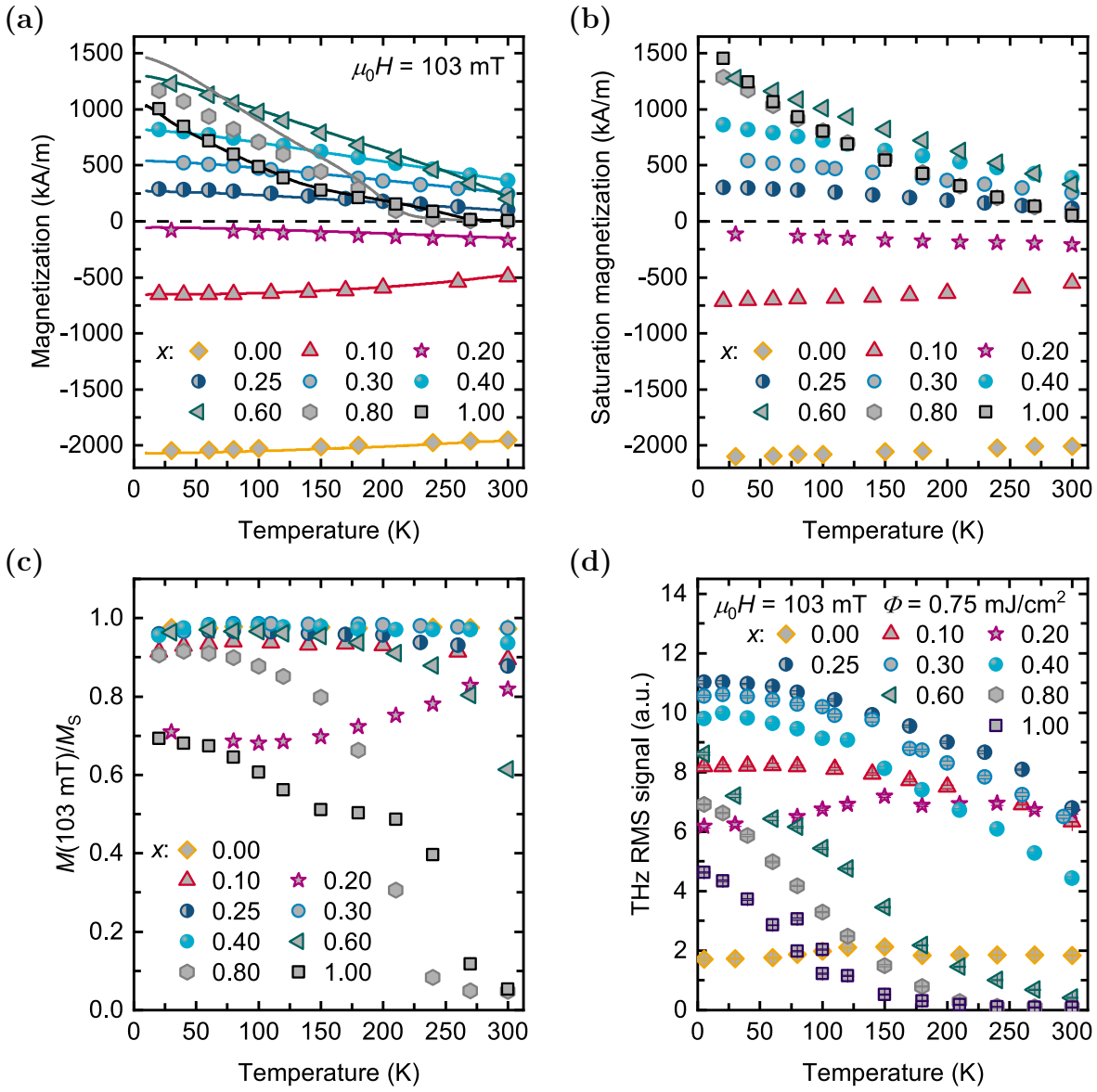

Figure 8.14: Temperature series of *sub.*/Pt(5 nm)/Gd_xFe_{1-x}(20 nm)/Si_3N_4(5 nm) samples with different Gd content x measured from room temperature down to $T = 5$ K. (a) shows the magnetization values measured with an in-plane applied magnetic field $\mu_0 H = 103$ mT. The symbols are the values taken from $M(H)$ loops measured at different temperatures (not shown). The lines were measured in a temperature sweep mode from $T = 300$ K to 5 K. (b) displays the saturation magnetization M_S taken from the $M(H)$ loops. (c) shows the ratio between $M(103\,\mathrm{mT})$ and M_S. The THz RMS amplitudes measured with a laser pump fluence $\Phi = 0.75\,\mathrm{mJ/cm^2}$ and an applied in-plane magnetic field $\mu_0 H = 103$ mT are displayed in (d). The error bars represent the statistical error of the RMS signals. Note that for $T < 100$ K, a separate temperature series was measured in addition to the measurements from 300 K to 80 K. For the sample with $x = 1$, an offset can be observed between the two measurement runs (see measurements at $T = 80$ K and 100 K), which might have been caused by the aging of the sample.

sample ($x = 1$). However, as a consequence of the fitting procedure used for the determination of α, the amplitudes of samples with a Fe-dominated net magnetization are slightly

overestimated, whereas the amplitudes of samples with a Gd-dominated net magnetization are slightly underestimated by the model. The high amplitude of the sample with $x = 1$ cannot be explained by the current model. Obviously, spin-polarized Gd electrons seem to play an important role here.

Additionally to the results discussed above, also first temperature series from room temperature down to $T = 5\,\mathrm{K}$ of the magnetic properties and the spintronic THz emission of the samples have been recorded. A summary of these results is given in figure 8.14. All samples except the ones with $x = 0$ and $x = 0.2$ show an increase in the THz amplitudes with decreasing temperatures. This can again be explained by a higher spin polarization at low temperatures, which is reflected in the higher magnetization values. Furthermore, the samples with high Gd content ($x \geq 0.8$) gradually change from the paramagnetic state at room temperature to a FI or FM (for $x = 1$) state at low temperatures. However, especially the strong increase in the amplitudes of the samples with $x \geq 0.6$ at lower temperatures could only be explained by an emission mechanism in which the Gd electrons are involved. The sample with $x = 0.2$ shows a slightly decreasing THz amplitude with falling temperatures. This is caused by a more preferred out-of-plane magnetic easy axis at lower temperatures. As the magnetization of the Gd magnetic sublattice increases with decreasing temperatures, the net magnetization of the sample decreases (as it is Fe-dominated at room temperature). Accordingly, the shape anisotropy also decreases with falling temperatures, and the effective magnetic anisotropy increases. The increasing K_{eff} is reflected in the decreasing values of $M(103\,\mathrm{mT})/M_{\mathrm{S}}$ for $x = 0.2$ (see figure 8.14c), as the sample cannot be fully magnetically saturated with the applied magnetic field $\mu_0 H = 103\,\mathrm{mT}$, leading in turn to the decrease in the THz amplitudes. For the Fe/Pt sample ($x = 0$), an almost constant THz amplitude can be observed for all temperatures.

To fully explain the results, temperature-dependent measurements of the electrical conductivity would be necessary. Furthermore, the model discussed above needs to be refined to include the influence of the Gd electrons. As indicated by the studies on the THz emission of $\mathrm{Gd}_x\mathrm{Fe}_{1-x}$ single layers at room temperature, also at low temperatures, other THz emission mechanisms besides the spin-to-charge current conversion via the inverse spin Hall effect in the Pt layer should be considered, especially for samples with high Gd content. However, this is a topic of ongoing research, and the development of a more sophisticated model and a more detailed discussion of the results is beyond the scope of this work.

8.6 Summary

In the presented study, the static magnetic properties, as well as the spintronic THz emission characteristics after excitation by femtosecond laser pulses of $\mathrm{Pt}(5\,\mathrm{nm})/\mathrm{Gd}_x\mathrm{Fe}_{1-x}(20\,\mathrm{nm})$ bilayers at room temperature have been systematically investigated in dependence on the Gd

content $0 \leq x \leq 1$ and compared to the Pt/Tb_xFe_{1-x} emitter system discussed in chapter 7. It could be shown that, similar to the Pt/Tb_xFe_{1-x} emitter system, the emitted terahertz signal is mainly caused by laser-excited spin-polarized Fe 3d electrons that give rise to a spin current into the Pt layer, where it becomes converted into a charge current pulse by the inverse spin Hall effect, leading to the emission of THz radiation. Accordingly, the emission amplitude follows the in-plane magnetization of the Fe magnetic sublattice of the Gd_xFe_{1-x} layers that gives a rough measure for the number of excitable spin-polarized 3d electrons. Therefore, also the Pt/Gd_xFe_{1-x} emitters show a composition-dependent inversion of the emitted THz signals that correlates with the magnetic compensation point. The composition dependence of the THz emission amplitude for different applied magnetic fields could be well described by the simple phenomenological model that has been developed to describe the amplitudes of the Pt/Tb_xFe_{1-x} samples. For samples with small Gd content $x \leq 0.05$, a substantial decrease in the electrical conductivity with increasing Gd content leads to a strong increase in the THz emission efficiency and, accordingly, the measured THz amplitude. In comparison to the Pt/Tb_xFe_{1-x} emitters, the magnetic anisotropy in Pt/Gd_xFe_{1-x} is smaller, and the alignment of the Gd and Fe magnetic sublattices is more collinear. Thus, these samples can be saturated with small applied magnetic fields. The magnetic anisotropy, which leads to a decrease in the THz emission amplitude of certain samples ($x = 0.2$ and $x = 0.25$) if small applied magnetic fields $\mu_0 H \leq 100\,\mathrm{mT}$ are used, is well resolved in the model. For high Gd contents $x \geq 0.6$, the samples become more and more paramagnetic at room temperature. Therefore, and due to the decreasing Fe contents, the THz signal gradually becomes smaller with rising x. In comparison to the Pt/Tb_xFe_{1-x} emitters, the Pt/Gd_xFe_{1-x} samples show, in general, higher THz signals that are caused by the higher THz emission efficiencies.

Besides the bilayer samples, also the THz emission of several single-layer $Gd_xFe_{1-x}(20\,\mathrm{nm})$ samples has been investigated in order to estimate the influence of the THz signal directly emitted by the ultrafast demagnetization of the magnetic layers. Here, only for the pure Fe layer, a significant contribution of about 14% of the THz signal of the bilayer samples has been found. However, for the single-layer samples with high Gd content ($x = 0.6$ and $x = 0.8$), the emitted THz signals that might be caused by the anomalous Hall effect give a significant contribution to the THz signal, that even overcomes the THz radiation that is caused by the inverse spin Hall effect in the Pt layer of the bilayer samples.

Furthermore, also temperature series from room temperature down to $T = 5\,\mathrm{K}$ have been performed on the Pt/Gd_xFe_{1-x} bilayers. The THz emission of Gd-rich samples is strongly enhanced at low temperatures, as the Gd_xFe_{1-x} layers that are in a paramagnetic state at room temperature become FI or FM (for $x = 1$) at low temperatures. For samples with $x \leq 0.6$, the composition dependence of the emitted THz radiation at $T \approx 80\,\mathrm{K}$ can still be well described by the developed model. However, for higher Gd contents, the THz signal significantly changes. Especially, the Pt/Gd sample ($x = 1$) shows a higher THz RMS

amplitude than the Pt/Fe sample ($x = 0$). Thus, the excitation of spin-polarized Gd electrons gives a significant contribution to the emitted signal.

The clarification of the origin of the emitted THz signals of the single-layer Gd_xFe_{1-x} samples with high Gd content $x > 0.6$ as well as the high THz signal of the bilayer samples with $x > 0.6$, especially at low temperatures, is a topic of ongoing research. In particular, the influence of the Gd electrons on the THz emission process and also other emission mechanisms like the anomalous Hall effect in Gd_xFe_{1-x} single layers, also at low temperatures, need to be investigated in further studies.

CHAPTER 9

Thermomagnetically switchable spintronic terahertz emitters

The THz emitting properties of the amorphous FI Gd_xFe_{1-x} layers combined with Pt discussed in chapter 8 can be applied in a material system with two FI Gd_xFe_{1-x} layers where the relative orientation of the Fe magnetic moments can be set by temperature in the presence of an external magnetic field. Depending on the relative alignment of the Fe moments, the spintronic emitter system can be either in a high- or in a low-amplitude THz emitting state. The development as well as the magnetic and THz emitting properties of such a system will be discussed in this chapter. The study opens a route for a new type of an efficient spintronic THz emitter system, which allows for a temperature-controlled switching of the emission state from high to low power.

The results were achieved in collaboration with Dr. Robert Schneider, Jannis Bensmann, Dr. Steffen Michaelis de Vasconcellos, and Prof. Rudolf Bratschitsch from the University of Münster and are predominantly published in [401].

9.1 Emitter concept

In the previous chapter, it has been shown that for $Pt(5\,nm)/Gd_xFe_{1-x}(20\,nm)$ systems with small Gd content ($x < 0.4$), mainly the Fe 3d electrons contribute to the spin current $\boldsymbol{J}_s$ that is launched from the Fe toward the Pt layer when the system is excited with femtosecond laser pulses. Therefore, an inversion of the emitted THz signal for samples where the net magnetization is dominated by the Gd compared to samples for which the net magnetization is dominated by the Fe magnetic moments can be observed. This characteristic was now used for the design of a five-layer spintronic THz emitter system with three THz emitting NM layers and two FI Gd_xFe_{1-x} layers. A schematic picture of the developed $Pt/Gd_{0.1}Fe_{0.9}/W/Gd_{0.3}Fe_{0.7}/Pt$ layer stack (without substrate and capping layer), as well as the excitation geometry that was used for the THz spectroscopy experiments is displayed in figure 9.1.

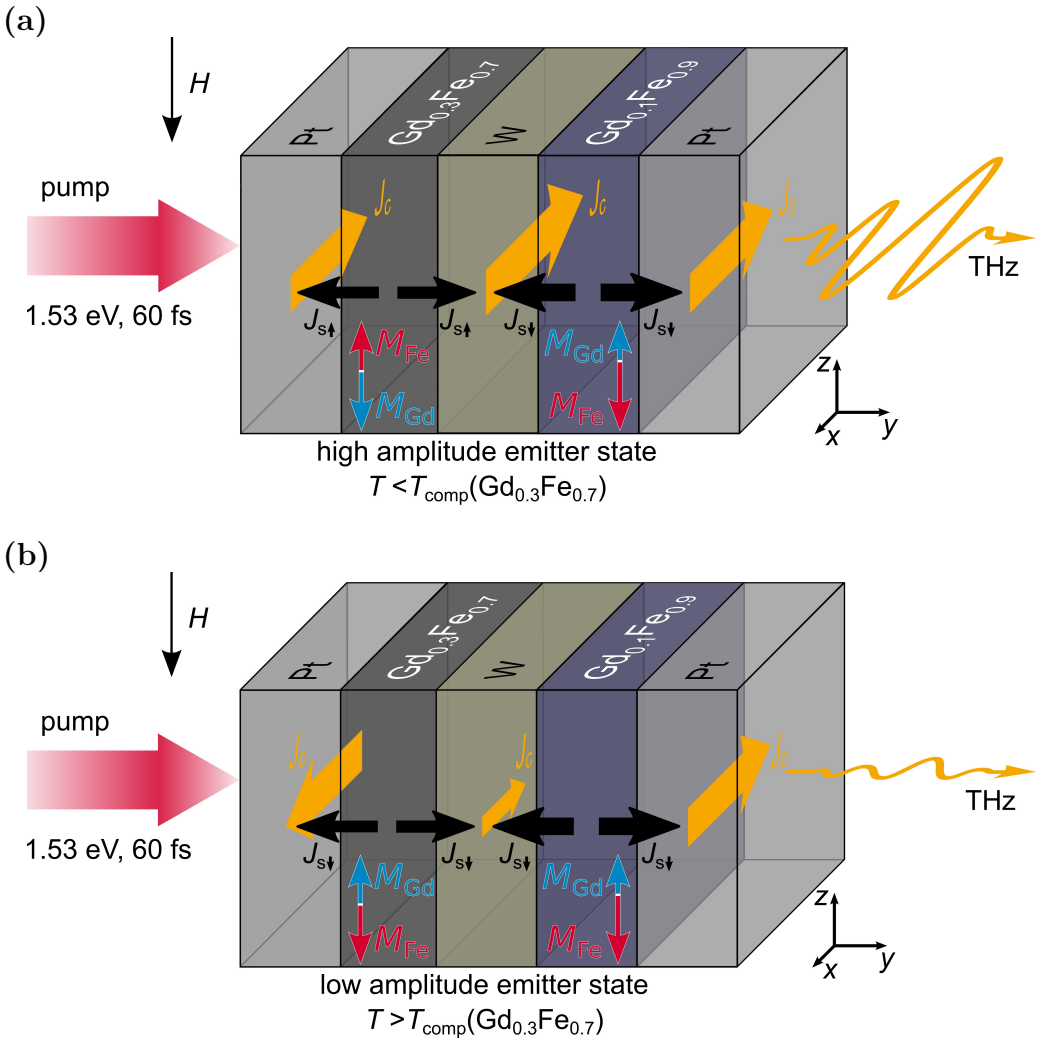

Figure 9.1: Illustration of the layer stacking and the excitation geometry for the THz emission spectroscopy. The excitation with a femtosecond laser pulse leads to the creation of spin currents $\boldsymbol{J}_\mathrm{s}$, caused mainly by Fe electrons of the FI $\mathrm{Gd}_x\mathrm{Fe}_{1-x}$ layers. In the Pt and W layers, the spin currents $\boldsymbol{J}_\mathrm{s}$ are converted into transverse charge currents $\boldsymbol{J}_\mathrm{c}$ due to the inverse spin Hall effect. W shows a negative spin Hall angle, whereas Pt exhibits a positive spin Hall angle. Note that only spin currents $\boldsymbol{J}_\mathrm{s}$ along with the layer stack (y-axis) are considered. Depending on the orientation of the Fe magnetic moments in the $\mathrm{Gd}_{0.3}\mathrm{Fe}_{0.7}$ layer, the system will be either (a) in a high-amplitude THz emitting state (for temperatures below the compensation temperature T_comp of the $\mathrm{Gd}_{0.3}\mathrm{Fe}_{0.7}$ layer) or (b) in a low-amplitude THz emitting state (for $T > T_\mathrm{comp}$), when the Fe moments of the two FI layers are aligned antiparallel or parallel, respectively.

The net magnetization of the $\mathrm{Gd}_{0.1}\mathrm{Fe}_{0.9}$ layer is dominated by the Fe magnetic moments for all temperatures. In contrast to that, the $\mathrm{Gd}_{0.3}\mathrm{Fe}_{0.7}$ layer shows a magnetic compensation point at the temperature T_comp if a suitable thickness is chosen, as will be discussed in detail later. At low temperatures ($T < T_\mathrm{comp}$), the net magnetization of this layer is dominated by the Gd magnetic moments, and therefore the Fe moments are aligned antiparallel to the external magnetic field H. For high temperatures ($T > T_\mathrm{comp}$), the net magnetization of the layer is

dominated by the Fe magnetic moments that will therefore be aligned parallel to the external magnetic field. Consequently, the relative alignment of the Fe magnetic moments of the two Gd_xFe_{1-x} layers can be controlled by temperature from antiparallel at low temperatures to parallel at high temperatures. Please note that instead of the used $Gd_{0.1}Fe_{0.9}$ layer, any FM layer suitable for use in spintronic THz emitters could be used.

When the system is excited by a femtosecond laser pump pulse, in the Gd_xFe_{1-x} layers, mainly the spin-polarized Fe 3d electrons are excited above the Fermi level, which gives rise to spin currents $\boldsymbol{J}_\mathrm{s}$ that flow into the neighboring W and Pt layers. Pt (positive spin Hall angle: $+1.2\% \leq \theta_\mathrm{sh} \leq +11\%$ [271, 294, 295]) and W (negative spin Hall angle: $-33\% \leq \theta_\mathrm{sh} \leq -7\%$ [296]) are well known for their large spin Hall angles and have been shown to be well suited for the use as THz emitting NM layers in spintronic THz emitter systems. [82, 300] In the case of antiparallel aligned Fe magnetic moments (for $T < T_\mathrm{comp}$, see figure 9.1a), the two spin currents $\boldsymbol{J}_\mathrm{s}$ injected into the Pt layers have opposite flow directions and spin polarizations. Also, the two spin currents $\boldsymbol{J}_\mathrm{s}$ injected into the W layer from the Gd_xFe_{1-x} layers have opposite signs in spin and current direction. Therefore, as Pt and W exhibit spin Hall angles with opposite signs, all four injected spin currents $\boldsymbol{J}_\mathrm{s}$ lead to charge currents $\boldsymbol{J}_\mathrm{c}$ in the NM layers in the same direction due to the inverse spin Hall effect, following $\boldsymbol{J}_\mathrm{c} \sim \theta_\mathrm{sh} \boldsymbol{J}_\mathrm{s} \times \boldsymbol{M}/|\boldsymbol{M}|$, where $\boldsymbol{M}$ denotes the corresponding magnetization of the Fe magnetic sublattices in the Gd_xFe_{1-x} layers. Thus, all three NM layers contribute constructively to the THz emission, which leads to a high-amplitude emitter state. In the case of parallel aligned Fe magnetic moments ($T > T_\mathrm{comp}$, see figure 9.1b), all spin currents $\boldsymbol{J}_\mathrm{s}$ have the same spin polarization. Therefore, the excited transverse charge currents $\boldsymbol{J}_\mathrm{c}$ in the two Pt layers flow in opposite directions due to the opposite current directions of the respective $\boldsymbol{J}_\mathrm{s}$. Furthermore, in the W layer, the two spin currents $\boldsymbol{J}_\mathrm{s}$ injected from the Gd_xFe_{1-x} layers contribute to the formation of $\boldsymbol{J}_\mathrm{c}$ with opposite signs. Consequently, the resulting THz pulse emitted by the three NM layers shows a low amplitude. The remaining signal derives only from the difference in the contributions of the two Gd_xFe_{1-x} layers due to the different amounts of excited Fe electrons.

9.2 Choice of suitable materials and layer thicknesses

To develop the five-layer system proposed above, a pre-study on a series of *sub.*/Pt(3 nm)/$Gd_{0.3}Fe_{0.7}(t)$/Si_3N_4(5 nm) samples with different $Gd_{0.3}Fe_{0.7}$ film thicknesses $1\,\mathrm{nm} \leq t \leq 10\,\mathrm{nm}$ that were prepared by magnetron sputtering at room temperature (see chapter 4 for details) has been performed. Gd, Pt, and Fe were deposited by DC sputtering. The $Gd_{0.3}Fe_{0.7}$ layers were prepared by co-sputtering from the elemental targets. For the Si_3N_4 capping layer, RF sputtering from a stoichiometric compound target was used. All depositions were done on 500 µm thick Al_2O_3(0001) substrates, polished on both sides, on which later on the THz

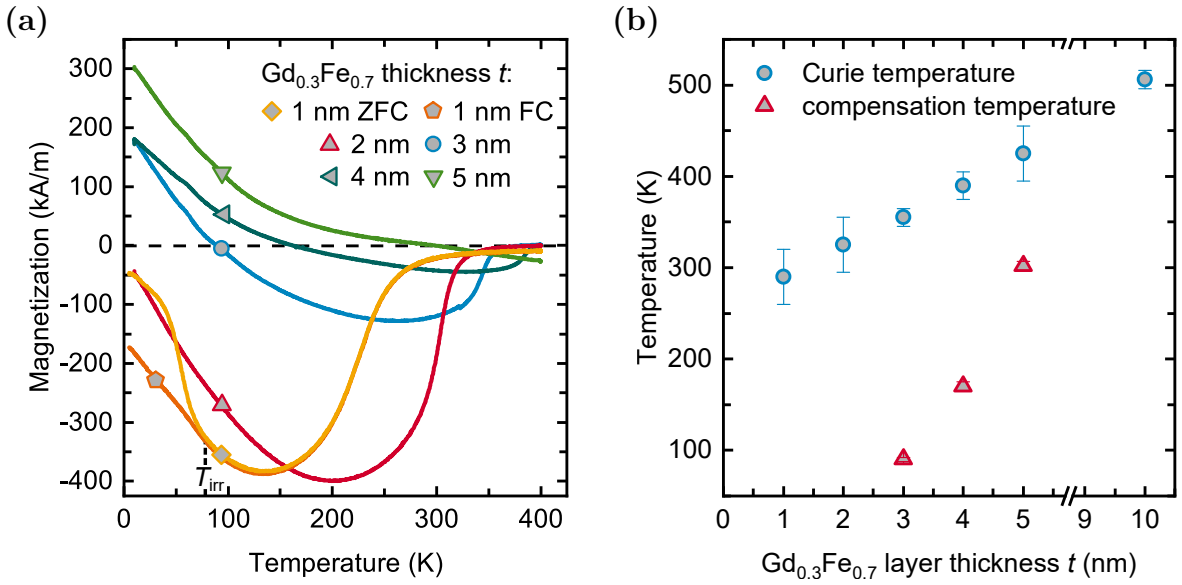

Figure 9.2: (a) $M(T)$ curves of *sub.*/Pt(5 nm)/$Gd_{0.3}Fe_{0.7}(t)$/Si_3N_4(5 nm) samples with different $Gd_{0.3}Fe_{0.7}$ film thicknesses t. Positive magnetization values represent Gd-dominated, whereas negative values represent Fe-dominated net magnetizations. The sample with $t = 1$ nm shows superparamagnetic behavior with an irreversibility temperature $T_{irr} \approx 80$ K. (b) shows the Curie temperature and the magnetic compensation temperature, extracted from $M(T)$ curves, for different layer thicknesses t. The shown errors were estimated from $M(T)$ measurements with different applied guiding fields.

spectroscopy was performed as well as on 525 µm thick Si(100) substrates with a 100 nm thick thermally oxidized SiO_2 layer on which the characterization of the magnetic properties was done. The aim of this study was to find a suitable layer thickness t, for which the $Gd_{0.3}Fe_{0.7}$ system shows a magnetic compensation point between 5 K and room temperature and ideally also shows a high THz emission amplitude. The compensation point of the $Gd_xFe_{1-x}(t)$ system is known to be strongly dependent on the composition but also on the method of preparation. [173, 184, 402–405] However, for thin films, the compensation point also shows a strong dependence on the layer thickness t. Therefore, as for smaller thicknesses the net magnetization of the layers becomes more Fe-dominated, the $Gd_{0.3}Fe_{0.7}$ composition was chosen as a starting point. The Pt layer not only acts as a THz emitting layer but also serves as a seed layer that, especially for the Si/SiO_2(100 nm) substrates, prevents the GdFe layers from reacting with the substrate and, therefore, also makes it possible to compare the experimental results from samples grown on the different substrates (see section 7.1 and appendix A.2, figure A.1).

For all of the prepared samples, SQUID-VSM $M(T)$ curves with different small applied guiding fields were recorded. The samples were first saturated with an applied in-plane magnetic field $\mu_0 H = 7$ T at room temperature, and then field cooled down to 10 K. Afterward, the field was reduced to a small value $\mu_0 H < 5$ mT, and the $M(T)$ curves were recorded from 10 K to 400 K in a temperature sweep mode. The results of the samples with 2 nm $\leq t \leq$ 5 nm

that were measured without an applied guiding field (effectively applied field $\mu_0 H \approx -4.5\,\mathrm{mT}$ due to trapped fluxes in the superconducting magnet of the MPMS3, see subsection 5.4.2) are shown in figure 9.2a. For the sample with $t = 1\,\mathrm{nm}$, field cooled and zero-field cooled $M(T)$ measurements have been performed, revealing a superparamagnetic behavior with an irreversibility temperature T_{irr} of about 80 K. These curves were measured in the following way: For the ZFC curve, the sample was cooled down in zero field from room temperature to 5 K, and then the magnetization was recorded with an applied in-plane magnetic field $\mu_0 H = 10\,\mathrm{mT}$ while warming up to 400 K. For the FC curve, the sample was cooled down from room temperature to 5 K in an applied in-plane magnetic field $\mu_0 H = 10\,\mathrm{mT}$. Then, the magnetization was recorded while warming up to 400 K with the magnetic field still applied. The results are also shown in figure 9.2a. For the 5 nm and 10 nm thick films, measurements from 300 K to 600 K were performed with the oven module of the MPMS3 in order to determine the Curie temperatures. The Curie temperature and the compensation point for the different $Gd_{0.3}Fe_{0.7}$ thicknesses t, extracted from the $M(T)$ curves, are shown in figure 9.2b. The errors for compensation points and Curie temperatures were estimated by the results of measurements with different applied guiding fields. A Curie temperature of about room temperature was observed for the 1 nm thin $Gd_{0.3}Fe_{0.7}$ layer, which increases almost linearly with the layer thickness up to 5 nm. No compensation point was detected for the thinnest layers of 1 nm and 2 nm. Thus, the net magnetization of these samples is Fe-dominated at all temperatures. For the thickest layer of 10 nm, no compensation point below the Curie temperature of about 500 K can be observed. Therefore, the net magnetization is Gd-dominated at all temperatures.

Additionally, THz emission spectroscopy measurements have been performed on all samples of the series. The THz spectroscopy results shown in this chapter have been measured by Dr. Robert Schneider and Jannis Bensmann in the group of Prof. Rudolf Bratschitsch at the University of Münster with the electro-optic sampling setup described in section 5.6. The THz electro-optic signals obtained at room temperature for an applied in-plane magnetic field of 200 mT and the corresponding RMS signals for the different $Gd_{0.3}Fe_{0.7}$ thicknesses t are shown in figures 9.3a and 9.3b, respectively. For $t \leq 4\,\mathrm{nm}$, the net magnetization of $Gd_{0.3}Fe_{0.7}$ is Fe-dominated, while for $t \geq 5\,\mathrm{nm}$, it is Gd-dominated at room temperature. Thus, the orientation of the Fe moments is reversed with respect to the direction of an applied magnetic field. As the spin current $\boldsymbol{J}_{\mathrm{s}}$ is dominated by the spin-polarized Fe electrons, the observed change in the sign of the THz waveforms between $t = 4\,\mathrm{nm}$ and $t = 5\,\mathrm{nm}$ corresponds to the thickness-dependent magnetic compensation point. [327, 394] For the applied magnetic field of $\mu_0 H = 200\,\mathrm{mT}$, the highest THz RMS signal was obtained for $t = 3\,\mathrm{nm}$ (see figure 9.3b). For $t = 1\,\mathrm{nm}$, the magnetic layer is in a paramagnetic state, as the Curie temperature is slightly below room temperature, resulting in a reduced THz signal. In figures 9.4a and 9.4b, the magnetization and THz RMS amplitudes with respect to the applied magnetic field for the

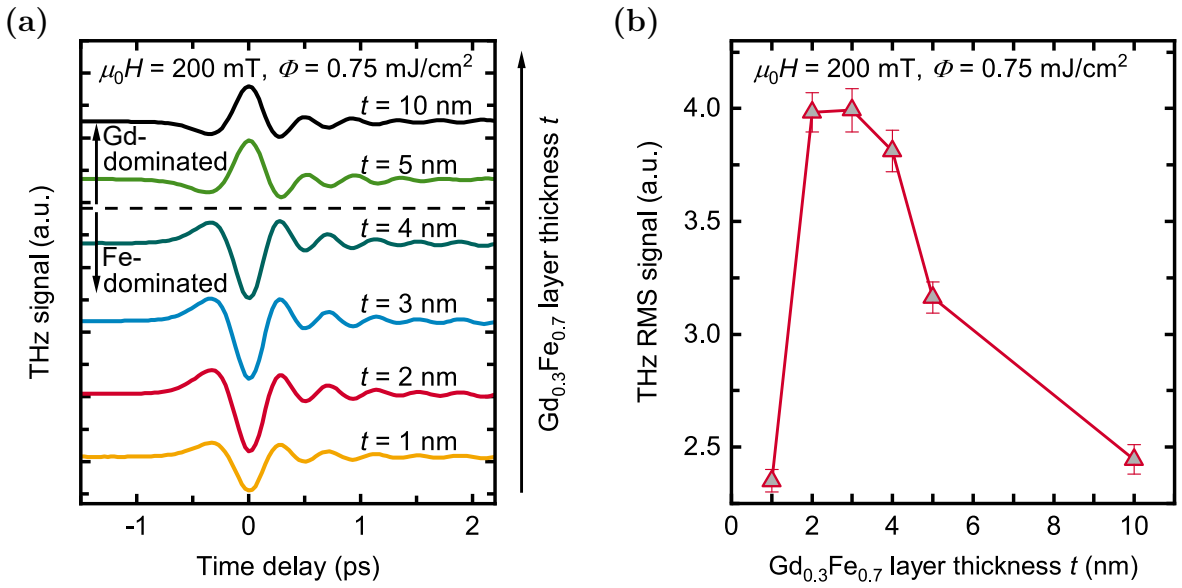

Figure 9.3: (a) THz electro-optic signals and (b) THz RMS signals of *sub.*/Pt(5 nm)/$Gd_{0.3}Fe_{0.7}(t)$/Si_3N_4(5 nm) samples with different $Gd_{0.3}Fe_{0.7}$ film thicknesses t measured at room temperature with an applied in-plane magnetic field of $\mu_0 H = 200$ mT and a laser pump fluence of $\Phi = 0.75$ mJ/cm^2. The error bars represent the statistical error of the RMS values and an additional error of 1.8% that is caused by small variations in the mounting of the samples. The RMS values are divided by a factor of 0.9 to compensate for the absorption of an additional polyethylene filter used in the room-temperature measurement setup. [299].

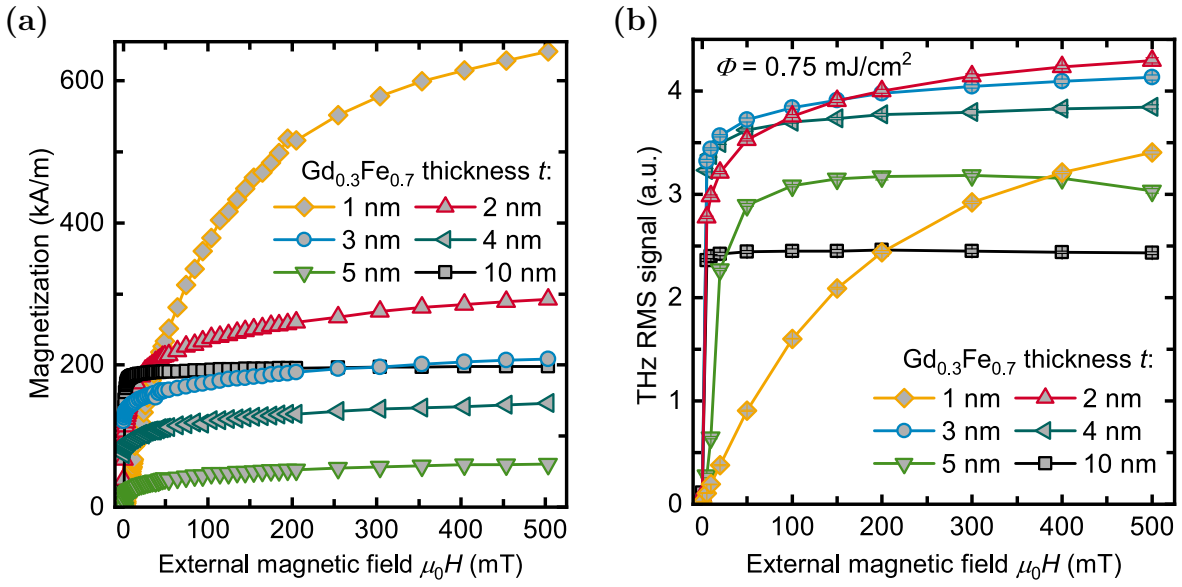

Figure 9.4: (a) $M(H)$ curves and (b) magnetic-field-dependent THz RMS signals of *sub.*/Pt(5 nm)/$Gd_{0.3}Fe_{0.7}(t)$/Si_3N_4(5 nm) samples with different $Gd_{0.3}Fe_{0.7}$ film thicknesses t measured at room temperature. For the THz spectroscopy measurements, a pump fluence of $\Phi = 0.75$ mJ/cm^2 was used. The RMS values are divided by a factor of 0.9 to compensate for the absorption of an additional polyethylene filter used in the room-temperature measurement setup. [299] The error bars represent the statistical error of the RMS values.

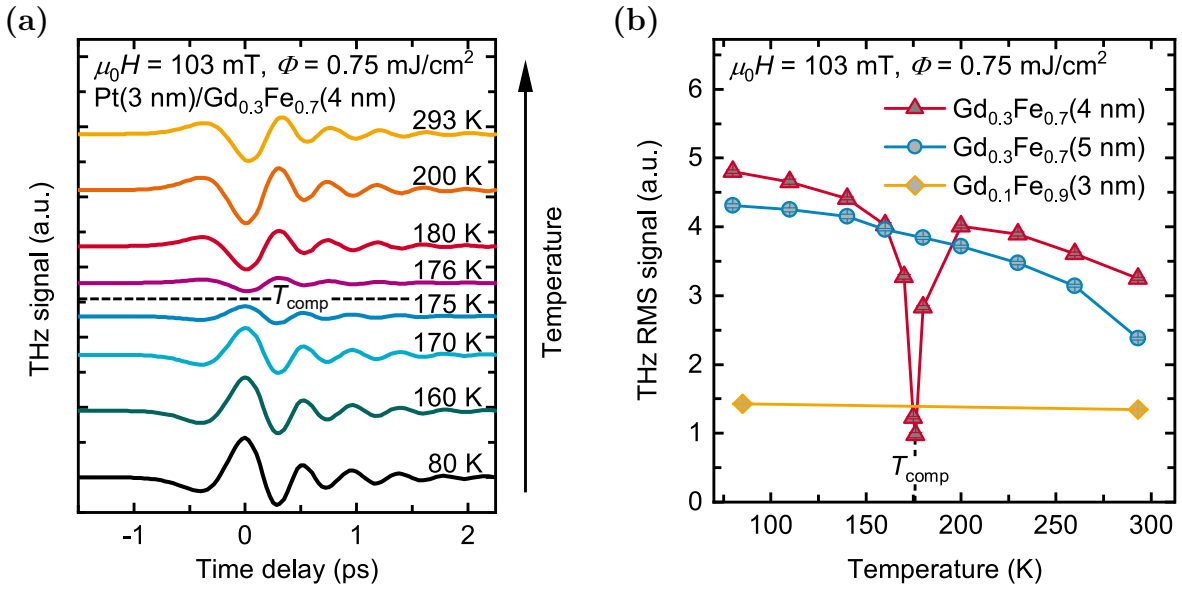

Figure 9.5: (a) THz electro-optic signals of a *sub.*/Pt(3 nm)/$Gd_{0.3}Fe_{0.7}$(4 nm)/Si_3N_4(5 nm) and (b) THz RMS signals of *sub.*/Pt(3 nm)/$Gd_{0.3}Fe_{0.7}(t)$/Si_3N_4(5 nm) (with t = 4 nm and t = 5 nm) and *sub.*/Pt(3 nm)/$Gd_{0.1}Fe_{0.9}(t)$/Si_3N_4(5 nm) samples measured at different temperatures with a pump fluence of $\Phi = 0.75\,\mathrm{mJ/cm^2}$ at an applied in-plane magnetic field of $\mu_0 H = 103\,\mathrm{mT}$. The RMS values were divided by a correction factor of 0.61 to compensate for the low-temperature measurement setup (mainly absorption losses of the emitted THz radiation at the 1 mm thick Al_2O_3 window of the cryostat [299, 406]). The error bars represent the statistical errors of the RMS values.

layer thicknesses 1 nm $\leq t \leq$ 10 nm are displayed. Similar to the Pt(5 nm)/Gd_xFe_{1-x}(20 nm) samples discussed in the previous chapter, the THz amplitude mainly follows the magnetization curves. The magnetization curves show the expected minimum for the sample with t = 5 nm, which reflects the compensation point that is close to room temperature. Additionally, temperature-dependent THz spectroscopy measurements have been performed on the samples with t = 4 nm and t = 5 nm. The measured THz electro-optic signals of the sample with t = 4 nm are displayed in figure 9.5a. Figure 9.5b shows the THz RMS signals in dependence on the temperature for the two samples. For the sample with t = 4 nm, the compensation point at $T_{comp} \approx 175\,\mathrm{K}$ can be observed, whereas the sample with t = 5 nm shows no compensation point below room temperature. Therefore, the THz spectroscopy results agree well with the magnetization measurements shown in figure 9.2. In order to generate a high-amplitude THz signal and to have a compensation point T_{comp} below room temperature, the $Gd_{0.3}Fe_{0.7}$ layer with a thickness of 3 nm was chosen for further investigations.

As the second magnetic layer, $Gd_{0.1}Fe_{0.9}$ with a thickness of 3 nm was exemplarily chosen for the proof of concept. As mentioned before, the net magnetization of that layer is dominated by the Fe magnetic moments for all temperatures (see also SQUID-VSM $M(T)$ curve in appendix A.5, figure A.15). The THz RMS amplitudes measured at 85 K and 293 K on a *sub.*/Pt(3 nm)/$Gd_{0.1}Fe_{0.9}(t)$/Si_3N_4(5 nm) sample that was prepared in the same way as described

above are shown in figure 9.5b. Between 5 K (not shown in the figure) and 293 K, the THz RMS amplitude of the sample only shows a small decrease of approximately 9.5%.

For the THz emitting Pt and W layers, thicknesses of 3 nm were chosen. For the Pt layers, this thickness has been found to show the highest THz amplitude in the thickness study on $Pt(t)/Co_{0.3}Fe_{0.7}(3\,nm)$ bilayers, discussed in section 6.2. For the W layer, it is important to mention here that it needs to be thick enough that the two Gd_xFe_{1-x} layers are sufficiently magnetically decoupled from each other. A detailed study on the interlayer coupling behavior for Pt and W interlayers (X) with different film thicknesses in a *sub.*/$Ir_{0.23}Mn_{0.77}(20\,nm)$/$Fe(3\,nm)/X/Fe(3\,nm)/Si_3N_4(5\,nm)$ spin-valve system is shown in section 10.2. Even a W layer thickness of only 2 nm has been shown to be sufficient to almost fully decouple the magnetic layers. A study by Wu *et al.* [300] on the thickness-dependent THz emission of W layers in *sub.*/$Co(4\,nm)/W(t)$ samples has shown increasing THz amplitudes for raising thicknesses up to 5 nm and the saturation of the amplitude for thicknesses from 5 nm to 10 nm. However, Seifert *et al.* [330] showed a maximum in the THz amplitude of *sub.*/ $Co_{0.4}Fe_{0.4}B_{0.2}(3\,nm)/W(t)$ samples for a W layer thickness of $t \approx 3$ nm. Furthermore, other studies on spintronic emitters with W layers, especially also on NM/FM/NM trilayer systems with NM materials with opposite spin Hall angles, used W thicknesses in the range from 1.8 nm to 4 nm [82, 310, 314, 315, 317]. Therefore, for this study, a W layer thickness of 3 nm was selected.

9.3 Demonstration of a thermomagnetically switchable emitter system

To demonstrate the functionality of the thermomagnetically switchable five-layer emitter system proposed above, *sub.*/$Pt(3\,nm)/Gd_{0.1}Fe_{0.9}(3\,nm)/W(3\,nm)/Gd_{0.3}Fe_{0.7}(3\,nm)/Pt(3\,nm)/Si_3N_4(5\,nm)$ samples were prepared by magnetron sputtering, with the parameters that were also used for the bilayer series. The Si_3N_4 layer prevents the spintronic layers from oxidation. For the magnetic measurements, depositions were performed on 525 µm thick p-doped Si(100) substrates with a 100 nm thick thermally oxidized SiO_2 layer on top. For the THz spectroscopy measurements, the spintronic emitters were sputtered on 500 µm thick $Al_2O_3(0001)$ substrates polished on both sides. To prove the emission scenarios presented in figure 9.1, temperature-dependent THz spectroscopy and magnetization measurements of the five-layer emitter system, both taken at an applied in-plane magnetic field $\mu_0 H = 103$ mT, were carried out. The results are presented in figure 9.6. The compensation point T_{comp} of the $Gd_{0.3}Fe_{0.7}$ layer can be observed as the minimum in the $M(T)$ curve in figure 9.6a at about 160 K. The shift of T_{comp} for the five-layer system compared to the $Pt/Gd_{0.3}Fe_{0.7}$ bilayer series toward higher temperatures can be explained by the different growth conditions of the $Gd_{0.3}Fe_{0.7}$ layer on W compared to Pt and by small deviations in the composition and film thickness.

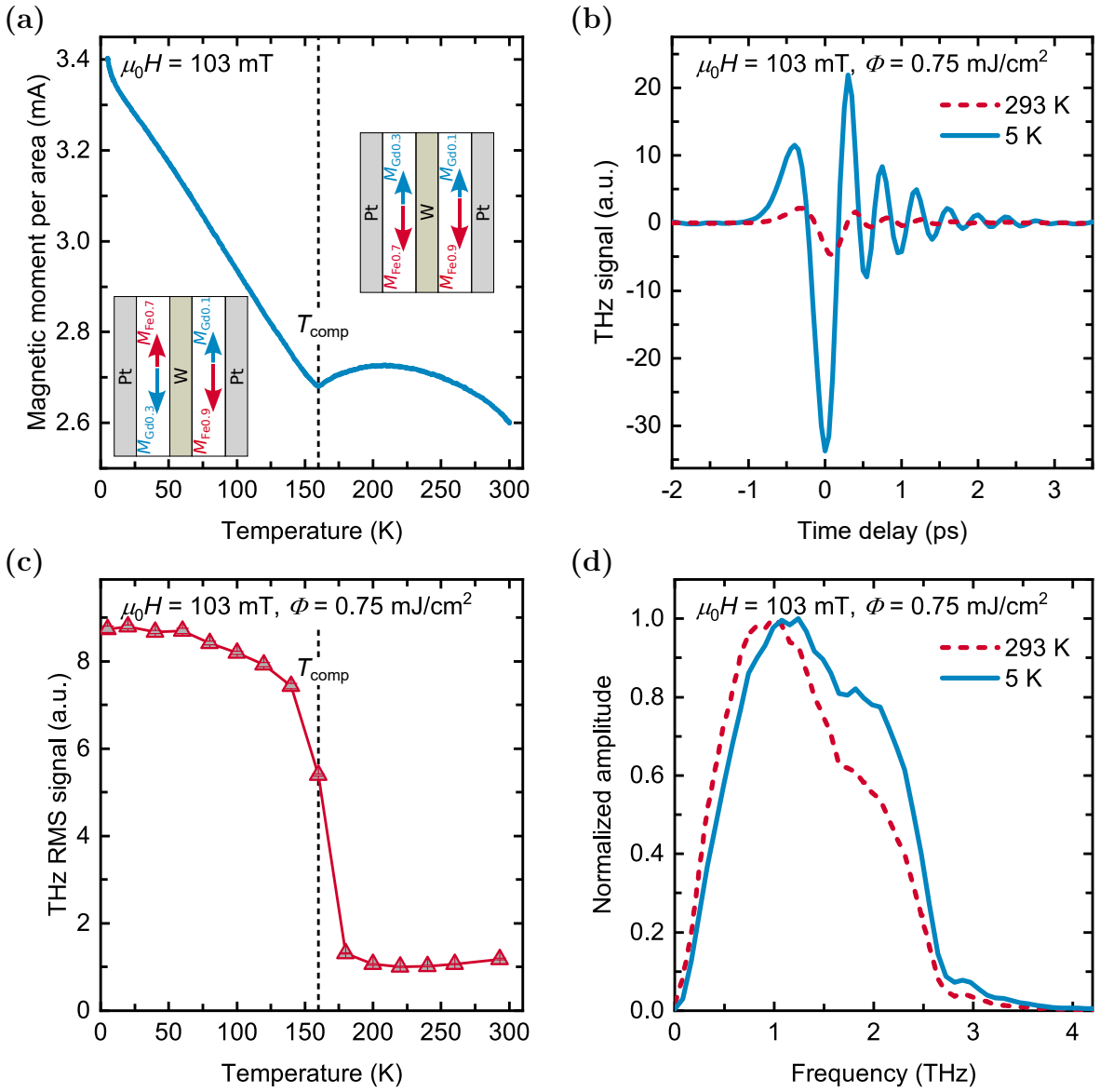

Figure 9.6: (a) Magnetic moment per area and (c) THz RMS signal (pump fluence $\Phi = 0.75\,\mathrm{mJ/cm^2}$) of a *sub.*/Pt(3 nm)/$Gd_{0.1}Fe_{0.9}$(3 nm)/W(3 nm)/$Gd_{0.3}Fe_{0.7}$(3 nm)/Pt(3 nm)/$Si_3N_4$(5 nm) sample measured at an applied in-plane magnetic field of $\mu_0 H = 103\,\mathrm{mT}$ for different temperatures. The minimum of the magnetic moment at 160 K and the strong reduction in the THz RMS signal can be attributed to the compensation point of the $Gd_{0.3}Fe_{0.7}$ layer, which is marked with the dotted line. The colored arrows in (a) show the schematic alignment of the magnetic moments of the Fe and Gd magnetic sublattices of the Gd_xFe_{1-x} layers for $T > T_{comp}(Gd_{0.3}Fe_{0.7})$ and $T < T_{comp}(Gd_{0.3}Fe_{0.7})$, respectively (see also figure 9.1). Note that the presented magnetic moments are normalized by the area of the films instead of the volume, as they derive from the two 3 nm thick Gd_xFe_{1-x} layers that contribute differently to the net moments. The error bars (within the symbols) represent the statistical errors of the RMS values. (b) and (d) display the THz electro-optic signal and the corresponding normalized spectrum for 5 K (high-amplitude emitter state) and 300 K (low-amplitude emitter state).

For $T < T_{\mathrm{comp}}$, the Fe moments of the FI layers in the five-layer emitter system are aligned antiparallel and therefore lead to a strong THz signal, while above the compensation point, the alignment is parallel, resulting in a drop in the THz signal by almost one order of magnitude (see figure 9.6c). The small remaining THz signal for temperatures above 160 K can be explained by the different Fe contents of the two FM layers. This behavior clearly confirms the emitter concept presented in section 9.1. Therefore, the emitter system allows to switch remotely from a high-amplitude THz emission state to a low-amplitude emission state via temperature. The THz electro-optic signals for the high- and low-amplitude emitter states and the corresponding frequency spectra are plotted in figures 9.6b and 9.6d, respectively. The measured electro-optic signal is not inverted for the two emitter states. Thus, the $Gd_{0.1}Fe_{0.9}$ contributes stronger to the signal than the $Gd_{0.3}Fe_{0.7}$ layer, a behavior that is expected due to the different amounts of Fe in the layers. Accordingly, also the increasing THz amplitude for high temperatures can be explained as the temperature dependence of the magnetization of the $Gd_{0.3}Fe_{0.7}$ layer is stronger compared to the $Gd_{0.1}Fe_{0.9}$ layer (see also figure 9.5). It should be mentioned here that in the bilayer studies shown in figure 9.5, the higher THz amplitude of the $Gd_{0.3}Fe_{0.7}$ layers compared to the $Gd_{0.1}Fe_{0.9}$ layer is caused by a lower electrical conductivity of these samples. Therefore, these amplitudes cannot be directly compared to the amplitudes of the five-layer system. The frequency spectrum shows a peak at lower frequencies in the high-temperature state compared to the low-temperature state. However, the origin of this frequency shift is so far not fully understood and has to be clarified in further studies.

9.4 Optimization of the emitter system

The emitter concept offers many possibilities for further optimizations. For instance, the switching temperature can be shifted toward higher or lower temperatures by adjusting the compensation point of the FI layer. This can be achieved by varying the film composition or film thickness. Besides, thinner layers or FM materials for the Fe-dominated Gd_xFe_{1-x} layer could be used to further increase the emission amplitude. In order to test the versatility of the emitter concept, two optimized layer stacks were prepared.

For the first sample, the aim was to achieve higher THz amplitudes by reducing the film thicknesses and using $Co_{0.4}Fe_{0.4}B_{0.2}$, which is well known as a highly efficient FM layer for the use in spintronic THz emitters [82], instead of the $Gd_{0.1}Fe_{0.9}$ layer. *Sub.*/Pt(2 nm)/$Co_{0.4}Fe_{0.4}B_{0.2}$(1.5 nm)/W(2 nm)/$Gd_{0.3}Fe_{0.7}$(3 nm)/Pt(2 nm)/Si_3N_4(5 nm) samples were prepared by magnetron sputtering as described above. The $Co_{0.4}Fe_{0.4}B_{0.2}$ layer was DC sputtered from a stoichiometric alloy target. The THz amplitude and the magnetic moment in dependence on the temperature are displayed in figure 9.7. The sample reveals a compensation temperature of the $Gd_{0.3}Fe_{0.7}$ layer of 116 K. The THz RMS amplitude of the sample

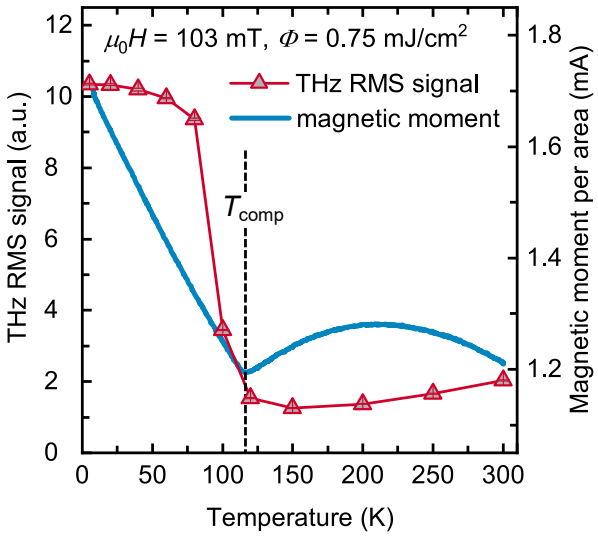

Figure 9.7: THz RMS amplitude and magnetic moment per area of a *sub.*/Pt(2 nm)/$Co_{0.4}Fe_{0.4}B_{0.2}$(1.5 nm)/W(2 nm)/$Gd_{0.3}Fe_{0.7}$(3 nm)/Pt(2 nm)/Si_3N_4(5 nm) emitter system measured at different temperatures with an applied in-plane magnetic field of $\mu_0 H = 103\,\mathrm{mT}$ and a pump fluence of $\Phi = 0.75\,\mathrm{mJ/cm^2}$. The compensation temperature T_{comp} of the $Gd_{0.3}Fe_{0.7}$ layer is marked with the dashed line. The error bars represent the statistical errors of the RMS values.

in the high-amplitude emitter state is increased by 21.0% compared to the *sub.*/Pt(3 nm)/$Gd_{0.1}Fe_{0.9}$(3 nm)/W(3 nm)/$Gd_{0.3}Fe_{0.7}$(3 nm)/Pt(3 nm)/Si_3N_4(5 nm) sample discussed in the previous section.

The aim of the second sample was to shift the switching temperature above room temperature. Therefore, the $Gd_{0.3}Fe_{0.7}$ layer thickness was increased to 5 nm. Instead of the $Gd_{0.1}Fe_{0.9}$ layer, a $Co_{0.4}Fe_{0.4}B_{0.2}$ layer with a thickness of 2 nm was used here. The high THz RMS signal of that system measured at room temperature, which is 9.2% lower than the RMS amplitude of the *sub.*/Pt(3 nm)/$Gd_{0.1}Fe_{0.9}$(3 nm)/W(3 nm)/$Gd_{0.3}Fe_{0.7}$(3 nm)/Pt(3 nm)/Si_3N_4(5 nm) sample discussed in the previous section, measured at 5 K, shows that the emitter is in the high-amplitude state at room temperature. However, as the used THz spectroscopy setup only allows for measurements at or below room temperature, no switching of the emitter state could be demonstrated for this system. In figure 9.8, a comparison of the THz RMS amplitudes and the measured electro-optic signals of different emitter systems at different temperatures is provided. The thermally switchable emitters show THz amplitudes that are comparable to other high-power spintronic emitter systems presented in the literature [82, 83].

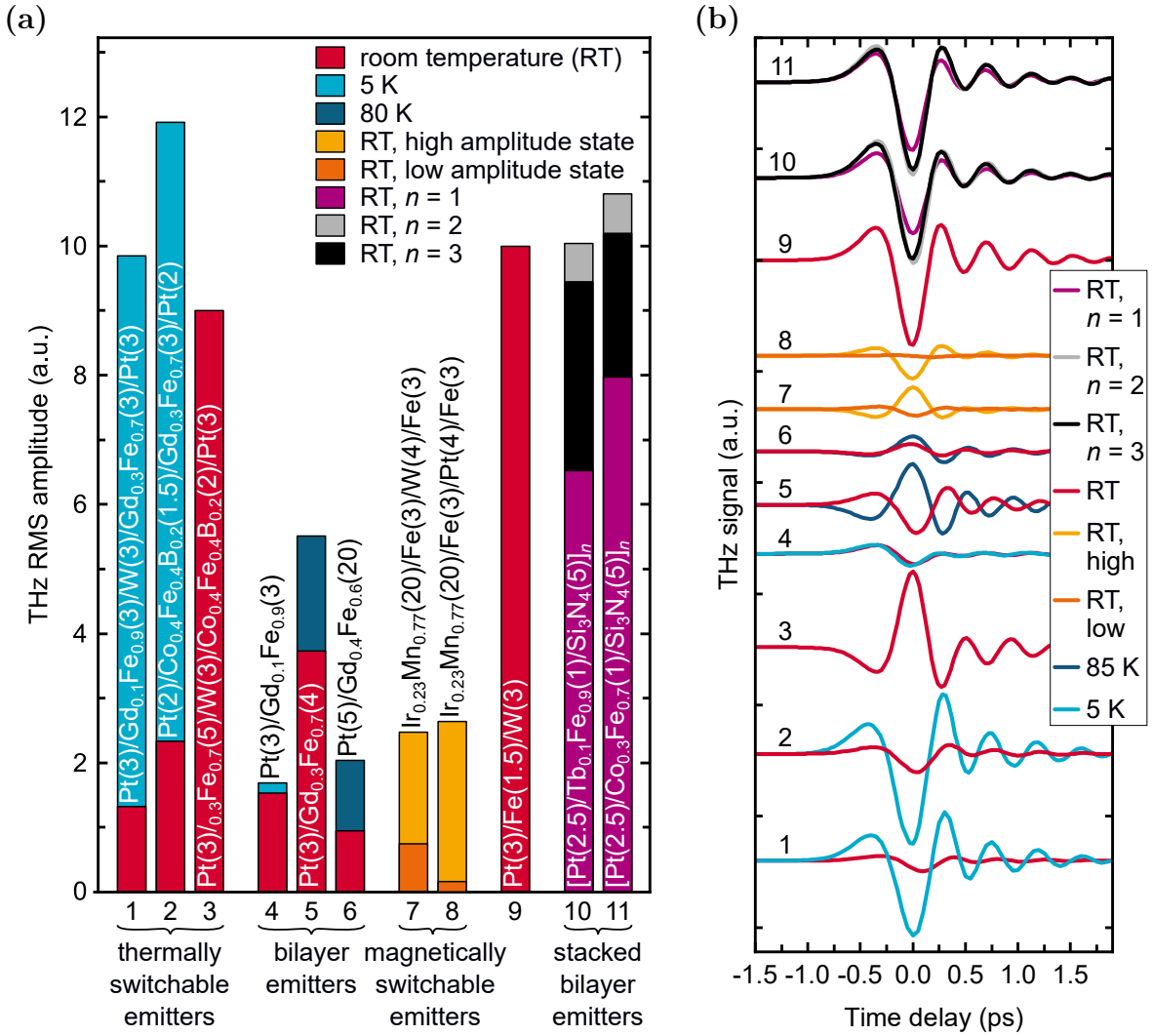

Figure 9.8: Comparison of (a) the THz RMS signals and (b) the THz electro-optic signals of different samples. The numbers in the brackets in the sample names denote the layer thicknesses in nm. For the comparison of the RMS amplitudes, the same time scales of the electro-optic signals as displayed in (b) (−1.5 to +1.9 ps), with the maximum absolute signal set to 0 ps, were used. The low-temperature results were divided by a correction factor of 0.61 to compensate for the low-temperature measurement setup (mainly absorption losses of the emitted THz radiation at the 1 mm thick Al_2O_3 window of the cryostat [299, 406]). Furthermore, the amplitudes of the samples 7–11 were divided by a correction factor of 0.9 to compensate for the absorption of an additional polyethylene filter, that was used in the measurement setup. All samples had 5 nm thick Si_3N_4 capping layers. The measurements were performed with a pump fluence of 0.75 mJ/cm^2. The samples 1–3 are the thermally switchable emitter systems described in the current chapter. Samples 1 and 2 were measured with an applied field $\mu_0 H = 103$ mT in the high- and low-amplitude states at 5 K and 300 K, respectively, sample 3 was measured in the high-amplitude state at 300 K with $\mu_0 H = 200$ mT. The samples 4–6 are exemplary bilayer emitters that are discussed in section 9.2 (samples 4 and 5) and chapter 8 (sample 6) measured at $\mu_0 H = 103$ mT. The samples 7 and 8 are magnetically switchable emitter systems that are discussed in detail in chapter 10. The low-amplitude states were measured at $\mu_0 H = 100$ mT, whereas the high-amplitude states were measured at $\mu_0 H = 9$ mT (sample 7) and $\mu_0 H = 15$ mT (sample 8). The samples 9–11 are thickness-optimized high-amplitude reference samples measured at $\mu_0 H = 200$ mT. Sample 9 is an emitter system with a comparable layer stack to one of the most powerful spintronic emitter systems presented in [82]. The samples 10 and 11 are thickness-optimized stacked bilayer emitters with n repetitions, comparable to the emitters presented in [83].

9.5 Summary

In this study, it was demonstrated that FI Gd_xFe_{1-x} layers with a suitable film thickness and composition can be utilized to control the THz emission state by temperature. First, the Curie temperature, the compensation temperature, and the THz emitting properties of $Pt(3\,nm)/Gd_{0.3}Fe_{0.7}(t)$ bilayers with $1\,nm \leq t \leq 10\,nm$ were investigated. The strongest THz emission was obtained for a $Gd_{0.3}Fe_{0.7}$ layer thickness of 3 nm, also exhibiting a compensation point. For the examined *sub.*/$Pt(3\,nm)/Gd_{0.1}Fe_{0.9}(3\,nm)/W(3\,nm)/Gd_{0.3}Fe_{0.7}(3\,nm)/Pt(3\,nm)/Si_3N_4(5\,nm)$ emitter system, it was shown that an antiparallel alignment of the Fe magnetic moments of the FI layers leads to high-amplitude THz radiation when the system is excited by an ultrashort laser pulse. In contrast, the signal is almost one order of magnitude lower for the parallel alignment of the Fe moments. The change in the relative alignment of the Fe moments was realized by combining a $Gd_{0.3}Fe_{0.7}$ layer, revealing a compensation point, with a Fe-dominated $Gd_{0.1}Fe_{0.9}$ layer. Thus, it is possible to switch the magnetic state in an applied magnetic field by changing the temperature to above or below the compensation point. Due to the positive spin Hall angle of Pt and the negative spin Hall angle of W, both materials contribute to the THz emission in a constructive manner for an antiparallel alignment of the Fe magnetic moments in the two FI layers. Furthermore, it was demonstrated that the amplitude can be increased further by using thinner layers and $Co_{0.4}Fe_{0.4}B_{0.2}$ instead of $Gd_{0.1}Fe_{0.9}$ and also that the working temperature for the high-amplitude emitter state can be adjusted by changing the compensation point by increasing the $Gd_{0.3}Fe_{0.7}$ layer thickness.

CHAPTER 10

Spin valves as magnetically switchable spintronic terahertz emitters

In this chapter, results on the use of spin-valve systems as spintronic THz emitters are presented. Despite the great potential of these systems, so far, there was only one study reported by Li *et al.* [407] that focuses on the use of a magnetic tunneling junction as a spintronic THz emitter. However, their investigated system was not optimized for the use as a spintronic THz emitter as the magnetic layers that were used had an out-of-plane magnetic easy axis. The aim of the work presented here was to realize a more optimized spintronic trilayer THz emitter system with two FM layers with an antiparallel in-plane alignment of the magnetization and a THz emitting NM layer in between them. Therefore, an additional exchange bias layer was used to pin the magnetization of one of the FM layers in a specific in-plane direction. Besides the potential to optimize the THz emission amplitudes, the presented spin-valve system offers the possibility to switch the emitter from a high- to a low-amplitude THz emission state by applying small magnetic fields.

The results were achieved in collaboration with Dr. Robert Schneider, Dr. Steffen Michaelis de Vasconcellos, and Prof. Rudolf Bratschitsch from the University of Münster and are predominantely published in [408].

10.1 Emitter concept

For this study, Fe was chosen for the FM layers as it is magnetically soft, and the THz emission properties are well known. As NM layer, either Pt (positive spin Hall angle: $+1.2\% \leq \theta_{\mathrm{sh,\,Pt}} \leq +11\%$ [271, 294, 295]) or W (negative spin Hall angle: $-33\% \leq \theta_{\mathrm{sh,\,W}} \leq -7\%$ [296]) was used. The NM layer is also needed to decouple the FM layers magnetically. An $Ir_{0.23}Mn_{0.77}$ exchange bias layer (see subsection 2.4.3 for details on the exchange bias effect) was used to pin the magnetization of the neighboring Fe layer. A schematic of the layer stack for a sample with Pt as NM layer (without substrate and capping layer) and the excitation

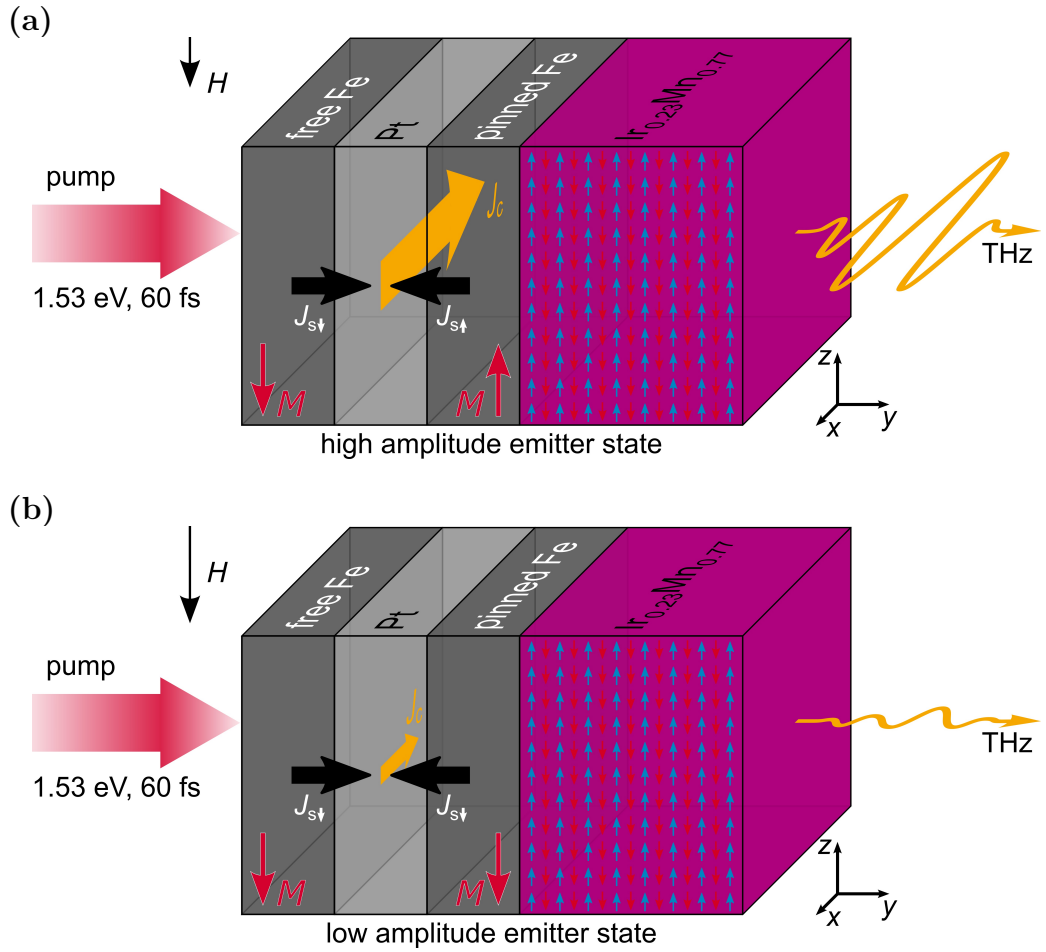

Figure 10.1: Illustration of the layer stacking and the excitation configuration. Excitation with a femtosecond laser pulse leads to the creation of spin currents $\boldsymbol{J}_\mathrm{s}$, caused by the spin-polarized Fe 3d electrons. In the Pt layer, the $\boldsymbol{J}_\mathrm{s}$ are converted into transverse charge currents $\boldsymbol{J}_\mathrm{c}$ due to the inverse spin Hall effect. Note that only $\boldsymbol{J}_\mathrm{s}$ along with the layer stack (y-axis) are considered. Depending on the direction of the magnetization $\boldsymbol{M}$ of the Fe layers (indicated by the red arrows), the system is either (a) in a high-amplitude THz emitting state or (b) in a low-amplitude THz emitting state, for an antiparallel or parallel magnetization alignment, respectively.

geometry that was used for the THz emission spectroscopy is plotted in figure 10.1. When the system is excited by a femtosecond laser pulse, two spin currents $\boldsymbol{J}_\mathrm{s}$ from each of the Fe layers caused by the spin-polarized Fe 3d electrons are launched toward the NM layer. In the NM layer, the spin currents $\boldsymbol{J}_\mathrm{s}$ are converted to charge currents $\boldsymbol{J}_\mathrm{c} \sim \theta_\mathrm{sh}\boldsymbol{J}_\mathrm{s} \times \boldsymbol{M}/|\boldsymbol{M}|$ by the inverse spin Hall effect, with $\boldsymbol{M}$ denoting the magnetization of the Fe layers. The charge currents $\boldsymbol{J}_\mathrm{c}$ then cause the emission of the radiation in the THz frequency regime. Depending on the relative magnetization orientation of the two Fe layers, the system is in either a high-amplitude THz emitting state where both $\boldsymbol{J}_\mathrm{s}$ contribute constructively to $\boldsymbol{J}_\mathrm{c}$ (see figure 10.1a) or in a low-amplitude THz emitting state where the two $\boldsymbol{J}_\mathrm{s}$ contribute in opposite directions to $\boldsymbol{J}_\mathrm{c}$ (see figure 10.1b). Note that for the system with W as NM layer, $\boldsymbol{J}_\mathrm{c}$ points in the opposite direction for the high-amplitude emitter state, as the sign of $\theta_{\mathrm{sh,\,W}}$

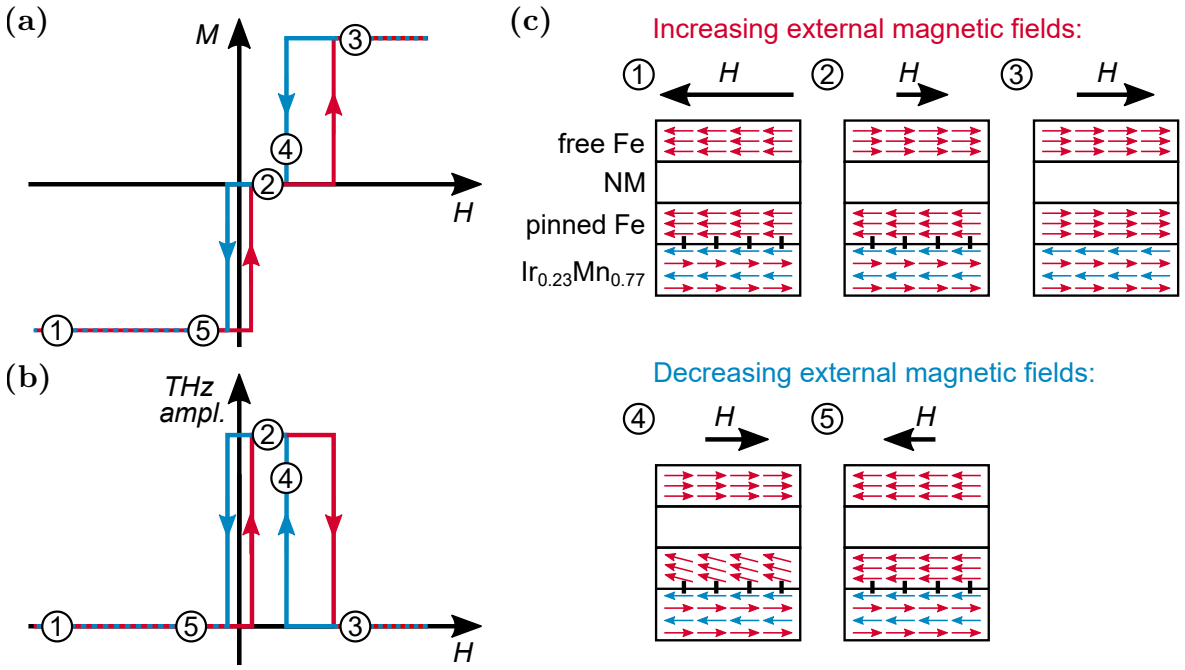

Figure 10.2: (a) shows a schematic in-plane $M(H)$ loop and (b) the corresponding THz emission amplitudes that are expected for an ideal trilayer system with an exchange-biased Fe layer and a free Fe layer that are magnetically decoupled from each other by a THz emitting NM layer. The schematics in (c) display the expected configuration of the magnetic moments in the layer stack for the marked points in the $M(H)$ loop.

is negative. The emitter state can be controlled by an external magnetic field H. Figure 10.2 shows (a) ideal magnetic and (b) THz amplitude hysteresis curves for such a system, as well as (c) schematic illustrations displaying the configuration of the magnetic moments for characteristic points in the $M(H)$ loop. The images assume that the exchange bias was set previously in the negative field direction. The $M(H)$ loop represents the superposition of the loop of the exchange-biased (pinned) Fe layer, which is shifted toward positive field values, and for which the coercivity is typically increased, and the loop of the soft magnetic free Fe layer, which is symmetric around zero field. In an ideal system that shows a sufficiently large exchange bias effect, for both, increasing and decreasing applied magnetic fields, a field region for which the magnetic moments in the two Fe layers point in opposite directions is expected. For two similar Fe layers, the net magnetization for that field region is zero. For high applied magnetic fields, the magnetic moments of both Fe layers will align parallel to the applied field.

10.2 Sample preparation and magnetic characterization

A series of *sub.*/$Ir_{0.23}Mn_{0.77}$(20 nm)/Fe(3 nm)/X/Fe(3 nm)/Si_3N_4(5 nm) samples with either Pt(3–5 nm) or W(2–4 nm) as interlayer X was prepared. All film depositions for the mag-

netic measurements were done by magnetron sputtering at room temperature (see chapter 4 for details on the preparation) on 525 µm thick p-doped Si(100) substrates with a 100 nm thick thermally oxidized SiO_2 layer. For the THz spectroscopy experiments, 500 µm thick Al_2O_3(0001) substrates polished on both sides were used. To prevent the spintronic layer stacks from oxidation, 5 nm thick Si_3N_4 capping layers were used. The $Ir_{0.23}Mn_{0.77}$, Fe, Pt, and W layers were deposited by DC sputtering. For the Si_3N_4 layers, RF sputtering was applied. The $Ir_{0.23}Mn_{0.77}$ and the Si_3N_4 layer were sputtered from stoichiometric compound targets.

Ir_xMn_{1-x}(111) alloys with different compositions have been shown to exhibit an AFM order that is suitable for the usage as an exchange bias layer. [150, 151, 154, 155, 409, 410] The exchange bias was set by saturating the magnetization of the Fe layers with an applied in-plane magnetic field of 388 mT at a temperature of 423 K and subsequent cooling of the sample down to room temperature with the external magnetic field still applied. The $Ir_{0.23}Mn_{0.77}$ layer thickness of 20 nm ensures that the blocking temperature of the $Ir_{0.23}Mn_{0.77}$ layer is low enough so that the exchange bias can be set with the applied temperature of 423 K and also that the layer is in a stable AFM state at room temperature. The chosen thickness of 3 nm for the Fe layers ensures that the layers are in a stable FM state at room temperature. Furthermore, as the exchange bias is an interface effect, which is inversely proportional to the thickness of the coupled FM layer [131], a small thickness results in a strong pinning effect for the pinned Fe layer.

As mentioned above, the NM layer needs to sufficiently magnetically decouple the two Fe layers. To investigate the exchange bias effect and the influence of a possible magnetic interlayer coupling between the two Fe layers, the magnetic properties of the samples with Pt and W interlayers of different thicknesses were investigated. Therefore, for all samples, the magnetic moment in dependence on the external magnetic field was measured by SQUID-VSM. Full loops and minor loops, which were measured from negative saturation up to field values for which only the magnetization of the free layer changed the direction, were recorded. The results are displayed in figure 10.3. Please note that the magnetic moment was normalized by the area of the samples rather than by the sample volume, as the two Fe layers contribute differently to the measured moment. The exchange bias for the pinned Fe layer was set in the negative field direction. The interlayer coupling between the two Fe layers through the NM layer is directly reflected in the loops, and also values for the coupling strength could be derived. [411] However, for the purpose of this work, it is sufficient to discuss the coupling qualitatively. For the sample with $X = \mathrm{Pt}(3\,\mathrm{nm})$ (see figure 10.3a), the loops of both Fe layers are shifted toward positive field values. Therefore, the Fe layers are still coupled ferromagnetically, and it cannot be clearly distinguished between the magnetic moment reorientation processes of the two Fe layers. The minor loop of the sample with $X = \mathrm{Pt}(4\,\mathrm{nm})$ (see figure 10.3c) shows a small shift toward negative field values, indicating a weak

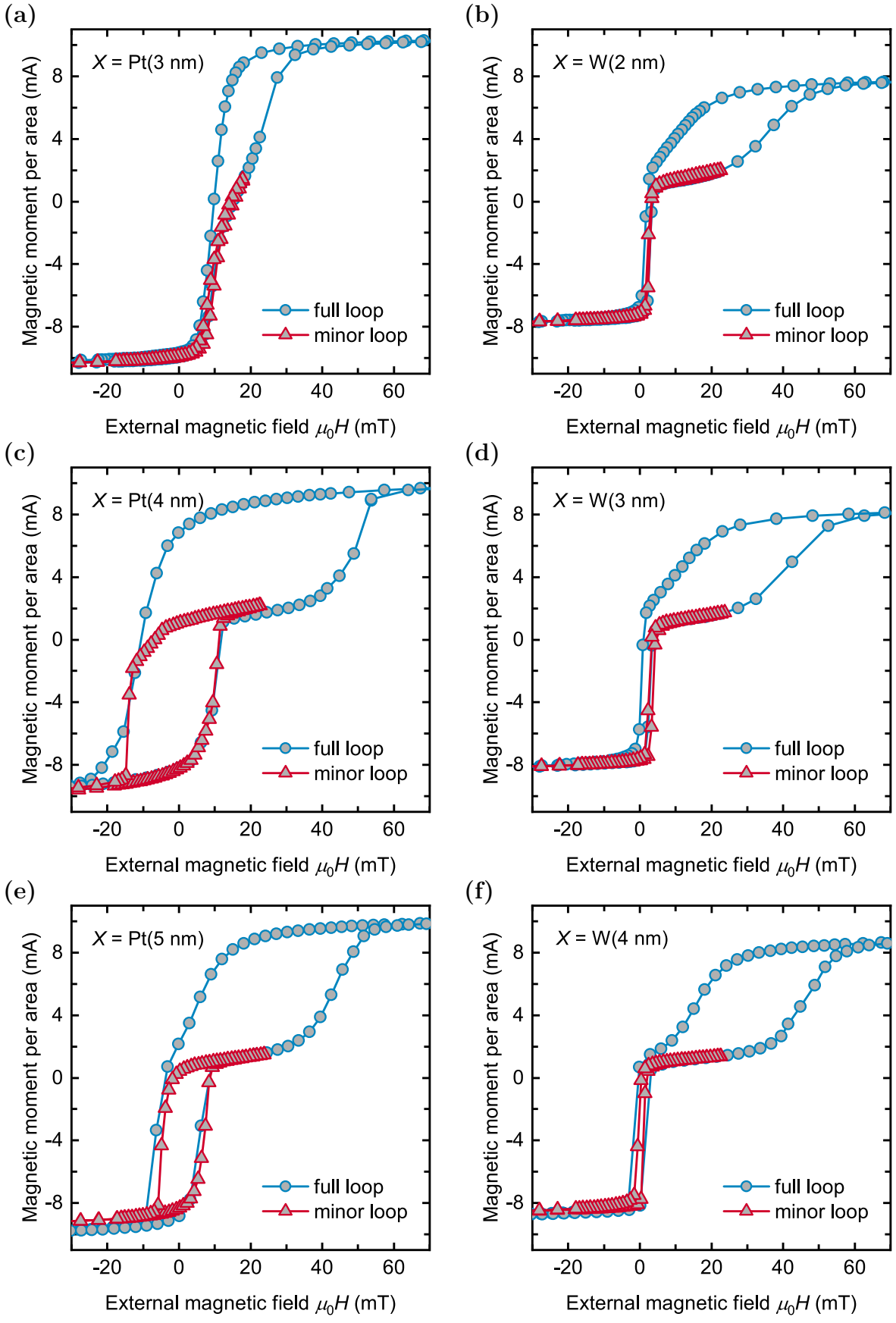

Figure 10.3: Room-temperature SQUID-VSM $M(H)$ loops and minor loops of *sub.*/$Ir_{0.23}Mn_{0.77}$(20 nm)/Fe(3 nm)/X/Fe(3 nm)/Si_3N_4(5 nm) samples with the denoted interlayers X.

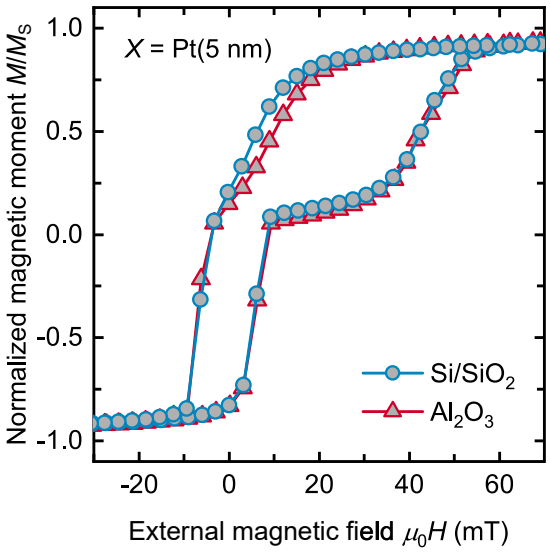

Figure 10.4: Comparison of room-temperature SQUID-VSM $M(H)$ loops between two *sub.*/$Ir_{0.23}Mn_{0.77}$(20 nm)/Fe(3 nm)/Pt(5 nm)/Fe(3 nm)/Si_3N_4(5 nm) samples deposited on a 500 µm thick Al_2O_3(0001) and a 525 µm thick Si(100) substrates with a 100 nm thick thermally oxidized SiO_2 layer, respectively. The measured magnetic moments M were normalized by the respective saturation magnetic moments M_S.

AFM coupling between the two Fe layers. This could be explained by a dominant RKKY type coupling (coupling strength $J_{RKKY} \sim -\sin(t)/t^2$) via the Pt spacer layer, which overcomes the FM coupling (coupling strength due to induced magnetic moments $J_{pe} \sim 1/\sinh(t)$, orange peel coupling strength $J_{op} \sim \exp(-t)$) for certain interlayer film thicknesses t. [113] However, also magnetostatic coupling caused by the sample geometry due to uncompensated magnetic poles near the edges might give a contribution. [412] For this loop, and also for the loops of all other investigated samples described below, a field region for which the magnetic moments of the two Fe layers are aligned antiparallel, and therefore the net magnetic moment is close to zero, can be observed. For samples with 5 nm thick Pt and 4 nm thick W interlayers, the Fe layers seem to be magnetically decoupled from each other, as no loop shift of the minor loops can be observed (see figures 10.3e and 10.3f). Though, different contributions of AFM and FM coupling mechanisms might just compensate each other. The samples with 2 nm and 3 nm thick W interlayers show a weak FM coupling, which is indicated by the shift of the minor loop toward positive field values (see figures 10.3b and 10.3d). However, to explain the coupling types for the different interlayers in detail is beyond the scope of this work. Please note that due to the different film growth of Fe on Pt compared to Fe on W, a small difference in the saturation magnetic moment of the two systems can be observed. For the purpose of this study, all interlayers except the 3 nm thick Pt layer sufficiently decouple the two Fe layers. An exemplary comparison of the $M(H)$ curves of the layer stack with $X =$ Pt(5 nm) sputtered on an Al_2O_3 substrate with the same layer stack sputtered on a Si/SiO_2(100 nm) substrate that is shown in figure 10.4 revealed no significant impact of the substrate on the magnetic properties.

10.3 Terahertz emission results

The samples with 4 nm thick Pt and 4 nm thick W NM layers were exemplarily chosen for further discussions. The SQUID-VSM loops for ascending (red triangles) and descending (blue circles) external magnetic fields for the sample with Pt and W interlayers are displayed in figures 10.5a and 10.5b, respectively. The solid arrows schematically show the magnetization alignment of the two Fe layers for ascending magnetic fields. For high applied magnetic fields, the magnetization of both Fe layers is saturated in the direction of the applied field. Coming from negative saturation, the magnetization of the free Fe layer changes at the small positive field value H_1, resulting in an antiparallel magnetization alignment of the two Fe layers. This orientation persists up to a field H_2, where the magnetization of the exchange-biased Fe starts to rotate toward the applied field direction. As the magnetization of the Fe layer on top of the $Ir_{0.23}Mn_{0.77}$ layer is exchange-biased in the negative field direction, for descending magnetic fields, the pinned Fe starts reversing its magnetization direction first. However, an antiparallel magnetization alignment can only be observed for a narrow field range (see figure 10.5b). For the sample with the Pt interlayer, the magnetization reversal of the pinned layer even fully overlaps with the reversal of the free layer (see figure 10.5a).

The switchability between antiparallel and parallel alignment of the two Fe layers allows the usage of the system as a switchable, efficient spintronic THz emitter, as described before and illustrated in figure 10.1. To demonstrate this functionality of the emitter systems, magnetic-field-dependent THz spectroscopy measurements were performed. All THz spectroscopy measurements were done by Dr. Robert Schneider in Münster with the electro-optic sampling setup described in section 5.6. The measurements were carried out under a dry nitrogen atmosphere at room temperature. Figures 10.5c and 10.5d show the THz RMS amplitude in dependence on the applied in-plane magnetic field for the samples with Pt and W of 4 nm thickness as the NM layer, respectively (see appendix A.6, figure A.16 for the THz spectroscopy results of the samples with Pt(5 nm) and W(3 nm) interlayers). For external magnetic field values where the magnetization alignment of the two Fe layers is antiparallel, the THz emission is increased by a factor of up to 15.7 for the sample with Pt and 3.3 for the sample with W, compared to the emitter state with parallel magnetization orientation. The amplitudes in the high-amplitude state reach about 25% of a Pt(3 nm)/Fe(1.5 nm)/W(3 nm) emitter (see section 9.4, figure 9.8 for a comparison of the amplitudes with other spintronic emitter systems). For both samples, a small THz signal for the parallel magnetization alignment of the Fe layers could still be measured. This remaining signal is higher for the sample with W compared to the sample with Pt. For both samples, ultrafast demagnetization of the Fe layers after laser excitation [237, 238] can be excluded to cause a significant contribution to the THz signals by measuring the THz emission for different excitation directions. The THz electro-optic signals of the two samples measured for laser irradiation from the substrate and the capping-layer side are displayed in figures 10.6a and 10.6b, respectively. The

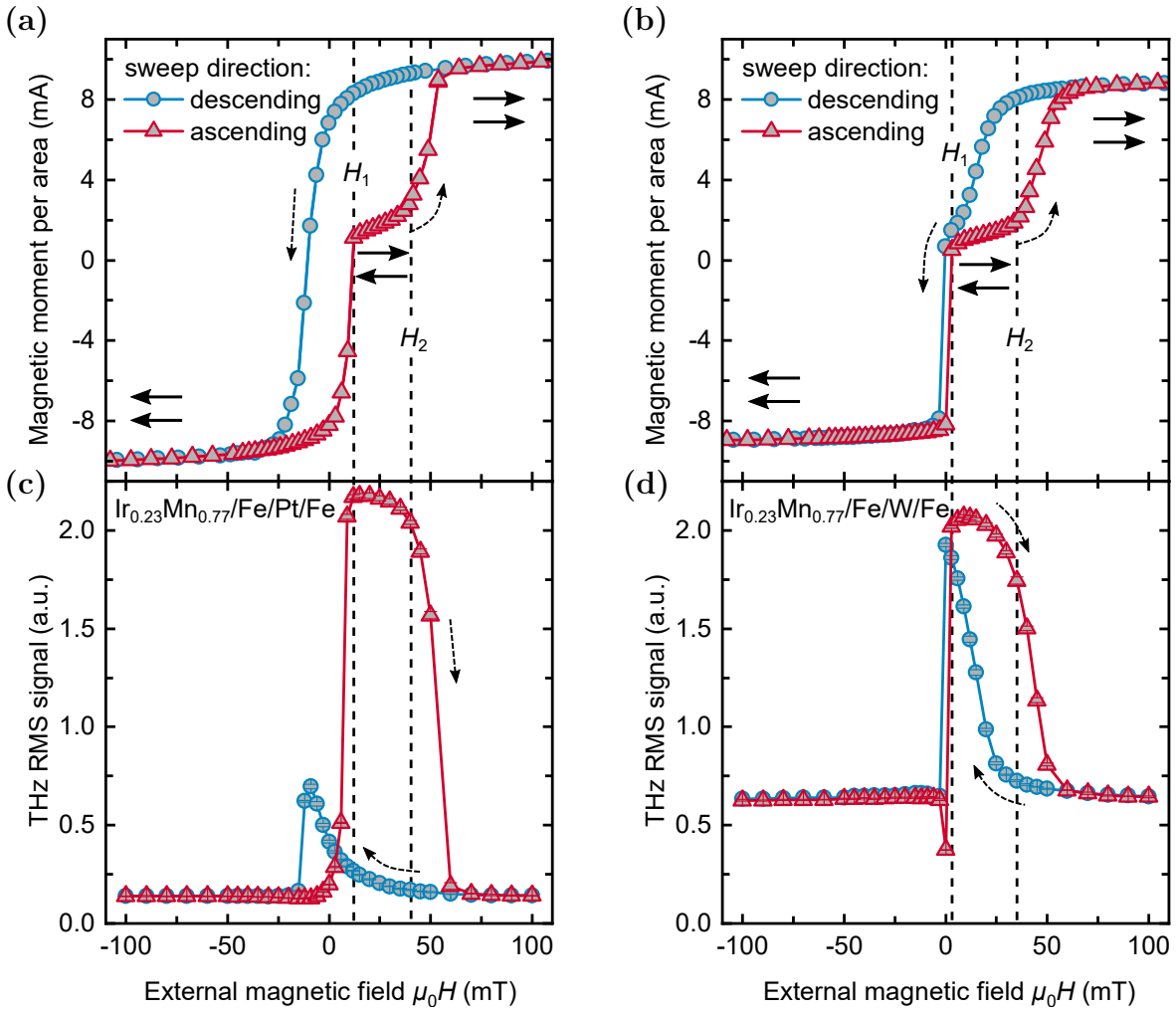

Figure 10.5: Comparison between room-temperature $M(H)$ and THz emission spectroscopy results measured on *sub.*/$Ir_{0.23}Mn_{0.77}$(20 nm)/Fe(3 nm)/Pt(4 nm)/Fe(3 nm)/Si_3N_4(5 nm) and *sub.*/$Ir_{0.23}Mn_{0.77}$(20 nm)/Fe(3 nm)/W(4 nm)/Fe(3 nm)/Si_3N_4(5 nm) samples. (a) and (b) display the magnetic moment per area in dependence of the applied in-plane magnetic field H. (c) and (d) display the THz RMS amplitude measured with a pump fluence of $\Phi = 0.75\,\mathrm{mJ/cm^2}$ in dependence on H. The red triangles and the blue circles show the values for increasing and decreasing applied magnetic fields coming from the saturated state, respectively. The dashed arrows symbolize the sweep direction. The solid black arrows schematically show the magnetization alignment of the two Fe layers for ascending magnetic fields. The error bars (within the symbols) represent the statistical errors of the THz RMS signals.

measurements were performed for the low-amplitude emitter states (in positive and negative magnetic saturation). For both samples, the signals are inverted for the two different field values. Furthermore, the signals are also inverted if the same field value but an excitation from the opposite sample side is used. THz emission due to ultrafast laser-induced demagnetization does not depend on the excitation direction. [223] This indicates that also for the low-amplitude emitter states, the THz emission is dominated by a spin-to-charge current conversion in the interlayer due to different contributions to $\boldsymbol{J}_\mathrm{c}$ of the two spin currents $\boldsymbol{J}_\mathrm{s}$

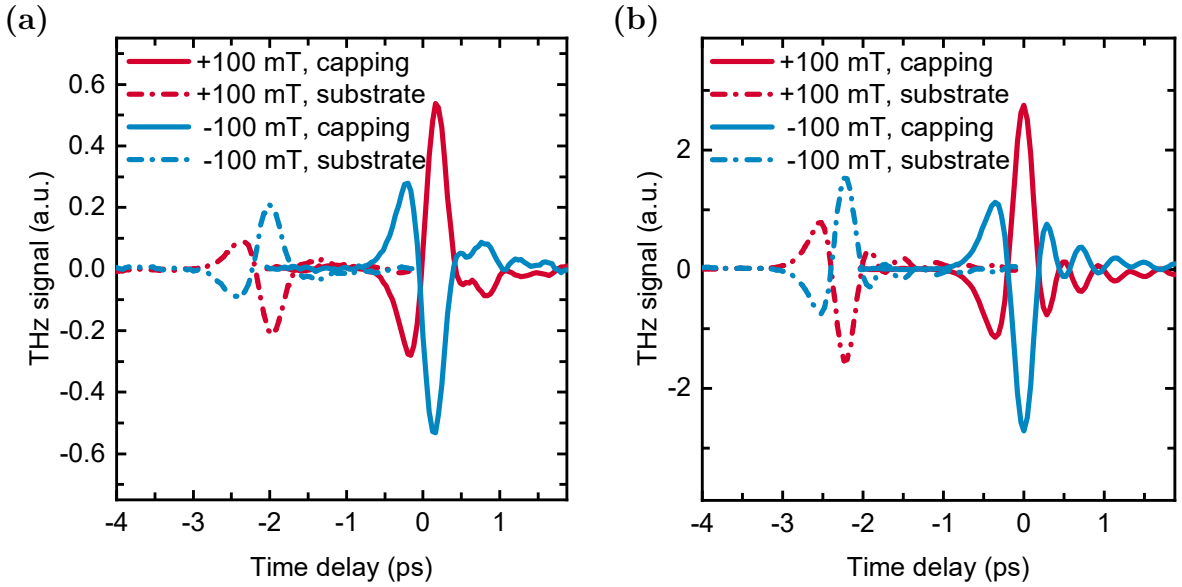

Figure 10.6: THz electro-optic signals of (a) *sub.*/$Ir_{0.23}Mn_{0.77}$(20 nm)/Fe(3 nm)/Pt(4 nm)/Fe(3 nm)/Si_3N_4(5 nm) and (b) *sub.*/$Ir_{0.23}Mn_{0.77}$(20 nm)/Fe(3 nm)/W(4 nm)/Fe(3 nm)/Si_3N_4(5 nm) samples measured at room temperature with laser excitation (pump fluence $\Phi = 0.75\,\mathrm{mJ/cm^2}$) from the capping layer and from the substrate side with applied in-plane magnetic fields $\mu_0 H = +100\,\mathrm{mT}$ and $-100\,\mathrm{mT}$.

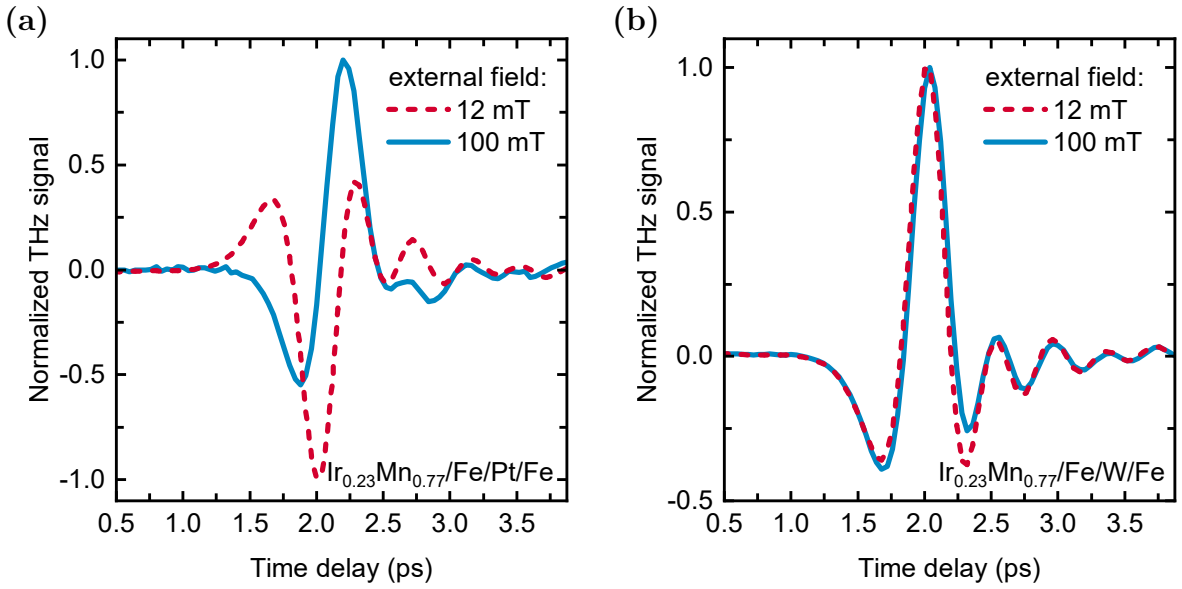

Figure 10.7: Room-temperature THz electro-optic signals of (a) *sub.*/$Ir_{0.23}Mn_{0.77}$(20 nm)/Fe(3 nm)/Pt(4 nm)/Fe(3 nm)/Si_3N_4(5 nm) and (b) *sub.*/$Ir_{0.23}Mn_{0.77}$(20 nm)/Fe(3 nm)/W(4 nm)/Fe(3 nm)/Si_3N_4(5 nm) samples measured with a pump fluence of $\Phi = 0.75\,\mathrm{mJ/cm^2}$ for applied in-plane magnetic fields of $\mu_0 H = 12\,\mathrm{mT}$ and 100 mT in ascending direction, representing the signals for the high- and the low-amplitude emitter state, respectively. Note that for the sake of better comparability, the signals are normalized to their maximum absolute values.

coming from different Fe layers. The small remaining THz signal for the low-amplitude state of the sample with Pt can be explained by a slightly higher contribution of the spin current $\boldsymbol{J}_\mathrm{s}$ coming from the pinned Fe layer. The relatively strong signal for the low-amplitude state of the sample with W is caused by significantly different contributions of the two spin currents $\boldsymbol{J}_\mathrm{s}$ to the charge current $\boldsymbol{J}_\mathrm{c}$, which can be explained by the different film growth of Fe on W compared to Fe grown on $\mathrm{Ir_{0.23}Mn_{0.77}}$. Here, the free Fe layer shows a higher contribution to $\boldsymbol{J}_\mathrm{c}$ than the pinned Fe layer. This also leads to the minimum of the THz signal for ascending and to the less prominent minimum for descending magnetic fields close to the switching fields from the low- to the high-amplitude state and vice versa (see figure 10.5d). At the minima, the Fe layers are close to a parallel magnetization alignment. However, the free layer is still in an intermediate magnetization state close to the saturated state and, therefore, contributes slightly less to the THz signal than in the saturated magnetic state. Thus, the contributions of the two $\boldsymbol{J}_\mathrm{s}$ are closer to full compensation, and the resulting THz signal is smaller than for the parallel aligned state. However, the shape of the THz signals for the low- and high-amplitude emitter states of the sample with Pt differs significantly, whereas, for the sample with W, the signal shapes for the two states are almost the same. Figures 10.7a and 10.7b show the normalized THz signals measured at 12 mT and 100 mT for ascending applied in-plane magnetic fields for the samples with Pt and W interlayers, respectively. The signals for the two field values represent the high- and low-amplitude emitter states. For the sample with Pt, the shape of the THz signal differs significantly for the two emitter states, indicating that another effect might contribute to the signal besides the inverse spin Hall effect. The inversion of the signal upon the magnetization switching of the pinned layer indicates that the $\boldsymbol{J}_\mathrm{s}$ coming from the pinned Fe layer contributes slightly

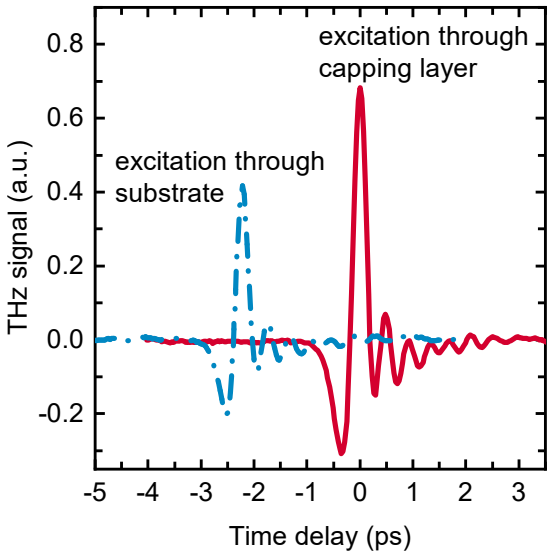

Figure 10.8: THz electro-optic signals of a *sub.*/$\mathrm{Ir_{0.23}Mn_{0.77}}$(20 nm)/Fe(3 nm)/$\mathrm{Si_3N_4}$(5 nm) reference sample measured at room temperature in different excitation geometries with an applied in-plane magnetic field $\mu_0 H = 200\,\mathrm{mT}$ with a pump fluence of $\Phi = 0.75\,\mathrm{mJ/cm^2}$.

more to $\boldsymbol{J}_c$ compared to the $\boldsymbol{J}_s$ coming from the free Fe layer. In contrast to that, the signal shapes are almost the same for the two emitter states of the sample with W. Therefore, here both signals can be attributed to an emission via the inverse spin Hall effect, where the $\boldsymbol{J}_s$ coming from the free Fe layer contributes more to $\boldsymbol{J}_c$ than the $\boldsymbol{J}_s$ coming from the pinned Fe layer. Furthermore, the impact of the $Ir_{0.23}Mn_{0.77}$(20 nm)/Fe(3 nm) bilayer on the THz emission was investigated. Contrary to THz spectroscopy studies on *sub.*/$Ir_{0.25}Mn_{0.75}$(0–10 nm)/Co(3 nm) bilayers reported by Chen *et al.* [327], the $Ir_{0.23}Mn_{0.77}$ layer used here does not exhibit any significant spin-to-charge current conversion, as shown by measurements of a reference $Ir_{0.23}Mn_{0.77}$(20 nm)/Fe(3 nm) bilayer with laser excitation from the capping and the substrate side (see figure 10.8). The electro-optic signal clearly does not show a change in the sign for the different excitation directions. This strongly indicates that the THz emission is directly caused by the ultrafast demagnetization of the Fe film and not by a spin to charge current conversion in the $Ir_{0.23}Mn_{0.77}$ layer via the inverse spin Hall effect.

10.4 Switchability with small magnetic fields

In contrast to other efficient spintronic THz emitters described in the literature, the emitter systems investigated here allow the switching from a high- to a low-amplitude emitter state

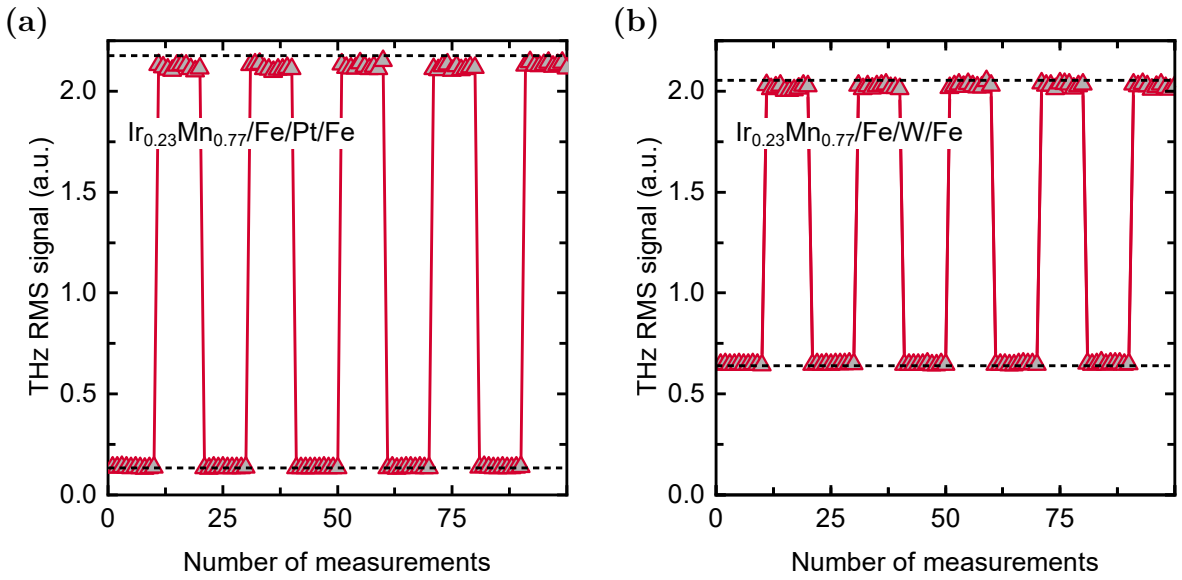

Figure 10.9: THz RMS amplitudes for the high- and low-amplitude emitter states of (a) *sub.*/$Ir_{0.23}Mn_{0.77}$(20 nm)/Fe(3 nm)/Pt(4 nm)/Fe(3 nm)/Si_3N_4(5 nm) and (b) *sub.*/$Ir_{0.23}Mn_{0.77}$(20 nm)/Fe(3 nm)/W(4 nm)/Fe(3 nm)/Si_3N_4(5 nm) samples measured at room temperature for multiple switching cycles with a pump fluence of $\Phi = 0.75\,\mathrm{mJ/cm^2}$. For the sample with Pt, in-plane magnetic fields of $\mu_0 H = -30\,\mathrm{mT}$ and $+20\,\mathrm{mT}$ were used to set the emitter states. For the sample with W, fields of $\mu_0 H = -10\,\mathrm{mT}$ and $+6\,\mathrm{mT}$ were used. The dashed lines mark the THz RMS amplitudes that were measured at the same field values for ascending magnetic fields in the magnetic-field-dependent THz loops shown in figures 10.5c and 10.5d.

by applying small magnetic fields, as a consequence of the relatively low coercivity of the free Fe layer. Due to the small field values in the millitesla range, fast switching rates can be achieved with an electromagnet. The reversibility of the switching processes for multiple switching cycles for both samples is shown in figure 10.9. For the sample with Pt, in-plane magnetic fields of $-30\,\mathrm{mT}$ and $+30\,\mathrm{mT}$ were used to set the emitter states, while for the sample with W, even smaller fields of $-10\,\mathrm{mT}$ and $+6\,\mathrm{mT}$ were applied. The field values were chosen according to the $M(H)$ minor loops shown in figures 10.3c and 10.3f in order to clearly reach the two different emitter states. After several switching cycles, the THz RMS signals for the high- and the low-amplitude emitter states remain constant and reach almost the values taken from figure 10.5 for ascending external magnetic fields, which are marked with the dashed lines, demonstrating the reversibility of the switching processes.

10.5 Thickness-optimized emitters

Further improvement of the emission amplitude could be achieved by decreasing the FM and AFM film thicknesses. Therefore, thickness-optimized versions of the emitters presented above were investigated. A series of *sub.*/$\mathrm{Ir_{0.23}Mn_{0.77}}(t)$/Fe(3 nm)/Al(3 nm) samples with different $\mathrm{Ir_{0.23}Mn_{0.77}}$ film thicknesses $t = 5, 7, 10\,\mathrm{nm}$ was prepared to find the minimum $\mathrm{Ir_{0.23}Mn_{0.77}}$ thickness for which an exchange bias effect is still observable. The Al layers only serve as cappings to prevent the underlying layers from oxidation. SQUID-VSM $M(H)$ loops that were measured after setting the exchange bias are displayed in figure 10.10. For the sample with $t = 7\,\mathrm{nm}$, a small exchange bias and an enhanced coercivity are still ob-

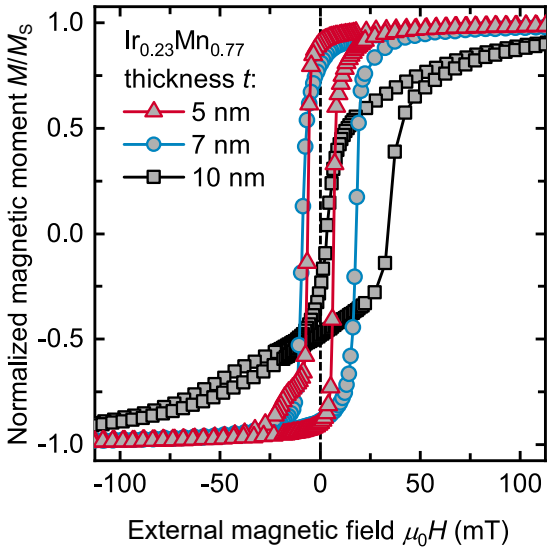

Figure 10.10: Room-temperature SQUID-VSM $M(H)$ loops of *sub.*/$\mathrm{Ir_{0.23}Mn_{0.77}}(t)$/Fe(3 nm)/Al(3 nm) samples with $t = 5, 7, 10\,\mathrm{nm}$. The measured magnetic moments were normalized by the respective saturation magnetic moments M_S.

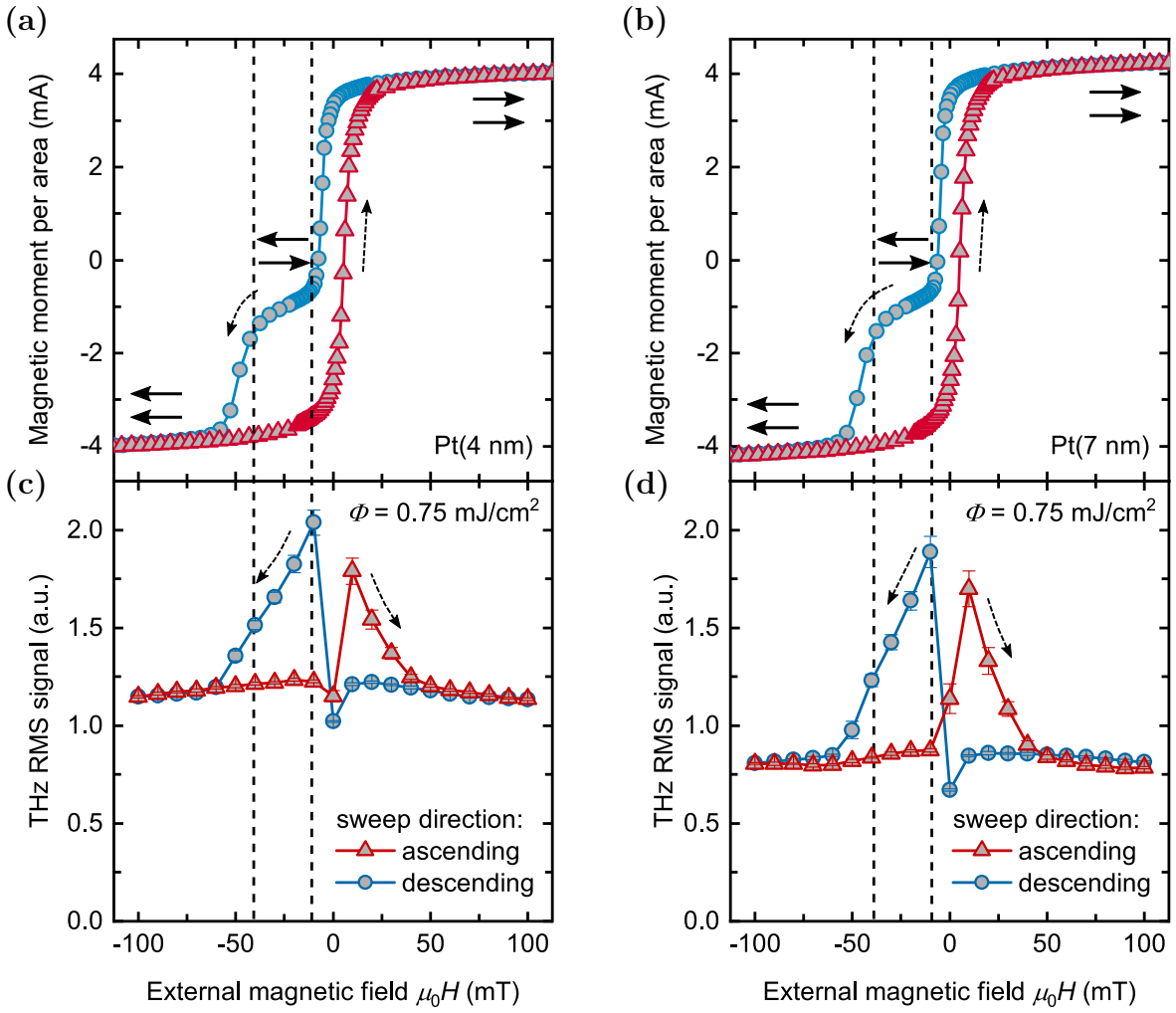

Figure 10.11: (a) and (b) show the magnetic moments per area of *sub.*/$Ir_{0.23}Mn_{0.77}$(7 nm)/Fe(1.5 nm)/Pt(t)/Fe(1.5 nm)/Si_3N_4(5 nm) samples with Pt thicknesses t of 4 nm and 7 nm measured in dependence of the applied in-plane magnetic field. (c) and (d) display the respective THz RMS amplitudes measured with a pump fluence of $\Phi = 0.75\,\mathrm{mJ/cm^2}$. The exchange bias was set in the positive field direction before the measurements. All values were recorded at room temperature. The red triangles and the blue circles show the values for increasing and decreasing applied magnetic fields coming from the saturated state, respectively. The dashed arrows indicate the sweep directions. The solid black arrows schematically show the magnetization alignment of the two Fe layers for descending magnetic fields. The field region for which an antiparallel magnetization alignment of the two Fe layers can be observed in the $M(H)$ loops is marked with the dashed lines. The error bars represent the statistical errors of the THz RMS signals.

servable. Therefore, this thickness was chosen for two *sub.*/$Ir_{0.23}Mn_{0.77}$(7 nm)/Fe(1.5 nm)/Pt(t)/Fe(1.5 nm)/Si_3N_4(5 nm) samples with Pt interlayer thicknesses t = 4 nm and 7 nm. SQUID-VSM $M(H)$ loops of these systems, which were measured after setting the exchange bias in positive field direction, clearly show an antiparallel magnetization alignment of the two Fe layers for certain applied fields (see figures 10.11a and 10.11a). Due to the reduced Fe thickness, the exchange bias is enhanced compared to the bilayer $Ir_{0.23}Mn_{0.77}$ thickness

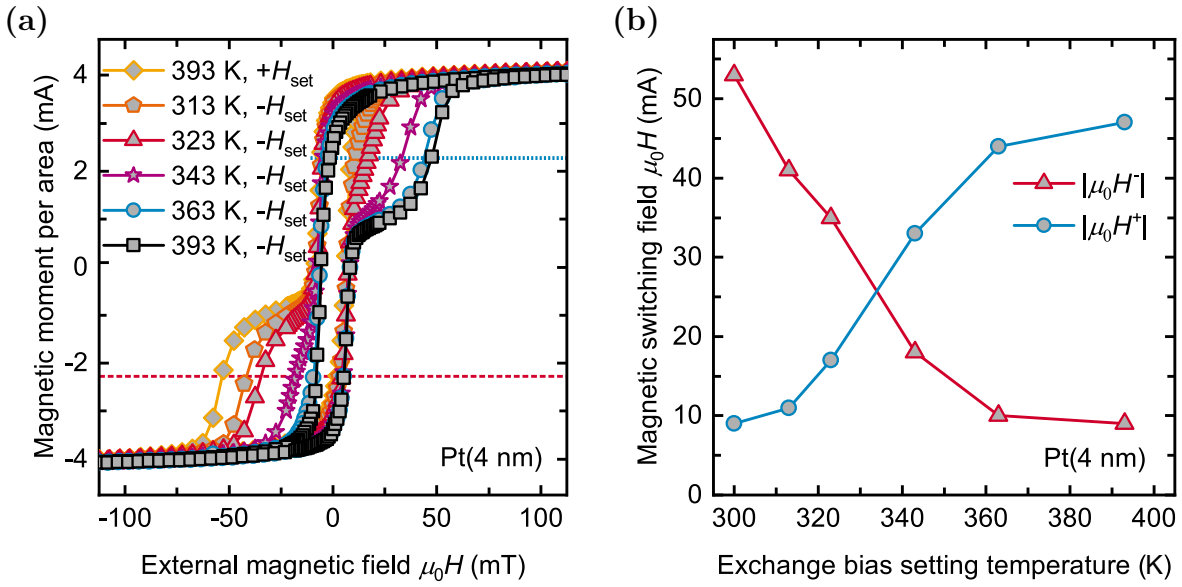

Figure 10.12: (a) Room-temperature SQUID-VSM $M(H)$ loops of a *sub.*/$Ir_{0.23}Mn_{0.77}$(7 nm)/Fe(1.5 nm)/Pt(4 nm)/Fe(1.5 nm)/Si_3N_4(5 nm) (*sub.* = Al_2O_3) sample measured for different exchange bias setting temperatures. For the first measured loop (yellow diamonds), the field $\mu_0 H_{set} = 500$ mT was applied in positive direction. For all other loops, which were measured sequentially for increasing exchange bias setting temperatures, H_{set} was applied in the negative direction. The magnetic switching fields of the pinned Fe layer in negative and positive field direction were read out for the magnetic moment values marked with the dashed red line and the dotted blue line, respectively. (b) shows the values of the magnetic switching fields after application of the exchange bias setting field $-H_{set}$ at different exchange bias setting temperatures.

series presented above. However, the THz emission amplitudes measured for different external fields, which are displayed in figures 10.11c and 10.11d, show a dependency that does not correlate with the SQUID-VSM $M(H)$ loops as was the case for the samples described in section 10.3. A SQUID-VSM $M(H)$ loop of the sample with $t = 4$ nm that was measured after the THz spectroscopy measurements were performed still showed a similar curve as the loop displayed in figure 10.11a that was measured on the sample deposited on the Si/SiO_2 substrate, directly after setting the exchange bias (see figure A.17 in appendix A.6). The discrepancy between the behavior of the THz signals and the magnetization loops can be explained by the influence of the laser pump pulse on the exchange bias. For sufficiently high laser pump fluences Φ, the exchange bias can be partially or even completely reset in the direction of an applied magnetic field due to the local heating of the $Ir_{0.23}Mn_{0.77}$ spin system induced by the laser pump pulses. [413–415] The laser-induced reset of the exchange bias led to the observed almost symmetric curves of the THz amplitudes measured for ascending and descending applied magnetic fields. In order to investigate the temperature, which is necessary to reverse the exchange bias direction, room-temperature SQUID-VSM $M(H)$ loops of the $Al_2O_3/Ir_{0.23}Mn_{0.77}$(7 nm)/Fe(1.5 nm)/Pt(4 nm)/Fe(1.5 nm)/Si_3N_4(5 nm) sample have been recorded after setting the exchange bias at different temperatures in the opposite direc-

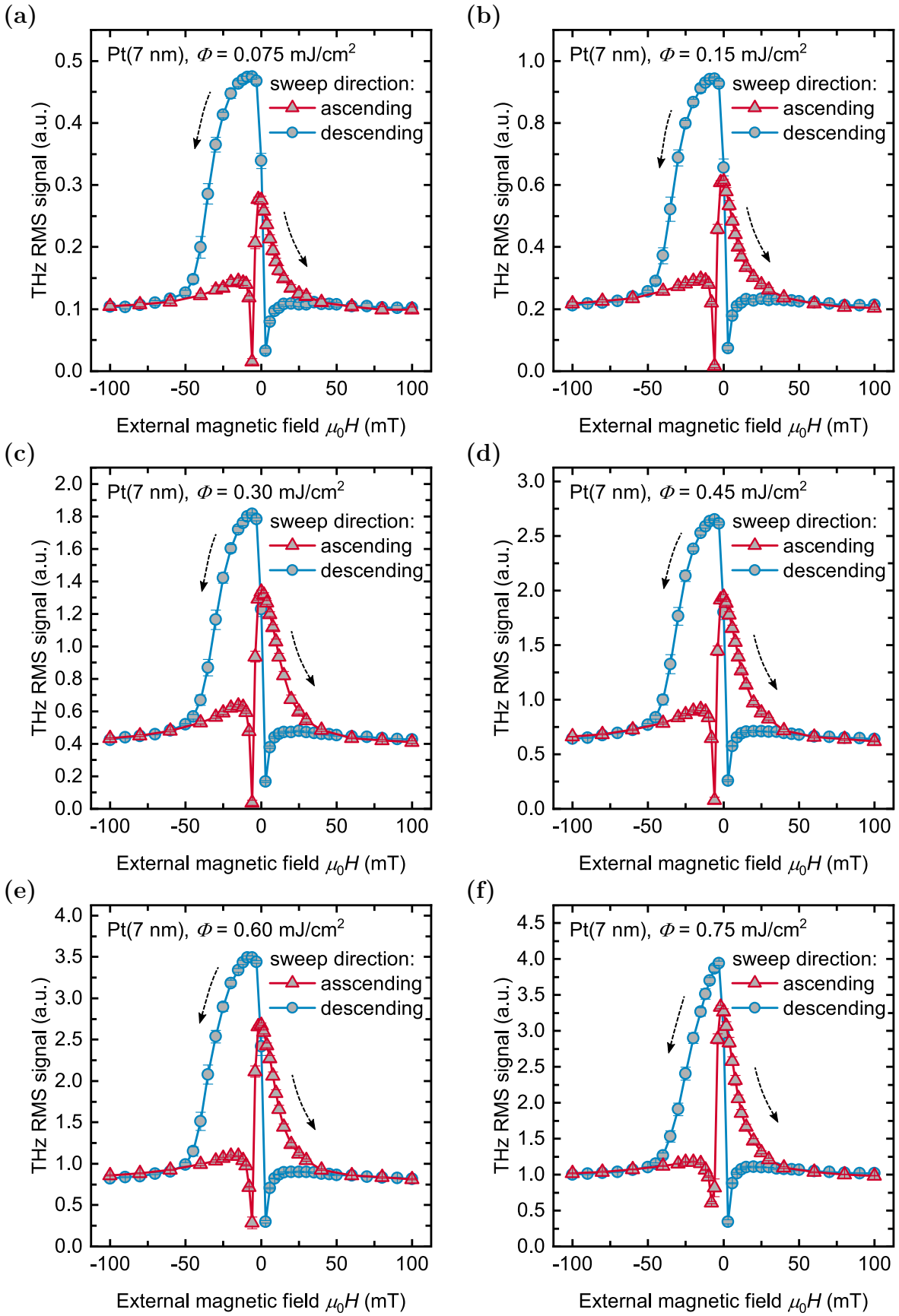

Figure 10.13: THz RMS signals of a *sub.*/$Ir_{0.23}Mn_{0.77}$(7 nm)/Fe(1.5 nm)/Pt(7 nm)/Fe(1.5 nm)/Si_3N_4(5 nm) sample measured at room temperature with different pump fluences Φ. The error bars represent the statistical errors of the RMS signals.

tion compared to the initial one. The results are displayed in figure 10.12. The measurements show that the blocking temperature of the system is in the range of $363\,\mathrm{K} \leq T_\mathrm{b} \leq 393\,\mathrm{K}$. Even for a setting temperature of 313 K, the exchange bias of the pinned layer is partially reversed. The reversed part increases for higher temperatures until the exchange bias is almost entirely reversed for $T = 363\,\mathrm{K}$. To further investigate the influence of the laser excitation on the exchange bias, a THz spectroscopy pump fluence series was measured for the sample with $t = 7\,\mathrm{nm}$. Before the measurements, the exchange bias was set by applying a magnetic field of $\mu_0 H = +200\,\mathrm{mT}$ and exciting the system at room temperature with a laser pump fluence of $1\,\mathrm{mJ/cm^2}$ (repetition rate 1 kHz) for 30 min. The measurements were sequentially performed without resetting the exchange bias, from negative to positive applied magnetic fields and vice versa. The results are displayed in the chronological order of the measurements in figure 10.13. Note that the displayed RMS signals were measured with a smaller delay time window than the results displayed in figure 10.11d and therefore are not directly comparable. For a pump fluence of $0.075\,\mathrm{mJ/cm^2}$, a similar behavior as for the samples with thicker $\mathrm{Ir_{0.23}Mn_{0.77}}$ layers discussed in section 10.3 can be observed. However, for increasing pump fluences, the THz amplitudes for ascending and descending applied magnetic fields become more and more symmetric. Figure 10.14a shows the maxima and minima (the RMS signals in the low-amplitude emitter states measured at $\mu_0 H = -100\,\mathrm{mT}$) of the THz amplitudes in dependence on the laser pump fluence. In figure 10.14b, the ratios between the maxima and minima are displayed. These show the clear trend that for increasing pump

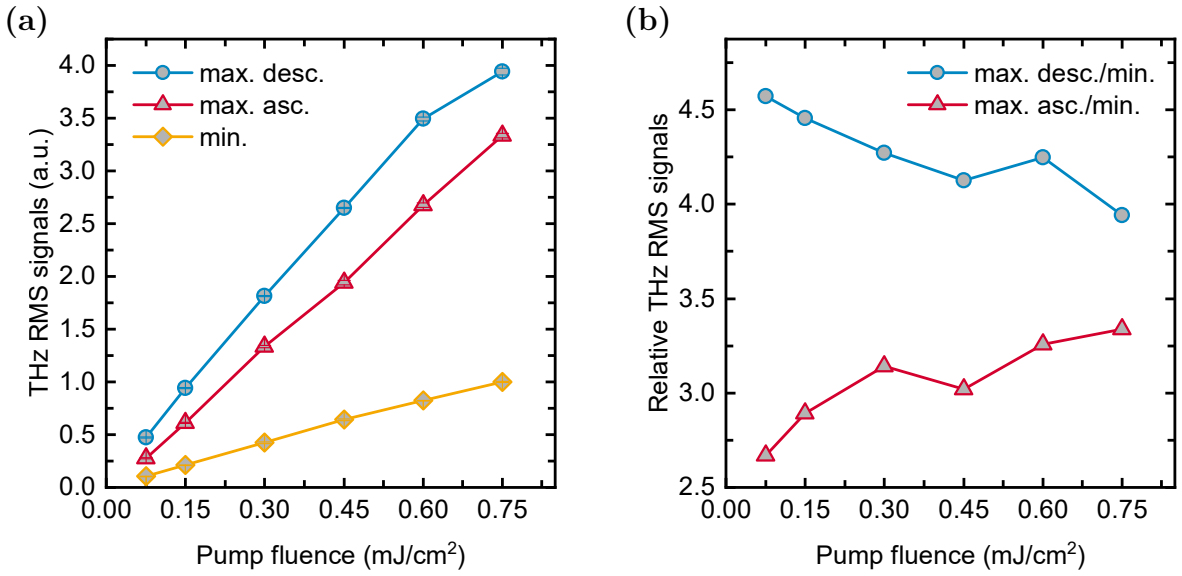

Figure 10.14: (a) shows the maxima (max.) for ascending (asc.) and descending (desc.) applied magnetic fields and the minima (min.) (the RMS signals in the low-amplitude emitter states measured at $\mu_0 H = -100\,\mathrm{mT}$) of the THz RMS signals of the measurements displayed in figure 10.13 in dependence on the laser pump fluence Φ. The error bars represent the statistical errors of the RMS signals. (b) displays the ratio between the maximum and the minimum values shown in (a).

fluences, the reached maxima become more and more independent from field sweep direction, as the exchange bias is reset during the measurements. Furthermore, the differences between the high- and low-amplitude emitter states (for descending applied magnetic fields) sequentially become smaller, as no complete antiparallel magnetization alignment of the Fe layers is reached anymore for high pump fluences. By comparison of the THz emission results with the $M(H)$ loops shown in figure 10.12, it can be estimated that the laser pump pulses lead to heating of the $Ir_{0.23}Mn_{0.77}$ spin system (see section 3.1 for an introduction to the three temperature model) up to temperatures in the range of $313\,\mathrm{K} \leq T_{\mathrm{sp,\,IrMn}} \leq 363\,\mathrm{K}$, so that the exchange bias is partially reversed.

An option that could be applied to allow the use of the emitter system in the high-amplitude state at high pump fluences would be to first set the emitter state by setting the exchange bias and afterward, coming from the saturated state in the exchange bias direction, applying a small field in the opposite direction to get the antiparallel magnetization of the Fe layers. The THz spectroscopy experiments could then be done in the high-amplitude state without an applied magnetic field. As no external field is applied, no laser-induced resetting of the exchange bias is expected. However, the drawback of this method is that the emitter system cannot be magnetically switched between the two emission states anymore.

10.6 Summary and outlook

In this section, the suitability of spin-valve systems with a pinned and a free FM Fe layer, decoupled from each other by either a W or a Pt layer, for the usage as efficient spintronic THz emitters has been demonstrated. The emitters allow the control of the THz emission amplitude by external magnetic fields. For the investigated $Ir_{0.23}Mn_{0.77}(20\,\mathrm{nm})$/Fe(3 nm)/Pt(4 nm)/Fe(3 nm) and $Ir_{0.23}Mn_{0.77}(20\,\mathrm{nm})$/Fe(3 nm)/W(4 nm)/Fe(3 nm) systems, the relative magnetization alignment of the two Fe layers can be changed by switching the magnetization of the free Fe layer with small applied in-plane magnetic fields $\mu_0 H \leq 30\,\mathrm{mT}$. This goes along with a change of the THz emission amplitude by a factor of up to 15.7 and 3.3 for the two systems, respectively. Due to the relatively small field values that are sufficient to control the magnetization alignment, short switching times can be achieved, which might be useful for future applications.

Furthermore, a first study on thickness-optimized systems with 7 nm thick $Ir_{0.23}Mn_{0.77}$ layers and 1.5 nm thick Fe layers has been performed. It could be shown that for these thinner layer stacks, the exchange bias is influenced by the heating of the $Ir_{0.23}Mn_{0.77}$ spin system induced by the laser pump pulses. Therefore, these emitters show the intended behavior only for small laser pump fluences.

One idea to overcome this problem would be to use patterning techniques on one of the Fe layers instead of the additional exchange bias layer. For a sufficiently small stripe pattern, a strong magnetic shape anisotropy in one in-plane axis along the stripes would be introduced. Therefore, the THz amplitude might be further increased, as no additional pinning layer would be needed, and higher pump fluences could be used. Instead of using a stripe patterning, also a magnetic layer system with a growth-induced in-plane magnetic easy axis along with a certain direction [308] could be used instead of one of the Fe layers.

Another idea is to make use of an emitter that can be switched from the low to the high-amplitude state and vice versa by applying an electrical current through an additional NM layer or NM conducting paths on top of the Si_3N_4 layer. The current would create an external magnetic field that could be used to switch the free FM layer. Therefore, this would be a method for on-chip control of the THz emission amplitude. Furthermore, it would allow shorter switching times between the two states.

CHAPTER 11

Summary

This work has been dedicated to the investigation of different spintronic THz emitters. The main emission process in such systems is based on a laser-induced generation of a spin current $\boldsymbol{J}_\mathrm{s}$ from a FM or FI layer toward a NM layer in which a conversion into a charge current $\boldsymbol{J}_\mathrm{c}$ via the inverse spin Hall effect occurs, leading to the emission of electromagnetic radiation in the THz frequency regime. The focus has been set on experimental studies of the influence of the magnetic properties of different FM/NM and FI/NM spintronic bilayers on the THz emission characteristics. Furthermore, efficient emitter systems that allow for switching the THz emission amplitude by temperature or small applied magnetic fields have been developed. For this purpose, more than 100 samples have been grown by magnetron sputter deposition. The magnetic properties and the THz emission characteristics of the emitter systems were investigated by SQUID-VSM measurements and THz-TDS, respectively. Additionally, the samples' structural, electrical, and optical properties were analyzed by various techniques. Moreover, a phenomenological model has been developed describing the experimentally measured THz emission amplitude of the investigated FI/NM sample series in dependence on the composition of the magnetic layers. In the following, the main results of the presented studies are summarized.

In the first study (see chapter 6), spintronic Pt/$\mathrm{Co}_x\mathrm{Fe}_{1-x}$ bilayers with varying Co content $0 \leq x \leq 1$ were investigated. The underlying idea was that the well known high spin polarization of FM $\mathrm{Co}_x\mathrm{Fe}_{1-x}$ alloys with $0.2 \lesssim x \lesssim 0.4$ might also be reflected in the THz emission amplitude of Pt/$\mathrm{Co}_x\mathrm{Fe}_{1-x}$ emitters. The layer thicknesses have been optimized with regard to the THz emission amplitude to 1 nm for the $\mathrm{Co}_x\mathrm{Fe}_{1-x}$ and 2.5 nm for the Pt layers. It has been shown that the THz emission only weakly depends on the Co content, indicating that laser-excited spin-polarized Fe and Co electrons contribute in a similar way to $\boldsymbol{J}_\mathrm{s}$. The magnetization and the THz emission amplitude show a maximum at slightly different Co contents x. The THz amplitude does not directly correlate with the measured net magnetization, as it depends on the efficiency to inject spin currents into the Pt layer J_s^*, which includes interface effects and the spin polarization of the $\mathrm{Co}_x\mathrm{Fe}_{1-x}$ close to the Fermi

edge, and the THz emission efficiency of the layer stack. The emission efficiency slightly decreases with increasing Co content. Accordingly, the estimated values of J_s^* have been shown to mainly follow the THz emission amplitude. Furthermore, the dependence of the THz emission on the laser pump fluence Φ has been investigated, revealing a stronger increase of the THz emission with rising Φ for samples with high Co content for $\Phi < 0.75\,\mathrm{mJ/cm^2}$. In addition, thickness-optimized stacked bilayer $[\mathrm{Pt/Co_{0.3}Fe_{0.7}/Si_3N_4}]_n$ emitters with $1 \leq n \leq 5$ have been prepared to further increase the THz emission amplitude. A maximum increase of the THz emission amplitude of 36 % has been observed for $n = 2$. The studies showed that $\mathrm{Co}_x\mathrm{Fe}_{1-x}$ layers can be used as efficient spin current injection layers in THz emitting spintronic bi-/multilayer systems. For thickness-optimized bilayers, a maximum increase of the THz emission amplitude of $\approx 46\%$ compared to Pt/Fe and $\approx 19\%$ compared to Pt/Co could be achieved for $x = 0.6$.

In the second and the in third study, $\mathrm{Pt}(5\,\mathrm{nm})/\mathrm{Tb}_x\mathrm{Fe}_{1-x}(20\,\mathrm{nm})$ (see chapter 7) and $\mathrm{Pt}(5\,\mathrm{nm})/\mathrm{Gd}_x\mathrm{Fe}_{1-x}(20\,\mathrm{nm})$ (see chapter 8) bilayers with varying RE content $0 \leq x \leq 1$ were investigated. The goal of these studies was to systematically investigate the role of FI layers with complex magnetic properties in spintronic emitter systems. Thus, the amorphous FI $RE_x\mathrm{Fe}_{1-x}$ alloys, which offer various magnetic states depending on the composition and temperature, were ideal candidates for these investigations. It could be shown that for both systems, mainly laser-excited spin-polarized Fe 3d electrons contribute to the generation of $\boldsymbol{J}_s$. Therefore, the THz emission amplitude follows the in-plane magnetization of the Fe magnetic sublattice, leading to a composition-dependent inversion of the THz signals close to the magnetic compensation point. For both series, the composition dependence of the THz emission amplitude for a fixed applied magnetic field of samples with $x \lesssim 0.6$ could be qualitatively described by a simple phenomenological model using only the measured THz electrical conductivity, the net magnetization, the absorption of the laser pump pulses, and the RE content of the samples. For low RE contents $x \lesssim 0.05$, a strong decrease in the electrical conductivity has been demonstrated to cause a strong increase in the THz emission efficiency and, accordingly, the measured THz amplitude. For higher RE contents, the THz amplitude has been found to be strongly dependent on the magnetic anisotropy of the samples. The $\mathrm{Pt/Tb}_x\mathrm{Fe}_{1-x}$ samples exhibit a strong perpendicular magnetic anisotropy for $0.15 < x < 0.5$. Thus, the maximum magnetic field applied for the THz emission experiments of $\mu_0 H = 544\,\mathrm{mT}$ is not sufficient to magnetically saturate the samples in in-plane direction for samples in this composition range and the THz amplitude accordingly shows a local minimum at $x = 0.4$ that correlates with a maximum in the measured effective magnetic anisotropy. Furthermore, the results of the magnetic and THz emission properties give a strong indication for complex canted states between the Fe, and Tb magnetic sublattices that could be caused by the high magnetic anisotropy in combination with the in-plane applied magnetic fields and the pronounced fanning cones especially of the Tb, but also the Fe magnetic sublattices in $\mathrm{Tb}_x\mathrm{Fe}_{1-x}$.

This makes the interpretation of the measured data challenging and also causes deviations from the developed model. For a more accurate description, element-specific measurements of the magnetic reversal behavior would be necessary. In contrast to that, the Gd_xFe_{1-x} alloys exhibit only a small perpendicular magnetic anisotropy for the samples with $x = 0.2$ and $x = 0.25$ and the Fe and Gd magnetic moments are more collinearly aligned. Therefore, the samples can be saturated with relatively small magnetic fields, and the developed model well describes the influence of the magnetic anisotropy that, in particular, plays a role for small applied magnetic fields $\mu_0 H \lesssim 100\,\mathrm{mT}$. For $\mu_0 H \gtrsim 100\,\mathrm{mT}$, high, almost constant THz amplitudes can be observed up to $x \approx 0.3$. For high RE contents, the RE_xFe_{1-x} alloys of both series become gradually paramagnetic with increasing x at room temperature. Combined with the decreasing Fe content, this leads to decreasing THz amplitudes. In general, the Pt/Gd_xFe_{1-x} samples show higher THz amplitudes due to higher impedance values, resulting in higher THz emission efficiencies. Besides the investigations at room temperature, also measurements at low temperatures ($T \approx 80\,\mathrm{K}$) have been performed. The THz emission of samples with a RE dominated net magnetization is strongly enhanced at low temperatures. Especially samples with RE_xFe_{1-x} layers that are in a paramagnetic state at room temperature become FI (or FM, for $x = 1$) at low temperatures and show surprisingly high THz amplitudes. The high THz amplitudes of the pure Pt/RE samples (the amplitude of the Pt/Gd sample even exceeds the amplitude of the Pt/Fe sample at low temperatures) give a strong indication that, at least for the RE rich samples at low temperatures, spin-polarized RE electrons play an important role for the emission process. Furthermore, this finding is supported by significant changes in the THz signal shapes for $x \gtrsim 0.7$. For samples with $x \lesssim 0.6$, the composition dependence of the emitted THz radiation at low temperatures can still be qualitatively described by the model developed for the room-temperature results. In addition to the bilayer samples, also the THz emission of several single-layer $Gd_xFe_{1-x}(20\,\mathrm{nm})$ samples have been investigated in order to estimate the influence of the THz signal directly emitted by the ultrafast demagnetization of the magnetic layers. Here, only for the pure Fe layer, a significant contribution of about 14% of the THz signal of the respective Pt/Fe bilayer reference sample has been found. However, for the single-layer samples with high Gd content ($x = 0.6$ and $x = 0.8$), the emitted THz signals that might be caused by the anomalous Hall effect give a significant contribution to the THz signal that even overcomes the THz radiation caused by the inverse spin Hall effect in the Pt layer of the bilayer reference samples. The studies demonstrated that the THz emission properties of Pt/RE_xFe_{1-x} bilayer systems can be systematically tailored by varying the magnetic properties of the FI layers. In particular, the polarization of the emitted THz signal can be switched by 180° by varying the temperature across the magnetic compensation point or the composition of the RE_xFe_{1-x} layer.

The observed inversion of the THz signal emitted by Pt/Gd_xFe_{1-x} layers with a Gd-dominated compared to a Fe-dominated net magnetization has been utilized to realize a functional emitter system as presented in the fourth study (see chapter 9). Here, it has been demonstrated that FI Gd_xFe_{1-x} layers with a suitable film thickness and composition can be utilized to control the THz emission state by temperature. To this end, a Pt(3 nm)/$Gd_{0.1}Fe_{0.9}$(3 nm)/W(3 nm)/$Gd_{0.3}Fe_{0.7}$(3 nm)/Pt(3 nm) emitter system has been developed. The $Gd_{0.3}Fe_{0.7}$ layer in this system shows a magnetic compensation point at around $T_{\mathrm{comp}} = 160\,\mathrm{K}$, whereas the magnetization of the $Gd_{0.1}Fe_{0.9}$ layer is Fe-dominated at all temperatures. Thus, the relative alignment of the Fe magnetic moments of the FI layers can be changed from antiparallel to parallel by adjusting the temperature from below to above T_{comp}. Due to the positive spin Hall angle of Pt and the negative spin Hall angle of W, all NM layers contribute to the THz emission in a constructive manner for an antiparallel alignment of the Fe magnetic moments in the FI layers. In contrast, the generated spin currents contribute destructively to the THz emission process for a parallel alignment. Therefore, heating the emitter from below to above T_{comp} leads to a drop in the THz emission amplitude of about one order of magnitude. The study demonstrated that the compensation point of suitable FI layers can be utilized for highly efficient spintronic emitter systems that allow for the switching of the THz emission between a low-amplitude and a high-amplitude state by temperature.

The last presented study (see chapter 10) demonstrated the suitability of spin-valve systems with a pinned and a free FM Fe layer, decoupled from each other by either a W or a Pt layer, for the usage as efficient spintronic THz emitters that allow for the control of the THz emission amplitude by small external magnetic fields. In the investigated $Ir_{0.23}Mn_{0.77}$(20 nm)/Fe(3 nm)/X/Fe(3 nm) systems with either X = Pt(4 nm) or X = W(4 nm), the magnetization of the pinned Fe layer is exchange-biased by an AFM $Ir_{0.23}Mn_{0.77}$ layer. Thus, the relative magnetization alignment of the two Fe layers can be changed by switching the magnetization of the free Fe layer with small applied in-plane magnetic fields $\mu_0 H \leq 30\,\mathrm{mT}$. This goes along with a change of the THz emission amplitude by a factor of up to 15.7, as for an antiparallel relative magnetization alignment, the spin currents launched from the Fe layers contribute in a constructive way to the THz emission, whereas for a parallel alignment, the spin currents contribute destructively to the THz emission. The relatively small field values that are sufficient to control the magnetization alignment allow for short switching times between the two emitter states, which could be useful for future applications.

The different studies shown in this work demonstrate that the THz emission properties of spintronic emitter systems can be tailored by using suitable magnetic layers and that also FI RE_xFe_{1-x} alloys can be used instead of FM layers to achieve efficient emitter systems. However, especially the high THz emission amplitudes observed at low temperatures and the THz emission of the Gd_xFe_{1-x} single layers that indicate the contribution of a different emission process, which is not based on the inverse spin Hall effect, are still not entirely

understood and need to be clarified in future works. The thermally and the magnetically switchable emitter systems might open the way for future applications as well as for further improvements in the THz emission amplitude.

APPENDIX A

Supplementary material

A.1 List of samples

In the following tables, all sputtered samples that were used for this work, with the sample numbers, the layer stacks, and the relevant sputter rates and angles are listed (the sputter rates for the capping layers are not included in the tables). The numbers in the brackets of the layer stacks denote the film thicknesses in nm. All magnetrons were adjusted to the similar sputter angle α unless mentioned in the footnotes. The sputter angles α are given as a distance in mm (see [342] for details). The sputter rates ϕ are given in Å/s. All metallic targets were sputtered with DC power supplies unless mentioned in the foot notes. For all Pt depositions, a sputter rate of $\phi_{\mathrm{Pt}} = 0.5\,\text{Å/s}$ was used.

Pt(5 nm)/Co_xFe_{1-x}(3 nm)/Si_3N_4(5 nm) series (chapter 6)

Number	Layer stack	α	ϕ_{Co}	ϕ_{Fe}
B171121_1	*sub.*/Pt(5)/$Co_{0.2}Fe_{0.8}$(3)/Si_3N_4(5)	18.0	0.20	0.43
B171121_2	*sub.*/Pt(5)/$Co_{0.4}Fe_{0.6}$(3)/Si_3N_4(5)	18.0	0.27	0.43
B171121_3	*sub.*/Pt(5)/$Co_{0.6}Fe_{0.4}$(3)/Si_3N_4(5)	18.0	0.35	0.25
B171121_4	*sub.*/Pt(5)/$Co_{0.8}Fe_{0.2}$(3)/Si_3N_4(5)	18.0	0.41	0.11
B171121_5	*sub.*/Pt(5)/Co(3)/Si_3N_4(5)	18.0	0.35	-
B171121_6	*sub.*/Pt(5)/Fe(3)/Si_3N_4(5)	18.0	-	0.25

Pt(t_{Pt})/$Co_{0.3}Fe_{0.7}$(t_{CoFe})/Si_3N_4(5 nm) series (chapter 6)

Number	Layer stack	α	ϕ_{Co}	ϕ_{Fe}
B171213_1	*sub.*/Pt(5)/$Co_{0.3}Fe_{0.7}$(3)/Si_3N_4(5)	17.5	0.16	0.40
B171213_2	*sub.*/Pt(5)/$Co_{0.3}Fe_{0.7}$(2)/Si_3N_4(5)	17.5	0.16	0.40
B171213_3	*sub.*/Pt(5)/$Co_{0.3}Fe_{0.7}$(1.5)/Si_3N_4(5)	17.5	0.16	0.40
B171213_4	*sub.*/Pt(5)/$Co_{0.3}Fe_{0.7}$(1)/Si_3N_4(5)	17.5	0.16	0.40
B171213_5	*sub.*/Pt(5)/$Co_{0.3}Fe_{0.7}$(0.75)/Si_3N_4(5)	17.5	0.16	0.40
B171213_6	*sub.*/Pt(5)/$Co_{0.3}Fe_{0.7}$(0.5)/Si_3N_4(5)	17.5	0.16	0.40
B171213_7	*sub.*/Pt(4)/$Co_{0.3}Fe_{0.7}$(3)/Si_3N_4(5)	17.5	0.16	0.40
B171213_8	*sub.*/Pt(3)/$Co_{0.3}Fe_{0.7}$(3)/Si_3N_4(5)	17.5	0.16	0.40
B171213_9	*sub.*/Pt(2)/$Co_{0.3}Fe_{0.7}$(3)/Si_3N_4(5)	17.5	0.16	0.40
B171213_10	*sub.*/Pt(1.5)/$Co_{0.3}Fe_{0.7}$(3)/Si_3N_4(5)	17.5	0.16	0.40
B171213_11	*sub.*/Pt(1)/$Co_{0.3}Fe_{0.7}$(3)/Si_3N_4(5)	17.5	0.16	0.40

Pt(2.5 nm)/Co_xFe_{1-x}(1 nm)/Si_3N_4(5 nm) series (chapter 6)

Number	Layer stack	α	ϕ_{Co}	ϕ_{Fe}
B181012_4	*sub.*/Pt(2.5)/Fe(1)/Si_3N_4(5)	17.5	0.40	-
B181012_5	*sub.*/Pt(2.5)/$Co_{0.2}Fe_{0.8}$(1)/Si_3N_4(5)	17.5	0.13	0.555
B181012_6	*sub.*/Pt(2.5)/$Co_{0.3}Fe_{0.7}$(1)/Si_3N_4(5)	17.5	0.16	0.40
B181012_7	*sub.*/Pt(2.5)/$Co_{0.4}Fe_{0.6}$(1)/Si_3N_4(5)	17.5	0.33	0.53
B181012_8	*sub.*/Pt(2.5)/$Co_{0.5}Fe_{0.5}$(1)/Si_3N_4(5)	17.5	0.29	0.31
B181012_9	*sub.*/Pt(2.5)/$Co_{0.6}Fe_{0.4}$(1)/Si_3N_4(5)	17.5	0.35	0.25
B181012_10	*sub.*/Pt(2.5)/$Co_{0.8}Fe_{0.2}$(1)/Si_3N_4(5)	17.5	0.41	0.11
B181012_11	*sub.*/Pt(2.5)/Co(1)/Si_3N_4(5)	17.5	-	0.35

Co_xFe_{1-x}(1 nm)/Si_3N_4(5 nm) series (chapter 6)

Number	Layer stack	α	ϕ_{Co}	ϕ_{Fe}
B210818_1	*sub.*/$Co_{0.3}Fe_{0.7}$(1)/Si_3N_4(5)	17.5	0.16	0.40
B210818_2	*sub.*/$Co_{0.6}Fe_{0.4}$(1)/Si_3N_4(5)	17.5	0.35	0.25
B210818_3	*sub.*/Co(1)/Si_3N_4(5)	17.5	0.35	-
B210818_4	*sub.*/Fe(1)/Si_3N_4(5)	17.5	-	0.40

$[Pt(2.5\,nm)/Co_{0.3}Fe_{0.7}(1\,nm)/Si_3N_4(5\,nm)]_n$ series (chapter 6)

Number	Layer stack	α	ϕ_{Co}	ϕ_{Fe}
B180502_4	*sub.*/Pt(2.5)/$Co_{0.3}Fe_{0.7}$(1)/Si_3N_4(5)	17.5	0.16	0.40
B180502_5	*sub.*/[Pt(2.5)/$Co_{0.3}Fe_{0.7}$(1)/Si_3N_4(5)]$_3$	17.5	0.16	0.40
B181017_1	*sub.*/[Pt(2.5)/$Co_{0.3}Fe_{0.7}$(1)/Si_3N_4(5)]$_2$	17.5	0.16	0.40
B181017_2	*sub.*/[Pt(2.5)/$Co_{0.3}Fe_{0.7}$(1)/Si_3N_4(5)]$_5$	17.5	0.16	0.40
B181017_3	*sub.*/[Pt(2.5)/$Co_{0.3}Fe_{0.7}$(1)/Si_3N_4(5)]$_4$	17.5	0.16	0.40

$[Pt(2.5\,nm)/Tb_{0.1}Fe_{0.9}(1\,nm)/Si_3N_4(5\,nm)]_n$ series (chapter 6)

Number	Layer stack	α	ϕ_{Tb}	ϕ_{Fe}
B180427_2	*sub.*/Pt(2.5)/$Tb_{0.1}Fe_{0.9}$(1)/Si_3N_4(5)	17.5 [1]	0.16	0.53
B180427_3	*sub.*/[Pt(2.5)/$Tb_{0.1}Fe_{0.9}$(1)/Si_3N_4(5)]$_3$	17.5 [1]	0.16	0.53
B190114_6	*sub.*/[Pt(2.5)/$Tb_{0.1}Fe_{0.9}$(1)/Si_3N_4(5)]$_2$	17.5 [2]	0.16	0.53
B190114_7	*sub.*/[Pt(2.5)/$Tb_{0.1}Fe_{0.9}$(1)/Si_3N_4(5)]$_5$	17.5 [2]	0.16	0.53
B190114_8	*sub.*/[Pt(2.5)/$Tb_{0.1}Fe_{0.9}$(1)/Si_3N_4(5)]$_4$	17.5 [2]	0.16	0.53

[1] Tb sputter angle $\alpha = 14\,mm$, [2] Tb sputter angle $\alpha = 12.5\,mm$

$[Pt(5\,nm)/Ni_{0.81}Fe_{0.19}(3\,nm)/Si_3N_4(5\,nm)]_n$ series (chapter 6)

Number	Layer stack	α	ϕ_{NiFe}
B171026_1	*sub.*/Pt(5)/$Ni_{0.81}Fe_{0.19}$(3)/Si_3N_4(5)	18	0.30
B171026_2	*sub.*/[Pt(5)/$Ni_{0.81}Fe_{0.19}$(3)/Si_3N_4(5)]$_2$	18	0.30
B171026_3	*sub.*/[Pt(5)/$Ni_{0.81}Fe_{0.19}$(3)/Si_3N_4(5)]$_3$	18	0.30
B171026_4	*sub.*/[Pt(5)/$Ni_{0.81}Fe_{0.19}$(3)/Si_3N_4(5)]$_5$	18	0.30
B171026_5	*sub.*/[Pt(5)/$Ni_{0.81}Fe_{0.19}$(3)/Si_3N_4(5)]$_4$	18	0.30

Reference samples (B180702_2 was also used as emitter for the THz transmission spectroscopy experiments to determine the THz conductivities)

Number	Layer stack	α	ϕ_{Fe}	ϕ_W
B180702_2	*sub.*/Pt(3)/Fe(1.5)/W(3)/Si_3N_4(5)	15	0.20	0.20
B190502_2	*sub.*/Pt(3)/Fe(3)/Si_3N_4(5)	17.5	0.16	-
B201118_3	*sub.*/Pt(3)/Fe(3)/Si_3N_4(5)	17.5	0.30	-

Pt(5 nm)/Tb_xFe_{1-x}(20 nm)/Co(2 nm) series (chapter 7)

Number	Layer stack	α	ϕ_{Tb}	ϕ_{Fe}
B170929_1	*sub.*/Pt(5)/Tb(20)/Co(2)	18.5	0.885 [1]	-
B170929_2	*sub.*/Pt(5)/$Tb_{0.1}Fe_{0.9}$(20)/Co(2)	18.5	0.16 [1]	0.53
B170929_3	*sub.*/Pt(5)/$Tb_{0.2}Fe_{0.8}$(20)/Co(2)	18.5	0.30 [1]	0.445
B170929_4	*sub.*/Pt(5)/$Tb_{0.3}Fe_{0.7}$(20)/Co(2)	18.5	0.36 [1]	0.31
B170929_5	*sub.*/Pt(5)/$Tb_{0.5}Fe_{0.5}$(20)/Co(2)	18.5	0.68 [1]	0.25
B170929_6	*sub.*/Pt(5)/$Tb_{0.7}Fe_{0.3}$(20)/Co(2)	18.5	0.885 [1]	0.14
B170929_7	*sub.*/Pt(5)/$Tb_{0.8}Fe_{0.2}$(20)/Co(2)	18.5	1.085 [1]	0.10
B170929_8	*sub.*/Pt(5)/Fe(20)/Co(2)	18.5	-	0.25
B170929_14	*sub.*/Pt(5)/$Tb_{0.9}Fe_{0.1}$(20)/Co(2)	18.5	2.00	0.085
B171212_1	*sub.*/Pt(5)/$Tb_{0.4}Fe_{0.6}$(20)/Co(2)	17.5	1.02	0.25
B171212_2	*sub.*/Pt(5)/$Tb_{0.45}Fe_{0.55}$(20)/Co(2)	17.5	0.53	0.16
B171212_3	*sub.*/Pt(5)/$Tb_{0.55}Fe_{0.45}$(20)/Co(2)	17.5	0.40	0.18
B171212_4	*sub.*/Pt(5)/$Tb_{0.6}Fe_{0.4}$(20)/Co(2)	17.5	0.47	0.26
B171229_1	*sub.*/Pt(5)/$Tb_{0.05}Fe_{0.95}$(20)/Co(2)	18.0 [2]	0.08 [1]	0.56
B171229_2	*sub.*/Pt(5)/$Tb_{0.15}Fe_{0.85}$(20)/Co(2)	18.0	0.24 [1]	0.50
B180124_1	*sub.*/Pt(5)/$Tb_{0.22}Fe_{0.78}$(20)/Co(2)	17.5	0.33 [1]	0.43
B180124_3	*sub.*/Pt(5)/$Tb_{0.24}Fe_{0.76}$(20)/Co(2)	17.5	0.36 [1]	0.42
B180124_5	*sub.*/Pt(5)/$Tb_{0.26}Fe_{0.74}$(20)/Co(2)	17.5	0.40 [1]	0.42
B180124_7	*sub.*/Pt(5)/$Tb_{0.28}Fe_{0.72}$(20)/Co(2)	17.5	0.39 [1]	0.37
B180125_1	*sub.*/Pt(5)/$Tb_{0.03}Fe_{0.97}$(20)/Co(2)	17.5 [3]	0.04 [1]	0.48
B180129_1	*sub.*/Pt(5)/$Tb_{0.015}Fe_{0.985}$(20)/Co(2)	17.5 [4]	0.02 [1]	0.48

[1] Tb sputtered with RF power supply, [2] Tb sputter angle $\alpha = 10\,\text{mm}$, [3] Tb sputter angle $\alpha = 6\,\text{mm}$, [4] Tb sputter angle $\alpha = 4\,\text{mm}$

Pt(5 nm)/Tb_xFe_{1-x}(20 nm)/Si_3N_4(5 nm) series (chapter 7)

Number	Layer stack	α	ϕ_{Tb}	ϕ_{Fe}
B171212_5	*sub.*/Pt(5)/$Tb_{0.6}Fe_{0.4}$(20)/Si_3N_4(5)	17.5	1.02	0.25
B171215_1	*sub.*/Pt(5)/$Tb_{0.4}Fe_{0.6}$(20)/Si_3N_4(5)	17.5	0.47	0.26
B171215_2	*sub.*/Pt(5)/$Tb_{0.2}Fe_{0.8}$(20)/Si_3N_4(5)	17.5	0.30	0.445
B171229_3	*sub.*/Pt(5)/$Tb_{0.1}Fe_{0.9}$(20)/Si_3N_4(5)	18.0	0.16 [1]	0.53
B171229_4	*sub.*/Pt(5)/$Tb_{0.15}Fe_{0.85}$(20)/Si_3N_4(5)	18.0	0.24 [1]	0.50
B171229_5	*sub.*/Pt(5)/$Tb_{0.05}Fe_{0.95}$(20)/Si_3N_4(5)	18.0 [2]	0.08	0.56
B180102_1	*sub.*/Pt(5)/$Tb_{0.2}Fe_{0.8}$(20)/Si_3N_4(5)	18.0	0.30 [1]	0.445
B180102_2	*sub.*/Pt(5)/$Tb_{0.3}Fe_{0.7}$(20)/Si_3N_4(5)	18.0	0.36 [1]	0.31
B180102_3	*sub.*/Pt(5)/$Tb_{0.5}Fe_{0.5}$(20)/Si_3N_4(5)	18.0	0.68	0.25
B180102_4	*sub.*/Pt(5)/$Tb_{0.7}Fe_{0.3}$(20)/Si_3N_4(5)	18.0	0.885	0.14
B180102_5	*sub.*/Pt(5)/$Tb_{0.8}Fe_{0.2}$(20)/Si_3N_4(5)	18.0	1.085	0.10
B180102_6	*sub.*/Pt(5)/$Tb_{0.9}Fe_{0.1}$(20)/Si_3N_4(5)	18.0	1.72	0.07 [3]
B180102_7	*sub.*/Pt(5)/Tb(20)/Si_3N_4(5)	18.0	1.72	-
B180102_8	*sub.*/Pt(5)/Fe(20)/Si_3N_4(5)	18.0	-	0.20 [3]
B180124_2	*sub.*/Pt(5)/$Tb_{0.22}Fe_{0.78}$(20)/Si_3N_4(5)	17.5	0.33 [1]	0.43
B180124_4	*sub.*/Pt(5)/$Tb_{0.24}Fe_{0.76}$(20)/Si_3N_4(5)	17.5	0.36 [1]	0.42
B180124_6	*sub.*/Pt(5)/$Tb_{0.26}Fe_{0.74}$(20)/Si_3N_4(5)	17.5	0.40 [1]	0.42
B180124_8	*sub.*/Pt(5)/$Tb_{0.28}Fe_{0.72}$(20)/Si_3N_4(5)	17.5	0.39 [1]	0.37
B180129_1	*sub.*/Pt(5)/$Tb_{0.03}Fe_{0.97}$(20)/Si_3N_4(5)	17.5 [4]	0.04	0.48
B180129_3	*sub.*/Pt(5)/$Tb_{0.015}Fe_{0.985}$(20)/Si_3N_4(5)	17.5 [5]	0.02	0.48

[1] Tb sputtered with RF power supply, [2] Tb sputter angle $\alpha = 10\,\text{mm}$, [3] Fe sputtered with RF power supply, [4] Tb sputter angle $\alpha = 6\,\text{mm}$, [5] Tb sputter angle $\alpha = 4\,\text{mm}$

Pt(5 nm)/Gd_xFe_{1-x}(20 nm)/Si_3N_4(5 nm) series (chapter 8)

Number	Layer stack	α	ϕ_{Gd}	ϕ_{Fe}
B180423_1	*sub.*/Pt(5)/$Gd_{0.20}Fe_{0.80}$(20)/Si_3N_4(5)	17.5	0.33	0.47
B180423_2	*sub.*/Pt(5)/$Gd_{0.40}Fe_{0.60}$(20)/Si_3N_4(5)	17.5	0.45	0.24
B180423_3	*sub.*/Pt(5)/$Gd_{0.60}Fe_{0.40}$(20)/Si_3N_4(5)	17.5	0.59	0.14
B180423_4	*sub.*/Pt(5)/$Gd_{0.80}Fe_{0.20}$(20)/Si_3N_4(5)	17.5	0.90	0.08
B180424_3	*sub.*/Pt(5)/Gd(20)/Si_3N_4(5)	17.5	0.60	-
B180430_1	*sub.*/Pt(5)/$Gd_{0.10}Fe_{0.90}$(20)/Si_3N_4(5)	17.5 [1]	0.21	0.67
B180430_2	*sub.*/Pt(5)/$Gd_{0.30}Fe_{0.70}$(20)/Si_3N_4(5)	17.5 [1]	0.47	0.39
B180430_3	*sub.*/Pt(5)/$Gd_{0.25}Fe_{0.75}$(20)/Si_3N_4(5)	17.5 [1]	0.30	0.32
B180507_1	*sub.*/Pt(5)/$Gd_{0.15}Fe_{0.85}$(20)/Si_3N_4(5)	17.5 [2]	0.10	0.20
B180507_2	*sub.*/Pt(5)/$Gd_{0.05}Fe_{0.95}$(20)/Si_3N_4(5)	17.5 [2]	0.10	0.67
B200207_1	*sub.*/Pt(5)/$Gd_{0.67}Fe_{0.33}$(20)/Si_3N_4(5)	17.5	0.74	0.13
B200207_2	*sub.*/Pt(5)/$Gd_{0.74}Fe_{0.26}$(20)/Si_3N_4(5)	17.5	0.80	0.10

[1] Gd sputter angle $\alpha = 15\,\text{mm}$, [2] Gd sputter angle $\alpha = 10\,\text{mm}$

Gd_xFe_{1-x}(20 nm)/Si_3N_4(5 nm) series (chapter 8)

Number	Layer stack	α	ϕ_{Gd}	ϕ_{Fe}
B181018_2	*sub.*/Fe(20)/Si_3N_4(5)	17.5	-	0.40
B181018_5	*sub.*/Gd(20)/Si_3N_4(5)	17.5	0.47 [1]	-
B190114_1	*sub.*/$Gd_{0.10}Fe_{0.90}$(20)/Si_3N_4(5)	17.5	0.21 [2]	0.67
B190114_2	*sub.*/$Gd_{0.20}Fe_{0.80}$(20)/Si_3N_4(5)	17.5	0.33	0.47
B190114_3	*sub.*/$Gd_{0.40}Fe_{0.60}$(20)/Si_3N_4(5)	17.5	0.45	0.24
B190114_4	*sub.*/$Gd_{0.60}Fe_{0.40}$(20)/Si_3N_4(5)	17.5	0.59	0.14
B190114_5	*sub.*/$Gd_{0.80}Fe_{0.20}$(20)/Si_3N_4(5)	17.5	0.90	0.08

[1] Gd sputter angle $\alpha = 15\,\text{mm}$, [2] Gd sputter angle $\alpha = 12.5\,\text{mm}$

Thermomagnetically switchable THz emitters (chapter 9)

Number	Layer stack	α	ϕ_{Gd}	ϕ_{Fe}	ϕ_{W}	ϕ_{CoFeB}
B181022_3	*sub.*/Pt(3)/$Gd_{0.1}Fe_{0.9}$(3)/W(3)/ $Gd_{0.3}Fe_{0.7}$(3)/Pt(3)/Si_3N_4(5)	17.5 [1]	0.21/ 0.47	0.67/ 0.39	0.25	-
B181022_4	*sub.*/Pt(3)/$Gd_{0.1}Fe_{0.9}$(3)/Si_3N_4(5)	17.5 [1]	0.21	0.67	-	-
B181023_4	*sub.*/Pt(3)/$Gd_{0.3}Fe_{0.7}$(1)/Si_3N_4(5)	17.5 [1]	0.47	0.39	-	-
B181023_5	*sub.*/Pt(3)/$Gd_{0.3}Fe_{0.7}$(2)/Si_3N_4(5)	17.5 [1]	0.47	0.39	-	-
B181023_6	*sub.*/Pt(3)/$Gd_{0.3}Fe_{0.7}$(3)/Si_3N_4(5)	17.5 [1]	0.47	0.39	-	-
B181023_7	*sub.*/Pt(3)/$Gd_{0.3}Fe_{0.7}$(4)/Si_3N_4(5)	17.5 [1]	0.47	0.39	-	-
B181023_8	*sub.*/Pt(3)/$Gd_{0.3}Fe_{0.7}$(5)/Si_3N_4(5)	17.5 [1]	0.47	0.39	-	-
B181023_9	*sub.*/Pt(3)/$Gd_{0.3}Fe_{0.7}$(10)/Si_3N_4(5)	17.5 [1]	0.47	0.39	-	-
B190605_1	*sub.*/Pt(3)/$Gd_{0.3}Fe_{0.7}$(5)/W(3)/ $Co_{0.4}Fe_{0.4}B_{0.2}$(2)/Pt(3)/Si_3N_4(5)	17.5	0.47	0.39	0.25	0.18
B191212_1	*sub.*/Pt(2)/$Co_{0.4}Fe_{0.4}B_{0.2}$(1.5)/W(2)/ $Gd_{0.3}Fe_{0.7}$(3)/Pt(2)/Si_3N_4(5)	17.5	0.47	0.39	0.38	0.14

[1] Gd sputter angle $\alpha = 15\,\mathrm{mm}$

Magnetically switchable THz emitters (chapter 10)

Number	Layer stack	α	ϕ_{IrMn}	ϕ_{Fe}	ϕ_{W}
B190417_1	*sub.*/$Ir_{0.23}Mn_{0.77}$(20)/Fe(3)/Si_3N_4(5)	17.5	0.42	0.30	-
B200309_1	*sub.*/$Ir_{0.23}Mn_{0.77}$(20)/Fe(3)/Pt(4)/ Fe(3)/Si_3N_4(5)	17.5	0.40	0.20	-
B200309_2	*sub.*/$Ir_{0.23}Mn_{0.77}$(20)/Fe(3)/Pt(5)/ Fe(3)/Si_3N_4(5)	17.5	0.40	0.20	-
B200309_3	*sub.*/$Ir_{0.23}Mn_{0.77}$(20)/Fe(3)/W(3)/ Fe(3)/Si_3N_4(5)	17.5	0.40	0.20	0.36
B200309_4	*sub.*/$Ir_{0.23}Mn_{0.77}$(20)/Fe(3)/W(4)/ Fe(3)/Si_3N_4(5)	17.5	0.40	0.20	0.36
B200414_1	*sub.*/$Ir_{0.23}Mn_{0.77}$(20)/Fe(3)/W(2)/ Fe(3)/Si_3N_4(5)	17.5	0.39	0.20	0.35
B200414_2	*sub.*/$Ir_{0.23}Mn_{0.77}$(10)/Fe(3)/Al(3)	17.5	0.39	0.20	-
B200414_3	*sub.*/$Ir_{0.23}Mn_{0.77}$(7)/Fe(3)/Al(3)	17.5	0.39	0.20	-
B200414_4	*sub.*/$Ir_{0.23}Mn_{0.77}$(5)/Fe(3)/Al(3)	17.5	0.39	0.20	-
B200421_1	*sub.*/$Ir_{0.23}Mn_{0.77}$(7)/Fe(1.5)/Pt(4)/ Fe(1.5)/Si_3N_4(5)	17.5	0.39	0.20	-
B200506_1	*sub.*/$Ir_{0.23}Mn_{0.77}$(7)/Fe(1.5)/Pt(7)/ Fe(1.5)/Si_3N_4(5)	17.5	0.39	0.20	-

A.2 Spintronic Pt/Co_xFe_{1-x} terahertz emitters

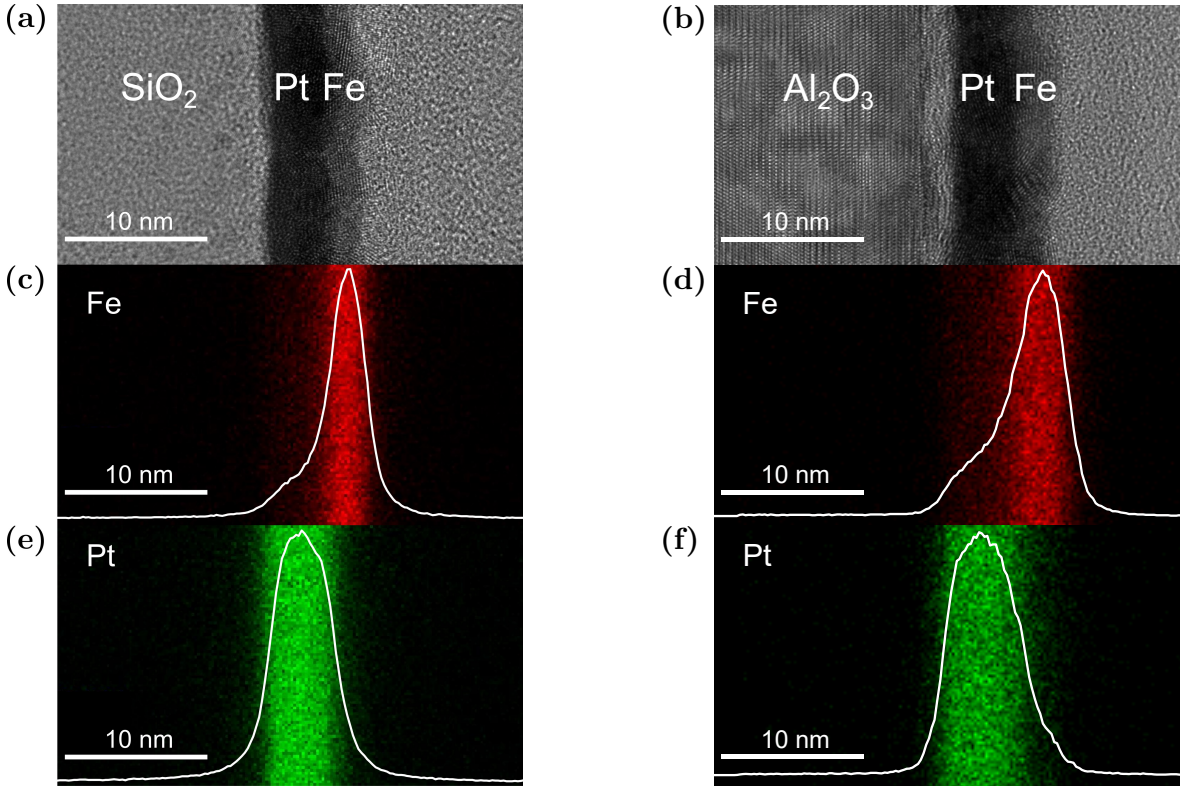

Figure A.1: Transmission electron microscopy results of *sub.*/Pt(3 nm)/Fe(3 nm)/Si_3N_4(5 nm) samples grown on (a, c, e) 525 µm thick p-doped Si(100) substrates with a 100 nm thick thermally oxidized SiO_2 layer and on (b, d, f) 500 µm thick Al_2O_3(0001) substrates. (a) and (b) show bright-field images of the samples, and (c–f) display corresponding EDX elemental maps for (c, d) Fe and (e, f) Pt. The white lines show the average Fe and Pt distributions in the layer stack.

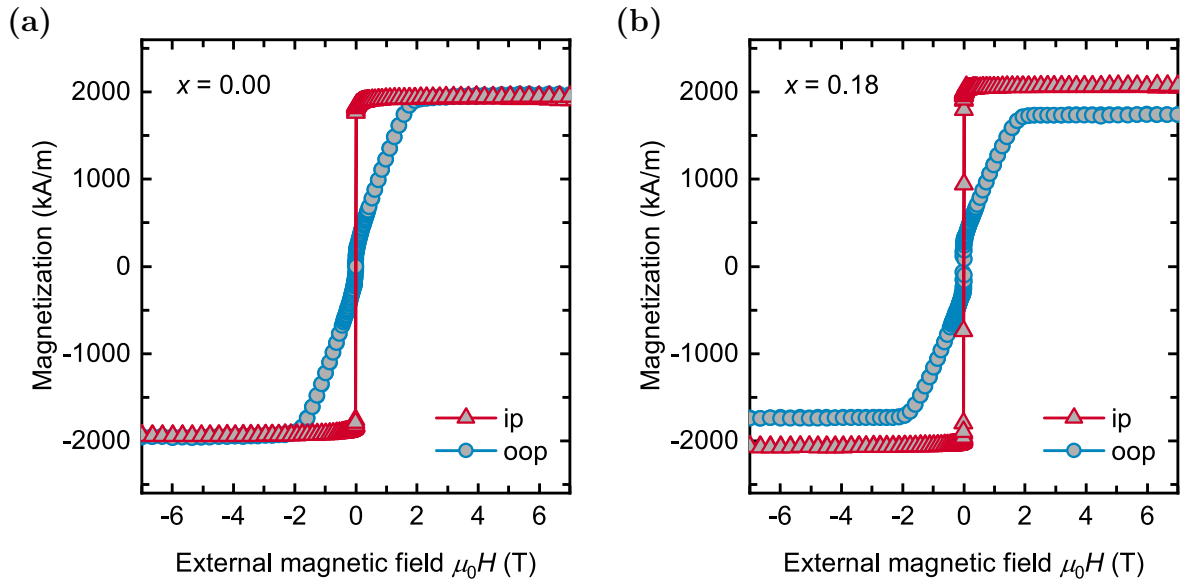

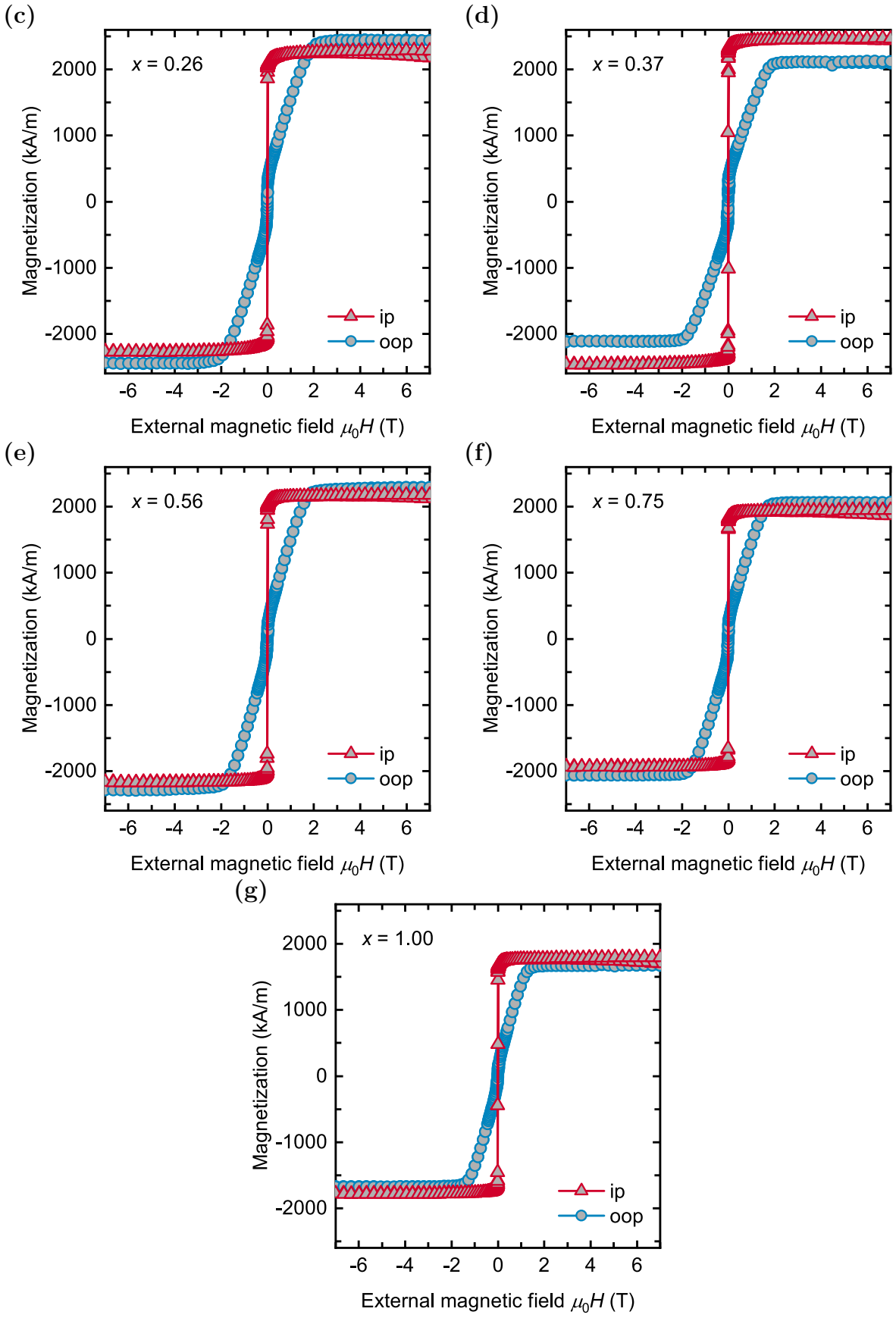

Figure A.2: Room-temperature SQUID-VSM $M(H)$ loops of *sub.*/Pt(5 nm)/Co_xFe_{1-x}(3 nm)/Si_3N_4(5 nm) samples with different Co content x measured in in-plane and out-of-plane direction.

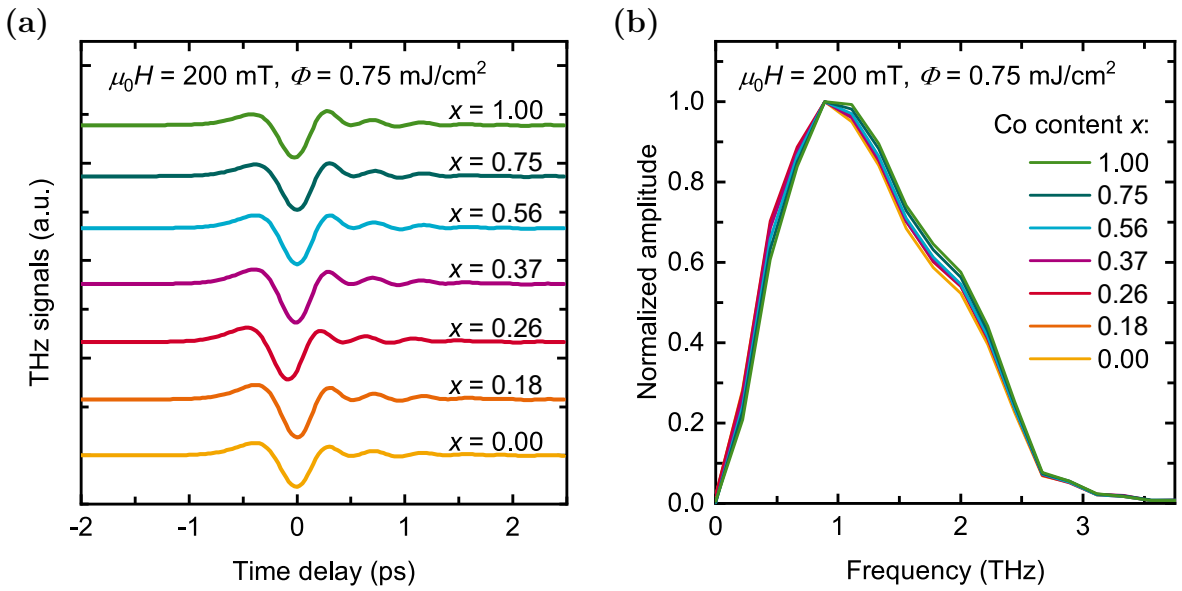

Figure A.3: (a) Measured THz electro-optic signals of *sub.*/Pt(5 nm)/Co_xFe_{1-x}(3 nm)/Si_3N_4(5 nm) samples with varying Co content x and (b) calculated corresponding frequency spectra that were normalized to the respective maxima.

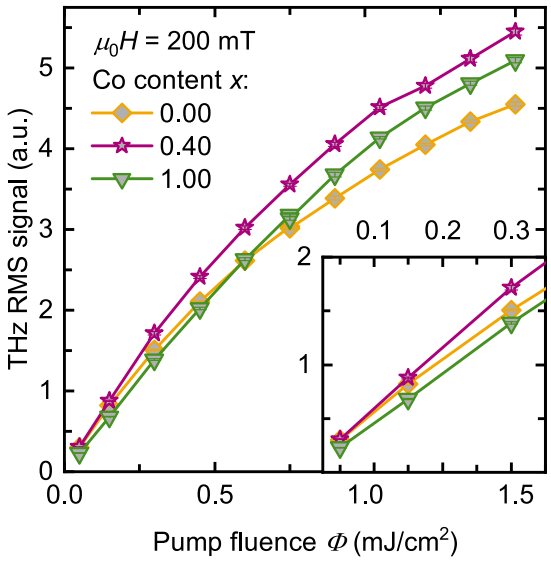

Figure A.4: THz RMS amplitudes of *sub.*/Pt(5 nm)/Co_xFe_{1-x}(3 nm)/Si_3N_4(5 nm) samples with Co content $x = 0$, $x = 0.4$, and $x = 1$ measured with an applied magnetic field $\mu_0 H$ = 200 mT in dependence on the laser pump fluence Φ. The inset shows the magnified image for small pump fluences. For $\Phi \leq 0.45\,\mathrm{mJ/cm^2}$, the sample with pure Pt/Fe ($x = 0$) shows a higher RMS signal than the sample with pure Pt/Co ($x = 1$). The error bars represent the statistical errors of the RMS values.

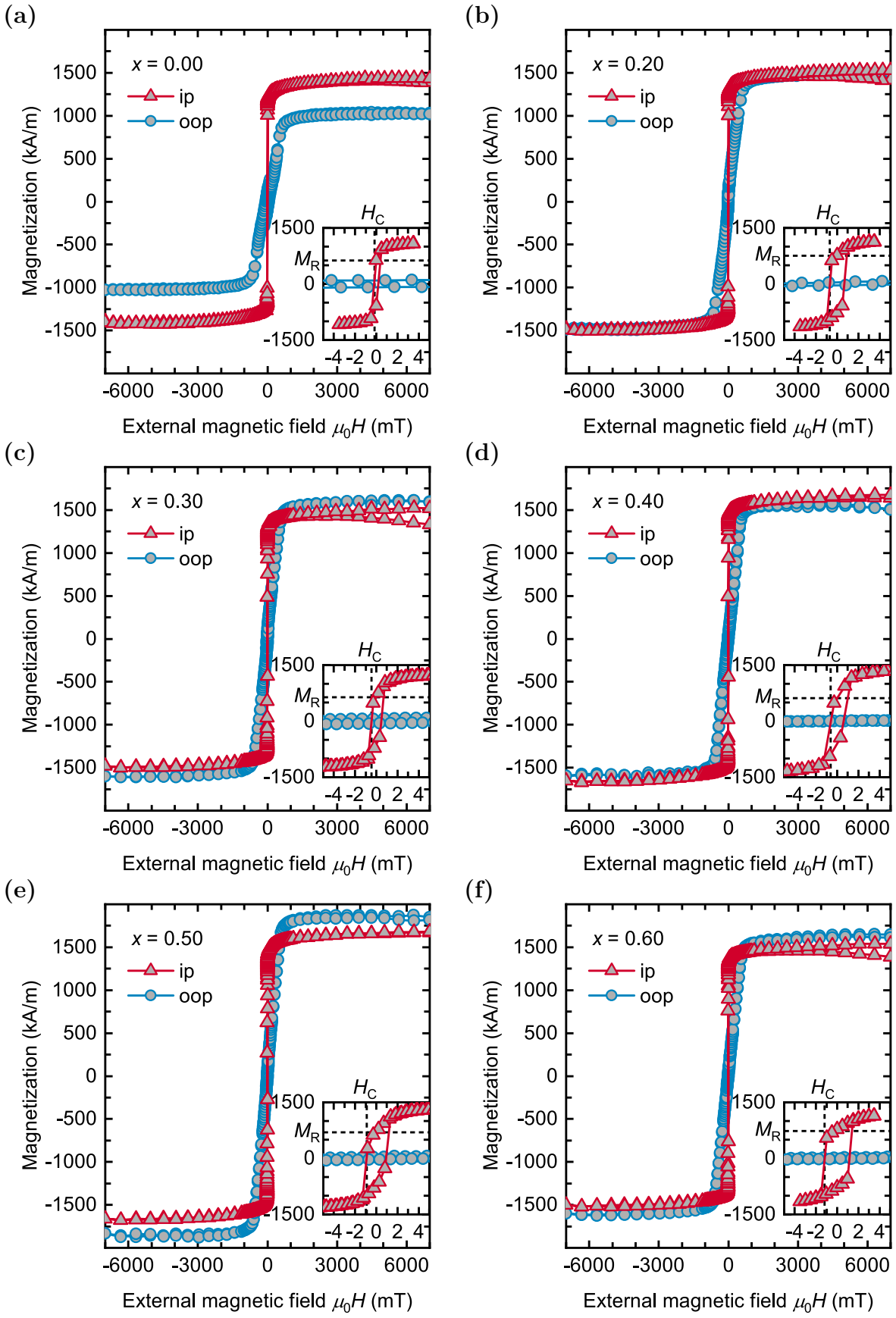
(a)
x = 0.00
ip
oop
Magnetization (kA/m)
External magnetic field $\mu_0 H$ (mT)
H_C
M_R
(b)
x = 0.20
(c)
x = 0.30
(d)
x = 0.40
(e)
x = 0.50
(f)
x = 0.60

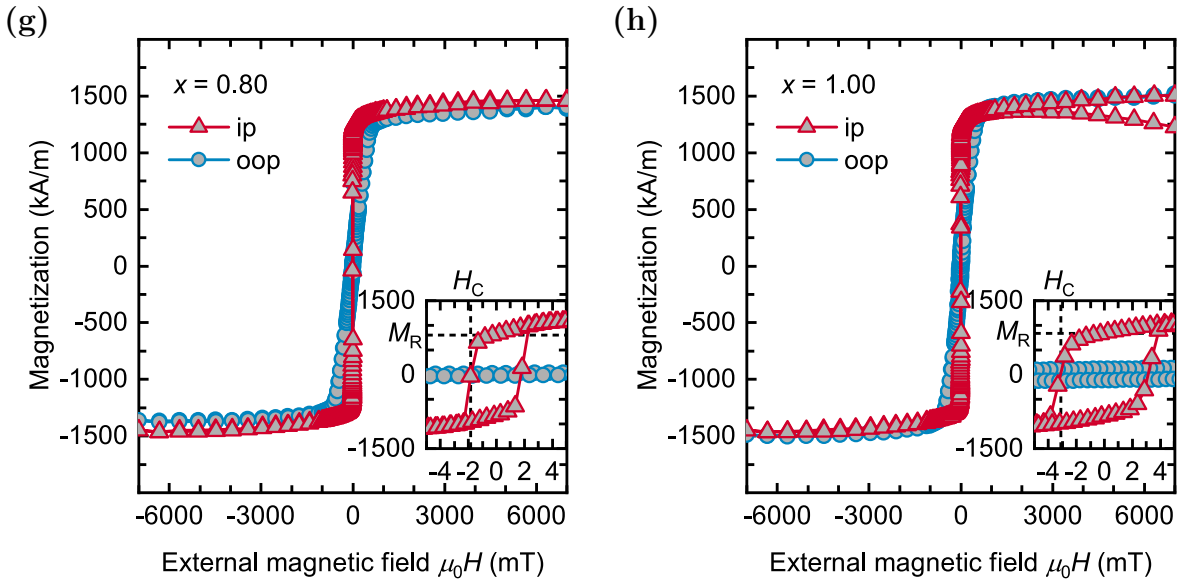

Figure A.5: Room-temperature SQUID-VSM $M(H)$ loops of *sub.*/Pt(2.5 nm)/Co_xFe_{1-x}(1 nm)/Si_3N_4(5 nm) samples with different Co content x measured in in-plane and out-of-plane direction. The insets show the magnified images for small field values with the remanence M_R and the coercivity H_C marked with dashed lines. The in-plane values of the samples with $x = 0$, $x = 0.2$, and $x = 0.6$ shown in the insets were measured separately from the loops for high field values shown in the main graphs with a smaller field steps than the main loops.

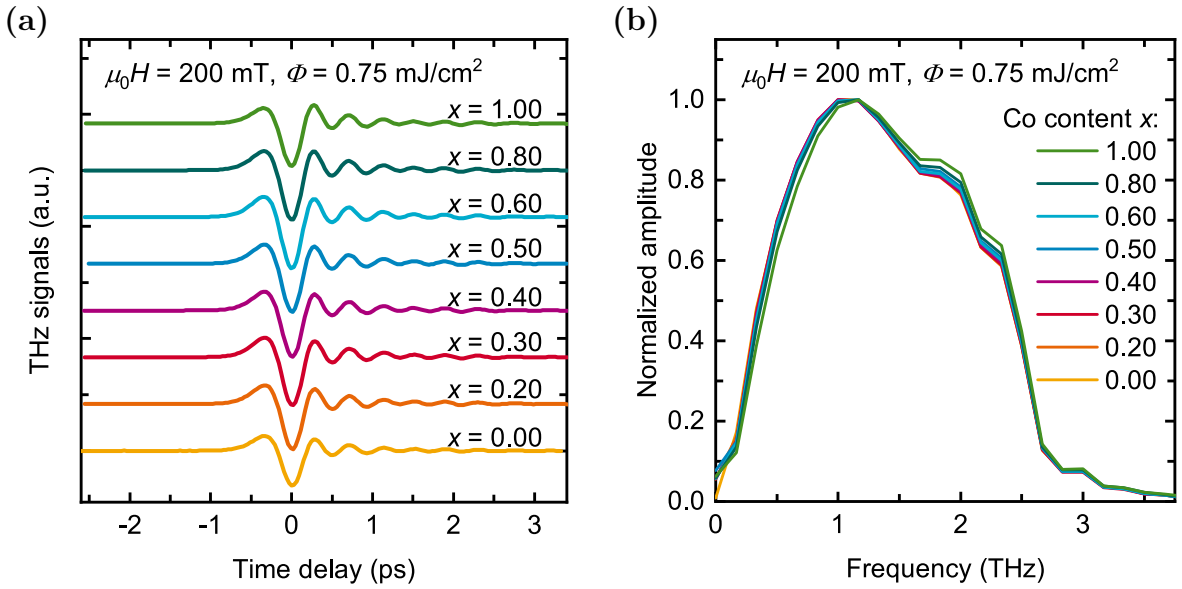

Figure A.6: (a) Measured THz electro-optic signals of *sub.*/Pt(2.5 nm)/Co_xFe_{1-x}(1 nm)/Si_3N_4(5 nm) samples with varying Co content and (b) calculated corresponding frequency spectra that were normalized to the respective maxima. A small increase in the THz emission at about 2 THz can be found for samples with high Co content ($x \geq 0.8$).

A.3 Spintronic Pt/Tb_xFe_{1-x} terahertz emitters

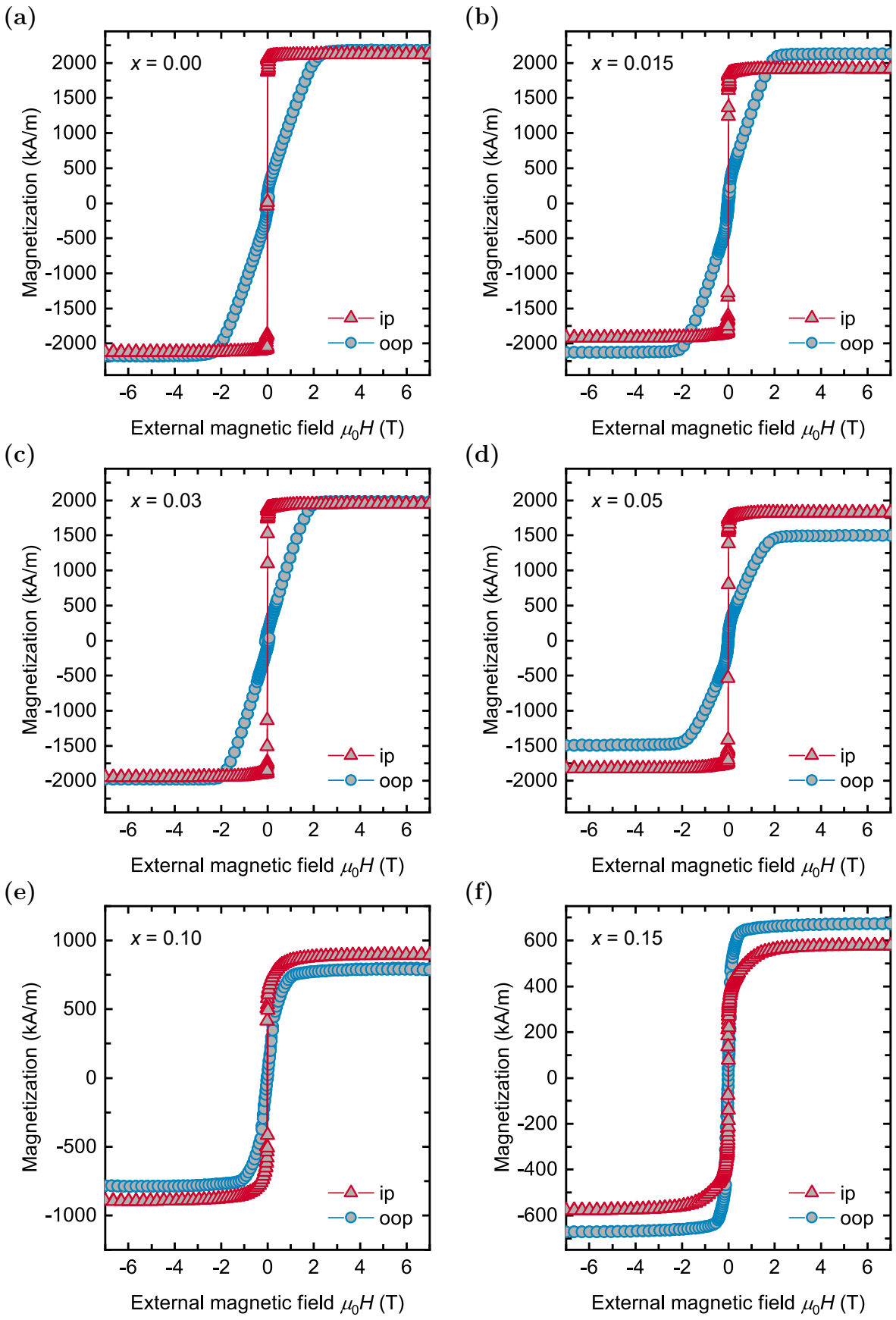

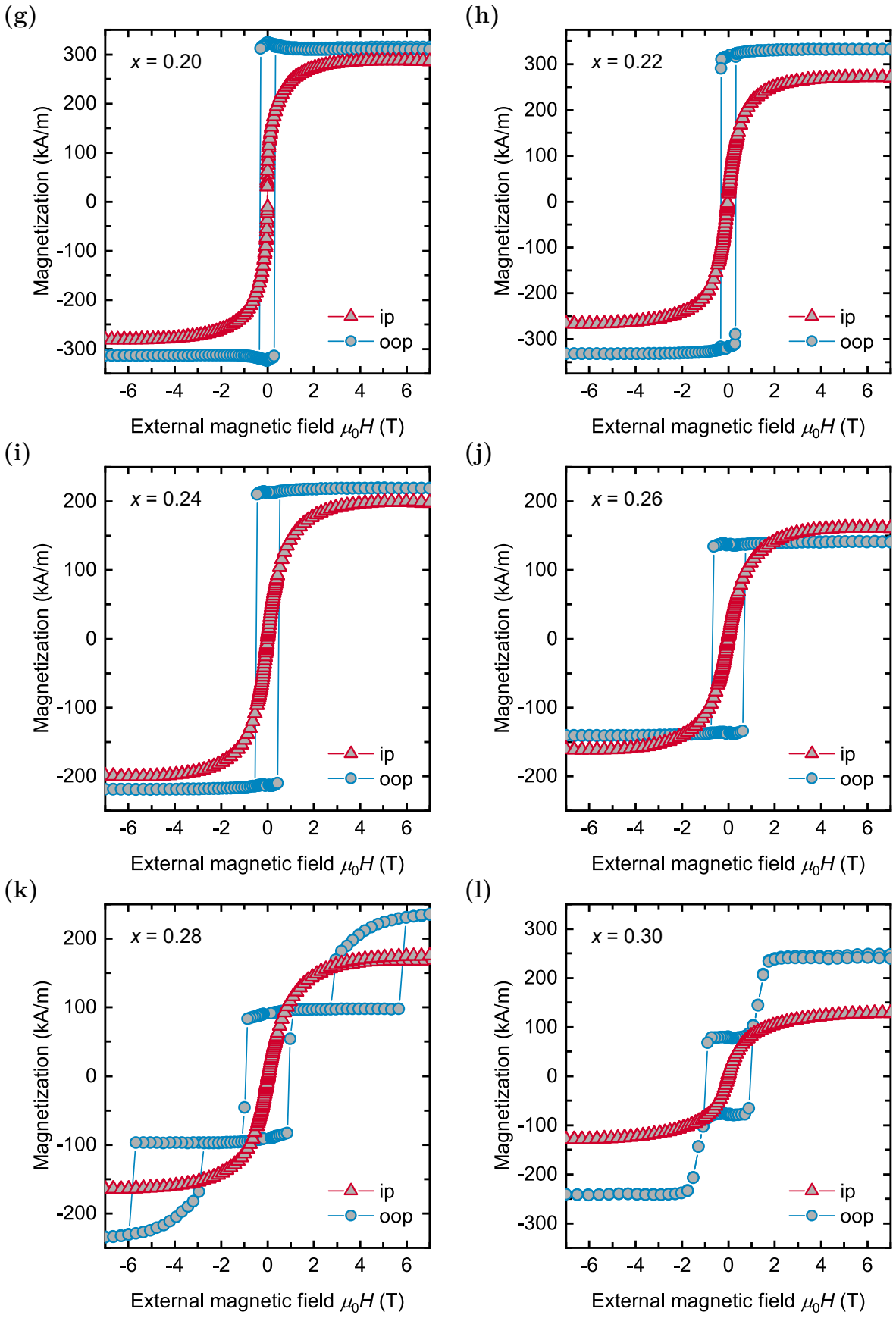
(g)
x = 0.20
(h)
x = 0.22
(i)
x = 0.24
(j)
x = 0.26
(k)
x = 0.28
(l)
x = 0.30
Magnetization (kA/m)
External magnetic field $\mu_0 H$ (T)
ip
oop

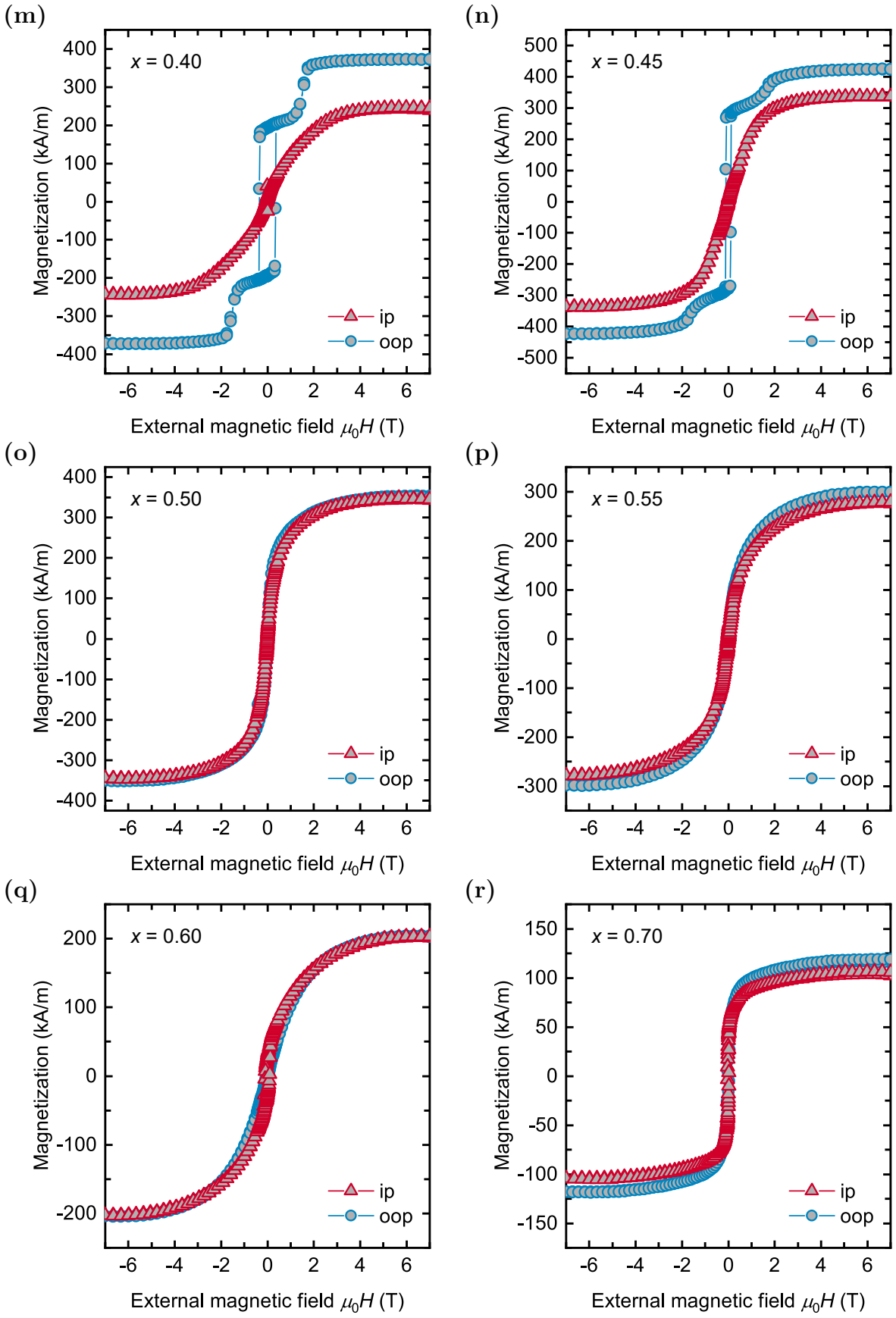
(m)
x = 0.40
(n)
x = 0.45
(o)
x = 0.50
(p)
x = 0.55
(q)
x = 0.60
(r)
x = 0.70
Magnetization (kA/m)
External magnetic field $\mu_0 H$ (T)
ip
oop

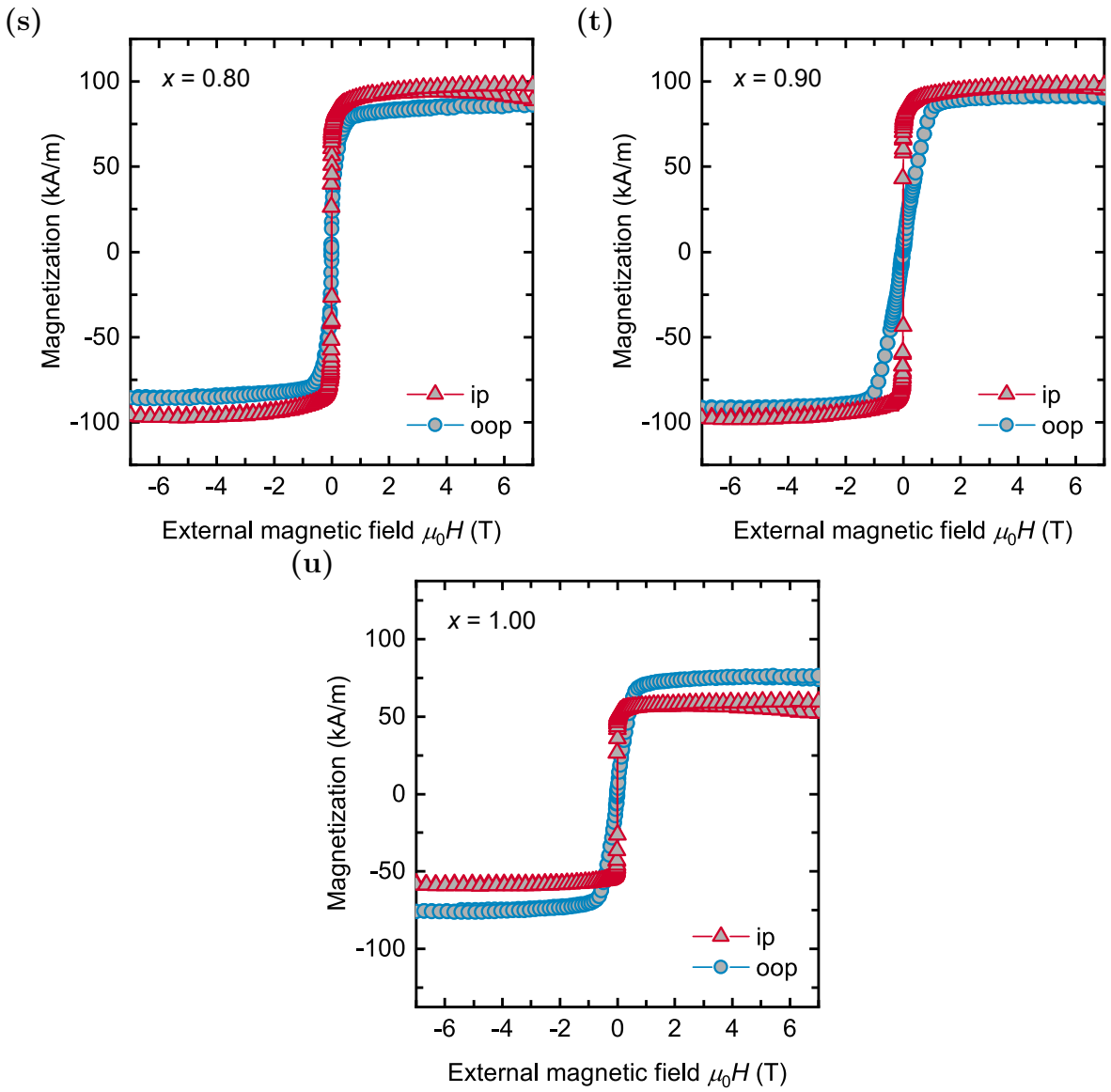

Figure A.7: SQUID-VSM $M(H)$ loops of *sub.*/Pt(5 nm)/Tb_xFe_{1-x}(20 nm)/Co(2 nm) samples with different Tb content x measured in in-plane and out-of-plane direction at 300 K.

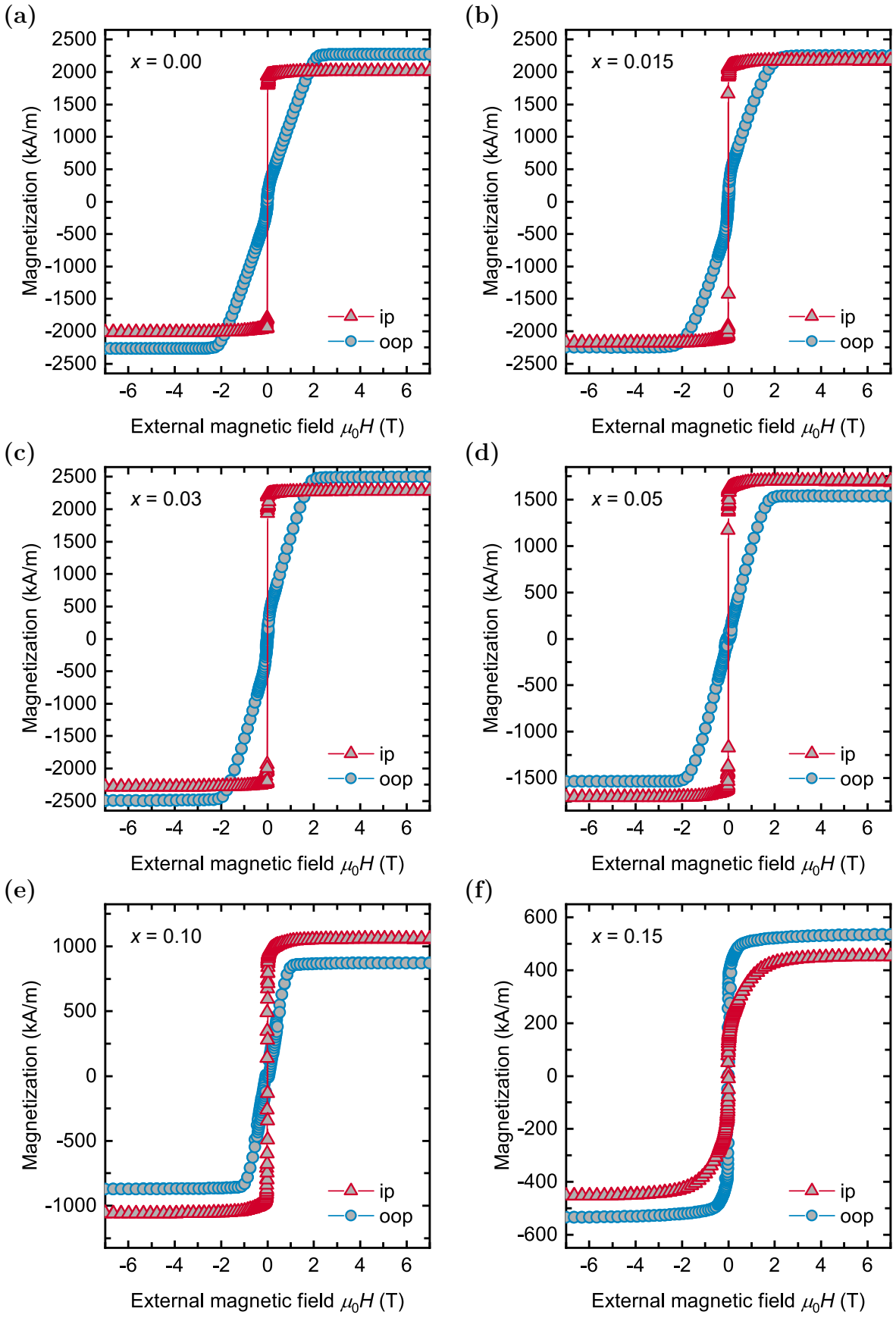
(a)
x = 0.00
(b)
x = 0.015
(c)
x = 0.03
(d)
x = 0.05
(e)
x = 0.10
(f)
x = 0.15
Magnetization (kA/m)
External magnetic field $\mu_0 H$ (T)
ip
oop

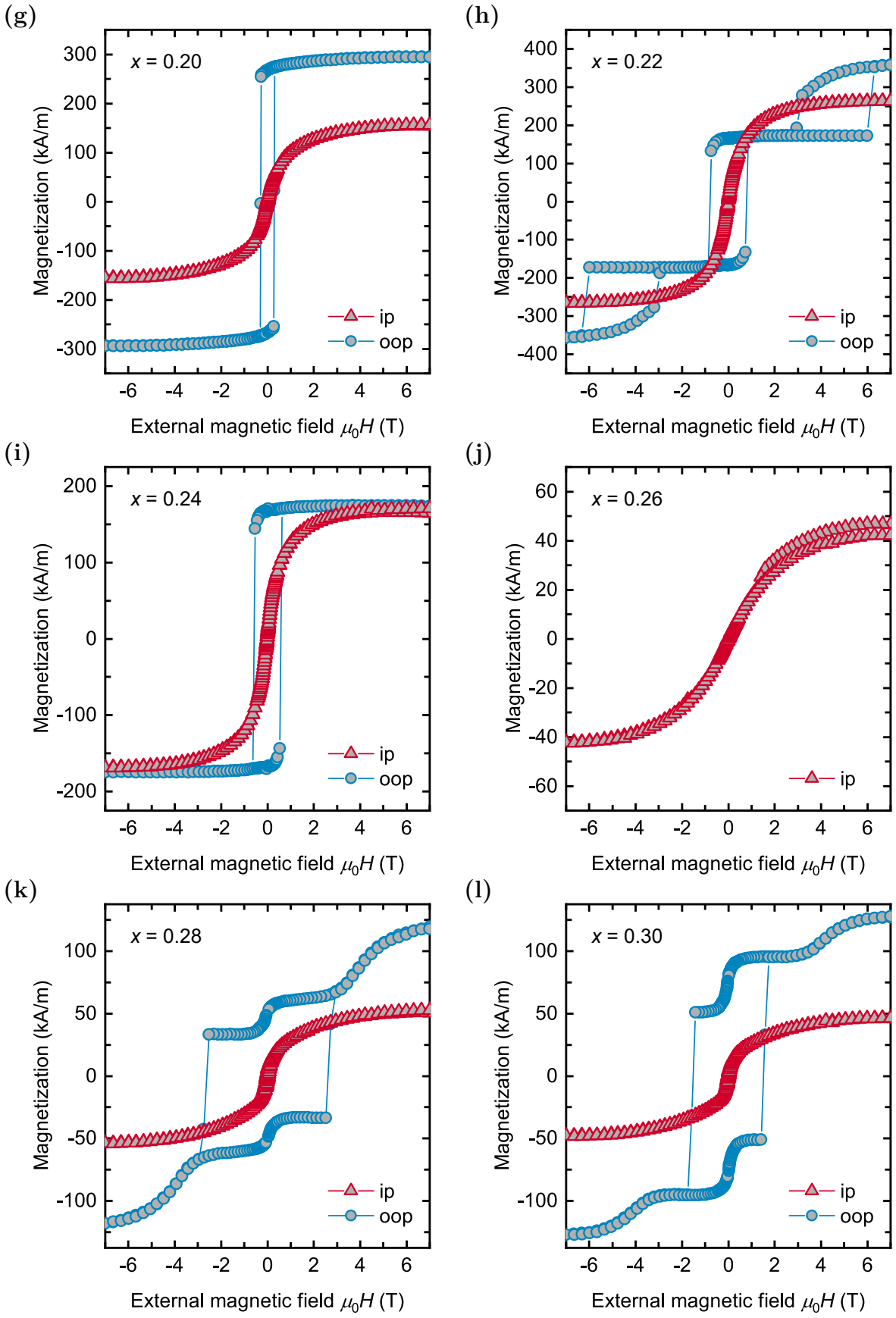
(g)
x = 0.20
(h)
x = 0.22
(i)
x = 0.24
(j)
x = 0.26
(k)
x = 0.28
(l)
x = 0.30
Magnetization (kA/m)
External magnetic field $\mu_0 H$ (T)
ip
oop

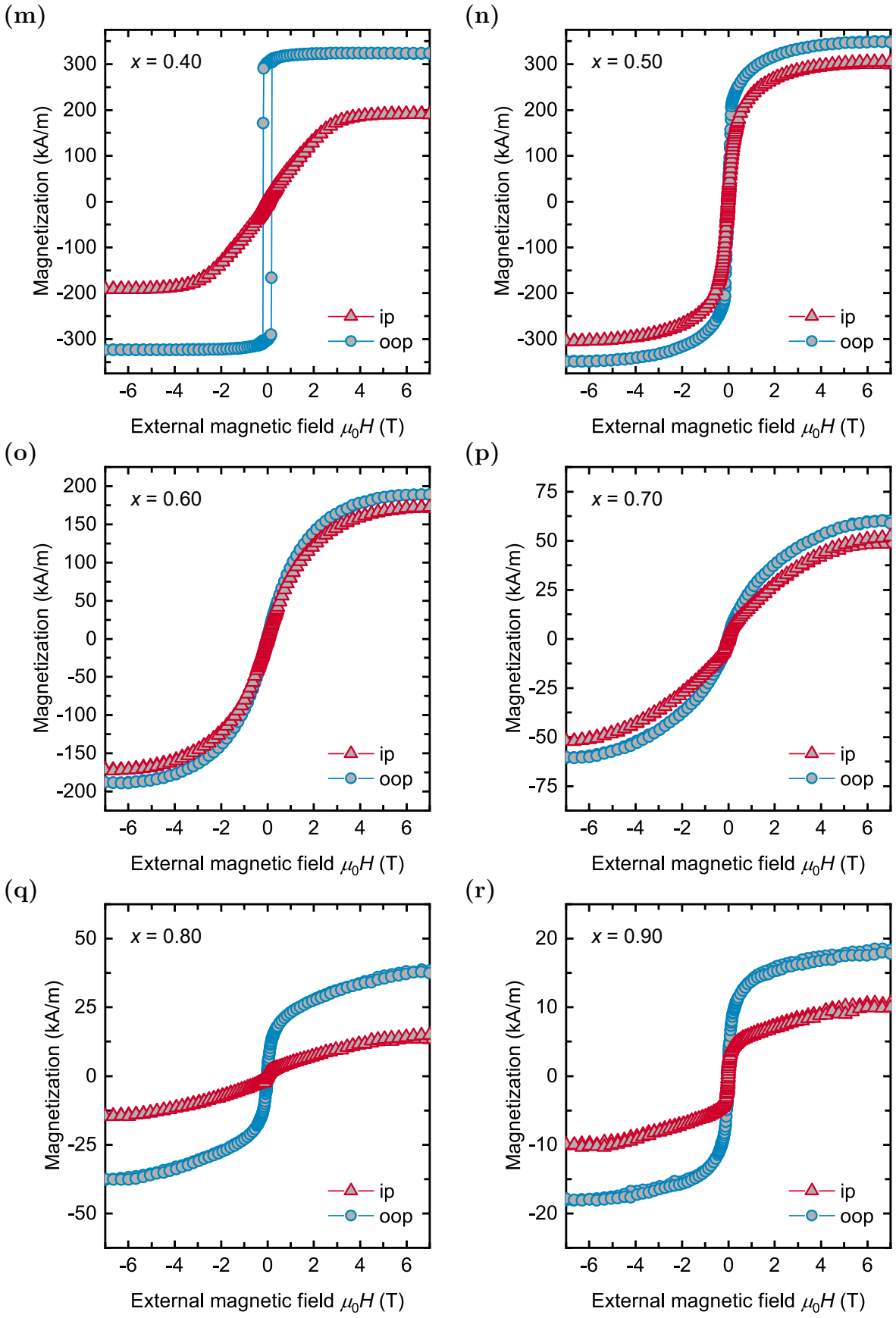
(m)
x = 0.40
(n)
x = 0.50
(o)
x = 0.60
(p)
x = 0.70
(q)
x = 0.80
(r)
x = 0.90
Magnetization (kA/m)
External magnetic field $\mu_0 H$ (T)
ip
oop

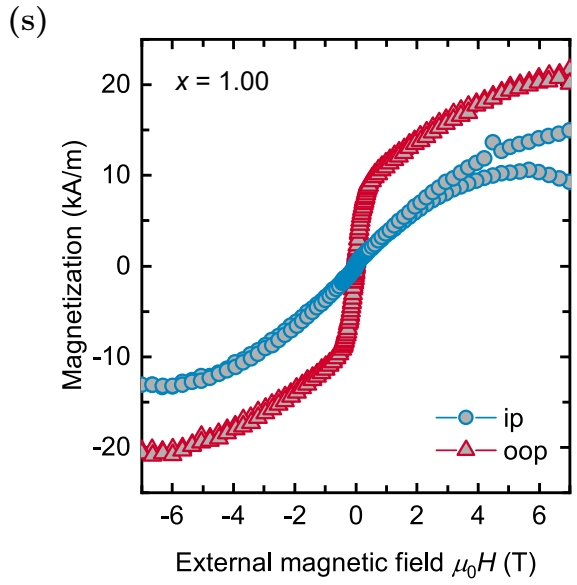

Figure A.8: SQUID-VSM $M(H)$ loops of *sub.*/Pt(5 nm)/Tb_xFe_{1-x}(20 nm)/Si_3N_4(5 nm) samples with different Tb content x measured in in-plane and out-of-plane direction at 300 K.

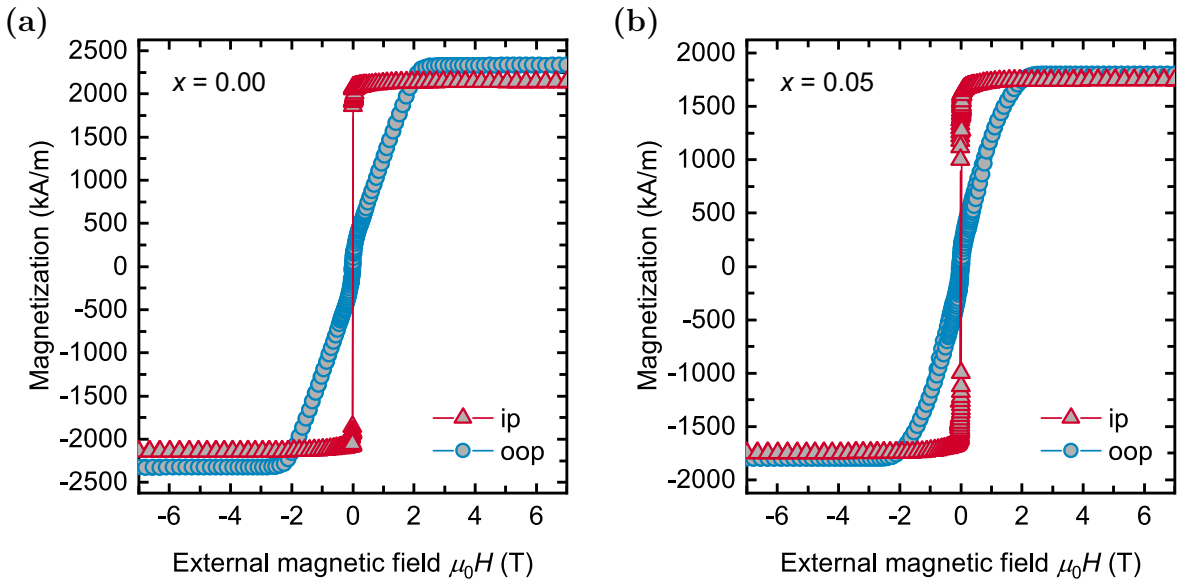

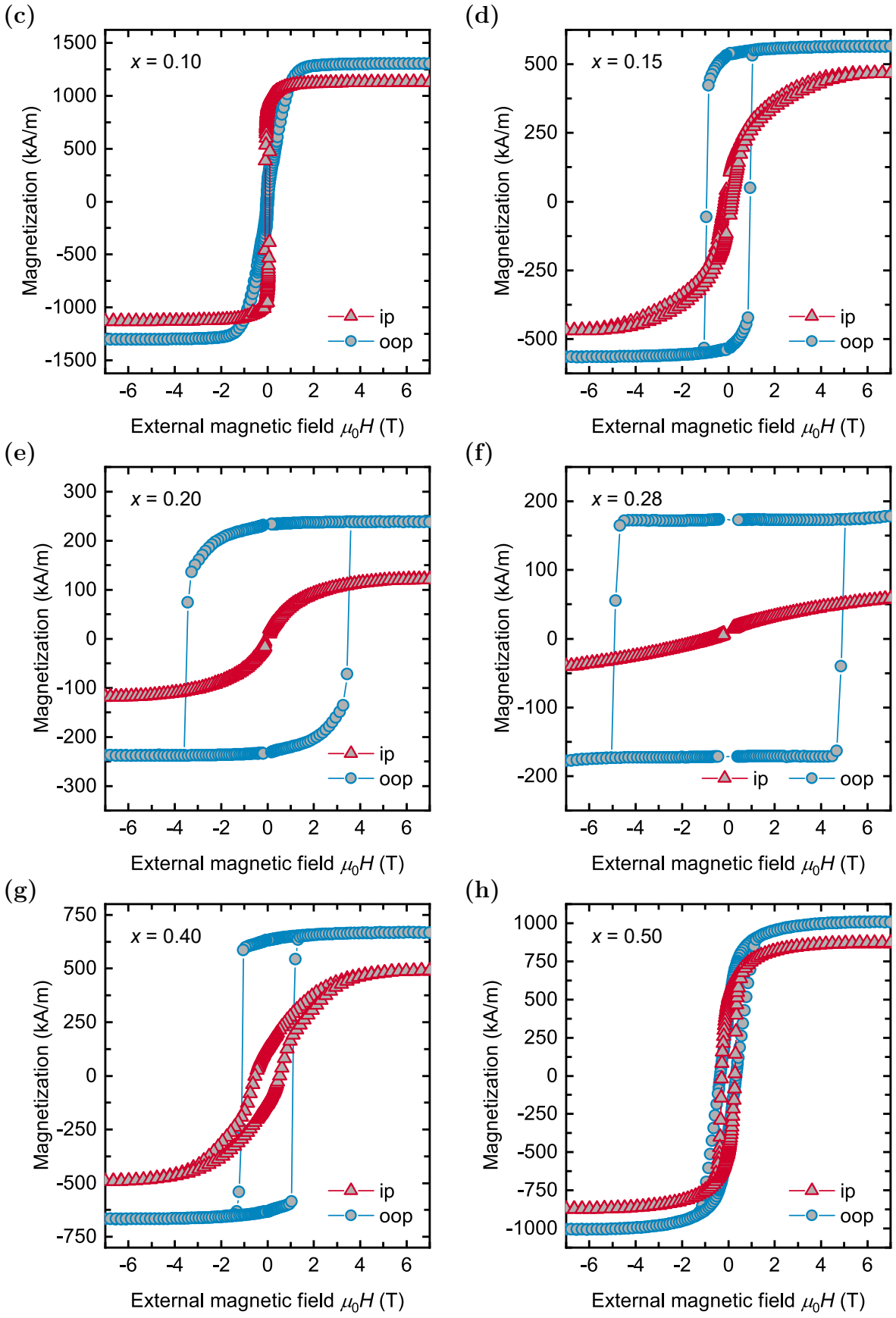
(c)
x = 0.10
(d)
x = 0.15
(e)
x = 0.20
(f)
x = 0.28
(g)
x = 0.40
(h)
x = 0.50
Magnetization (kA/m)
External magnetic field $\mu_0 H$ (T)
ip
oop

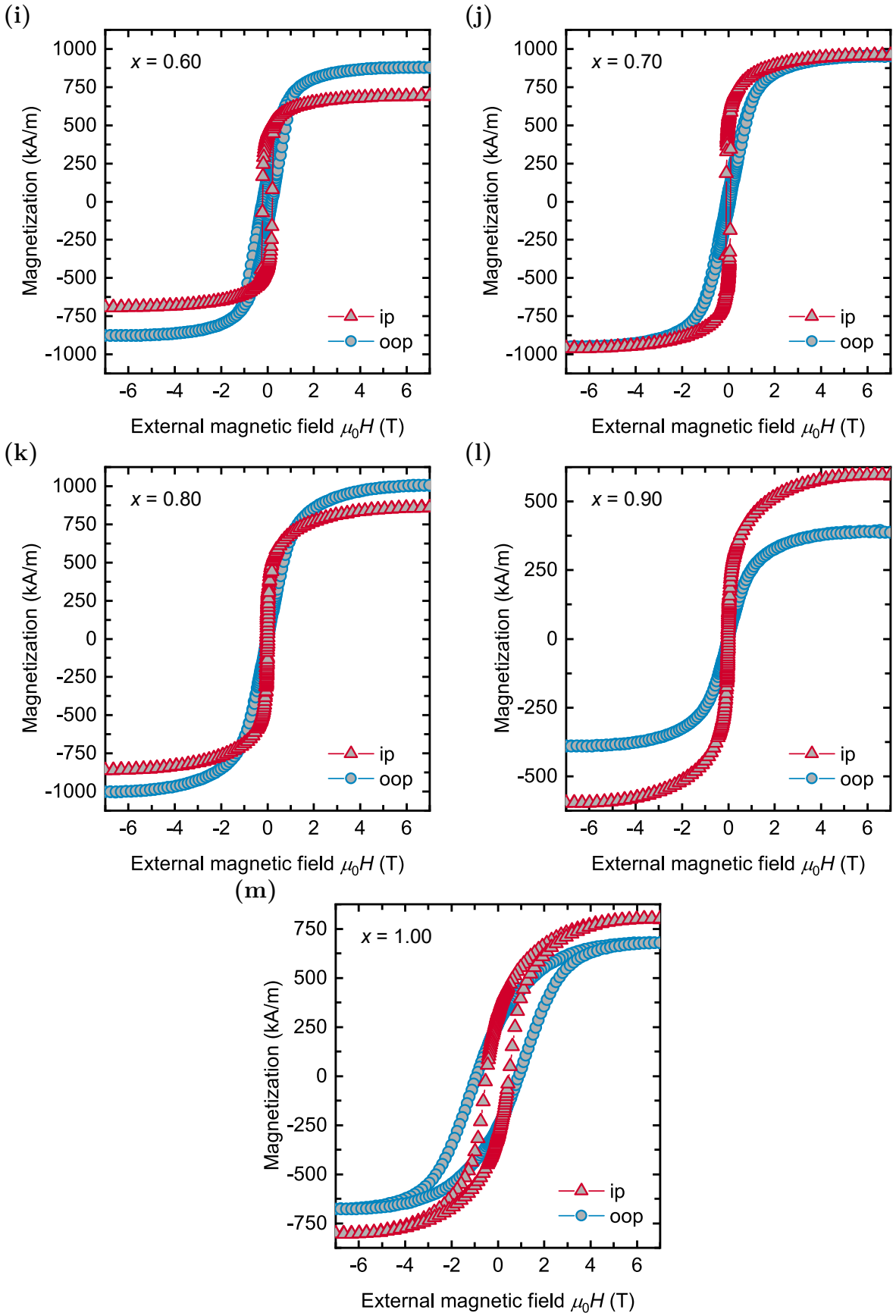

Figure A.9: SQUID-VSM $M(H)$ loops of *sub.*/Pt(5 nm)/Tb_xFe_{1-x}(20 nm)/Si_3N_4(5 nm) samples with different Tb content x measured in in-plane and out-of-plane direction at 79 K.

A.4 Spintronic Pt/Gd_xFe_{1-x} terahertz emitters

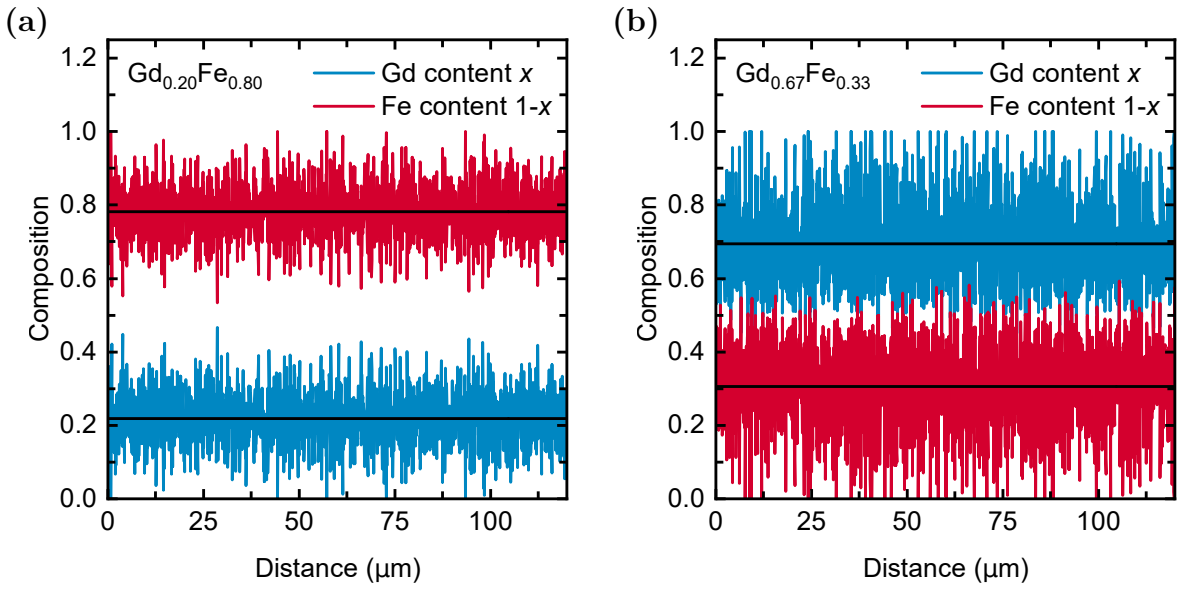

Figure A.10: Scanning electron microscope EDX linescans measured on (a) *sub.*/Pt(5 nm)/$Gd_{0.20}Fe_{0.80}$(20 nm)/Si_3N_4(5 nm) and (b) *sub.*/Pt(5 nm)/$Gd_{0.67}Fe_{0.33}$(20 nm)/Si_3N_4(5 nm) samples.

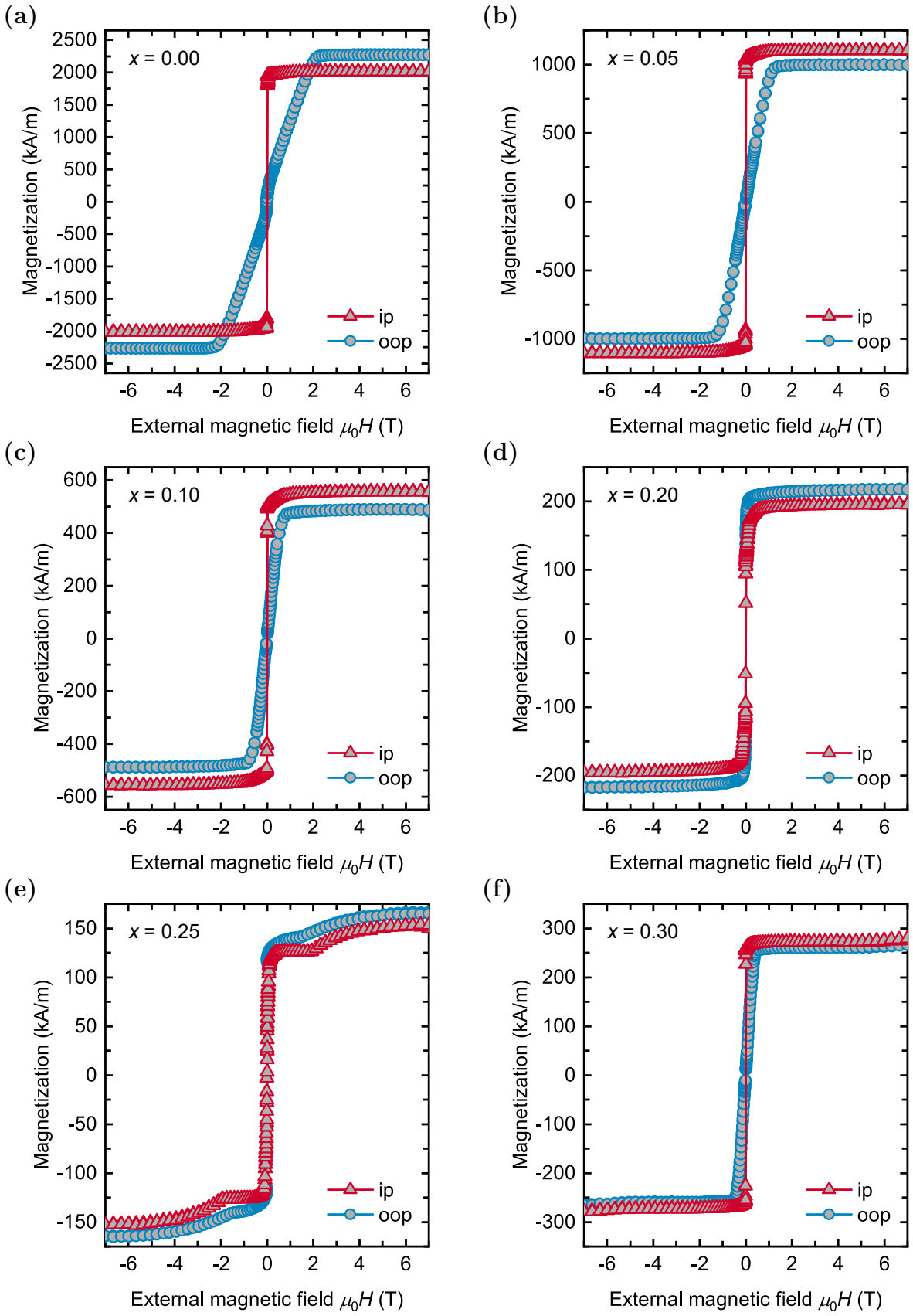
(a)
x = 0.00
Magnetization (kA/m)
2500
2000
1500
1000
500
0
-500
-1000
-1500
-2000
-2500
ip
oop
-6 -4 -2 0 2 4 6
External magnetic field $\mu_0 H$ (T)
(b)
x = 0.05
Magnetization (kA/m)
1000
500
0
-500
-1000
ip
oop
-6 -4 -2 0 2 4 6
External magnetic field $\mu_0 H$ (T)
(c)
x = 0.10
Magnetization (kA/m)
600
400
200
0
-200
-400
-600
ip
oop
-6 -4 -2 0 2 4 6
External magnetic field $\mu_0 H$ (T)
(d)
x = 0.20
Magnetization (kA/m)
200
100
0
-100
-200
ip
oop
-6 -4 -2 0 2 4 6
External magnetic field $\mu_0 H$ (T)
(e)
x = 0.25
Magnetization (kA/m)
150
100
50
0
-50
-100
-150
ip
oop
-6 -4 -2 0 2 4 6
External magnetic field $\mu_0 H$ (T)
(f)
x = 0.30
Magnetization (kA/m)
300
200
100
0
-100
-200
-300
ip
oop
-6 -4 -2 0 2 4 6
External magnetic field $\mu_0 H$ (T)

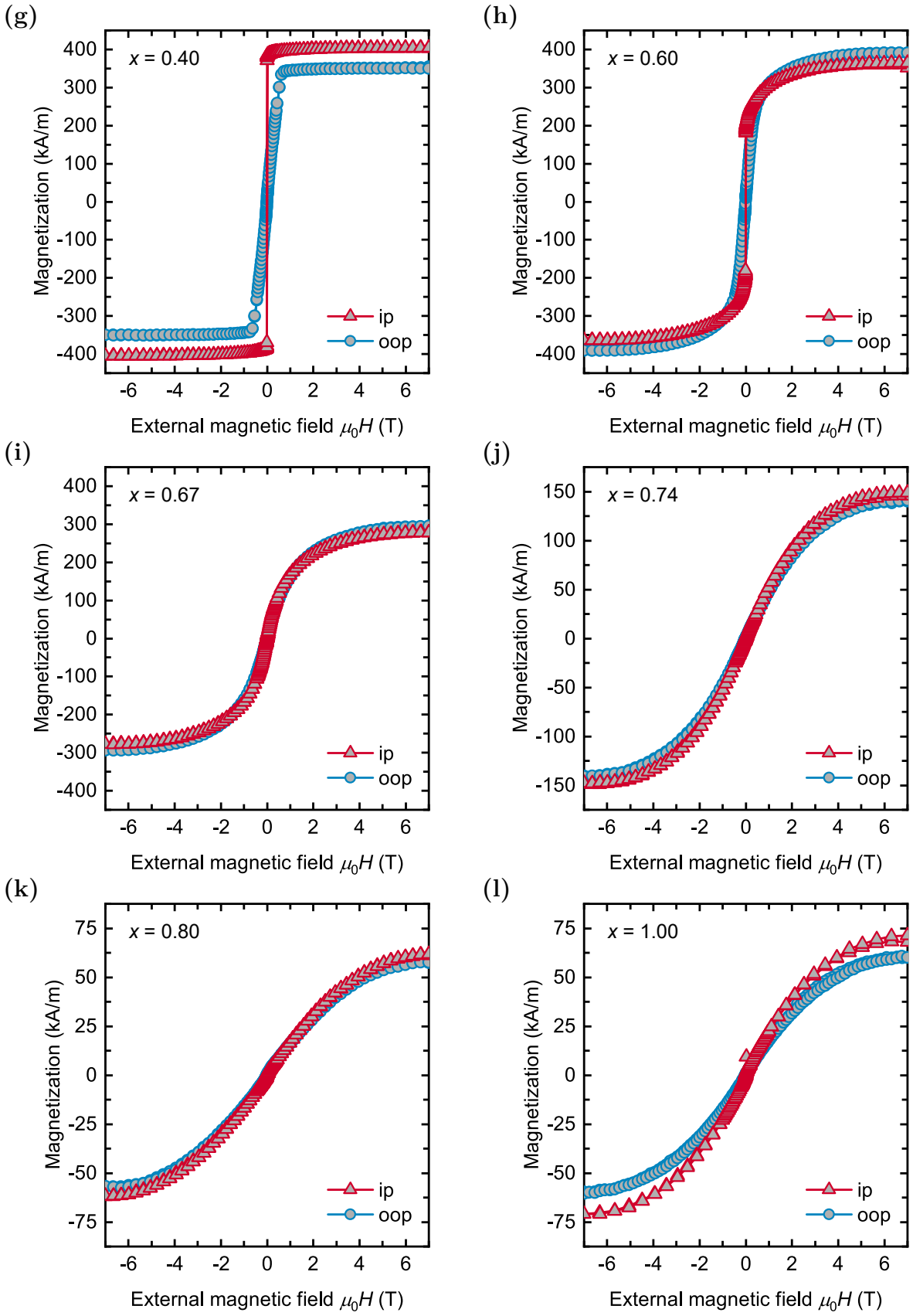

Figure A.11: Room-temperature SQUID-VSM $M(H)$ loops of *sub.*/Pt(5 nm)/Gd_xFe_{1-x}(20 nm)/Si_3N_4(5 nm) samples with different Gd content x measured in in-plane and out-of-plane direction.

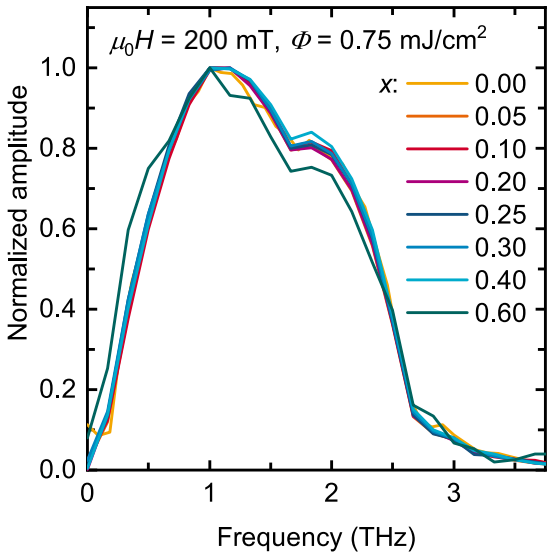

Figure A.12: Emission spectra of *sub.*/Pt(5 nm)/Gd_xFe_{1-x}(20 nm)/Si_3N_4(5 nm) samples with varying Gd content x, normalized to their respective maxima, measured at room temperature with an applied magnetic field $\mu_0 H = 200\,\mathrm{mT}$ and a laser pump fluence $\Phi = 0.75\,\mathrm{mJ/cm^2}$.

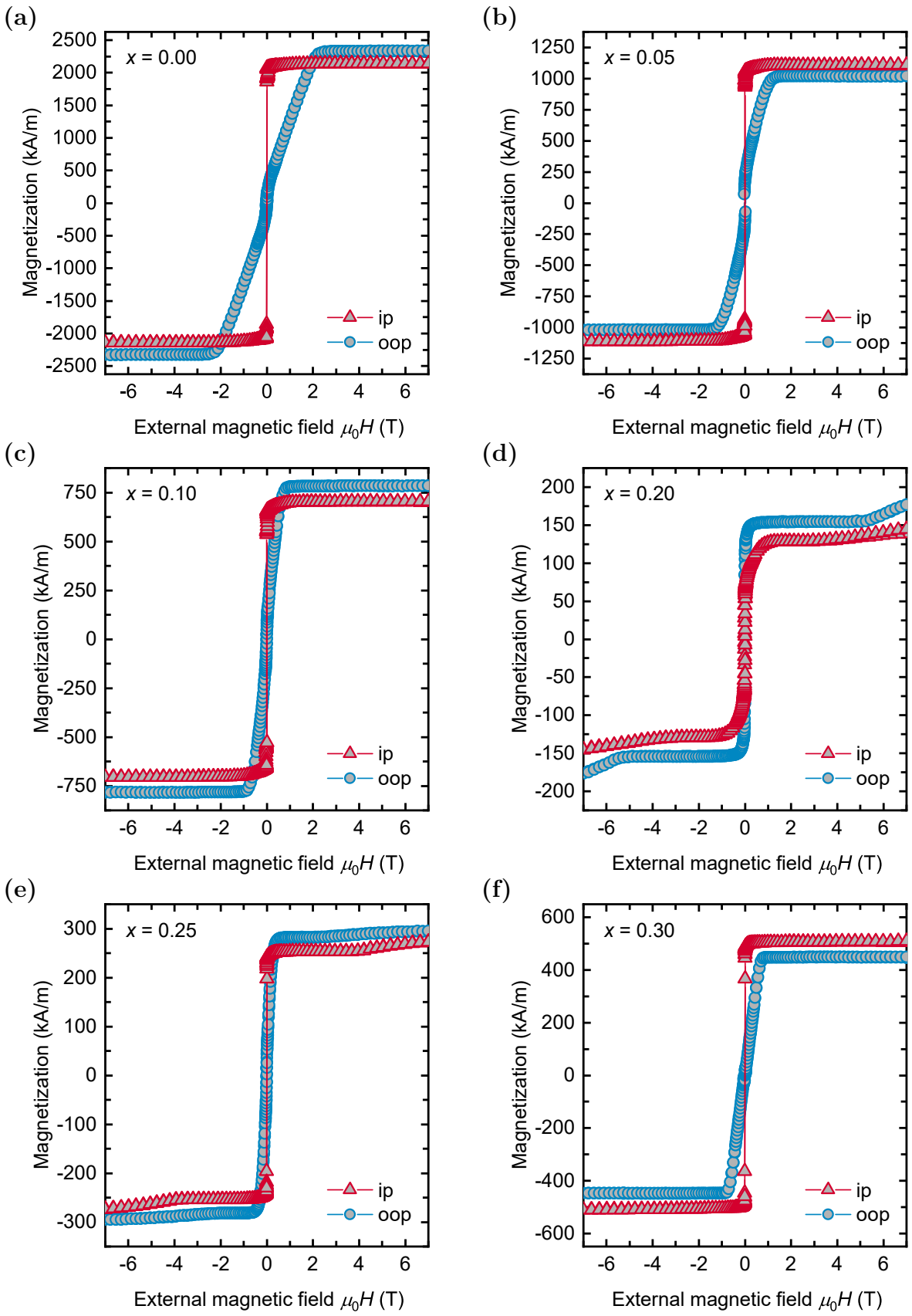
(a)
x = 0.00
Magnetization (kA/m)
External magnetic field $\mu_0 H$ (T)
ip
oop
(b)
x = 0.05
Magnetization (kA/m)
External magnetic field $\mu_0 H$ (T)
ip
oop
(c)
x = 0.10
Magnetization (kA/m)
External magnetic field $\mu_0 H$ (T)
ip
oop
(d)
x = 0.20
Magnetization (kA/m)
External magnetic field $\mu_0 H$ (T)
ip
oop
(e)
x = 0.25
Magnetization (kA/m)
External magnetic field $\mu_0 H$ (T)
ip
oop
(f)
x = 0.30
Magnetization (kA/m)
External magnetic field $\mu_0 H$ (T)
ip
oop

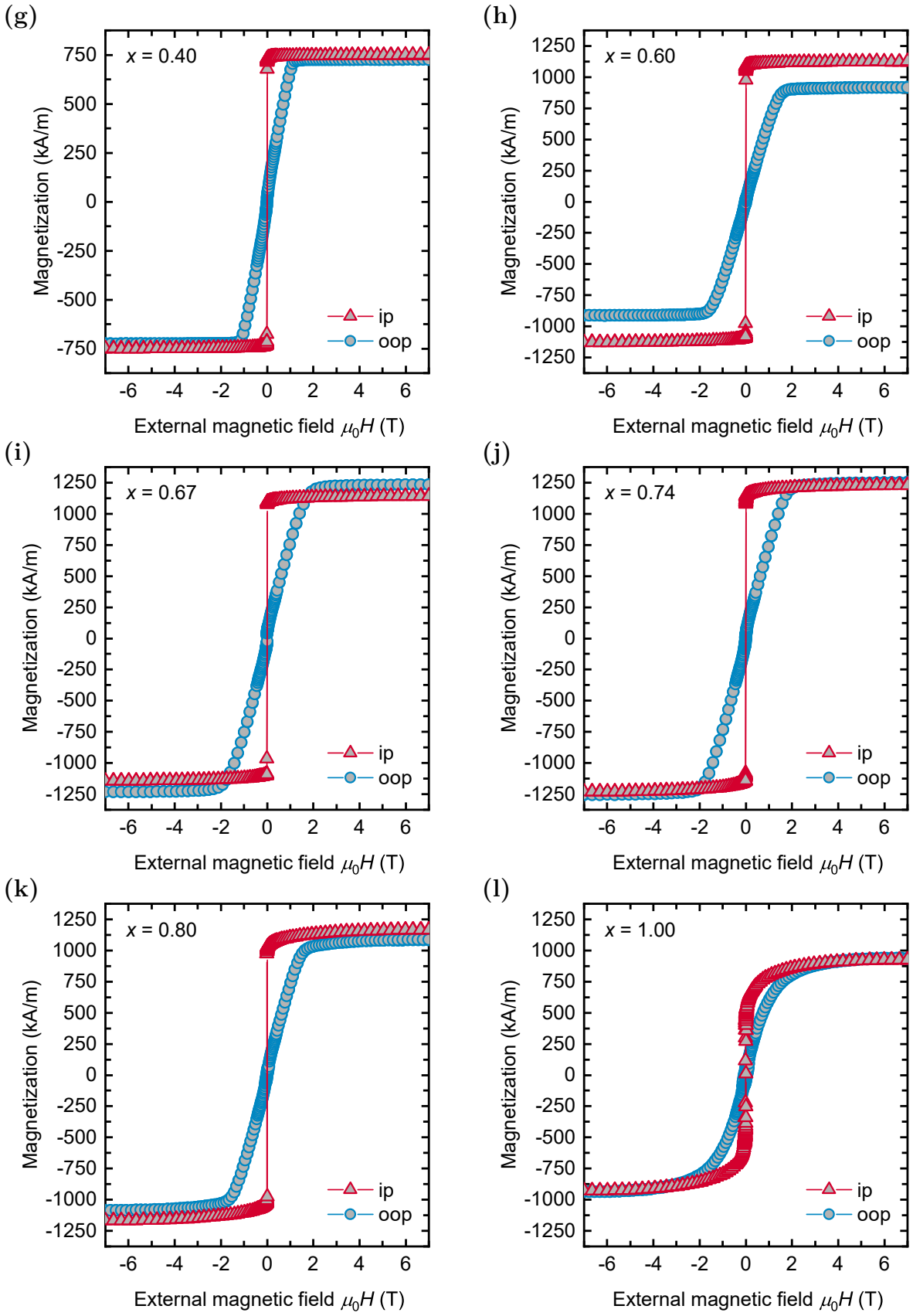

Figure A.13: SQUID-VSM $M(H)$ loops of *sub.*/Pt(5 nm)/Gd_xFe_{1-x}(20 nm)/Si_3N_4(5 nm) samples with different Gd content x measured in in-plane and out-of-plane direction at T = 79 K.

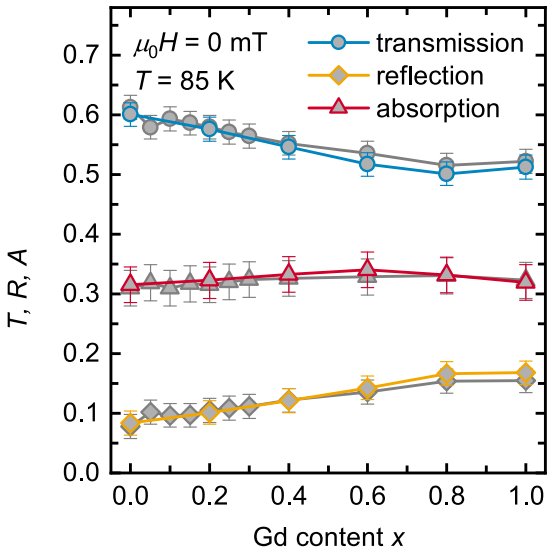

Figure A.14: Transmission T, reflection R, and absorption A of the 1.53 eV pump laser in *sub.*/Pt(5 nm)/Gd_xFe_{1-x}(20 nm)/Si_3N_4(5 nm) samples with different Gd content x measured at the temperature $T = 85$ K. The room-temperature results are displayed in gray.

A.5 Thermomagnetically switchable spintronic terahertz emitters

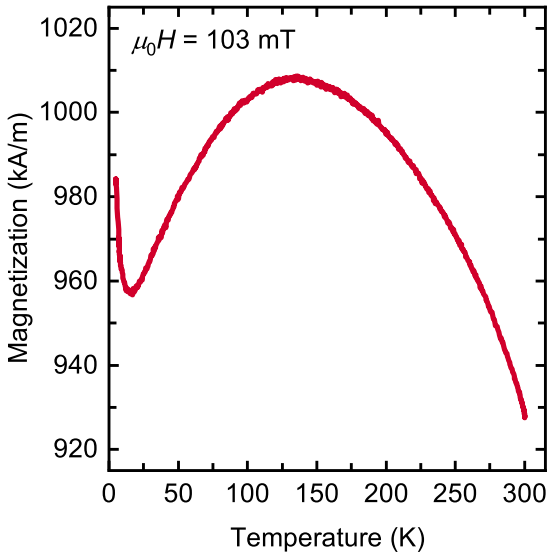

Figure A.15: SQUID-VSM $M(T)$ curve of a *sub.*/Pt(3 nm/$Gd_{0.1}Fe_{0.9}$(3 nm)/Si_3N_4(5 nm) sample measured with an applied magnetic field $\mu_0 H = 103$ mT from 300 K to 5 K in a temperature sweep mode during the cool down.

A.6 Spin valves as magnetically switchable spintronic terahertz emitters

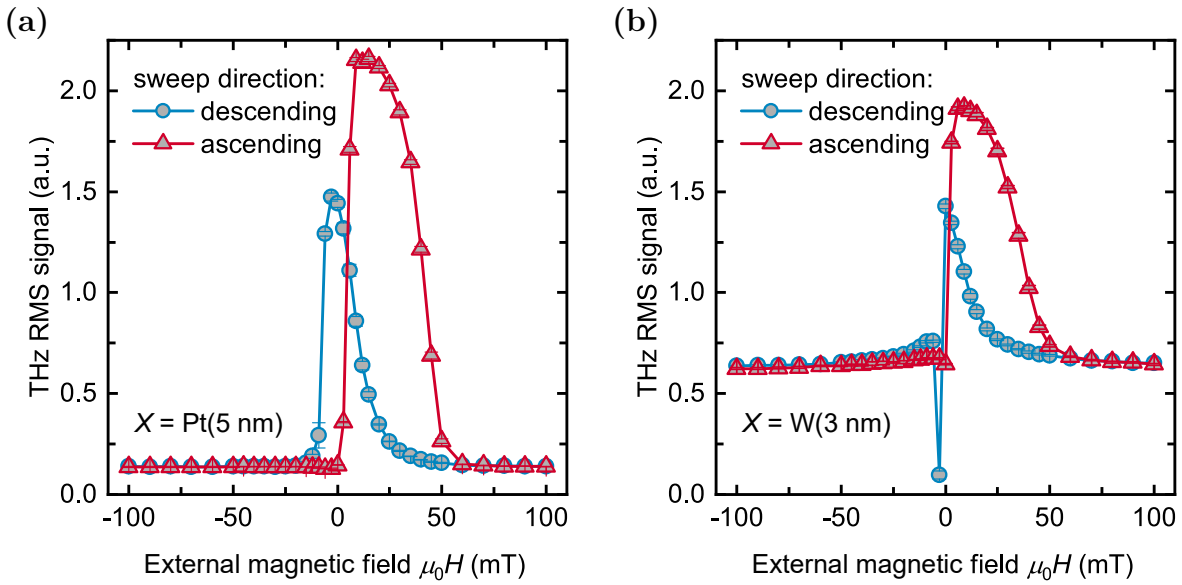

Figure A.16: THz RMS signals of *sub.*/$Ir_{0.23}Mn_{0.77}$(20 nm)/Fe(3 nm)/*X*/Fe(3 nm)/Si_3N_4(5 nm) samples with (a) Pt(5 nm) and (b) W(3 nm) interlayer *X* measured in dependence on the applied magnetic field with a laser pump fluence of $\Phi = 0.75\,\mathrm{mJ/cm^2}$.

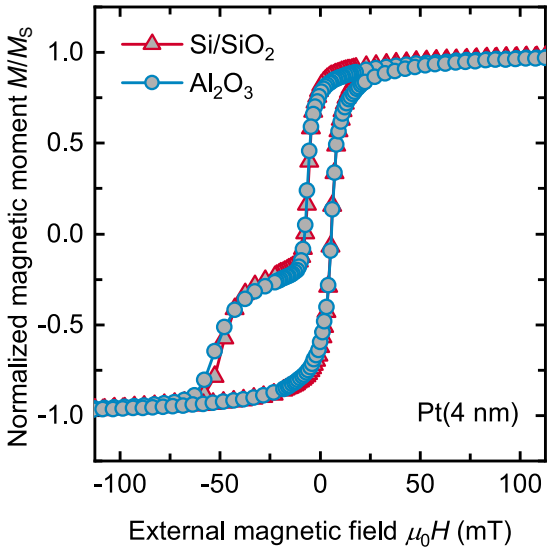

Figure A.17: SQUID-VSM $M(H)$ loops of *sub.*/$Ir_{0.23}Mn_{0.77}$(7 nm)/Fe(1.5 nm)/Pt(4 nm)/Fe(1.5 nm)/Si_3N_4(5 nm) samples deposited on 500 µm thick Al_2O_3(0001) substrates and on 525 µm thick Si(100) substrates with a 100 nm thermally oxidized SiO_2 layer. The magnetic moments M were normalized to the respective saturation magnetic moments M_S. The measurement of the sample on Si/SiO_2 was performed after setting the exchange bias, whereas the sample on Al_2O_3 was measured after the THz spectroscopy experiments with a laser pump fluence of $\Phi = 0.75\,\mathrm{mJ/cm^2}$ (see main text for details).

APPENDIX B

Bibliography

[1] M. Tonouchi, "Cutting-edge terahertz technology", Nat. Photonics **1**, 97 (2007) 10.1038/nphoton.2007.3.

[2] A. J. Lee, D. J. Spence, and H. M. Pask, "Terahertz sources based on stimulated polariton scattering", Prog. Quantum. Electron. **71**, 100254 (2020) 10.1016/j.pquantelec.2020.100254.

[3] J. Federici and L. Moeller, "Review of terahertz and subterahertz wireless communications", J. Appl. Phys. **107**, 111101 (2010) 10.1063/1.3386413.

[4] S. Koenig, D. Lopez-Diaz, J. Antes, F. Boes, R. Henneberger, A. Leuther, A. Tessmann, R. Schmogrow, D. Hillerkuss, R. Palmer, T. Zwick, C. Koos, W. Freude, O. Ambacher, J. Leuthold, and I. Kallfass, "Wireless sub-THz communication system with high data rate", Nat. Photonics **7**, 977 (2013) 10.1038/NPHOTON.2013.275.

[5] T. Nagatsuma, G. Ducournau, and C. C. Renaud, "Advances in terahertz communications accelerated by photonics", Nat. Photonics **10**, 371 (2016) 10.1038/nphoton.2016.65.

[6] K. B. Cooper and G. Chattopadhyay, "Submillimeter-wave radar: Solid-state system design and applications", IEEE Microwave **15**, 51 (2014) 10.1109/MMM.2014.2356092.

[7] E. Heinz, T. May, D. Born, G. Zieger, S. Anders, V. Zakosarenko, H.-G. Meyer, and C. Schäffel, "Passive 350 GHz video imaging systems for security applications", J Infrared Milli Terahz Waves **36**, 879 (2015) 10.1007/s10762-015-0170-8.

[8] B. Cheng, Z. Cui, B. Lu, Y. Qin, Q. Liu, P. Chen, Y. He, J. Jiang, X. He, X. Deng, J. Zhang, and L. Zhu, "340 GHz 3-D imaging radar with 4Tx-16Rx MIMO array", IEEE Trans. THz Sci. Technol. **8**, 509 (2018) 10.1109/TTHZ.2018.2853551.

[9] B. Ferguson and X.-C. Zhang, "Materials for terahertz science and technology", Nat. Mater. **1**, 26 (2002) 10.1038/nmat708.

[10] E. Pickwell and V. P. Wallace, "Biomedical applications of terahertz technology", J. Phys. D: Appl. Phys. **39**, R301 (2006) 10.1088/0022-3727/39/17/R01.

[11] Y. Peng, C. Shi, Y. Zhu, M. Gu, and S. Zhuang, "Terahertz spectroscopy in biomedical field: A review on signal-to-noise ratio improvement", PhotoniX **1**, R301 (2020) 10.1186/s43074-020-00011-z.

[12] K. Su, Y.-C. Shen, and J. A. Zeitler, "Terahertz sensor for non-contact thickness and quality measurement of automobile paints of varying complexity", IEEE Trans. THz Sci. Technol. **4**, 432 (2014) 10.1109/TTHZ.2014.2325393.

[13] M. Naftaly, N. Vieweg, and A. Deninger, "Industrial applications of terahertz sensing: State of play", Sensors **19**, 4203 (2019) 10.3390/s19194203.

[14] D. Alves-Lima, J. Song, X. Li, A. Portieri, Y. Shen, J. A. Zeitler, and H. Lin, "Review of terahertz pulsed imaging for pharmaceutical film coating analysis", Sensors **20**, 1441 (2020) 10.3390/s20051441.

[15] M. Hangyo, M. Tani, and T. Nagashima, "Terahertz time-domain spectroscopy of solids: A review", Int. J. Infrared Millim. Waves **26**, 1661 (2005) 10.1007/s10762-005-0288-1.

[16] T. Kampfrath, K. Tanaka, and K. A. Nelson, "Resonant and nonresonant control over matter and light by intense terahertz transients", Nat. Photonics **7**, 680 (2013) 10.1038/nphoton.2013.184.

[17] D. Nicoletti and A. Cavalleri, "Nonlinear light–matter interaction at terahertz frequencies", Adv. Opt. Photon. **8**, 401 (2016) 10.1364/AOP.8.000401.

[18] D. M. Mittleman, "Perspective: Terahertz science and technology", J. Appl. Phys. **122**, 230901 (2017) 10.1063/1.5007683.

[19] P. Salén, M. Basini, S. Bonetti, J. Hebling, M. Krasilnikov, A. Y. Nikitin, G. Shamuilov, Z. Tibai, V. Zhaunerchyk, and V. Goryashko, "Matter manipulation with extreme terahertz light: Progress in the enabling THz technology", Phys. Rep. **836**, 1 (2019) 10.1016/j.physrep.2019.09.002.

[20] T. F. Nova, A. Cartella, A. Cantaluppi, M. Först, D. Bossini, R. V. Mikhaylovskiy, A. V. Kimel, R. Merlin, and A. Cavalleri, "An effective magnetic field from optically driven phonons", Nat. Phys. **13**, 132 (2017) 10.1038/NPHYS3925.

[21] S. F. Maehrlein, I. Radu, P. Maldonado, A. Paarmann, M. Gensch, A. M. Kalashnikova, R. V. Pisarev, M. Wolf, P. M. Oppeneer, J. Barker, and T. Kampfrath, "Dissecting spin-phonon equilibration in ferrimagnetic insulators by ultrafast lattice excitation", Sci. Adv. **4**, eaar5164 (2018) 10.1126/sciadv.aar5164.

[22] K. Olejník, T. Seifert, Z. Kašpar, V. Novák, P. Wadley, R. P. Campion, M. Baumgartner, P. Gambardella, P. Němec, J. Wunderlich, J. Sinova, P. Kužel, M. Müller, T. Kampfrath, and T. Jungwirth, "Terahertz electrical writing speed in an antiferromagnetic memory", Sci. Adv. **4**, eaar3566 (2018) 10.1126/sciadv.aar3566.

[23] S. Schlauderer, C. Lange, S. Baierl, T. Ebnet, C. P. Schmid, D. C. Valovcin, A. K. Zvezdin, A. V. Kimel, R. V. Mikhaylovskiy, and R. Huber, "Temporal and spectral fingerprints of ultrafast all-coherent spin switching", Nature **569**, 383 (2019) 10.1038/s41586-019-1174-7.

[24] S. P. Langley, "The bolometer and radiant energy", Proc. Am. Acad. Arts Sci. **16**, 342 (1880) 10.2307/25138616.

[25] H. Rubens and E. F. Nichols, "Heat rays of great wave length", Phys. Rev. **4**, 314 (1897) 10.1103/PhysRevSeriesI.4.314.

[26] P. H. Siegel, "Terahertz technology", IEEE Trans. Microwave Theory Techn. **50**, 910 (2002) 10.1109/22.989974.

[27] B. S. Williams, "Terahertz quantum-cascade lasers", Nat. Photonics **1**, 517 (2007) 10.1038/nphoton.2007.166.

[28] D. J. Paul, "The progress towards terahertz quantum cascade lasers on silicon substrates", Laser Photonics Rev. **4**, 610 (2010) 10.1002/lpor.200910038.

[29] L. Li, L. Chen, J. Zhu, J. Freeman, P. Dean, A. Valavanis, A. G. Davies, and E. H. Linfield, "Terahertz quantum cascade lasers with $> 1\,\mathrm{W}$ output powers", Electron. lett. **50**, 309 (2014) 10.1049/el.2013.4035.

[30] A. Maestrini, B. Thomas, H. Wang, C. Jung, J. Treuttel, Y. Jin, G. Chattopadhyay, I. Mehdi, and G. Beaudin, "Schottky diode-based terahertz frequency multipliers and mixers", C. R. Phys. **11**, 480 (2010) 10.1016/j.crhy.2010.05.002.

[31] I. Mehdi, J. V. Siles, C. Lee, and E. Schlecht, "THz diode technology: Status, prospects, and applications", Proc. IEEE **105**, 990 (2017) 10.1109/JPROC.2017.2650235.

[32] G. Ducournau, P. Szriftgiser, T. Akalin, A. Beck, D. Bacquet, E. Peytavit, and J. F. Lampin, "Highly coherent terahertz wave generation with a dual-frequency Brillouin fiber laser and a $1.55\,\mu\mathrm{m}$ photomixer", Opt. Lett. **36**, 2044 (2011) 10.1364/OL.36.002044.

[33] M. H. Eissa, A. Malignaggi, and D. Kissinger, "A 13.5-dBm 200–255-GHz 4-way power amplifier and frequency source in 130-nm BiCMOS", IEEE Solid-State Circuits Lett. **2**, 268 (2019) 10.1109/LSSC.2019.2951689.

[34] L. John, A. Tessmann, A. Leuther, P. Neininger, T. Merkle, and T. Zwick, "Broadband 300-GHz power amplifier MMICs in InGaAs mHEMT technology", IEEE Trans. THz Sci. Technol. **10**, 309 (2020) 10.1109/TTHZ.2020.2965808.

[35] D. H. Auston, "Picosecond optoelectronic switching and gating in silicon", Appl. Phys. Lett. **26**, 101 (1975) 10.1063/1.88079.

[36] D. H. Auston, K. P. Cheung, J. A. Valdmanis, and D. A. Kleinman, "Cherenkov radiation from femtosecond optical pulses in electro-optic media", Phys. Rev. Lett. **53**, 1555 (1984) 10.1103/PhysRevLett.53.1555.

[37] B. B. Hu and M. C. Nuss, "Imaging with terahertz waves", Opt. Lett. **20**, 1716 (1995) 10.1364/OL.20.001716.

[38] M. Awad, M. Nagel, H. Kurz, J. Herfort, and K. Ploog, "Characterization of low temperature GaAs antenna array terahertz emitters", Appl. Phys. Lett. **91**, 181124 (2007) 10.1063/1.2800885.

[39] D. R. Bacon, T. B. Gill, M. Rosamond, A. D. Burnett, A. Dunn, L. Li, E. H. Linfield, A. G. Davies, P. Dean, and J. R. Freeman, "Photoconductive arrays on insulating substrates for high-field terahertz generation", Opt. Express **28**, 17219 (2020) 10.1364/OE.391656.

[40] Y. C. Shen, P. C. Upadhya, E. H. Linfield, H. E. Beere, and A. G. Davies, "Ultrabroadband terahertz radiation from low-temperature-grown GaAs photoconductive emitters", Appl. Phys. Lett. **83**, 3117 (2003) 10.1063/1.1619223.

[41] P. J. Hale, J. Madeo, C. Chin, S. S. Dhillon, J. Mangeney, J. Tignon, and K. M. Dani, "20 THz broadband generation using semi-insulating GaAs interdigitated photoconductive antennas", Opt. Express **22**, 26358 (2014) 10.1364/OE.22.026358.

[42] A. Dreyhaupt, S. Winnerl, T. Dekorsy, and M. Helm, "High-intensity terahertz radiation from a microstructured large-area photoconductor", Appl. Phys. Lett. **86**, 121114 (2005) 10.1063/1.1891304.

[43] C. W. Berry, N. Wang, M. R. Hashemi, M. Unlu, and M. Jarrahi, "Significant performance enhancement in photoconductive terahertz optoelectronics by incorporating plasmonic contact electrodes", Nat. Commun. **4**, 1622 (2013) 10.1038/ncomms2638.

[44] K. Kuznetsov, A. Klochkov, A. Leontyev, E. Klimov, S. Pushkarev, G. Galiev, and G. Kitaeva, "Improved InGaAs and InGaAs/InAlAs photoconductive antennas based on (111)-oriented substrates", Electronics **9**, 495 (2020) 10.3390/electronics9030495.

[45] I. Kostakis, D. Saeedkia, and M. Missous, "Terahertz generation and detection using low temperature grown InGaAs-InAlAs photoconductive antennas at 1.55 µm pulse excitation", IEEE Trans. THz Sci. Technol. **2**, 617 (2012) 10.1109/TTHZ.2012.2219047.

[46] A. Takazato, M. Kamakura, T. Matsui, J. Kitagawa, and Y. Kadoya, "Terahertz wave emission and detection using photoconductive antennas made on low-temperature-grown InGaAs with 1.56 µm pulse excitation", Appl. Phys. Lett. **91**, 011102 (2007) 10.1063/1.2754370.

[47] X. Ropagnol, M. Khorasaninejad, M. Raeiszadeh, S. Safavi-Naeini, M. Bouvier, C. Y. Côté, A. Laramée, M. Reid, M. A. Gauthier, and T. Ozaki, "Intense THz pulses with large ponderomotive potential generated from large aperture photoconductive antennas", Opt. Express **24**, 11299 (2016) 10.1364/OE.24.011299.

[48] N. M. Burford and M. O. El-Shenawee, "Review of terahertz photoconductive antenna technology", Opt. Eng **56**, 010901 (2017) 10.1117/1.OE.56.1.010901.

[49] M. T. Hibberd, V. Frey, B. F. Spencer, P. W. Mitchell, P. Dawson, M. J. Kappers, R. A. Oliver, C. J. Humphreys, and D. M. Graham, "Dielectric response of wurtzite gallium nitride in the terahertz frequency range", Solid State Commun. **247**, 68 (2016) 10.1016/j.ssc.2016.08.017.

[50] Q. Guo, Y. Kume, Y. Fukuhara, T. Tanaka, M. Nishio, H. Ogawa, M. Hiratsuka, M. Tani, and M. Hangyo, "Observation of ultra-broadband terahertz emission from ZnTe films grown by metaloganic vapor epitaxy", Solid State Commun. **141**, 188 (2007) 10.1016/j.ssc.2006.10.023.

[51] P. Y. Han and X.-C. Zhang, "Free-space coherent broadband terahertz time-domain spectroscopy", Meas. Sci. Technol. **12**, 1747 (2001) 10.1088/0957-0233/12/11/301.

[52] G. L. Dakovski, B. Kubera, and J. Shan, "Localized terahertz generation via optical rectification in ZnTe", J. Opt. Soc. Am. B **22**, 1667 (2005) 10.1364/JOSAB.22.001667.

[53] A. Nahata, A. S. Weling, and T. F. Heinz, "A wideband coherent terahertz spectroscopy system using optical rectification and electro–optic sampling", Appl. Phys. Lett. **69**, 2321 (1996) 10.1063/1.117511.

[54] K. Aoki, J. Savolainen, and M. Havenith, "Broadband terahertz pulse generation by optical rectification in GaP crystals", Appl. Phys. Lett. **110**, 201103 (2017) 10.1063/1.4983371.

[55] H. Hirori, A. Doi, F. Blanchard, and K. Tanaka, "Single-cycle terahertz pulses with amplitudes exceeding 1 MV/cm generated by optical rectification in $LiNbO_3$", Appl. Phys. Lett. **98**, 091106 (2011) 10.1063/1.3560062.

[56] X.-J. Wu, J.-L. Ma, B.-L. Zhang, S.-S. Chai, Z.-J. Fang, C.-Y. Xia, D.-Y. Kong, J.-G. Wang, H. Liu, C.-Q. Zhu, X. Wang, C.-J. Ruan, and Y.-T. Li, "Highly efficient generation of 0.2 mJ terahertz pulses in lithium niobate at room temperature with sub-50 fs chirped Ti:sapphire laser pulses", Opt. Express **26**, 7107 (2018) 10.1364/OE.26.007107.

[57] C. Vicario, M. Jazbinsek, A. V. Ovchinnikov, O. V. Chefonov, S. I. Ashitkov, M. B. Agranat, and C. P. Hauri, "High efficiency THz generation in DSTMS, DAST and OH1 pumped by Cr:forsterite laser", Opt. Express **23**, 4573 (2015) 10.1364/OE.23.004573.

[58] P. Y. Han, M. Tani, F. Pan, and X. C. Zhang, "Use of the organic crystal DAST for terahertz beam applications", Opt. Lett. **25**, 675 (2000) 10.1364/OL.25.000675.

[59] C. Somma, G. Folpini, J. Gupta, K. Reimann, M. Woerner, and T. Elsaesser, "Ultrabroadband terahertz pulses generated in the organic crystal DSTMS", Opt. Lett. **40**, 3404 (2015) 10.1364/OL.40.003404.

[60] M. Shalaby and C. P. Hauri, "Demonstration of a low-frequency three-dimensional terahertz bullet with extreme brightness", Nat. Commun. **6**, 5976 (2015) 10.1038/ncomms6976.

[61] Y. Zhang, X. Zhang, S. Li, J. Gu, Y. Li, Z. Tian, C. Ouyang, M. He, J. Han, and W. Zhang, "A broadband THz-TDS system based on DSTMS emitter and LTG InGaAs/InAlAs photoconductive antenna detector", Sci. Rep. **6**, 26949 (2016) 10.1038/srep26949.

[62] K. H. Yang, P. L. Richards, and Y. R. Shen, "Generation of far-infrared radiation by picosecond light pulses in $LiNbO_3$", Appl. Phys. Lett. **19**, 320 (1971) 10.1063/1.1653935.

[63] J. R. Morris and Y. R. Shen, "Far-infrared generation by picosecond pulses in electro-optical materials", Opt. Commun. **3**, 81 (1971) 10.1016/0030-4018(71)90182-9.

[64] H. Hamster, A. Sullivan, W. Gordon, W. White, and R. W. Falcone, "Subpicosecond, electromagnetic pulses from intense laser-plasma interaction", Phys. Rev. Lett **71**, 2725 (1993) 10.1103/PhysRevLett.71.2725.

[65] M. D. Thomson, V. Blank, and H. G. Roskos, "Terahertz white-light pulses from an air plasma photo-induced by incommensurate two-color optical fields", Opt. Express **18**, 23173 (2010) 10.1364/OE.18.023173.

[66] E. Matsubara, M. Nagai, and M. Ashida, "Ultrabroadband coherent electric field from far infrared to 200 THz using air plasma induced by 1 fs pulses", Appl. Phys. Lett. **101**, 011105 (2012) 10.1063/1.4732524.

[67] J. A. Fülöp, S. Tzortzakis, and T. Kampfrath, "Laser–driven strong–field terahertz sources", Adv. Optical Mater. **8**, 1900681 (2020) 10.1002/adom.201900681.

[68] C. Bull, S. M. Hewett, R. Ji, C.-H. Lin, T. Thomson, D. M. Graham, and P. W. Nutter, "Spintronic terahertz emitters: Status and prospects from a materials perspective", APL Mater. **9**, 090701 (2021) 10.1063/5.0057511.

[69] F. Blanchard, B. E. Schmidt, X. Ropagnol, N. Thiré, T. Ozaki, R. Morandotti, D. G. Cooke, and F. Légaré, "Terahertz pulse generation from bulk GaAs by a tilted-pulse-front excitation at 1.8 µm", Appl. Phys. Lett. **105**, 241106 (2014) 10.1063/1.4904005.

[70] F. Blanchard, L. Razzari, H. C. Bandulet, G. Sharma, R. Morandotti, J. C. Kieffer, T. Ozaki, M. Reid, H. F. Tiedje, H. K. Haugen, and F. A. Hegmann, "Generation of 1.5 µJ single-cycle terahertz pulses by optical rectification from a large aperture ZnTe crystal", Opt. Express **15**, 13212 (2007) 10.1364/OE.15.013212.

[71] J. A. Fülöp, G. Polónyi, B. Monoszlai, G. Andriukaitis, T. Balciunas, A. Pugzlys, G. Arthur, A. Baltuska, and J. Hebling, "Highly efficient scalable monolithic semiconductor terahertz pulse source", Optica **3**, 1075 (2016) 10.1364/OPTICA.3.001075.

[72] K.-L. Yeh, M. C. Hoffmann, J. Hebling, and K. A. Nelson, "Generation of 10 µJ ultrashort terahertz pulses by optical rectification", Appl. Phys. Lett. **90**, 171121 (2007) 10.1063/1.2734374.

[73] J. A. Fülöp, Z. Ollmann, C. Lombosi, C. Skrobol, S. Klingebiel, L. Pálfalvi, F. Krausz, S. Karsch, and J. Hebling, "Efficient generation of THz pulses with 0.4 mJ energy", Opt. Express **22**, 20155 (2014) 10.1364/OE.22.020155.

[74] T. Seifert, S. Jaiswal, M. Sajadi, G. Jakob, S. Winnerl, M. Wolf, M. Kläui, and T. Kampfrath, "Ultrabroadband single-cycle terahertz pulses with peak fields of 300 kV/cm from a metallic spintronic emitter", Appl. Phys. Lett. **110**, 252402 (2017) 10.1063/1.4986755.

[75] C. Ruchert, C. Vicario, and C. P. Hauri, "Scaling submillimeter single-cycle transients toward megavolts per centimeter field strength via optical rectification in the organic crystal OH1", Opt. Lett. **37**, 899 (2012) 10.1364/OL.37.000899.

[76] T. I. Oh, Y. S. You, N. Jhajj, E. W. Rosenthal, H. M. Milchberg, and K. Y. Kim, "Intense terahertz generation in two-color laser filamentation: energy scaling with terawatt laser systems", New J. Phys. **15**, 075002 (2013) 10.1088/1367-2630/15/7/075002.

[77] A. D. Koulouklidis, C. Gollner, V. Shumakova, V. Y. Fedorov, A. Pugžlys, A. Baltuška, and S. Tzortzakis, "Observation of extremely efficient terahertz generation from mid-infrared two-color laser filaments", Nat. Commun. **11**, 292 (2020) 10.1038/s41467-019-14206-x.

[78] C. P. Hauri, C. Ruchert, C. Vicario, and F. Ardana, "Strong-field single-cycle THz pulses generated in an organic crystal", Appl. Phys. Lett. **99**, 161116 (2011) 10.1063/1.3655331.

[79] I. Dey, K. Jana, V. Y. Fedorov, A. D. Koulouklidis, A. Mondal, M. Shaikh, D. Sarkar, A. D. Lad, S. Tzortzakis, A. Couairon, and G. R. Kumar, "Highly efficient broadband terahertz generation from ultrashort laser filamentation in liquids", Nat. Commun. **8**, 1184 (2017) 10.1038/s41467-017-01382-x.

[80] C. Vicario, A. V. Ovchinnikov, S. I. Ashitkov, M. B. Agranat, V. E. Fortov, and C. P. Hauri, "Generation of 0.9-mJ THz pulses in DSTMS pumped by a Cr:Mg_2SiO_4 laser", Opt. Lett. **39**, 6632 (2014) 10.1364/OL.39.006632.

[81] T. Kampfrath, M. Battiato, P. Maldonado, G. Eilers, J. Nötzold, S. Mährlein, V. Zbarsky, F. Freimuth, Y. Mokrousov, S. Blügel, M. Wolf, I. Radu, P. M. Oppeneer, and M. Münzenberg, "Terahertz spin current pulses controlled by magnetic heterostructures", Nat. Nanotechnol. **8**, 256 (2013) 10.1038/nnano.2013.43.

[82] T. Seifert, S. Jaiswal, U. Martens, J. Hannegan, L. Braun, P. Maldonado, F. Freimuth, A. Kronenberg, J. Henrizi, I. Radu, E. Beaurepaire, Y. Mokrousov, P. M. Oppeneer, M. Jourdan, G. Jakob, D. Turchinovich, L. M. Hayden, M. Wolf, M. Münzenberg, M. Kläui, and T. Kampfrath, "Efficient metallic spintronic emitters of ultrabroadband terahertz radiation", Nat. Photonics **10**, 483 (2016) 10.1038/nphoton.2016.91.

[83] D. Yang, J. Liang, C. Zhou, L. Sun, R. Zheng, S. Luo, Y. Wu, and J. Qi, "Powerful and tunable THz emitters based on the Fe/Pt magnetic heterostructure", Adv. Opt. Mater. **4**, 1944 (2016) 10.1002/adom.201600270.

[84] M. T. Hibberd, D. S. Lake, N. A. B. Johansson, T. Thomson, S. P. Jamison, and D. M. Graham, "Magnetic-field tailoring of the terahertz polarization emitted from a spintronic source", Appl. Phys. Lett. **114**, 031101 (2019) 10.1063/1.5055736.

[85] T. Bartel, P. Gaal, K. Reimann, M. Woerner, and T. Elsaesser, "Generation of single-cycle THz transients with high electric-field amplitudes", Opt. Lett. **30**, 2805 (2005) 10.1364/OL.30.002805.

[86] J. M. D. Coey, *Magnetism and magnetic materials* (Cambridge University Press, Cambridge, England and New York, NY, USA, 2009), ISBN: 9780521816144.

[87] S. Blundell, *Magnetism in condensed matter*, Oxford master series in condensed matter physics (Oxford University Press, Oxford, England, 2003), ISBN: 0-19-850592-2.

[88] W. Heisenberg, "Zur Theorie des Ferromagnetismus", Z. Phys. **49**, 619 (1928) 10.1007/BF01328601.

[89] H. Kramers, "L'interaction entre les atomes magnétogènes dans un cristal paramagnétique", Physica **1**, 182 (1934) 10.1016/S0031-8914(34)90023-9.

[90] P. W. Anderson, "Antiferromagnetism. Theory of superexchange interaction", Phys. Rev. **79**, 350 (1950) 10.1103/PhysRev.79.350.

[91] I. Dzyaloshinsky, "A thermodynamic theory of "weak" ferromagnetism of antiferromagnetics", J. Phys. Chem. Solids **4**, 241 (1958) 10.1016/0022-3697(58)90076-3.

[92] T. Moriya, "Anisotropic superexchange interaction and weak ferromagnetism", Phys. Rev. **120**, 91 (1960) 10.1103/PhysRev.120.91.

[93] M. A. Ruderman and C. Kittel, "Indirect exchange coupling of nuclear magnetic moments by conduction electrons", Phys. Rev. **96**, 99 (1954) 10.1103/PhysRev.96.99.

[94] T. Kasuya, "A theory of metallic ferro- and antiferromagnetism on Zener's model", Prog. Theor. Phys. **16**, 45 (1956) 10.1143/PTP.16.45.

[95] K. Yosida, "Magnetic properties of Cu-Mn alloys", Phys. Rev. **106**, 893 (1957) 10.1103/PhysRev.106.893.

[96] C. Zener, "Interaction between the d-shells in the transition metals. II. Ferromagnetic compounds of manganese with perovskite structure", Phys. Rev. **82**, 403 (1951) 10.1103/PhysRev.82.403.

[97] M. T. Johnson, P. J. H. Bloemen, den Broeder, F. J. A., and J. J. d. Vries, "Magnetic anisotropy in metallic multilayers", Rep. Prog. Phys. **59**, 1409 (1996) 10.1088/0034-4885/59/11/002.

[98] G. W. Fernando, *Metallic multilayers and their applications: Theory, experiments, and applications related to thin metallic multilayers*, Vol. 4, Handbook of metal physics (Elsevier Science, Amsterdam, Netherlands, 2008), ISBN: 978-0444517036.

[99] H. J. G. Draaisma and W. J. M. de Jonge, "Surface and volume anisotropy from dipole–dipole interactions in ultrathin ferromagnetic films", J. Appl. Phys. **64**, 3610 (1988) 10.1063/1.341397.

[100] C. Kittel, *Einführung in die Festkörperphysik*, 15. ed. (Oldenbourg, München, Germany, 2013), ISBN: 978-3-486-59755-4.

[101] P. F. Carcia, A. D. Meinhaldt, and A. Suna, "Perpendicular magnetic anisotropy in Pd/Co thin film layered structures", Appl. Phys. Lett. **47**, 178 (1985) 10.1063/1.96254.

[102] O. Ciubotariu, A. Semisalova, K. Lenz, and M. Albrecht, "Strain-induced perpendicular magnetic anisotropy and Gilbert damping of $Tm_3Fe_5O_{12}$ thin films", Sci. Rep. **9**, 17474 (2019) 10.1038/s41598-019-53255-6.

[103] C. Holzmann, A. Ullrich, O.-T. Ciubotariu, and M. Albrecht, "Stress-induced magnetic properties of gadolinium iron garnet nanoscale-thin films: Implications for spintronic devices", ACS Appl. Nano Mater. **5**, 1023 (2022) 10.1021/acsanm.1c03687.

[104] T. D. Clemons, R. H. Kerr, and A. Joos, "3.10 - Multifunctional magnetic nanoparticles: Design, synthesis, and biomedical applications", in *Comprehensive nanoscience and nanotechnology*, edited by D. L. Andrews, R. H. Lipson, and T. Nann, Second Edition (Academic Press, Oxford, England, 2019), pp. 193–210, ISBN: 978-0-12-812296-9, 10.1016/B978-0-12-803581-8.10462-X.

[105] J. Frenkel and J. Dorfman, "Spontaneous and induced magnetisation in ferromagnetic bodies", Nature **126**, 274 (1930) 10.1038/126274a0.

[106] C. P. Bean and J. D. Livingston, "Superparamagnetism", J. Appl. Phys. **30**, 120S (1959) 10.1063/1.2185850.

[107] M. Knobel, W. C. Nunes, L. M. Socolovsky, E. de Biasi, J. M. Vargas, and J. C. Denardin, "Superparamagnetism and other magnetic features in granular materials: A review on ideal and real systems", J. Nanosci. Nanotechnol. **8**, 2836 (2008) 10.1166/jnn.2008.15348.

[108] G. C. Papaefthymiou, "Nanoparticle magnetism", Nano Today **4**, 438 (2009) 10.1016/j.nantod.2009.08.006.

[109] Y. Shiratsuchi, M. Yamamoto, Y. Endo, D. Li, and S. D. Bader, "Superparamagnetic behavior of ultrathin Fe films grown on Al_2O_3(0001) substrates", J. Appl. Phys. **94**, 7675 (2003) 10.1063/1.1628408.

[110] Y. Shiratsuchi, Y. Endo, and M. Yamamoto, "Transition from superparamagnetic to ferromagnetic state of ultrathin Fe films grown on inclined Al_2O_3(0001) substrates", Thin Solid Films **464**, 141 (2004) 10.1016/j.tsf.2004.06.039.

[111] Y. Shiratsuchi, T. Murakami, Y. Endo, and M. Yamamoto, "Evolution of magnetic state of ultrathin Co films with Volmer–Weber growth", Jpn. J. Appl. Phys. **44**, 8456 (2005) 10.1143/JJAP.44.8456.

[112] Y. Shiratsuchi, Y. Endo, and M. Yamamoto, "Magnetism of ultrathin Fe films in the vicinity of transition from ferromagnetism to superparamagnetism", Mater. Sci. Forum **512**, 165 (2006) 10.4028/www.scientific.net/MSF.512.165.

[113] P. Omelchenko, B. Heinrich, and E. Girt, "Measurements of interlayer exchange coupling of Pt in Py|Pt|Py system", Appl. Phys. Lett. **113**, 142401 (2018) 10.1063/1.5050935.

[114] É. Trémolet de Lacheisserie, D. Gignoux, and M. Schlenker, *Magnetism: Materials and applications* (Springer, New York, NY, USA, 2005), ISBN: 0-387-23063-7.

[115] G. Schütz, R. Wienke, W. Wilhelm, W. B. Zeper, H. Ebert, and K. Spörl, "Spin-dependent X-ray absorption in Co/Pt multilayers and $Co_{50}Pt_{50}$ alloy", J. Appl. Phys. **67**, 4456 (1990) 10.1063/1.344903.

[116] W. J. Antel, M. M. Schwickert, T. Lin, W. L. O'Brien, and G. R. Harp, "Induced ferromagnetism and anisotropy of Pt layers in Fe/Pt(001) multilayers", Phys. Rev. B **60**, 12933 (1999) 10.1103/PhysRevB.60.12933.

[117] F. Wilhelm, P. Poulopoulos, A. Scherz, H. Wende, K. Baberschke, M. Angelakeris, N. K. Flevaris, J. Goulon, and A. Rogalev, "Interface magnetism in 3d/5d multilayers probed by X-ray magnetic circular dichroism", Phys. Status Solidi A **196**, 33 (2003) 10.1002/pssa.200306346.

[118] T. Kuschel, C. Klewe, J.-M. Schmalhorst, F. Bertram, O. Kuschel, T. Schemme, J. Wollschläger, S. Francoual, J. Strempfer, A. Gupta, M. Meinert, G. Götz, D. Meier, and G. Reiss, "Static magnetic proximity effect in Pt/NiFe2O4 and Pt/Fe bilayers investigated by X-ray resonant magnetic reflectivity", Phys. Rev. Lett. **115**, 097401 (2015) 10.1103/PhysRevLett.115.097401.

[119] W. L. Lim, N. Ebrahim-Zadeh, J. C. Owens, H. G. E. Hentschel, and S. Urazhdin, "Temperature-dependent proximity magnetism in Pt", Appl. Phys. Lett. **102**, 162404 (2013) 10.1063/1.4802954.

[120] B. D. Schrag, A. Anguelouch, S. Ingvarsson, G. Xiao, Y. Lu, P. L. Trouilloud, A. Gupta, R. A. Wanner, W. J. Gallagher, P. M. Rice, and S. S. P. Parkin, "Néel "orange-peel" coupling in magnetic tunneling junction devices", Appl. Phys. Lett. **77**, 2373 (2000) 10.1063/1.1315633.

[121] J. C. S. Kools, "Effect of energetic particle bombardment during sputter deposition on the properties of exchange–biased spin–valve multilayers", J. Appl. Phys. **77**, 2993 (1995) 10.1063/1.359565.

[122] P. Grünberg, R. Schreiber, Y. Pang, M. B. Brodsky, and H. Sowers, "Layered magnetic structures: Evidence for antiferromagnetic coupling of Fe layers across Cr interlayers", Phys. Rev. Lett. **57**, 2442 (1986) 10.1103/PhysRevLett.57.2442.

[123] P. Grünberg, R. Schreiber, Y. Pang, U. Walz, M. B. Brodsky, and H. Sowers, "Layered magnetic structures: Evidence for antiferromagnetic coupling of Fe layers across Cr interlayers", J. Appl. Phys. **61**, 3750 (1987) 10.1063/1.338656.

[124] S. S. P. Parkin, N. More, and K. P. Roche, "Oscillations in exchange coupling and magnetoresistance in metallic superlattice structures: Co/Ru, Co/Cr, and Fe/Cr", Phys. Rev. Lett. **64**, 2304 (1990) 10.1103/PhysRevLett.64.2304.

[125] P. Bruno, "Theory of interlayer magnetic coupling", Phys. Rev. B **52**, 411 (1995) 10.1103/PhysRevB.52.411.

[126] D. M. Edwards, J. Mathon, R. B. Muniz, and M. S. Phan, "Oscillations in the exchange coupling of ferromagnetic layers separated by a nonmagnetic metallic layer", Electrochem. Solid-State Lett. **3**, 4941 (1991) 10.1088/0953-8984/3/26/015.

[127] P. Bruno and C. Chappert, "Oscillatory coupling between ferromagnetic layers separated by a nonmagnetic metal spacer", Phys. Rev. Lett. **67**, 1602 (1991) 10.1103/PhysRevLett.67.1602.

[128] J. Mathon, D. M. Edwards, R. B. Muniz, and M. S. Phan, "Theory of oscillatory exchange coupling in magnetic multilayers", Electrochem. Solid-State Lett. **104**, 1721 (1992) 10.1016/0304-8853(92)91523-V.

[129] Y. Yafet, "Ruderman-Kittel-Kasuya-Yosida range function of a one-dimensional free-electron gas", Phys. Rev. B **36**, 3948 (1987) 10.1103/PhysRevB.36.3948.

[130] P. Bruno, "Theory of interlayer exchange interactions in magnetic multilayers", J. Phys.: Condens. Matter **11**, 9403 (1999) 10.1088/0953-8984/11/48/305.

[131] J. Nogués and I. K. Schuller, "Exchange bias", Electrochem. Solid-State Lett. **192**, 203 (1999) 10.1016/S0304-8853(98)00266-2.

[132] W. H. Meiklejohn and C. P. Bean, "New magnetic anisotropy", Phys. Rev. **105**, 904 (1957) 10.1103/PhysRev.105.904.

[133] W. H. Meiklejohn and C. P. Bean, "New magnetic anisotropy", Phys. Rev. **102**, 1413 (1956) 10.1103/PhysRev.102.1413.

[134] W. H. Meiklejohn, "Exchange anisotropy – A review", J. Appl. Phys. **33**, 1328 (1962) 10.1063/1.1728716.

[135] I. Jacobs and C. Bean, "6. Fine particles, thin films and exchange anisotropy (effects of finite dimensions and interfaces on the basic properties of ferromagnets)", in *Spin arrangements and crystal structure, domains, and micromagnetics*, edited by G. T. Rado and H. Suhl (Academic Press, 1963), pp. 271–350, ISBN: 978-0-12-575303-6, 10.1016/B978-0-12-575303-6.50013-0.

[136] F. Radu and H. Zabel, "Exchange bias effect of ferro-/antiferromagnetic heterostructures", in *Magnetic heterostructures*, Vol. 227, edited by G. Höhler, A. Fujimori, J. Kühn, T. Müller, F. Steiner, J. Trümper, C. Varma, P. Wölfle, H. Zabel, and S. D. Bader, Springer Tracts in Modern Physics (Springer, Berlin and Heidelberg, Germany, 2008), pp. 97–184, ISBN: 978-3-540-73461-1, 10.1007/978-3-540-73462-8_3.

[137] T. J. Moran, J. M. Gallego, and I. K. Schuller, "Increased exchange anisotropy due to disorder at permalloy/CoO interfaces", J. Appl. Phys. **78**, 1887 (1995) 10.1063/1.360225.

[138] T. J. Moran, J. Nogués, D. Lederman, and I. K. Schuller, "Perpendicular coupling at Fe-FeF_2 interfaces", Appl. Phys. Lett. **72**, 617 (1998) 10.1063/1.120823.

[139] J. Nogués, T. J. Moran, D. Lederman, I. K. Schuller, and K. V. Rao, "Role of interfacial structure on exchange-biased FeF_2-Fe", Phys. Rev. B **59**, 6984 (1999) 10.1103/PhysRevB.59.6984.

[140] A. E. Berkowitz and J. H. Greiner, "Exchange anisotropy and strain interactions in the Ni–NiO system", J. Appl. Phys. **36**, 3330 (1965) 10.1063/1.1702976.

[141] J. Bransky, I. Bransky, and A. A. Hirsch, "Exchange anisotropy in thin cobalt films deposited on a CoO single–crystal substrate", J. Appl. Phys. **41**, 183 (1970) 10.1063/1.1658318.

[142] R. Jungblut, R. Coehoorn, M. T. Johnson, J. aan de Stegge, and A. Reinders, "Orientational dependence of the exchange biasing in molecular-beam-epitaxy-grown $Ni_{80}Fe_{20}$/$Fe_{50}Mn_{50}$ bilayers (invited)", J. Appl. Phys. **75**, 6659 (1994) 10.1063/1.356888.

[143] C. Tsang, N. Heiman, and K. Lee, "Exchange induced unidirectional anisotropy at FeMn-$Ni_{80}Fe_{20}$ interfaces", J. Appl. Phys. **52**, 2471 (1981) 10.1063/1.328970.

[144] D. Mauri, E. Kay, D. Scholl, and J. K. Howard, "Novel method for determining the anisotropy constant of MnFe in a NiFe/MnFe sandwich", J. Appl. Phys. **62**, 2929 (1987) 10.1063/1.339374.

[145] W. Stoecklein, S. S. P. Parkin, and J. C. Scott, "Ferromagnetic resonance studies of exchange-biased permalloy thin films", Phys. Rev. B **38**, 6847 (1988) 10.1103/PhysRevB.38.6847.

[146] M. Tsunoda, Y. Tsuchiya, M. Konoto, and M. Takahashi, "Microstructure of antiferromagnetic layer affecting on magnetic exchange coupling in trilayered Ni-Fe/25at% Ni-Mn/Ni-Fe films", J. Magn. Magn. Mater. **171**, 29 (1997) 10.1016/S0304-8853(97)00054-1.

[147] T. J. Klemmer, V. R. Inturi, M. K. Minor, and J. A. Barnard, "Exchange induced unidirectional anisotropy observed using Cr–Al antiferromagnetic films", Appl. Phys. Lett. **70**, 2915 (1997) 10.1063/1.119052.

[148] K. A. Seu, H. Huang, J. F. Lesoine, H. D. Showman, W. F. Egelhoff, L. Gan, and A. C. Reilly, "Co layer thickness dependence of exchange biasing for IrMn/Co and FeMn/Co", Electrochem. Solid-State Lett. **93**, 6611 (2003) 10.1063/1.1555332.

[149] K. T.-Y. Kung, L. K. Louie, and G. L. Gorman, "MnFe structure–exchange anisotropy relation in the NiFe/MnFe/NiFe system", J. Appl. Phys. **69**, 5634 (1991) 10.1063/1.347920.

[150] R. Nakatani, H. Hoshiya, K. Hoshino, and Y. Sugita, "Exchange coupling of (Mn-Ir, Fe-Mn)/Ni-Fe-Co and Ni-Fe-Co/(Mn-Ir, Fe-Mn) films formed by ion beam sputtering", IEEE Trans. Magn. **33**, 3682 (1997) 10.1109/20.619537.

[151] K. Li, Y. Wu, G. Han, P. Luo, L. An, J. Qiu, Z. Guo, and Y. Zheng, "Exchange coupling between ferromagnetic and laminated antiferromagnetic layers and its application", J. Appl. Phys. **94**, 5905 (2003) 10.1063/1.1616644.

[152] B. Dieny, V. S. Speriosu, S. Parkin, B. A. Gurney, D. R. Wilhoit, and D. Mauri, "Giant magnetoresistive in soft ferromagnetic multilayers", Phys. Rev. B **43**, 1297 (1991) 10.1103/PhysRevB.43.1297.

[153] J. Kools, "Exchange-biased spin-valves for magnetic storage", IEEE Trans. Magn. **32**, 3165 (1996) 10.1109/20.508381.

[154] H. Iwasaki, A. T. Saito, O. Tsutai, and M. Sahashi, "Excellent reliability of CoFe-IrMn spin valves", IEEE Trans. Magn. **33**, 2875 (1997) 10.1109/20.617783.

[155] H. N. Fuke, K. Saito, Y. Kamiguchi, H. Iwasaki, and M. Sahashi, "Spin-valve giant magnetoresistive films with antiferromagnetic Ir-Mn layers", J. Appl. Phys. **81**, 4004 (1997) 10.1063/1.364920.

[156] M. N. Baibich, J. M. Broto, A. Fert, F. van Nguyen Dau, F. Petroff, P. Etienne, G. Creuzet, A. Friederich, and J. Chazelas, "Giant magnetoresistance of (001)Fe/(001)Cr magnetic superlattices", Phys. Rev. Lett. **61**, 2472 (1988) 10.1103/PhysRevLett.61.2472.

[157] G. Binasch, P. Grünberg, F. Saurenbach, and W. Zinn, "Enhanced magnetoresistance in layered magnetic structures with antiferromagnetic interlayer exchange", Phys. Rev. B **39**, 4828 (1989) 10.1103/PhysRevB.39.4828.

[158] G. Scheunert, O. Heinonen, R. Hardeman, A. Lapicki, M. Gubbins, and R. M. Bowman, "A review of high magnetic moment thin films for microscale and nanotechnology applications", Appl. Phys. Rev. **3**, 011301 (2016) 10.1063/1.4941311.

[159] P. Weiss, "The magnetic properties of the alloys of the ferromagnetic metals: Iron-nickel, nickel-cobalt, cobalt-iron", Trans. Faraday Soc. **8**, 149 (1912) 10.1039/TF9120800149.

[160] D. I. Bardos, "Mean magnetic moments in bcc Fe–Co alloys", J. Appl. Phys. **40**, 1371 (1969) 10.1063/1.1657673.

[161] R. H. Victora and L. M. Falicov, "Calculated magnetization of iron-cobalt disordered alloys", Phys. Rev. B **30**, 259 (1984) 10.1103/PhysRevB.30.259.

[162] K. Schwarz, P. Mohn, P. Blaha, and J. Kubler, "Electronic and magnetic structure of BCC Fe-Co alloys from band theory", J. Phys. F: Met. Phys. **14**, 2659 (1984) 10.1088/0305-4608/14/11/021.

[163] J. M. MacLaren, T. C. Schulthess, W. H. Butler, R. Sutton, and M. McHenry, "Electronic structure, exchange interactions, and Curie temperature of FeCo", J. Appl. Phys. **85**, 4833 (1999) 10.1063/1.370036.

[164] E. I. Cooper, C. Bonhote, J. Heidmann, Y. Hsu, P. Kern, J. W. Lam, M. Ramasubramanian, N. Robertson, L. T. Romankiw, and H. Xu, "Recent developments in high-moment electroplated materials for recording heads", IBM J. Res. & Dev. **49**, 103 (2005) 10.1147/rd.491.0103.

[165] Y. Chen, K. Sin, H. Jiang, Y. Tang, K. Sasaki, A. Torabi, L. Wang, M. Park, D. Bai, Y. Shen, P. Luo, F. Liu, K. Stoev, W. Lin, and J. Zhu, "High moment materials and fabrication processes for shielded perpendicular write head beyond 200 $\mathrm{Gb/in^2}$", IEEE Trans. Magn. **43**, 609 (2007) 10.1109/TMAG.2006.888200.

[166] M. T. Kief, V. Inturi, M. Benakli, I. Tabakovic, M. Sun, O. Heinonen, S. Riemer, and V. Vas'ko, "High magnetic saturation poles for advanced perpendicular writers", IEEE Trans. Magn. **44**, 113 (2008) 10.1109/TMAG.2007.911028.

[167] M. F. Collins and J. B. Forsyth, "The magnetic moment distribution in some transition metal alloys", Philos. Mag. **8**, 401 (1963) 10.1080/14786436308211141.

[168] J. C. Slater, "The ferromagnetism of nickel", Phys. Rev. **49**, 537 (1936) 10.1103/PhysRev.49.537.

[169] L. Pauling, "The nature of the interatomic forces in metals", Phys. Rev. **54**, 899 (1938) 10.1103/PhysRev.54.899.

[170] S. Kobe and A. R. Ferchmin, "Amorphous magnetism and magnetic materials: Bibliography 1950-1976", J. Mater. Sci. **12**, 1713 (1977) 10.1007/BF00566234.

[171] P. Hansen, "Chapter 4 – Magnetic amorphous alloys", in *Handbook of magnetic materials*, Vol. 6, edited by K. H. J. Buschow (Elsevier, Amsterdam, Netherlands, 1991), pp. 289–452, ISBN: 978-0-444-88952-2, 10.1016/S1567-2719(05)80058-7.

[172] Y. Mimura and N. Imamura, "Magnetic properties of amorphous Tb–Fe thin films prepared by rf sputtering", Appl. Phys. Lett. **28**, 746 (1976) 10.1063/1.88638.

[173] P. Hansen, C. Clausen, G. Much, M. Rosenkranz, and K. Witter, "Magnetic and magneto–optical properties of rare–earth transition–metal alloys containing Gd, Tb, Fe, Co", J. Appl. Phys. **66**, 756 (1989) 10.1063/1.343551.

[174] J. Rhyne and T. McGuire, "Magnetism of rare-earth elements, alloys, and compounds", IEEE Trans. Magn. **8**, 105 (1972) 10.1109/TMAG.1972.1067267.

[175] C. D. Graham, "Magnetic behavior of gadolinium near the Curie point", J. Appl. Phys. **36**, 1135 (1965) 10.1063/1.1714135.

[176] W. C. Thoburn, S. Legvold, and F. H. Spedding, "Magnetic properties of terbium metal", Phys. Rev. **112**, 56 (1958) 10.1103/PhysRev.112.56.

[177] J. F. Herbst, J. J. Croat, and W. B. Yelon, "Structural and magnetic properties of $Nd_2Fe_{14}B$ (invited)", J. Appl. Phys. **57**, 4086 (1985) 10.1063/1.334680.

[178] K. Kumar, "$RETM_5$ and RE_2TM_{17} permanent magnets development", J. Appl. Phys. **63**, R13 (1988) 10.1063/1.341084.

[179] S. Landin and J. Ågren, "Thermodynamic assessment of Fe-Tb and Fe-Dy phase diagrams and prediction of Fe-Tb-Dy phase diagram", J. Alloys Compd. **207**, 449 (1994) 10.1016/0925-8388(94)90261-5.

[180] W. Zhang, C. Li, X. Su, and K. Han, "An updated evaluation of the Fe-Gd (iron-gadolinium) system", J. Phase Equilib. Diffus. **19**, 56 (1998) 10.1007/s11669-006-5005-9.

[181] H. Okamoto, "Supplemental literature review of binary phase diagrams: Bi-Ce, Bi-Er, C-Ce, C-La, C-Pr, Cd-I, Cr-Cu, Cu-Er, Er-Sb, F-Sm, F-Yb, and Fe-Gd", J. Phase Equilib. Diffus. **34**, 350 (2013) 10.1007/s11669-013-0240-3.

[182] N. Imamura, Y. Mimura, and T. Kobayashi, "Amorphous Gd-Fe alloy films prepared by RF cosputtering technique", IEEE Trans. Magn. **12**, 55 (1976).

[183] Y. Mimura, N. Imamura, and T. Kobayashi, "Magnetic properties and Curie point writing in amorphous metallic films", IEEE Trans. Magn. **12**, 779 (1976).

[184] Y. Mimura, N. Imamura, T. Kobayashi, A. Okada, and Y. Kushiro, "Magnetic properties of amorphous alloy films of Fe with Gd, Tb, Dy, Ho, or Er", J. Appl. Phys. **49**, 1208 (1978) 10.1063/1.325008.

[185] C. Vittoria, P. Lubitz, and V. Ritz, "Magnetic properties of amorphous and crystalline $GdFe_2$", J. Appl. Phys. **49**, 4908 (1978) 10.1063/1.325525.

[186] N. Sato, "Magnetic properties of amorphous Tb–Fe thin films with an artificially layered structure", J. Appl. Phys. **59**, 2514 (1986) 10.1063/1.336999.

[187] J. M. D. Coey, "Amorphous magnetic order", J. Appl. Phys. **49**, 1646 (1978) 10.1063/1.324880.

[188] B. Hebler, A. Hassdenteufel, P. Reinhardt, H. Karl, and M. Albrecht, "Ferrimagnetic Tb–Fe alloy thin films: Composition and thickness dependence of magnetic properties and all-optical switching", Front. Mater. **3**, 162408 (2016) 10.3389/fmats.2016.00008.

[189] J. J. Rhyne, J. H. Schelleng, and N. C. Koon, "Anomalous magnetization of amorphous $TbFe_2$, $GdFe_2$, and YFe_2", Phys. Rev. B **10**, 4672 (1974) 10.1103/PhysRevB.10.4672.

[190] N. H. Duc and P. Brommer, "Chapter 2 – Magnetoelasticity in nanoscale heterogeneous magnetic materials", in *Handbook of magnetic materials*, Vol. 14, edited by K. H. J. Buschow (Elsevier, Amsterdam, Netherlands, 2002), pp. 89–198, ISBN: 978-0-444-51144-7, 10.1016/S1567-2719(09)60006-8.

[191] J. P. Eymery, A. Fnidiki, R. Krishnan, M. Tessier, and J. P. Vitton, "Conversion-electron Mössbauer spectroscopy studies in amorphous Tb-Fe films", Phys. Rev. B **38**, 11931 (1988) 10.1103/PhysRevB.38.11931.

[192] V. S. Rusakov, B. S. Vvedensky, E. T. Voropaeva, and E. N. Nikolaev, "Mössbauer spectroscopy and magneto-optical studies of Tb-Fe films", IEEE Trans. Magn. **28**, 2524 (1992) 10.1109/20.179544.

[193] T. Ruckert, J. Tappert, R. A. Brand, and W. Keune, "Mössbauer-effect study of amorphous $Tb_{1-x}Fe_x$ films", J. Magn. Magn. Mater. **165**, 411 (1997) 10.1016/S0304-8853(96)00572-0.

[194] C. Schubert, *Magnetic order and coupling phenomena: A study of magnetic structure and magnetization reversal processes in rare-earth-transition-metal based alloys and heterostructures*, Springer Theses Series (Springer, Cham, Germany, 2014), ISBN: 978-3-319-07106-0.

[195] M. Tewes, J. Zweck, and H. Hoffmann, "Short-range order in amorphous FeTb", J. Magn. Magn. Mater. **95**, 43 (1991) 10.1017/s042482010017373x.

[196] M. Tewes, J. Zweck, and H. Hoffmann, "Derivation of partial pair distribution functions for amorphous FeTb from electron scattering data based on a new concept", J. Phys. Condens. Matter **6**, 835 (1994) 10.1088/0953-8984/6/4/004.

[197] R. Lizárraga, "Structural and magnetic properties of the Gd-based bulk metallic glasses $GdFe_2$, $GdCo_2$, and $GdNi_2$ from first principles", Phys. Rev. B **94**, 688 (2016) 10.1103/PhysRevB.94.174201.

[198] A. G. Dirks, J. Biesterbos, and K. Buschow, "Magnetic compensation temperatures of amorphous rare earth-cobalt alloys", Physica B **86**, 761 (1977) 10.1016/0378-4363(77)90676-3.

[199] F. Hellman and E. M. Gyorgy, "Growth-induced magnetic anisotropy in amorphous Tb-Fe", Phys. Rev. Lett. **68**, 1391 (1992) 10.1103/PhysRevLett.68.1391.

[200] F. Hellman, "Surface–induced ordering: A model for vapor–deposition growth of amorphous materials", Appl. Phys. Lett. **64**, 1947 (1994) 10.1063/1.111751.

[201] R. J. Gambino and J. J. Cuomo, "Selective resputtering–induced anisotropy in amorphous films", J. Vac. Sci. Technol. **15**, 296 (1978) 10.1116/1.569574.

[202] Y. Nishihara, T. Katayama, Y. Yamaguchi, S. Ogawa, and T. Tsushima, "Anisotropic distribution of atomic pairs induced by the preferential resputtering effect in amorphous Gd-Fe and Gd-Co films", Jpn. J. Appl. Phys. **17**, 1083 (1978) 10.1143/JJAP.17.1083.

[203] V. G. Harris and T. Pokhil, "Evidence for selective resputtering as the growth mechanism of pair-order anisotropy in amorphous TbFe films", Bull. Mater. Sci. **22**, 503 (1999) 10.1007/BF02749962.

[204] S. Tsunashima, H. Takagi, K. Kamegaki, T. Fujii, and S. Uchiyama, "Magnetoelastic contribution to perpendicular anisotropy in amorphous Gd-Co and Gd-Fe films", IEEE Trans. Magn. **14**, 844 (1978) 10.1109/TMAG.1978.1059907.

[205] A. Hernando, C. Prados, and C. Prieto, "Anisotropy, magnetostriction and local chemical order in amorphous Tb_xFe_{1-x} ($0.1 < x < 0.55$) thin films", J. Magn. Magn. Mater. **157**, 501 (1996) 10.1016/0304-8853(95)01124-2.

[206] T. Mizoguchi and G. S. Cargill III, "Magnetic anisotropy from dipolar interactions in amorphous ferrimagnetic alloys", J. Appl. Phys. **50**, 3570 (1979) 10.1063/1.326303.

[207] H. Fu, M. Mansuripur, and P. Meystre, "Generic source of perpendicular anisotropy in amorphous rare-earth-transition-metal films", Phys. Rev. Lett. **66**, 1086 (1991) 10.1103/PhysRevLett.66.1086.

[208] T. C. Hufnagel, S. Brennan, P. Zschack, and B. M. Clemens, "Structural anisotropy in amorphous Fe-Tb thin films", Phys. Rev. B **53**, 12024 (1996) 10.1103/PhysRevB.53.12024.

[209] C. Prados, E. Marinero, and A. Hernando, "Magnetic interactions and anisotropy in amorphous TbFe films", J. Magn. Magn. Mater. **165**, 414 (1997) 10.1016/S0304-8853(96)00573-2.

[210] R. Skomski and D. J. Sellmyer, "Anisotropy of rare-earth magnets", J. Rare Earths **27**, 675 (2009) 10.1016/S1002-0721(08)60314-2.

[211] M. Ding and S. J. Poon, "Tunable perpendicular magnetic anisotropy in GdFeCo amorphous films", Electrochem. Solid-State Lett. **339**, 51 (2013) 10.1016/j.jmmm.2013.03.007.

[212] M. Krupinski, J. Hintermayr, P. Sobieszczyk, and M. Albrecht, "Control of magnetic properties in ferrimagnetic GdFe and TbFe thin films by He^+ and Ne^+ irradiation", Phys. Rev. Mater. **5**, 024405 (2021) 10.1103/PhysRevMaterials.5.024405.

[213] S. Mondal, A. Talapatra, J. Arout Chelvane, J. R. Mohanty, and A. Barman, "Role of magnetic anisotropy in the ultrafast magnetization dynamics of Gd-Fe thin films of different thicknesses", Phys. Rev. B **100**, 10.1103/PhysRevB.100.054436 (2019) 10.1103/PhysRevB.100.054436.

[214] A. Talapatra, J. Arout Chelvane, and J. Mohanty, "Tuning magnetic microstructure in Gd-Fe thin films: Experiment and simulation", J. Magn. Magn. Mater. **448**, 360 (2018) 10.1016/j.jmmm.2017.07.092.

[215] C. Schubert, B. Hebler, H. Schletter, A. Liebig, M. Daniel, R. Abrudan, F. Radu, and M. Albrecht, "Interfacial exchange coupling in Fe-Tb/[Co/Pt] heterostructures", Phys. Rev. B **87**, 054415 (2013) 10.1103/PhysRevB.87.054415.

[216] E. Beaurepaire, J.-C. Merle, A. Daunois, and J.-Y. Bigot, "Ultrafast spin dynamics in ferromagnetic nickel", Phys. Rev. Lett. **76**, 4250 (1996) 10.1103/PhysRevLett.76.4250.

[217] G. L. Eesley, "Observation of nonequilibrium electron heating in copper", Phys. Rev. Lett. **51**, 2140 (1983) 10.1103/PhysRevLett.51.2140.

[218] R. W. Schoenlein, W. Z. Lin, J. G. Fujimoto, and G. L. Eesley, "Femtosecond studies of nonequilibrium electronic processes in metals", Phys. Rev. Lett. **58**, 1680 (1987) 10.1103/PhysRevLett.58.1680.

[219] H. E. Elsayed-Ali, T. B. Norris, M. A. Pessot, and G. A. Mourou, "Time-resolved observation of electron-phonon relaxation in copper", Phys. Rev. Lett. **58**, 1212 (1987) 10.1103/PhysRevLett.58.1212.

[220] J. Hohlfeld, E. Matthias, R. Knorren, and K. H. Bennemann, "Nonequilibrium magnetization dynamics of nickel", Phys. Rev. Lett. **78**, 4861 (1997) 10.1103/PhysRevLett.78.4861.

[221] A. Scholl, L. Baumgarten, R. Jacquemin, and W. Eberhardt, "Ultrafast spin dynamics of ferromagnetic thin films observed by fs spin-resolved two-photon photoemission", Phys. Rev. Lett. **79**, 5146 (1997) 10.1103/PhysRevLett.79.5146.

[222] G. P. Zhang and W. Hübner, "Laser-induced ultrafast demagnetization in ferromagnetic metals", Phys. Rev. Lett. **85**, 3025 (2000) 10.1103/PhysRevLett.85.3025.

[223] T. J. Huisman, R. V. Mikhaylovskiy, A. Tsukamoto, T. Rasing, and A. V. Kimel, "Simultaneous measurements of terahertz emission and magneto-optical Kerr effect for resolving ultrafast laser-induced demagnetization dynamics", Phys. Rev. B **92**, 259 (2015) 10.1103/PhysRevB.92.104419.

[224] K. Bobowski, M. Gleich, N. Pontius, C. Schüßler-Langeheine, C. Trabant, M. Wietstruk, B. Frietsch, and M. Weinelt, "Influence of the pump pulse wavelength on the ultrafast demagnetization of Gd(0 0 0 1) thin films", J. Condens. Matter Phys. **29**, 234003 (2017) 10.1088/1361-648X/aa6c92.

[225] K. Bühlmann, R. Gort, G. Salvatella, S. Däster, A. Fognini, T. Bähler, C. Dornes, C. A. F. Vaz, A. Vaterlaus, and Y. Acremann, "Ultrafast demagnetization in iron: Separating effects by their nonlinearity", Struct. Dyn. **5**, 044502 (2018) 10.1063/1.5040344.

[226] V. López-Flores, N. Bergeard, V. Halté, C. Stamm, N. Pontius, M. Hehn, E. Otero, E. Beaurepaire, and C. Boeglin, "Role of critical spin fluctuations in ultrafast demagnetization of transition-metal rare-earth alloys", Phys. Rev. B **87**, 259 (2013) 10.1103/PhysRevB.87.214412.

[227] C. D. Stanciu, F. Hansteen, A. V. Kimel, A. Kirilyuk, A. Tsukamoto, A. Itoh, and T. Rasing, "All-optical magnetic recording with circularly polarized light", Phys. Rev. Lett. **99**, 047601 (2007) 10.1103/PhysRevLett.99.047601.

[228] K. Vahaplar, A. M. Kalashnikova, A. V. Kimel, D. Hinzke, U. Nowak, R. Chantrell, A. Tsukamoto, A. Itoh, A. Kirilyuk, and T. Rasing, "Ultrafast path for optical magnetization reversal via a strongly nonequilibrium state", Phys. Rev. Lett. **103**, 117201 (2009) 10.1103/PhysRevLett.103.117201.

[229] I. Radu, K. Vahaplar, C. Stamm, T. Kachel, N. Pontius, H. A. Dürr, T. A. Ostler, J. Barker, R. F. L. Evans, R. W. Chantrell, A. Tsukamoto, A. Itoh, A. Kirilyuk, T. Rasing, and A. V. Kimel, "Transient ferromagnetic-like state mediating ultrafast reversal of antiferromagnetically coupled spins", Nature **472**, 205 (2011) 10.1038/nature09901.

[230] A. Hassdenteufel, B. Hebler, C. Schubert, A. Liebig, M. Teich, M. Helm, M. Aeschlimann, M. Albrecht, and R. Bratschitsch, "Thermally assisted all-optical helicity dependent magnetic switching in amorphous $Fe_{100-x}Tb_x$ alloy films", Adv. Mater. **25**, 3122 (2013) 10.1002/adma.201300176.

[231] S. Mangin, M. Gottwald, C.-H. Lambert, D. Steil, V. Uhlíř, L. Pang, M. Hehn, S. Alebrand, M. Cinchetti, G. Malinowski, Y. Fainman, M. Aeschlimann, and E. E. Fullerton, "Engineered materials for all-optical helicity-dependent magnetic switching", Nat. Mater. **13**, 286 (2014) 10.1038/nmat3864.

[232] C.-H. Lambert, S. Mangin, B. S. D. C. S. Varaprasad, Y. K. Takahashi, M. Hehn, M. Cinchetti, G. Malinowski, K. Hono, Y. Fainman, M. Aeschlimann, and E. E. Fullerton, "All-optical control of ferromagnetic thin films and nanostructures", Science **345**, 1337 (2014) 10.1126/science.1253493.

[233] M. S. El Hadri, P. Pirro, C.-H. Lambert, S. Petit-Watelot, Y. Quessab, M. Hehn, F. Montaigne, G. Malinowski, and S. Mangin, "Two types of all-optical magnetization switching mechanisms using femtosecond laser pulses", Phys. Rev. B **94**, 10.1103/PhysRevB.94.064412 (2016) 10.1103/PhysRevB.94.064412.

[234] M. S. El Hadri, P. Pirro, C.-H. Lambert, N. Bergeard, S. Petit-Watelot, M. Hehn, G. Malinowski, F. Montaigne, Y. Quessab, R. Medapalli, E. E. Fullerton, and S. Mangin, "Electrical characterization of all-optical helicity-dependent switching in ferromagnetic Hall crosses", Appl. Phys. Lett. **108**, 092405 (2016) 10.1063/1.4943107.

[235] Y. K. Takahashi, R. Medapalli, S. Kasai, J. Wang, K. Ishioka, S. H. Wee, O. Hellwig, K. Hono, and E. E. Fullerton, "Accumulative magnetic switching of ultrahigh-density recording media by circularly polarized light", Phys. Rev. Appl. **6**, 3200904 (2016) 10.1103/PhysRevApplied.6.054004.

[236] R. John, M. Berritta, D. Hinzke, C. Müller, T. Santos, H. Ulrichs, P. Nieves, J. Walowski, R. Mondal, O. Chubykalo-Fesenko, J. McCord, P. M. Oppeneer, U. Nowak, and M. Münzenberg, "Magnetisation switching of FePt nanoparticle recording medium by femtosecond laser pulses", Sci. Rep. **7**, 4114 (2017) 10.1038/s41598-017-04167-w.

[237] E. Beaurepaire, G. M. Turner, S. M. Harrel, M. C. Beard, J.-Y. Bigot, and C. A. Schmuttenmaer, "Coherent terahertz emission from ferromagnetic films excited by femtosecond laser pulses", Appl. Phys. Lett. **84**, 3465 (2004) 10.1063/1.1737467.

[238] L. Huang, J.-W. Kim, S.-H. Lee, S.-D. Kim, M. van Tien, K. P. Shinde, J.-H. Shim, Y. Shin, H. J. Shin, S. Kim, J. Park, S.-Y. Park, Y. S. Choi, H.-J. Kim, J.-I. Hong, D. E. Kim, and D.-H. Kim, "Direct observation of terahertz emission from ultrafast spin dynamics in thick ferromagnetic films", Appl. Phys. Lett. **115**, 142404 (2019) 10.1063/1.5087236.

[239] L. Huang, S.-H. Lee, S.-D. Kim, J.-H. Shim, H. J. Shin, S. Kim, J. Park, S.-Y. Park, Y. S. Choi, H.-J. Kim, J.-I. Hong, D. E. Kim, and D.-H. Kim, "Universal field-tunable terahertz emission by ultrafast photoinduced demagnetization in Fe, Ni, and Co ferromagnetic films", Sci. Rep. **10**, 15843 (2020) 10.1038/s41598-020-72855-1.

[240] M. Battiato, K. Carva, and P. M. Oppeneer, "Superdiffusive spin transport as a mechanism of ultrafast demagnetization", Phys. Rev. Lett. **105**, 027203 (2010) 10.1103/PhysRevLett.105.027203.

[241] M. Battiato, K. Carva, and P. M. Oppeneer, "Theory of laser-induced ultrafast superdiffusive spin transport in layered heterostructures", Phys. Rev. B **86**, 10.1103/PhysRevB.86.024404 (2012) 10.1103/PhysRevB.86.024404.

[242] D. Rudolf, C. La-O-Vorakiat, M. Battiato, R. Adam, J. M. Shaw, E. Turgut, P. Maldonado, S. Mathias, P. Grychtol, H. T. Nembach, T. J. Silva, M. Aeschlimann, H. C. Kapteyn, M. M. Murnane, C. M. Schneider, and P. M. Oppeneer, "Ultrafast magnetization enhancement in metallic multilayers driven by superdiffusive spin current", Nat. Commun. **3**, 1037 (2012) 10.1038/ncomms2029.

[243] A. Kirilyuk, A. V. Kimel, and T. Rasing, "Ultrafast optical manipulation of magnetic order", Rev. Mod. Phys. **82**, 2731 (2010) 10.1103/RevModPhys.82.2731.

[244] J.-Y. Bigot and M. Vomir, "Ultrafast magnetization dynamics of nanostructures", Ann. Phys. **525**, 2 (2013) 10.1002/andp.201200199.

[245] J. Walowski and M. Münzenberg, "Perspective: Ultrafast magnetism and THz spintronics", J. Appl. Phys. **120**, 140901 (2016) 10.1063/1.4958846.

[246] K. Carva, P. Baláž, and I. Radu, "Chapter 2 – Laser-induced ultrafast magnetic phenomena", in *Handbook of Magnetic Materials*, Vol. 26, edited by E. Brück (Elsevier, 2017), pp. 291–463, ISBN: 978-0-444-63927-1, 10.1016/bs.hmm.2017.09.003.

[247] J.-Y. Bigot, M. Vomir, and E. Beaurepaire, "Coherent ultrafast magnetism induced by femtosecond laser pulses", Nat. Physics **5**, 515 (2009) 10.1038/nphys1285.

[248] B. Koopmans, J. J. M. Ruigrok, F. D. Longa, and W. J. M. de Jonge, "Unifying ultrafast magnetization dynamics", Phys. Rev. Lett. **95**, 267207 (2005) 10.1103/PhysRevLett.95.267207.

[249] B. Koopmans, G. Malinowski, F. Dalla Longa, D. Steiauf, M. Fähnle, T. Roth, M. Cinchetti, and M. Aeschlimann, "Explaining the paradoxical diversity of ultrafast laser-induced demagnetization", Nat. Mater. **9**, 259 (2010) 10.1038/nmat2593.

[250] M. Krauß, T. Roth, S. Alebrand, D. Steil, M. Cinchetti, M. Aeschlimann, and H. C. Schneider, "Ultrafast demagnetization of ferromagnetic transition metals: The role of the Coulomb interaction", Phys. Rev. B **80**, 208 (2009) 10.1103/PhysRevB.80.180407.

[251] G. P. Zhang, W. Hübner, G. Lefkidis, Y. Bai, and T. F. George, "Paradigm of the time-resolved magneto-optical Kerr effect for femtosecond magnetism", Nat. Phys. **5**, 499 (2009) 10.1038/nphys1315.

[252] G. Lefkidis, G. P. Zhang, and W. Hübner, "Angular momentum conservation for coherently manipulated spin polarization in photoexcited NiO: An ab initio calculation", Phys. Rev. Lett. **103**, 217401 (2009) 10.1103/PhysRevLett.103.217401.

[253] G. Malinowski, F. Dalla Longa, J. H. H. Rietjens, P. V. Paluskar, R. Huijink, H. J. M. Swagten, and B. Koopmans, "Control of speed and efficiency of ultrafast demagnetization by direct transfer of spin angular momentum", Nat. Phys. **4**, 855 (2008) 10.1038/nphys1092.

[254] D. J. Hilton, R. D. Averitt, C. A. Meserole, G. L. Fisher, D. J. Funk, D. J. Thompson, and A. J. Taylor, "Terahertz emission via ultrashort-pulse excitation of magnetic metal films", Opt. Lett. **29**, 1805 (2004).

[255] J. Shen, X. Fan, Z. Chen, M. F. DeCamp, H. Zhang, and J. Q. Xiao, "Damping modulated terahertz emission of ferromagnetic films excited by ultrafast laser pulses", Appl. Phys. Lett. **101**, 072401 (2012) 10.1063/1.4737400.

[256] A. Melnikov, I. Razdolski, T. O. Wehling, E. T. Papaioannou, V. Roddatis, P. Fumagalli, O. Aktsipetrov, A. I. Lichtenstein, and U. Bovensiepen, "Ultrafast transport of laser-excited spin-polarized carriers in Au/Fe/MgO(001)", Phys. Rev. Lett. **107**, 076601 (2011) 10.1103/PhysRevLett.107.076601.

[257] E. Saitoh, M. Ueda, H. Miyajima, and G. Tatara, "Conversion of spin current into charge current at room temperature: Inverse spin-Hall effect", Appl. Phys. Lett. **88**, 182509 (2006) 10.1063/1.2199473.

[258] V. P. Zhukov, E. V. Chulkov, and P. M. Echenique, "Lifetimes and inelastic mean free path of low-energy excited electrons in Fe, Ni, Pt, and Au: Ab initio GW+T calculations", Phys. Rev. B **73**, 465 (2006) 10.1103/PhysRevB.73.125105.

[259] D. Gall, "Electron mean free path in elemental metals", J. Appl. Phys. **119**, 085101 (2016) 10.1063/1.4942216.

[260] D. M. Nenno, L. Scheuer, D. Sokoluk, S. Keller, G. Torosyan, A. Brodyanski, J. Lösch, M. Battiato, M. Rahm, R. H. Binder, H. C. Schneider, R. Beigang, and E. T. Papaioannou, "Modification of spintronic terahertz emitter performance through defect engineering", Sci. Rep. **9**, 13348 (2019) 10.1038/s41598-019-49963-8.

[261] D. M. Nenno, R. Binder, and H. C. Schneider, "Simulation of hot-carrier dynamics and terahertz emission in laser-excited metallic bilayers", Phys. Rev. Appl. **11**, 054083 (2019) 10.1103/PhysRevApplied.11.054083.

[262] K. Uchida, S. Takahashi, K. Harii, J. Ieda, W. Koshibae, K. Ando, S. Maekawa, and E. Saitoh, "Observation of the spin Seebeck effect", Nature **455**, 778 (2008) 10.1038/nature07321.

[263] K. Uchida, J. Xiao, H. Adachi, J. Ohe, S. Takahashi, J. Ieda, T. Ota, Y. Kajiwara, H. Umezawa, H. Kawai, G. E. W. Bauer, S. Maekawa, and E. Saitoh, "Spin Seebeck insulator", Nat. Mater. **9**, 894 (2010) 10.1038/nmat2856.

[264] A. Slachter, F. L. Bakker, J.-P. Adam, and B. J. van Wees, "Thermally driven spin injection from a ferromagnet into a non-magnetic metal", Nat. Phys. **6**, 879 (2010) 10.1038/nphys1767.

[265] G. E. W. Bauer, E. Saitoh, and B. J. van Wees, "Spin caloritronics", Nat. Mater. **11**, 391 (2012) 10.1038/nmat3301.

[266] Y. Sasaki, Y. Kota, S. Iihama, K. Z. Suzuki, A. Sakuma, and S. Mizukami, "Effect of Co and Fe stoichiometry on terahertz emission from Ta/$(Co_xFe_{1-x})_{80}B_{20}$/MgO thin films", Phys. Rev. B **100**, 140406(R) (2019) 10.1103/PhysRevB.100.140406.

[267] R. Rouzegar, L. Brandt, L. Nadvornik, D. A. Reiss, A. L. Chekhov, O. Gueckstock, C. In, M. Wolf, T. S. Seifert, P. W. Brouwer, G. Woltersdorf, and T. Kampfrath, "Laser-induced terahertz spin transport in magnetic nanostructures arises from the same force as ultrafast demagnetization", arXiv:2103.11710v2 [cond–mat.mes–hall] (2021) 10.48550/arXiv.2103.11710.

[268] T. S. Seifert, S. Jaiswal, J. Barker, S. T. Weber, I. Razdolski, J. Cramer, O. Gueckstock, S. F. Maehrlein, L. Nadvornik, S. Watanabe, C. Ciccarelli, A. Melnikov, G. Jakob, M. Münzenberg, S. T. B. Goennenwein, G. Woltersdorf, B. Rethfeld, P. W. Brouwer, M. Wolf, M. Kläui, and T. Kampfrath, "Femtosecond formation dynamics of the spin Seebeck effect revealed by terahertz spectroscopy", Nat. Commun. **9**, 2899 (2018) 10.1038/s41467-018-05135-2.

[269] A. Hirohata, K. Yamada, Y. Nakatani, I.-L. Prejbeanu, B. Diény, P. Pirro, and B. Hillebrands, "Review on spintronics: Principles and device applications", J. Magn. Magn. Mater. **509**, 166711 (2020) 10.1016/j.jmmm.2020.166711.

[270] Y. Wu, Y. Xu, Z. Luo, Y. Yang, H. Xie, Q. Zhang, and X. Zhang, "Charge–spin interconversion and its applications in magnetic sensing", J. Appl. Phys. **129**, 060902 (2021) 10.1063/5.0039926.

[271] A. Hoffmann, "Spin Hall effects in metals", IEEE Trans. Magn. **49**, 5172 (2013) 10.1109/TMAG.2013.2262947.

[272] J. Sinova, S. O. Valenzuela, J. Wunderlich, C. H. Back, and T. Jungwirth, "Spin Hall effects", Rev. Mod. Phys. **87**, 1213 (2015) 10.1103/RevModPhys.87.1213.

[273] Y. A. Bychkov and E. I. Rashba, "Properties of a 2D electron gas with lifted spectral degeneracy", J. Exp. Theor. Phys. **39**, 78 (1984).

[274] V. M. Edelstein, "Spin polarization of conduction electrons induced by electric current in two-dimensional asymmetric electron systems", Solid State Commun. **73**, 233 (1990) 10.1016/0038-1098(90)90963-C.

[275] D. Bercioux and P. Lucignano, "Quantum transport in Rashba spin-orbit materials: A review", Rep. Prog. Phys. **78**, 106001 (2015) 10.1088/0034-4885/78/10/106001.

[276] C. R. Ast, J. Henk, A. Ernst, L. Moreschini, M. C. Falub, D. Pacilé, P. Bruno, K. Kern, and M. Grioni, "Giant spin splitting through surface alloying", Phys. Rev. Lett. **98**, 186807 (2007) 10.1103/PhysRevLett.98.186807.

[277] J. C. R. Sánchez, L. Vila, G. Desfonds, S. Gambarelli, J. P. Attané, J. M. de Teresa, C. Magén, and A. Fert, "Spin-to-charge conversion using Rashba coupling at the interface between non-magnetic materials", Nat. Commun. **4**, 2944 (2013) 10.1038/ncomms3944.

[278] J. Shen, Z. Feng, P. Xu, D. Hou, Y. Gao, and X. Jin, "Spin-to-charge conversion in Ag/Bi bilayer revisited", Phys. Rev. Lett. **126**, 197201 (2021) 10.1103/PhysRevLett.126.197201.

[279] N. A. Sinitsyn, "Semiclassical theories of the anomalous Hall effect", J. Phys. Condens. Matter **20**, 023201 (2008) 10.1088/0953-8984/20/02/023201.

[280] N. Nagaosa, J. Sinova, S. Onoda, A. H. MacDonald, and N. P. Ong, "Anomalous Hall effect", Rev. Mod. Phys. **82**, 1539 (2010) 10.1103/RevModPhys.82.1539.

[281] E. H. Hall, "On a new action of the magnet on electric currents", Am. J. Math. **2**, 287 (1879) 10.2307/2369245.

[282] B. F. Miao, S. Y. Huang, D. Qu, and C. L. Chien, "Inverse spin Hall effect in a ferromagnetic metal", Phys. Rev. Lett. **111**, 066602 (2013) 10.1103/PhysRevLett.111.066602.

[283] E. H. Hall, "XVIII. On the "rotational coefficient" in nickel and cobalt", Lond. Edinb. Dublin philos. mag. j. sci. **12**, 157 (1881) 10.1080/14786448108627086.

[284] M. I. Dyakonov and V. I. Perel, "Current-induced spin orientation of electrons in semiconductors", Phys. Lett. A **35**, 459 (1971) 10.1016/0375-9601(71)90196-4.

[285] Y. K. Kato, R. C. Myers, A. C. Gossard, and D. D. Awschalom, "Observation of the spin Hall effect in semiconductors", Science **306**, 1910 (2004) 10.1126/science.1105514.

[286] J. Wunderlich, B. Kaestner, J. Sinova, and T. Jungwirth, "Experimental observation of the spin-Hall effect in a two-dimensional spin-orbit coupled semiconductor system", Phys. Rev. Lett. **94**, 047204 (2005) 10.1103/PhysRevLett.94.047204.

[287] J. Smit, "The spontaneous Hall effect in ferromagnetics I", Phys. Technol. **21**, 877 (1955) 10.1016/S0031-8914(55)92596-9.

[288] J. Smit, "The spontaneous Hall effect in ferromagnetics II", Phys. Technol. **24**, 39 (1958) 10.1016/S0031-8914(58)93541-9.

[289] L. Berger, "Side-jump mechanism for the Hall effect of ferromagnets", Phys. Rev. B **2**, 4559 (1970) 10.1103/PhysRevB.2.4559.

[290] R. Karplus and J. M. Luttinger, "Hall effect in ferromagnetics", Phys. Rev. **95**, 1154 (1954) 10.1103/PhysRev.95.1154.

[291] M. Gradhand, D. V. Fedorov, P. Zahn, and I. Mertig, "Extrinsic spin Hall effect from first principles", Phys. Rev. Lett. **104**, 186403 (2010) 10.1103/PhysRevLett.104.186403.

[292] S. Lowitzer, M. Gradhand, D. Ködderitzsch, D. V. Fedorov, I. Mertig, and H. Ebert, "Extrinsic and intrinsic contributions to the spin Hall effect of alloys", Phys. Rev. Lett. **106**, 056601 (2011) 10.1103/PhysRevLett.106.056601.

[293] A. Fert and P. M. Levy, "Spin Hall effect induced by resonant scattering on impurities in metals", Phys. Rev. Lett. **106**, 157208 (2011) 10.1103/PhysRevLett.106.157208.

[294] X. Tao, Q. Liu, B. Miao, R. Yu, Z. Feng, L. Sun, B. You, J. Du, K. Chen, S. Zhang, L. Zhang, Z. Yuan, Di Wu, and H. Ding, "Self-consistent determination of spin Hall angle and spin diffusion length in Pt and Pd: The role of the interface spin loss", Sci. Adv. **4**, eaat1670 (2018) 10.1126/sciadv.aat1670.

[295] M. Isasa, E. Villamor, L. E. Hueso, M. Gradhand, and F. Casanova, "Temperature dependence of spin diffusion length and spin Hall angle in Au and Pt", Phys. Rev. B **91**, 024402 (2015) 10.1103/PhysRevB.91.024402.

[296] C.-F. Pai, L. Liu, Y. Li, H. W. Tseng, D. C. Ralph, and R. A. Buhrman, "Spin transfer torque devices utilizing the giant spin Hall effect of tungsten", Appl. Phys. Lett. **101**, 122404 (2012) 10.1063/1.4753947.

[297] T. Seifert, U. Martens, S. Günther, M. A. W. Schoen, F. Radu, X. Z. Chen, I. Lucas, R. Ramos, M. H. Aguirre, P. A. Algarabel, A. Anadón, H. S. Körner, J. Walowski, C. Back, M. R. Ibarra, L. Morellón, E. Saitoh, M. Wolf, C. Song, K. Uchida, M. Münzenberg, I. Radu, and T. Kampfrath, "Terahertz spin currents and inverse spin Hall effect in thin-film heterostructures containing complex magnetic compounds", SPIN **07**, 1740010 (2017) 10.1142/S2010324717400100.

[298] D. L. Mills, *Nonlinear optics* (Springer, Berlin and Heidelberg, Germany, 1998), ISBN: 978-3-540-64182-7, 10.1007/978-3-642-58937-9.

[299] R. Schneider, "Ultraschnelle spintronische THz-Emitter", Dissertation (Westfälische Wilhelms-Universität Münster, Münster, Germany, 2020).

[300] Y. Wu, M. Elyasi, X. Qiu, M. Chen, Y. Liu, L. Ke, and H. Yang, "High-performance THz emitters based on ferromagnetic/nonmagnetic heterostructures", Adv. Mater. **29**, 1603031 (2017) 10.1002/adma.201603031.

[301] Z. Feng, H. Qiu, D. Wang, C. Zhang, S. Sun, B. Jin, and W. Tan, "Spintronic terahertz emitter", J. Appl. Phys. **129**, 010901 (2021) 10.1063/5.0037937.

[302] E. T. Papaioannou and R. Beigang, "THz spintronic emitters: A review on achievements and future challenges", Nanophotonics **10**, 1243 (2021) 10.1515/nanoph-2020-0563.

[303] L. Cheng, Z. Li, D. Zhao, and E. E. M. Chia, "Studying spin–charge conversion using terahertz pulses", APL Mater. **9**, 070902 (2021) 10.1063/5.0051217.

[304] W. Wu, C. Yaw Ameyaw, M. F. Doty, and M. B. Jungfleisch, "Principles of spintronic THz emitters", J. Appl. Phys. **130**, 091101 (2021) 10.1063/5.0057536.

[305] T. S. Seifert, L. Cheng, Z. Wei, T. Kampfrath, and J. Qi, "Spintronic sources of ultrashort terahertz electromagnetic pulses", Appl. Phys. Lett. **120**, 180401 (2022) 10.1063/5.0080357.

[306] R. Adam, G. Chen, D. E. Bürgler, T. Shou, I. Komissarov, S. Heidtfeld, H. Hardtdegen, M. Mikulics, C. M. Schneider, and R. Sobolewski, "Magnetically and optically tunable terahertz radiation from Ta/NiFe/Pt spintronic nanolayers generated by femtosecond laser pulses", Appl. Phys. Lett. **114**, 212405 (2019) 10.1063/1.5099201.

[307] D. Khusyainov, S. Ovcharenko, M. Gaponov, A. Buryakov, A. Klimov, N. Tiercelin, P. Pernod, V. Nozdrin, E. Mishina, A. Sigov, and V. Preobrazhensky, "Polarization control of THz emission using spin-reorientation transition in spintronic heterostructure", Sci. Rep. **11**, 697 (2021) 10.1038/s41598-020-80781-5.

[308] P. Koleják, G. Lezier, K. Postava, J.-F. Lampin, N. Tiercelin, and M. Vanwolleghem, "360° polarization control of terahertz spintronic emitters using uniaxial FeCo/$TbCo_2$/FeCo trilayers", ACS Photonics **9**, 1274 (2022) 10.1021/acsphotonics.1c01782.

[309] G. Lezier, P. Koleják, J.-F. Lampin, K. Postava, M. Vanwolleghem, and N. Tiercelin, "Fully reversible magnetoelectric voltage controlled THz polarization rotation in magnetostrictive spintronic emitters on PMN-PT", Appl. Phys. Lett. **120**, 152404 (2022) 10.1063/5.0080372.

[310] P. Agarwal, R. Medwal, A. Kumar, H. Asada, Y. Fukuma, R. S. Rawat, M. Battiato, and R. Singh, "Ultrafast photo–thermal switching of terahertz spin currents", Adv. Funct. Mater. **31**, 2010453 (2021) 10.1002/adfm.202010453.

[311] D. Kong, X. Wu, B. Wang, T. Nie, M. Xiao, C. Pandey, Y. Gao, L. Wen, W. Zhao, C. Ruan, J. Miao, Y. Li, and L. Wang, "Broadband spintronic terahertz emitter with magnetic–field manipulated polarizations", Adv. Optical Mater. **7**, 1900487 (2019) 10.1002/adom.201900487.

[312] O. Gueckstock, L. Nádvorník, T. S. Seifert, M. Borchert, G. Jakob, G. Schmidt, G. Woltersdorf, M. Kläui, M. Wolf, and T. Kampfrath, "Modulating the polarization of broadband terahertz pulses from a spintronic emitter at rates up to 10 kHz", Optica **8**, 1013 (2021) 10.1364/OPTICA.430504.

[313] W. Wu, S. Lendinez, M. Taghipour Kaffash, R. D. Schaller, H. Wen, and M. B. Jungfleisch, "Modification of terahertz emission spectrum using microfabricated spintronic emitters", J. Appl. Phys. **128**, 103902 (2020) 10.1063/5.0013676.

[314] Y. Liu, Z. Bai, Y. Xu, X. Wu, Y. Sun, H. Li, T. Sun, R. Kong, C. Pandey, M. Kraft, Q. Song, W. Zhao, T. Nie, and L. Wen, "Generation of tailored terahertz waves from monolithic integrated metamaterials onto spintronic terahertz emitters", Nanotechnology **32**, 105201 (2021) 10.1088/1361-6528/abcc98.

[315] B. Wang, S. Shan, X. Wu, C. Wang, C. Pandey, T. Nie, W. Zhao, Y. Li, J. Miao, and L. Wang, "Picosecond nonlinear spintronic dynamics investigated by terahertz emission spectroscopy", Appl. Phys. Lett. **115**, 121104 (2019) 10.1063/1.5117179.

[316] M. Chen, Y. Wu, Y. Liu, K. Lee, X. Qiu, P. He, J. Yu, and H. Yang, "Current–enhanced broadband THz emission from spintronic devices", Adv. Opt. Mater. **7**, 1801608 (2019) 10.1002/adom.201801608.

[317] U. Nandi, M. S. Abdelaziz, S. Jaiswal, G. Jakob, O. Gueckstock, S. M. Rouzegar, T. S. Seifert, M. Kläui, T. Kampfrath, and S. Preu, "Antenna-coupled spintronic terahertz emitters driven by a 1550 nm femtosecond laser oscillator", Appl. Phys. Lett. **115**, 022405 (2019) 10.1063/1.5089421.

[318] E. T. Papaioannou, G. Torosyan, S. Keller, L. Scheuer, M. Battiato, V. K. Mag-Usara, J. L'huillier, M. Tani, and R. Beigang, "Efficient terahertz generation using Fe/Pt spintronic emitters pumped at different wavelengths", IEEE Trans. Magn. **54**, 9100205 (2018) 10.1109/TMAG.2018.2847031.

[319] R. I. Herapath, S. M. Hornett, T. S. Seifert, G. Jakob, M. Kläui, J. Bertolotti, T. Kampfrath, and E. Hendry, "Impact of pump wavelength on terahertz emission of a cavity-enhanced spintronic trilayer", Appl. Phys. Lett. **114**, 041107 (2019) 10.1063/1.5048297.

[320] R. Beigang, E. Papaioannou, L. Scheuer, S. Keller, G. Torosyan, M. Rahm, D. Sokoluk, M. Talara, Y. Oda, H. Kitahara, J. Afalla, V. K. Mag-usara, and M. Tani, "Efficient terahertz generation using Fe/Pt spintronic emitters pumped at different wavelengths", in Terahertz, RF, millimeter, and submillimeter-wave technology and applications XII, Vol. 10917, edited by L. P. Sadwick and T. Yang (2019), pp. 74 –80, ISBN: 9781510624764, 10.1117/12.2514564.

[321] T. J. Huisman, R. V. Mikhaylovskiy, J. D. Costa, F. Freimuth, E. Paz, J. Ventura, P. P. Freitas, S. Blügel, Y. Mokrousov, T. Rasing, and A. V. Kimel, "Femtosecond control of electric currents in metallic ferromagnetic heterostructures", Nat. Nanotechnol. **11**, 455 (2016) 10.1038/nnano.2015.331.

[322] G. Torosyan, S. Keller, L. Scheuer, R. Beigang, and E. T. Papaioannou, "Optimized spintronic terahertz emitters based on epitaxial grown Fe/Pt layer structures", Sci. Rep. **8**, 1311 (2018) 10.1038/s41598-018-19432-9.

[323] H. S. Qiu, K. Kato, K. Hirota, N. Sarukura, M. Yoshimura, and M. Nakajima, "Layer thickness dependence of the terahertz emission based on spin current in ferromagnetic heterostructures", Opt. Express **26**, 15247 (2018) 10.1364/OE.26.015247.

[324] G. Li, R. Medapalli, R. V. Mikhaylovskiy, F. E. Spada, T. Rasing, E. E. Fullerton, and A. V. Kimel, "THz emission from Co/Pt bilayers with varied roughness, crystal structure, and interface intermixing", Phys. Rev. Mater. **3**, 084415 (2019) 10.1103/PhysRevMaterials.3.084415.

[325] Y. Sasaki, Y. Takahashi, and S. Kasai, "Laser-induced terahertz emission in Co_2MnSi/Pt structure", Appl. Phys. Express **13**, 093003 (2020) 10.35848/1882-0786/abb1c9.

[326] T. J. Huisman, C. Ciccarelli, A. Tsukamoto, R. V. Mikhaylovskiy, T. Rasing, and A. V. Kimel, "Spin-photo-currents generated by femtosecond laser pulses in a ferrimagnetic GdFeCo/Pt bilayer", Appl. Phys. Lett. **110**, 072402 (2017) 10.1063/1.4976202.

[327] M. Chen, R. Mishra, Y. Wu, K. Lee, and H. Yang, "Terahertz emission from compensated magnetic heterostructures", Adv. Opt. Mater. **6**, 1800430 (2018) 10.1002/adom.201800430.

[328] H. Qiu, L. Zhou, C. Zhang, J. Wu, Y. Tian, S. Cheng, S. Mi, H. Zhao, Q. Zhang, Di Wu, B. Jin, J. Chen, and P. Wu, "Ultrafast spin current generated from an antiferromagnet", Nat. Phys. **17**, 388 (2021) 10.1038/s41567-020-01061-7.

[329] Y. Sasaki, K. Z. Suzuki, and S. Mizukami, "Annealing effect on laser pulse-induced THz wave emission in Ta/CoFeB/MgO films", Appl. Phys. Lett. **111**, 102401 (2017) 10.1063/1.5001696.

[330] T. S. Seifert, N. M. Tran, O. Gueckstock, S. M. Rouzegar, L. Nadvornik, S. Jaiswal, G. Jakob, V. V. Temnov, M. Münzenberg, M. Wolf, M. Kläui, and T. Kampfrath, "Terahertz spectroscopy for all-optical spintronic characterization of the spin-Hall-effect metals Pt, W and $Cu_{80}Ir_{20}$", J. Phys. D: Appl. Phys. **51**, 364003 (2018) 10.1088/1361-6463/aad536.

[331] O. Gueckstock, L. Nádvorník, M. Gradhand, T. S. Seifert, G. Bierhance, R. Rouzegar, M. Wolf, M. Vafaee, J. Cramer, M. A. Syskaki, G. Woltersdorf, I. Mertig, G. Jakob, M. Kläui, and T. Kampfrath, "Terahertz spin-to-charge conversion by interfacial skew

scattering in metallic bilayers", Adv. Mater. **33**, e2006281 (2021) 10.1002/adma.202006281.

[332] W.-T. Lu, Y. Zhao, M. Battiato, Y. Wu, and Z. Yuan, "Interface reflectivity of a superdiffusive spin current in ultrafast demagnetization and terahertz emission", Phys. Rev. B **101**, 1243 (2020) 10.1103/PhysRevB.101.014435.

[333] Q. Zhang, Y. Yang, Z. Luo, Y. Xu, R. Nie, X. Zhang, and Y. Wu, "Terahertz emission from an exchange-coupled synthetic antiferromagnet", Phys. Rev. Appl. **13**, 054016 (2020) 10.1103/PhysRevApplied.13.054016.

[334] Y. Ogasawara, Y. Sasaki, S. Iihama, A. Kamimaki, K. Z. Suzuki, and S. Mizukami, "Laser-induced terahertz emission from layered synthetic magnets", Appl. Phys. Express **13**, 063001 (2020) 10.35848/1882-0786/ab88c2.

[335] Z. Feng, R. Yu, Y. Zhou, H. Lu, W. Tan, H. Deng, Q. Liu, Z. Zhai, L. Zhu, J. Cai, B. Miao, and H. Ding, "Highly efficient spintronic terahertz emitter enabled by metal-dielectric photonic crystal", Adv. Opt. Mater. **6**, 1800965 (2018) 10.1002/adom.201800965.

[336] S. Swann, "Magnetron sputtering", Phys. Technol. **19**, 67 (1988) 10.1088/0305-4624/19/2/304.

[337] W. R. Grove, "VII. On the electro-chemical polarity of gases", Phil. Trans. R. Soc. **142**, 87 (1852) 10.1098/rstl.1852.0008.

[338] J. E. Greene, "Review article: Tracing the recorded history of thin-film sputter deposition: From the 1800s to 2017", J. Vac. Sci. Technol. A **35**, 05C204 (2017) 10.1116/1.4998940.

[339] P. Kelly and R. Arnell, "Magnetron sputtering: A review of recent developments and applications", Vacuum **56**, 159 (2000) 10.1016/S0042-207X(99)00189-X.

[340] R. K. Waits, "Planar magnetron sputtering", J. Vac. Sci. Technol. **15**, 179 (1978) 10.1116/1.569451.

[341] BESTEC GmbH, "Engineering drawings M4500C0003" (2016).

[342] BESTEC GmbH, "Instruction manual 450 deposition system: UHV sputter system, Universität Augsburg" (2016).

[343] M. Ohring, *Materials science of thin films: Deposition and structure*, 2. ed. (Academic Press, San Diego, CA, USA, 2002), ISBN: 978-0-12-524975-1.

[344] H. R. Verma, *Atomic and nuclear analytical methods: XRF, Mössbauer, XPS, NAA and Ion-Beam spectroscopic techniques* (Springer, Berlin and Heidelberg, Germany, 2007), ISBN: 978-3-540-30277-3.

[345] L. C. Feldman and J. M. Poate, "Rutherford backscattering and channeling analysis of interfaces and epitaxial structures", Annu. Rev. Mater. Sci. **12**, 149 (1982) 10.1146/annurev.ms.12.080182.001053.

[346] H. Bethe, "Zur Theorie des Durchgangs schneller Korpuskularstrahlen durch Materie", Ann. Phys. **397**, 325 (1930) 10.1002/andp.19303970303.

[347] H. Bethe, "Bremsformel für Elektronen relativistischer Geschwindigkeit", Z. Physik **76**, 293 (1932) 10.1007/BF01342532.

[348] W. K. Chu, J. W. Mayer, M.-A. Nicolet, T. M. Buck, G. Amsel, and F. Eisen, "Principles and applications of ion beam techniques for the analysis of solids and thin films", Thin Solid Films **17**, 1 (1973) 10.1016/0040-6090(73)90002-3.

[349] M. Mayer, "SIMNRA User's Guide" (1997).

[350] M. Mayer, "SIMNRA, a simulation program for the analysis of NRA, RBS and ERDA", AIP Conf Proc **475**, 541 (1999) 10.1063/1.59188.

[351] D. Shindo and T. Oikawa, *Analytical electron microscopy for materials science* (Springer, Tokyo, Japan, 2002), ISBN: 978-4-431-70336-5, 10.1007/978-4-431-66988-3.

[352] S. Ii, "Nanoscale chemical analysis in various interfaces with energy dispersive X-ray spectroscopy and transmission electron microscopy", in *X-Ray spectroscopy*, edited by S. K. Sharma (InTech, 2012), ISBN: 978-953-307-967-7, 10.5772/31645.

[353] Shimadzu Corporation, "EDX series instruction manual - Operation: Shimadzu energy dispersive X-ray flourescence spectrometer", (2009).

[354] J. Kerr, "XLIII. On rotation of the plane of polarization by reflection from the pole of a magnet", Lond. Edinb. Dublin philos. mag. j. sci. **3**, 321 (1877) 10.1080/14786447708639245.

[355] A. Hubert and R. Schäfer, *Magnetic domains: The analysis of magnetic microstructures* (Springer, Berlin, Germany, 2000), ISBN: 3-540-64108-4.

[356] Z. Q. Qiu and S. D. Bader, "Surface magneto-optic Kerr effect", Rev. Sci. Instrum. **71**, 1243 (2000) 10.1063/1.1150496.

[357] T. Popmintchev, M.-C. Chen, P. Arpin, M. M. Murnane, and H. C. Kapteyn, "The attosecond nonlinear optics of bright coherent X-ray generation", Nat. Photonics **4**, 822 (2010) 10.1038/nphoton.2010.256.

[358] J. C. Fuggle and N. Mårtensson, "Core-level binding energies in metals", J. Electron Spectrosc. Relat. Phenom. **21**, 275 (1980) 10.1016/0368-2048(80)85056-0.

[359] D. A. Shirley, R. L. Martin, S. P. Kowalczyk, F. R. McFeely, and L. Ley, "Core-electron binding energies of the first thirty elements", Phys. Rev. B **15**, 544 (1977) 10.1103/PhysRevB.15.544.

[360] F. Willems, S. Sharma, C. V Korff Schmising, J. K. Dewhurst, L. Salemi, D. Schick, P. Hessing, C. Strüber, W. D. Engel, and S. Eisebitt, "Magneto-optical functions at the 3p resonances of Fe, Co, and Ni: Ab initio description and experiment", Phys. Rev. Lett. **122**, 217202 (2019) 10.1103/PhysRevLett.122.217202.

[361] S. Jana, R. S. Malik, Y. O. Kvashnin, I. L. M. Locht, R. Knut, R. Stefanuik, I. Di Marco, A. N. Yaresko, M. Ahlberg, J. Åkerman, R. Chimata, M. Battiato, J. Söderström, O. Eriksson, and O. Karis, "Analysis of the linear relationship between asymmetry and magnetic moment at the M edge of 3d transition metals", Phys. Rev. Research **2**, 013180 (2020) 10.1103/PhysRevResearch.2.013180.

[362] C. Möller, H. Probst, J. Otto, K. Stroh, C. Mahn, S. Steil, V. Moshnyaga, G. S. M. Jansen, D. Steil, and S. Mathias, "Ultrafast element-resolved magneto-optics using a fiber-laser-driven extreme ultraviolet light source", Rev. Sci. Instrum. **92**, 065107 (2021) 10.1063/5.0050883.

[363] M. Cardona and L. Ley, *Photoemission in solids I* (Springer, Berlin and Heidelberg, Germany, 1978), ISBN: 978-3-540-08685-7, 10.1007/3-540-08685-4.

[364] R. L. Fagaly, "Superconducting quantum interference device instruments and applications", Rev. Sci. Instrum. **77**, 10.1063/1.2354545 (2006) 10.1063/1.2354545.

[365] J. Clarke and A. I. Braginski, *The SQUID handbook* (Wiley-VCH, Weinheim, Germany, 2004), ISBN: 3-527-40229-2.

[366] C. Granata and A. Vettoliere, "Nano superconducting quantum interference device: A powerful tool for nanoscale investigations", Phys. Rep. **614**, 1 (2016) 10.1016/j.physrep.2015.12.001.

[367] R. Doll and M. Näbauer, "Experimental proof of magnetic flux quantization in a superconducting ring", Phys. Rev. Lett. **7**, 51 (1961) 10.1103/PhysRevLett.7.51.

[368] B. S. Deaver and W. M. Fairbank, "Experimental evidence for quantized flux in superconducting cylinders", Phys. Rev. Lett. **7**, 43 (1961) 10.1103/PhysRevLett.7.43.

[369] B. D. Josephson, "Possible new effects in superconductive tunnelling", Phys. Lett. **1**, 251 (1962) 10.1016/0031-9163(62)91369-0.

[370] P. W. Anderson and J. M. Rowell, "Probable observation of the Josephson superconducting tunneling effect", Phys. Rev. Lett. **10**, 230 (1963) 10.1103/PhysRevLett.10.230.

[371] D. D. Coon and M. D. Fiske, "Josephson AC and step structure in the supercurrent tunneling characteristic", Phys. Rev. **138**, A744 (1965) 10.1103/PhysRev.138.A744.

[372] Quantum Design GmbH, "Magnetic property measurement system SQUID VSM user's manual: Part number 1500–100, A1" (2007).

[373] Quantum Design GmbH, "MPMS 3 oven option user's manual: Part number 1505–200, A2" (2016).

[374] M. Buchner, K. Höfler, B. Henne, V. Ney, and A. Ney, "Tutorial: Basic principles, limits of detection, and pitfalls of highly sensitive SQUID magnetometry for nanomagnetism and spintronics", J. Appl. Phys. **124**, 161101 (2018) 10.1063/1.5045299.

[375] Quantum Design GmbH, "Accuracy of the reported moment: Sample shape effects: SQUID VSM application note 1500–015" (2010).

[376] Quantum Design GmbH, "Using SQUID VSM superconducting magnets at low fields: Application note 1500–011" (2010).

[377] Quantum Design GmbH, "Accuracy of the reported moment: Axial and radial sample positioning error: Application note 1500–010" (2010).

[378] A.-O. Mandru, O. Yıldırım, M. A. Marioni, H. Rohrmann, M. Heigl, O.-T. Ciubotariu, M. Penedo, X. Zhao, M. Albrecht, and H. J. Hug, "Pervasive artifacts revealed from magnetometry measurements of rare earth-transition metal thin films", J. Vac. Sci. Technol. A **38**, 023409 (2020) 10.1116/1.5135504.

[379] R. Szewczyk, "Technical B-H saturation magnetization curve models for SPICE, FEM and MoM simulations", J. Autom. Mob. Robot. Intell. Syst. **10**, 3 (2016) 10.14313/JAMRIS_2-2016/10.

[380] M. Sharrock and J. McKinney, "Kinetic effects in coercivity measurements", IEEE Trans. Magn. **17**, 3020 (1981) 10.1109/TMAG.1981.1061755.

[381] D. K. Schroder, *Semiconductor material and device characterization*, 3. ed. (IEEE Press Wiley-Interscience and IEEE Xplore, Hoboken and Piscataway, NJ, USA, 2006), ISBN: 9780471739067, 10.1002/0471749095.

[382] F. Wenner, "A method of measuring earth resistivity", Bull. Natl. Bur. Stand. **12**, 469 (1915) 10.6028/bulletin.282.

[383] L. Valdes, "Resistivity measurements on germanium for transistors", Proc. IRE **42**, 420 (1954) 10.1109/JRPROC.1954.274680.

[384] R. Schneider, M. Fix, R. Heming, S. Michaelis de Vasconcellos, M. Albrecht, and R. Bratschitsch, "Magnetic-field-dependent THz emission of spintronic TbFe/Pt layers", ACS Photonics **5**, 3936 (2018) 10.1021/acsphotonics.8b00839.

[385] Q. Wu and X.-C. Zhang, "Free–space electro–optic sampling of terahertz beams", Appl. Phys. Lett. **67**, 3523 (1995) 10.1063/1.114909.

[386] A. Nahata, D. H. Auston, T. F. Heinz, and C. Wu, "Coherent detection of freely propagating terahertz radiation by electro–optic sampling", Appl. Phys. Lett. **68**, 150 (1996) 10.1063/1.116130.

[387] T. S. Narasimhamurty, *Photoelastic and electro-optic properties of crystals* (Springer, Boston, MA, USA, 1981), ISBN: 978-1-4757-0027-5, 10.1007/978-1-4757-0025-1.

[388] Q. Wu, M. Litz, and X.-C. Zhang, "Broadband detection capability of ZnTe electro–optic field detectors", Appl. Phys. Lett. **68**, 2924 (1996) 10.1063/1.116356.

[389] Q. Wu and X.-C. Zhang, "7 terahertz broadband GaP electro-optic sensor", Appl. Phys. Lett. **70**, 1784 (1997) 10.1063/1.118691.

[390] Q. Wu and X.-C. Zhang, "Free-space electro-optics sampling of mid-infrared pulses", Appl. Phys. Lett. **71**, 1285 (1997) 10.1063/1.119873.

[391] R. Schneider, M. Fix, J. Bensmann, S. Michaelis de Vasconcellos, M. Albrecht, and R. Bratschitsch, "Composition-dependent ultrafast THz emission of spintronic CoFe/Pt thin films", Appl. Phys. Lett. **120**, 042404 (2022) 10.1063/5.0076699.

[392] L. Gan, R. D. Gomez, C. J. Powell, R. D. McMichael, P. J. Chen, and W. F. Egelhoff, "Thin Al, Au, Cu, Ni, Fe, and Ta films as oxidation barriers for Co in air", J. Appl. Phys. **93**, 8731 (2003) 10.1063/1.1543873.

[393] J. K. Lang, Y. Baer, and P. A. Cox, "Study of the 4f and valence band density of states in rare-earth metals. II. Experiment and results", Phys. Rev. Lett. **11**, 121 (1981) 10.1088/0305-4608/11/1/015.

[394] R. Schneider, M. Fix, J. Bensmann, S. Michaelis de Vasconcellos, M. Albrecht, and R. Bratschitsch, "Spintronic GdFe/Pt THz emitters", Appl. Phys. Lett. **115**, 152401 (2019) 10.1063/1.5120249.

[395] L. Oroszlány, A. Deák, E. Simon, S. Khmelevskyi, and L. Szunyogh, "Magnetism of gadolinium: A first-principles perspective", Phys. Rev. Lett. **115**, 096402 (2015) 10.1103/PhysRevLett.115.096402.

[396] A. B. Shick, W. E. Pickett, and C. S. Fadley, "Electron correlation effects and magnetic ordering at the Gd(0001) surface", Phys. Rev. B **61**, R9213 (2000) 10.1103/PhysRevB.61.R9213.

[397] T. S. Seifert, U. Martens, F. Radu, M. Ribow, M. Berritta, L. Nádvorník, R. Starke, T. Jungwirth, M. Wolf, I. Radu, M. Münzenberg, P. M. Oppeneer, G. Woltersdorf, and T. Kampfrath, "Frequency-independent terahertz anomalous Hall effect in $DyCo_5$, $Co_{32}Fe_{68}$, and $Gd_{27}Fe_{73}$ thin films from DC to 40 THz", Adv. Mater. **33**, e2007398 (2021) 10.1002/adma.202007398.

[398] M. Hartmann and T. R. McGuire, "Relationship between Faraday rotation and Hall effect in amorphous rare-earth-transition-metal alloys", Phys. Rev. Lett. **51**, 1194 (1983) 10.1103/PhysRevLett.51.1194.

[399] T. Stobiecki, K. Kowalski, and Z. Obuszko, "Charge transfer and Hall effect in amorphous GdCo, GdCoMo and GdFe films", Physica B+C **130**, 94 (1985) 10.1016/0378-4363(85)90194-9.

[400] Q. Zhang, Z. Luo, H. Li, Y. Yang, X. Zhang, and Y. Wu, "Terahertz emission from anomalous Hall effect in a single-layer ferromagnet", Phys. Rev. Appl. **12**, 054027 (2019) 10.1103/PhysRevApplied.12.054027.

[401] M. Fix, R. Schneider, J. Bensmann, S. Michaelis de Vasconcellos, R. Bratschitsch, and M. Albrecht, "Thermomagnetic control of spintronic THz emission enabled by ferrimagnets", Appl. Phys. Lett. **116**, 012402 (2020) 10.1063/1.5132624.

[402] R. C. Taylor, "Magnetic properties of amorphous Gd–Fe films prepared by evaporation", J. Appl. Phys. **47**, 1164 (1976) 10.1063/1.322698.

[403] S. R. Lee, A. E. Miller, and H. A. Blackstead, "Ferromagnetic resonance behavior of evaporated Gd–Fe alloy films", J. Appl. Phys. **60**, 3982 (1986) 10.1063/1.337521.

[404] E. Jesenská, T. Ishibashi, L. Beran, M. Pavelka, J. Hamrle, R. Antoš, J. Zázvorka, and M. Veis, "Optical and magneto-optical properties of Gd_xFe_{100-x} thin films close to the compensation point", Sci. Rep. **9**, 16547 (2019) 10.1038/s41598-019-52252-z.

[405] R. C. Bhatt, L.-X. Ye, Y.-C. Luo, and T.-h. Wu, "Study of RE_xFe_{100-x} (RE = Tb, Dy, Gd) ferrimagnets for SOT application", J. Appl. Phys. **125**, 113902 (2019) 10.1063/1.5090852.

[406] V. E. Rogalin, I. A. Kaplunov, and G. I. Kropotov, "Optical materials for the THz range", Opt. Spectrosc. **125**, 1053 (2018) 10.1134/S0030400X18120172.

[407] J. Li, Z. Jin, B. Song, S. Zhang, C. Guo, C. Wan, X. Han, Z. Cheng, C. Zhang, X. Lin, G. Ma, and J. Yao, "Magnetic-field-free terahertz emission from a magnetic tunneling junction", Jpn. J. Appl. Phys. **58**, 090913 (2019) 10.7567/1347-4065/ab3b75.

[408] M. Fix, R. Schneider, S. Michaelis de Vasconcellos, R. Bratschitsch, and M. Albrecht, "Spin valves as magnetically switchable spintronic THz emitters", Appl. Phys. Lett. **117**, 132407 (2020) 10.1063/5.0025746.

[409] R. Nakatani, H. Hoshiya, K. Hoshino, and Y. Sugita, "Exchange coupling in (Mn–Ir, Fe–Mn)/Co/Ni–Fe multilayers", Jpn. J. Appl. Phys. **38**, 722 (1999) 10.1143/JJAP.38.722.

[410] H. Yoda, H. Iwasaki, T. Kobayashi, A. Tsutai, and M. Sahashi, "Dual-element GMR/inductive heads for gigabits density recording using CoFe spin-valves", IEEE Trans. Magn. **32**, 3363 (1996) 10.1109/20.538627.

[411] H. S. Tarazona, W. Alayo, C. V. Landauro, and J. Quispe-Marcatoma, "Effect of the strong coupling on the exchange bias field in IrMn/Py/Ru/Co spin valves", J. Magn. Magn. Mater. **446**, 44 (2018) 10.1016/j.jmmm.2017.09.004.

[412] A. Anguelouch, B. D. Schrag, G. Xiao, Y. Lu, P. L. Trouilloud, R. A. Wanner, W. J. Gallagher, and S. S. P. Parkin, "Two-dimensional magnetic switching of micron-size films in magnetic tunnel junctions", Appl. Phys. Lett. **76**, 622 (2000) 10.1063/1.125838.

[413] I. Berthold, U. Löschner, J. Schille, R. Ebert, and H. Exner, "Exchange bias realignment using a laser-based direct-write technique", Phys. Procedia **56**, 1136 (2014) 10.1016/j.phpro.2014.08.028.

[414] I. Berthold, M. Müller, R. Ebert, J. Schille, U. Löschner, H. Exner, P. Matthes, and M. Albrecht, "Selective realignment of the exchange biased magnetization direction in spintronic layer stacks using continuous and pulsed laser radiation", Proc. of SPIE **8967**, 89671F (2014) 10.1117/12.2039487.

[415] I. Berthold, M. Müller, S. Klötzer, R. Ebert, S. Thomas, P. Matthes, M. Albrecht, and H. Exner, "Investigation of selective realignment of the preferred magnetic direction in spin-valve layer stacks using laser radiation", Appl. Surf. Sci. **302**, 159 (2014) 10.1016/j.apsusc.2014.02.133.

APPENDIX C

Abbreviations

AFM	antiferromagnetic
AHE	anomalous Hall effect
BL	blocked
DC	direct current
DMI	Dzyaloshinsky-Moriya interaction
EA	magnetic easy axis
EB	exchange bias
EDX	energy-dispersive X-ray spectroscopy
EUV	extreme ultraviolet
FC	field cooled
FI	ferrimagnetic
FM	ferromagnetic
GMR	giant magneto resistance
IB	insulating barrier
ip	in-plane
IREE	inverse Rashba-Edelstein effect
ISHE	inverse spin Hall effect
MOKE	magneto optical Kerr effect
MPMS	Magnetic Properties Measurement System
NM	non-magnetic metal
oop	out-of-plane
OR	optical rectification
PCA	photoconductive antenna
PM	paramagnetic
P-MOKE	polar magneto optical Kerr effect
RBS	Rutherford backscattering spectroscopy
RE	rare earth

RF	radio frequency
RKKY	Ruderman–Kittel–Kasuya–Yosida
RMS	root mean square
SHE	spin Hall effect
SP	superparamagnetic
SSE	spin(-dependent) Seebeck effect
SQUID	superconducting quantum interference device
SQUID-VSM	superconducting quantum interference device-vibrating sample magnetometer
TEM	transmission electron microscope
THz	terahertz
THz-TDS	terahertz time domain spectroscopy
TM	transition metal
T-MOKE	transversal magneto optical Kerr effect
ZFC	zero field cooled

APPENDIX D

Publication list

D.1 Publications included in this work

[1] R. Schneider*, **M. Fix***, Jannis Bensmann, S. Michaelis de Vasconcellos, M. Albrecht and R. Bratschitsch, "Composition-dependent ultrafast THz emission of spintronic CoFe/Pt thin films", Appl. Phys. Lett. **120**, 042404 (2022) 10.1063/5.0076699.

[2] **M. Fix***, R. Schneider*, S. Michaelis de Vasconcellos, R. Bratschitsch and M. Albrecht, "Spin valves as magnetically switchable spintronic THz emitters", Appl. Phys. Lett. **117**, 132407 (2020) 10.1063/5.0025746 (paper was selected as an "Editor's Pick").

[3] **M. Fix***, R. Schneider*, J. Bensmann, S. Michaelis de Vasconcellos, R. Bratschitsch and M. Albrecht, "Thermomagnetic control of spintronic THz emission enabled by ferrimagnets", Appl. Phys. Lett. **116**, 012402 (2020) 10.1063/1.5132624 (paper was selected as "Featured").

[4] R. Schneider*, **M. Fix***, J. Bensmann, S. Michaelis de Vasconcellos, M. Albrecht and R. Bratschitsch, "Spintronic GdFe/Pt THz emitters, Appl. Phys. Lett. **115**", 152401 (2019) 10.1063/1.5120249 (paper was selected as an "Editor's Pick").

[5] R. Schneider, **M. Fix**, R. Heming, S. Michaelis de Vasconcellos, M. Albrecht and R. Bratschitsch, "Magnetic-field-dependent THz emission of spintronic TbFe/Pt layers", ACS Photonics **5**, 3936 (2018) 10.1021/acsphotonics.8b00839.

* These authors contributed equally to this work.

D.2 Publications not included in this work

[1] B. Carey, N. K. Wessling, P. Steeger, C. Klusmann, R. Schneider, **M. Fix**, R. Schmidt, M. Albrecht, S. Michaelis de Vasconcellos, R. Bratschitsch, A. Arora, "High-performance broadband Faraday rotation spectroscopy of 2D materials and thin magnetic films", arXiv:2204.12809 [cond-mat.mes-hall] (2022) 10.48550/arXiv.2204.12809.

[2] R. Hosseinifar, E. Golias, I. Kumberg, Q. Guillet, K. Frischmuth, S. Thakur, **M. Fix**, M. Albrecht, F. Kronast, W. Kuch, "Influence of magnetic domain walls on all-optical magnetic toggle switching in a ferrimagnetic GdFe film", Beilstein J. Nanotechnol. **13**, 74 (2022) 10.3762/bjnano.13.5.

[3] P. B. Aravind, M. Heigl, **M. Fix**, F. Groß, J. Gräfe, A. Mary, C. R. Rajgowrav, M. Krupiński, M. Marszałek, S. Thomas, M. R. Anantharaman and M. Albrecht, "Bistability of magnetic states in Fe-Pd nanocap arrays", Nanotechnology **30**, 405705 (2019) 10.1088/1361-6528/ab2d7f.

APPENDIX E

Conference contributions

06/2022	International Conference on Nanostructured Materials (NANO), Sevilla (ES), "Composition-dependent ultrafast THz emission of spintronic Co_xFe_{1-x}/Pt thin films", oral contribution
01/2022	Joint Magnetism and Magnetic Materials Conference and International Magnetics Conference (MMM-INTERMAG), virtual conference, "Magnetically switchable spintronic terahertz emitters", oral contribution
06/2021	The European Conference Physics of Magnetism (PM), virtual conference, "Magnetically switchable spintronic terahertz emitters", oral contribution (award for the best oral contribution)
11/2020	Magnetism and Magnetic Materials Conference (MMM), virtual conference, "Thermomagnetic control of spintronic THz emission enabled by ferrimagnets", oral contribution
11/2019	Magnetism and Magnetic Materials Conference (MMM), Las Vegas (US), "Composition-dependent spintronic THz emission of rare earth-transition metal alloys combined with Pt", poster contribution
08/2019	Joint European Magnetic Symposia (JEMS), Uppsala (SE), "Composition-dependent THz emission of spintronic $Tb_{1-x}Fe_x$/Pt bilayers", oral contribution
05/2019	LIV Zakopane School of Physics, Zakopane (PL), "Composition-dependent THz emission of $Tb_{1-x}Fe_x$/Pt bilayers", oral contribution

E Conference contributions

04/2019 DPG Spring Meeting of the Condensed Matter Section, Regensburg (DE), "Composition-dependent THz emission of $Tb_{1-x}Fe_x$/Pt bilayers", oral contribution

09/2018 European School on Magnetism (ESM), Krakow (PL), "Magnetic-field-dependent THz emission of spintronic Tb_xFe_{1-x}/Pt bilayers", poster contribution

09/2018 Joint European Magnetic Symposia (JEMS), Mainz (DE), "Hysteresis-free switching between collinear and vortex states in closely packed FePd cap arrays", poster contribution

08/2018 Spins Waves and Interactions Symposium, Greifswald (DE), "Magnetic-field-dependent THz emission of spintronic Tb_xFe_{1-x}/Pt bilayers", poster contribution

APPENDIX F

Acknowledgments

At this point, I would like to thank all the people without whose help I wouldn't have been able to finish this work successfully. However, such a list will never be complete and also not be capable of expressing all my gratitude to the persons I mention.

My special thanks go to Prof. Manfred Albrecht for giving me the opportunity to do this research in the magnetism group of his chair Experimental Physics IV at the University of Augsburg. I very much appreciated the freedom and motivation he gives his PhD students to try out different ideas and his support for their realization. Whenever I had open questions regarding my research, he always took the time to discuss the results and helped me with his enormous knowledge about magnetic thin film systems. I'm furthermore thankful that I got the opportunity to participate in many conferences and visit our cooperating groups worldwide. It is also due to his way of leading the chair that the working atmosphere at EP IV is amazing. I would also like to thank Prof. Rudolf Bratschitsch from the University of Münster for being my second reviewer and for all the fruitful discussions during the many zoom meetings. Without the collaboration with his group, this work would have never been possible.

Further thanks go to all other cooperators at the University of Münster who helped me realize this work. In particular, the many discussions with Dr. Robert Schneider, who also performed most of the THz spectroscopy experiments, led to the understanding of at least most of our investigated spintronic emitter systems. Moreover, this work was only enabled by him setting up the utilized THz measurement setups. I would also like to mention Jannis Bensmann for his contribution to the measurements and Dr. Steffen Michaelis de Vasconcellos for his helpful input on our publications and the discussions in our meetings.

Especially, I want to thank all of my colleagues at EP IV who helped create the best working atmosphere you can think of and made the time during my PhD research unforgettable.

For all the technical support, I want to thank all of the current and former technicians at EP IV, Wolfgang Reiber, Birgit Knoblich, Olga Lik, Wolfgang Brückner, Simon Stork, and

Fabian Hirschberger. In particular, I would like to mention Wolfgang Reiber for performing the RBS measurements for this work, Birgit Knoblich for the TEM sample preparation, and Olga Lik for taking care of the MPMS3 and the Bestec sputter chamber. Further thanks go to Bettina Schestak and Claudia Löflath for their constant support regarding all bureaucratic and organization questions.

Additionally, I want to thank Dr. Aladin Ullrich for performing the TEM measurements, Florian Jung for doing the SEM measurements, Dr. Felix Timmermann for building and introducing me to the Dampfechse, Theodor Grünwald for his helpfulness whenever any problem appeared, and Dr. Marc Lindorf for introducing me to some of the measurement devices.

All my current and former colleagues of the magnetism group Dr. Clemens Mühlenhoff, Dr. Nataliia Schmidt, Dr. Mariam Hassan, Dr. Michal Krupiński, Timo Schmidt, and especially my office neighbors Michael Heigl, Johannes Seyd, Dr. Oana-Tereza Ciubotariu, and Christian Holzmann I want to thank for the constant exchange regarding all kinds of magnetism "problems". Especially all the discussions in our office helped me a lot in getting a better understanding of magnetism in general. However, the essential point is that I enjoyed the excellent company in the office that made it always a pleasure for me to go there.

Further thanks go to my master and bachelor students Ahmad Reza Etemadi and Michael Kühn. It was a pleasure working with you.

Besides the help regarding my research, what I appreciated most about my time at EP IV was that I got to know all these wonderful people with whom I really enjoy spending my time, not only at the university but also privately. The regular D&D evenings with Johannes, Marc, Felix, Julian, Michi that also helped me for a smooth start at the chair and accompanied my whole PhD time, the many sauna evenings at Theos house, all the wine tastings, playing music with Flo and Manu, and also sharing a flat with Felix and later on with Flo contributed to a perfect PhD time.

Furthermore, I want to thank my brother Manuel for proofreading my work, for many discussions about various physics problems, and for his mostly constructive but sometimes also nasty comments, and Ina for providing him the time to do so.

Last, I also want to thank my family, especially my parents, and all of my friends for supporting me during my whole life. Most of all, I'm grateful to Viana for taking the load off from me, in particular by taking care of our son Niko, during the time I was writing this thesis. You and Niko are the greatest possible enrichment in my life!